Yu-Shiba-Rusinov States of Molecules on Pb(100)

Dissertation

zur Erlangung des Doktorgrades
der Mathematisch-Naturwissenschaftlichen Fakultät
der Christian-Albrechts-Universität zu Kiel

vorgelegt von

Jan Benedikt Homberg

Kiel, 2022

Erster Gutachter: Prof. Dr. Richard Berndt

Zweiter Gutachter: Prof. Dr. Kai Rossnagel

Dritte Gutachterin: Prof. Dr. Katharina J. Franke

Tag der mündlichen Prüfung: 13.07.2022

Eidesstattliche Erklärung

Hiermit erkläre ich, dass ich diese Arbeit - abgesehen von der Beratung durch meine wissenschaftlichen Betreuer - nach Inhalt und Form eigenständig angefertigt habe. Es wurden ausschließlich die im Text angegebenen Hilfsmittel verwendet. Diese Arbeit wurde weder ganz noch in Teilen an anderer Stelle im Rahmen eines Prüfungsverfahrens vorgelegt, veröffentlicht oder zur Veröffentlichung eingereicht. Frühere Promotionsversuche wurden von mir nicht unternommen. Mir wurde bisher kein akademischer Grad entzogen und es ist auch kein Verfahren dazu im Gange. Die Arbeit ist unter Einhaltung der Regeln guter wissenschaftlicher Praxis der Deutschen Forschungsgemeinschaft entstanden.

Folgende Teile der Arbeit wurden in wissenschaftlichen Fachzeitschriften veröffentlicht oder zur Veröffentlichung eingereicht:

- **Section 4.1:**
  Jan Homberg, Alexander Weismann, Richard Berndt und Manuel Gruber.
  Inducing and Controlling Molecular Magnetism through Supramolecular Manipulation.
  ACS Nano, **14**(12):17387–17395 (Nov 2020).
- **Section 5.3:**
  Jan Homberg, Alexander Weismann, Troels Markussen und Richard Berndt.
  Resonance-enhanced Vibrational Spectroscopy of Molecules on a Superconductor.
  eingereicht bei PRL; zur Veröffentlichung angenommen (Jul 2022).

Kiel, den

Jan Benedikt Homberg

Zusammenfassung

In dieser Arbeit werden (Metall-)Phthalocyanin-Moleküle, welche auf einer supraleitenden Pb(100) Oberfläche adsorbiert sind, mittels Tieftemperatur-Rastertunnelmikroskopie (STM) untersucht. Obwohl die Moleküle in der Gasphase diamagnetisch sind, entwickeln sie ein magnetisches Nettomoment, wenn sie zu Supramolekülen zusammengefügt werden oder sich zu selbstgeordneten Inseln gruppieren. Dies wird durch die Beobachtung von Yu-Shiba-Rusinov (YSR)-Zuständen deutlich.

Um dieses Phänomen zu untersuchen, werden H_2-Phthalocyanin (H_2Pc)-Supramoleküle durch Manipulation mit der STM-Spitze manuell auf der Oberfläche zusammengesetzt. Es wird gezeigt, dass sich das niedrigste unbesetzte Molekülorbital (LUMO) des zentralen Moleküls in Richtung des Fermi-Niveaus verschiebt und teilweise besetzt wird, was zu dem für den YSR-Zustand ursächlichen magnetischen Moment führt. Diese Interpretation wird mit Messungen des differentiellen Leitwerts untermauert, die zeigen, dass die laterale Verteilung des YSR-Zustands der Form des LUMOs folgt. Die beobachteten YSR-Zustände und LUMO-Resonanzen werden im Detail untersucht und mit Hilfe von Dichtefunktionaltheorie (DFT)-Rechnungen wird ein phänomenologisches Modell entwickelt, das die zugrunde liegenden molekularen Wechselwirkungen erklärt. Es wird gezeigt, dass elektrostatische Wechselwirkungen eine wichtige Rolle spielen, während Hybridisierung zwischen den Molekülen vernachlässigbar ist. Die magnetischen Momente werden darüber hinaus durch gezielte Relokalisierung der inneren Wasserstoffatome benachbarter H_2Pc-Moleküle fein abgestimmt.

Des Weiteren werden Blei-Phthalocyanin (PbPc)-Moleküle auf Pb(100) untersucht. Es wird gezeigt, dass diese Moleküle durch einen ähnlichen Mechanismus YSR-Zustände aufweisen, die im Vergleich zu H_2Pc ausgeprägter sind. Der Einfluss verschiedener Adsorptionsgeometrien und Nachbarmoleküle wird im Detail untersucht. Dabei werden Hinweise auf einen möglichen Einfluss der elektrostatischen Dipole molekularer Nachbarn gefunden. Mittels Abgleich einer Bogoliubov-de Gennes Modellfunktion mit den experimentellen YSR-Spektren werden Kopplungsparameter des Systems bestimmt.

Darüber hinaus werden die scharfen YSR-Resonanzen eingesetzt, um Molekülschwingungen von PbPc mittels inelastischer Elektronentunnelspektroskopie (IETS) zu untersuchen. Im Vergleich zu früheren Messungen wird eine deutlich höhere Empfindlichkeit erzielt, wodurch 46 verschiedene Schwingungsanregungen beobachtet werden. Ein Vergleich mit DFT-Rechnungen von Molekülen auf der Oberfläche zeigt eine gute Übereinstimmung, die eine Zuordnung der beobachteten Moden erlaubt. Die hohe spektrale Energieauflösung wird genutzt, um Energieverschiebungen der Schwingungsmoden zu untersuchen, die durch die Anwesenheit der STM-Spitze, durch verschiedene Nachbarmoleküle oder durch das Hinzufügen zusätzlicher Nachbarmoleküle verursacht werden. Außerdem werden räumliche Intensitätsverteilungen verschiedener Schwingungsmoden gemessen und mit Rechnungsergebnissen verglichen.

Ergänzend werden Untersuchungen an drei weiteren Molekülen mit YSR-Zuständen gezeigt. Ein noch nicht identifiziertes Molekül bildet selbstorganisierte Supramoleküle in Verbindung mit H_2Pc, wodurch dessen YSR-Zustände beeinflusst werden. Aluminium-Phthalocyanin (AlPc)-Moleküle auf Pb(100) weisen ein ähnliches Verhalten auf wie H_2Pc und erlangen ebenfalls ein magnetisches Nettomoment, nachdem sie zu einem Supramolekül zusammengefügt wurden. YSR-verstärkte IETS-Messungen von Schwingungsanregungen an AlPc werden mit den Ergebnissen von PbPc verglichen. YSR-Zustände an der STM-Spitze werden durch die Aufnahme einzelner Manganphthalocyanin (MnPc)-Moleküle erreicht, was für zukünftige Studien interessant sein könnte. Darüber hinaus wird eine Au-Pb-Oberfläche auf Pb(100) untersucht.

Schließlich wird der Zusammenbau, Test und Neuentwurf einer selbstgebauten NEG-Pumpe gezeigt (NEG: non-evaporable getter). Sie wird mit anderen NEG-Pumpen verglichen und die Vor- und Nachteile gegenüber vergleichbaren kommerziellen Pumpen werden erörtert.

Abstract

In this thesis, (metal-)phthalocyanine molecules adsorbed on a superconducting Pb(100) surface are investigated with low-temperature scanning tunneling microscopy (STM). Although the molecules are originally diamagnetic, they acquire a net magnetic moment upon assembly into supramolecules or within self-assembled islands. This effect is revealed by the observation of Yu-Shiba-Rusinov (YSR) resonances on the respective molecules.
To study this phenomenon, H_2-phthalocyanine (H_2Pc) supramolecules are manually assembled on the surface via manipulation with the STM tip. It is shown that the lowest unoccupied molecular orbital (LUMO) of the central molecule shifts toward the Fermi level and thus becomes partially filled, which results in the net magnetic moment responsible for the YSR state. To reinforce this interpretation, differential conductance measurements are presented, which demonstrate that the lateral distribution of the YSR state follows the shape of the LUMO. The observed YSR states and LUMO resonances are analyzed in detail, and with support from density functional theory (DFT) calculations a phenomenological model is developed that explains the underlying molecular interactions. It is shown that electrostatic interactions play an important role while hybridization between the molecules is negligible. The magnetic moments are furthermore finely tuned by targeted repositioning of the inner hydrogen atoms of neighboring H_2Pc molecules.
In addition, lead phthalocyanine (PbPc) molecules on Pb(100) are investigated. It is shown that these molecules exhibit YSR states due to a similar mechanism. However, more pronounced YSR states are observed on PbPc compared to H_2Pc. The influence of different adsorption geometries and neighbor molecules is studied in detail, revealing a possible influence of the electrostatic dipole moments of molecular neighbors. Coupling parameters of the system are obtained by fitting a Bogoliubov-de Gennes (BdG) model function to experimental YSR spectra.
Furthermore, the sharp YSR resonances are utilized for inelastic electron tunneling spectroscopy (IETS) of molecular vibrations of PbPc. A significantly higher sensitivity is obtained compared to earlier experiments, and thus 46 separate vibrational excitations are observed. Good agreement is found in comparison with results from on-surface DFT calculations allowing an assignment of the observed modes. The high spectral energy resolution is used to study energy shifts of the vibrational modes caused by the presence of the STM tip, by different neighbor molecules, or by adding neighbor molecules. Moreover, intensity maps of different vibrational modes are measured and compared to calculation results.

Supplementary, three other molecules carrying YSR states are investigated. A yet unidentified molecule forms self-assembled supramolecules in combination with H_2Pc, affecting its YSR states. Aluminum phthalocyanine (AlPc) molecules on Pb(100) show a similar behavior as H_2Pc by acquiring a net magnetic moment and YSR states upon cluster assembly. YSR enhanced IETS measurements of vibrational excitations on AlPc are compared to the results from PbPc. YSR states on the STM tip are achieved by picking up single manganese phthalocyanine (MnPc) molecules, which may be interesting for future studies. In addition, a Au-Pb surface layer on Pb(100) is investigated.

Finally, the construction, test, and redesign of a home-built non evaporable getter (NEG) pump is presented. It is compared to other NEG pumps and the pros and cons to comparable commercially available pumps are discussed.

Contents

List of Figures

List of Tables

List of Abbreviations

AES	Auger electron spectroscopy
BCS	Bardeen-Cooper-Schrieffer
BdG	Bogoliubov-de Gennes
DFT	density functional theory
DOS	density of states
FWHM	full width at half maximum
HOMO	highest occupied molecular orbital
IETS	inelastic electron tunneling spectroscopy
LDOS	local density of states
LUMO	lowest unoccupied molecular orbital
LUSO	lowest unoccupied supramolecular orbital
MAR	multiple Andreev reflections
NEG	non evaporable getter
NN	nearest neighbors
NNN	next nearest neighbors
SQUID	superconducting quantum interference device
STM	scanning tunneling microscope/microscopy
STS	scanning tunneling spectroscopy
TMP	turbomolecular pump
UHV	ultra-high vacuum
YSR	Yu-Shiba-Rusinov

Molecules

AlPc	aluminum phthalocyanine
ClAlPc	chlorinated aluminum phthalocyanine
CoPc	cobalt phthalocyanine
CuPc	copper phthalocyanine
FePc	iron phthalocyanine
H_0Pc	phthalocyanine with an empty macrocycle (i. e. Pc^{2-})
PbPc	lead phthalocyanine
Pc / H_2Pc	phthalocyanine
MPc	metal phthalocyanine
MnPc	manganese phthalocyanine
MX	molecule X: unknown molecule (see Section A.1)
NiPc	nickel phthalocyanine
SnPc	tin phthalocyanine
ZnPc	zinc phthalocyanine

Chapter 1
Introduction

Yu-Shiba-Rusinov (YSR) states occur when magnetic impurities, e. g., single atoms or molecules, interact with a superconducting substrate. The magnetic moment of the impurity induces a pair-breaking potential for the Cooper pairs of the substrate, leading to quasiparticle excitations inside the superconducting energy gap. This phenomenon was first theoretically predicted by Yu[1], Shiba[2], and Rusinov[3] in the late 1960s.

YSR states have gained a lot of interest in the recent years since it was realized that they may serve as building blocks for topological phases[4–6]. Majorana fermions emerge at the boundaries of topological superconductors[7] and may open the route to topological quantum computing, a theoretical concept proposed by Kitaev in 1997 [8]. A major advantage of topological quantum computing over the most common approaches to quantum computing is that it inherently avoids decoherence[9]. A possible realization of Majorana bound states at the end of atomic chains on the surface of a superconductor was suggested by Nadj-Perge et al. in 2013 [10] and demonstrated in experiment one year later[11]. This finding has fueled a great amount of ongoing research on spin chains on superconductors specifically[12–21], but also on YSR states themselves[22–30]. Furthermore, it was recently proposed to build qubits (quantum bits, which can assume a superposition of their two states) directly out of two coupled YSR impurities[31, 32].

Apart from their possible application in quantum computing, YSR states are a fascinating subject of investigation by themselves. Their distinctive appearance in differential conductance spectra[33, 34] and their strong dependence on system parameters, such as the coupling strength of the impurity to the substrate[35], makes them ideal experimental subjects which offer insight into the quantum states of the impurity. After only a few experimental studies on YSR states before[33, 34], the groundbreaking work of Franke et al. published in 2011 [35] significantly advanced the understanding of YSR states. Since then, many studies have followed and in this context, e. g., the competition of magnetic and superconducting interaction[24, 35, 36], effects of magnetic anisotropy[37], quasiparticle transitions and lifetimes[23, 38], the orbital structure of atoms[39, 40], wave-function hybridization[26, 27, 30], impurity-substrate hybridization[41], and the spin polarization of YSR states[42, 43] have been experimentally investigated.

The spectral properties of YSR resonances furthermore allow them to be utilized as probes in fundamental research. Schneider et al. used YSR states at the tip of their scanning tunneling microscope (STM) for atomic-scale spin-polarization measurements[44], while Huang et al. determined the alignment of two spins to each other via YSR-YSR tunneling[29].

Most of the studies mentioned above have used low-temperature scanning tunneling microscopy (STM), which is also the experimental method of this work. To my knowledge, however, I am

the first to show YSR states on originally diamagnetic molecules. So far, mostly 3d transition metal atoms or metal-organic molecules from those have been used as magnetic impurities.
Via the observation of emerging YSR resonances, I demonstrate that H_2-phthalocyanine (H_2Pc) molecules on a Pb(100) surface acquire a net magnetic moment upon manual assembly into supramolecular clusters. The spin moment varies among the molecules, which is due to electrostatic interaction as shown by model calculations. Furthermore, the moments are finely tuned by repositioning the hydrogen atoms of the inner macrocycle of neighboring molecules.
In addition, I investigated lead phthalocyanine (PbPc) molecules on Pb(100), which also become magnetic via intermolecular interaction. YSR resonances positioned further within the superconducting gap are observed. Their detailed examination indicates that the magnetic moments of the molecules are influenced by electrostatic dipoles of neighboring PbPc molecules.
On this system, I furthermore demonstrate that YSR states can be utilized to significantly enhance the sensitivity of molecular vibrational spectroscopy. An improvement of approximately one order of magnitude has been achieved in comparison to earlier studies. The high energy resolution of this technique enables the observation of small energy shifts of individual vibrational modes, which occur, e. g., upon tip approach or changes of molecular neighbors.

The structure of this thesis is as follows:
In Chapter 2, basic concepts and working principles of STM (2.1) are first introduced, including a brief explanation of the tunneling current. Furthermore, scanning tunneling spectroscopy (STS) and inelastic electron tunneling spectroscopy (IETS) are addressed. Afterward, the fundamentals of superconductivity are explained (2.2) as far as they are necessary for the understanding of the YSR states and my experiments on them. Finally, the YSR states themselves are thematized (2.3). After a brief outline of the previous studies in this field, the fundamental models used to explain the phenomenon are introduced. At the end, the Bogoliubov-de Gennes (BdG) approach is shown that I use to model experimental spectra containing YSR resonances.
In Chapter 3, the two laboratory setups I used for the experiments are presented. In addition, the sample preparation technique as well as properties of the phthalocyanine molecules are addressed.
Chapter 4 is dedicated to the findings on H_2Pc on Pb(100). The major part of this chapter has been published in a paper in ACS Nano titled *Inducing and Controlling Molecular Magnetism through Supramolecular Manipulation*[45] (4.1). The corresponding Supporting Information are reproduced right after (4.2). In addition, the phenomenon of intermolecular state enhancement is presented, that I have observed and interpreted in the scope of the H_2Pc investigations (4.3).
In Chapter 5, the observations and results on the system of PbPc on Pb(100) are shown. It starts with the adsorption geometry of the self-assembled islands (5.1). Four different groups of molecules have been observed, which also show differently pronounced YSR states. The YSR states on PbPc and their dependence on molecular neighbors are studied in detail (5.2). Utilizing the sharp YSR resonances, vibrational excitations on PbPc have been observed with unprecedented sensitivity. A manuscript with the corresponding findings is currently under review for publication in Physical Review Letters, entitled *Resonance-enhanced Vibrational Spectroscopy of Molecules on a Superconductor*, and is also reproduced in this thesis (5.3). The associated Supplemental Materials are shown thereafter (5.4). Furthermore, the new technique of YSR enhanced IETS is used to map individual vibrational modes (5.5). Leaning on the manual assembly of H_2Pc supramolecules, a manually assembled PbPc cluster (5.6) and measurements thereon

are shown, which confirm and supplement my previous observations. In addition, reasons for different heights of spectral YSR peaks (5.7) relevant for YSR enhanced IETS are addressed, the deliberate (de-)metallation of single molecules (5.8) is demonstrated, and supporting STS measurements of different molecular orbitals are shown (5.9).
Finally, a summary and an outlook to possible studies that may follow are given in Chapter 6.

Chapter 2

Fundamentals

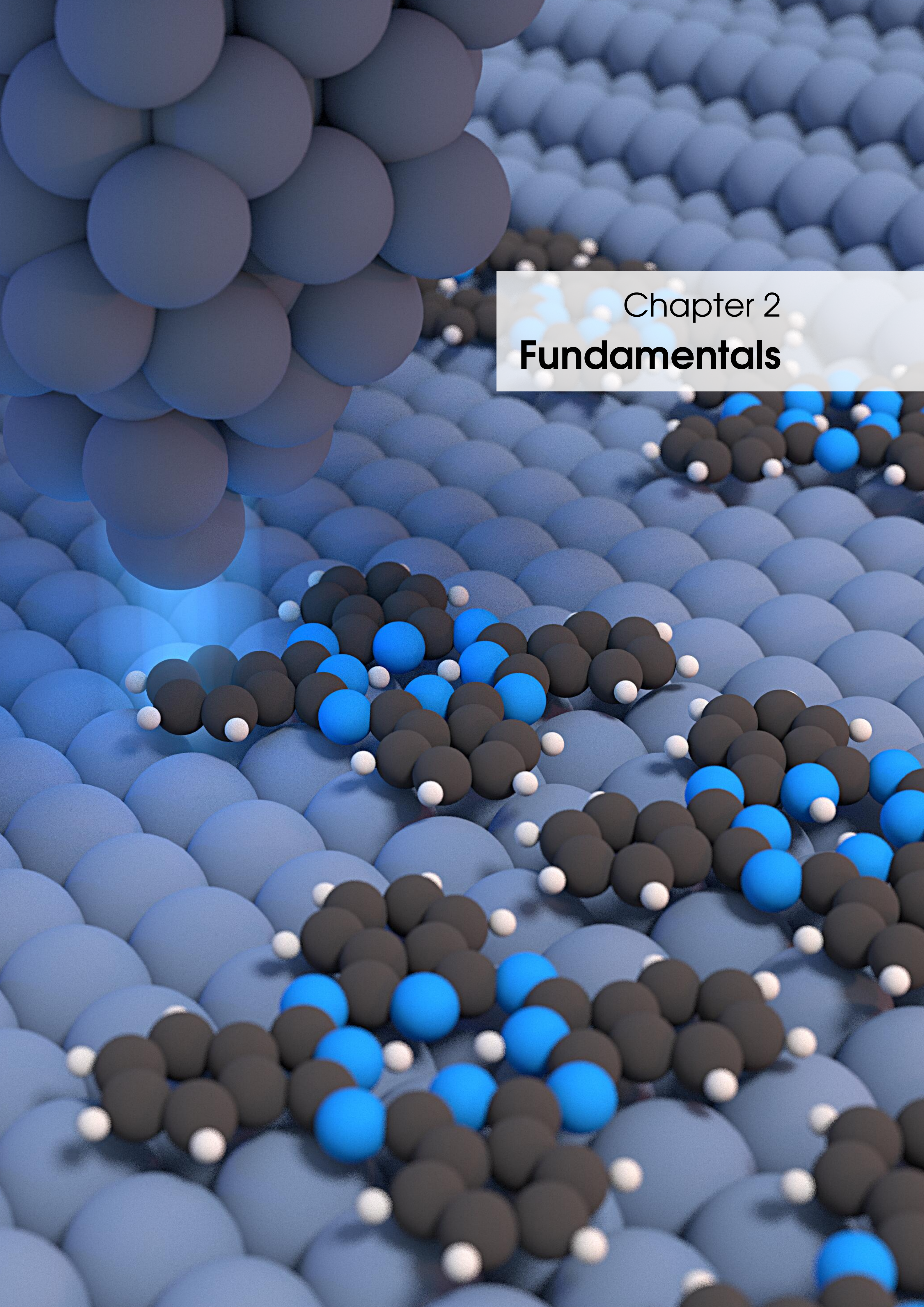

Previous page:
Model illustration of H_2Pc molecules on a Pb(100) surface, and a Pb tip in close proximity. The rendering was created with Blender[46].

2.1 Scanning Tunneling Microscopy

Ever since the STM has been invented in the early 1980s by Binnig and Rohrer[47,48], its importance and spread have increased, especially in the field of nanosciences. However, the underlying mechanism remains the same and has been described in many publications. For a detailed description, the reader is referred to the References 49–51. Here, I will explain the basic functionality only very briefly.

A very sharp metal tip is scanned via piezo crystals above a conducting sample at small distances, i. e. below 1 nm. By applying a voltage bias between tip and sample, a tunneling current occurs. The tunneling current is strongly depending on the distance between tip and sample, which enables a very high resolution at which single molecules and atoms can be resolved[52]. I will address the tunneling current in the next Section 2.1.1 in more detail. To achieve the necessary stability in the tunneling contact, the STM is typically set in an ultra-high vacuum (UHV) environment at low temperatures. The setups used in the scope of this thesis will be described in Chapter 3.

In STM, there are different ways to map the sample surface. In constant-current scanning mode, the tunneling current is kept constant at a specific setpoint via a feedback loop. This technique allows the ***topograph*** of the sample to be mapped and is used for all topographs shown in the following, unless stated otherwise. Complementary, the z-position can be kept constant during scanning (the z-axis is orthogonal to the sample surface), which is then called constant-height mode.
In addition to the mapping of the sample surface in real space, it is possible to measure the energy landscape of the sample via STS, which will be addressed in Section 2.1.2. In Section 2.1.3 IETS is discussed, which enables the measurement of, e. g., vibrational modes of single molecules[53].

Furthermore, STM allows not only imaging of the sample, but also its manipulation. For example, single molecules can be moved across the sample surface[54] or switched between different states, e. g., structural isomers[55]. Additionally, the metallation and demetallation of single molecules is possible[56,57].

All of the mentioned mapping and manipulation techniques are demonstrated in the experimental section of this thesis.

2.1.1 The Tunneling Current

The tunneling current is a quantum mechanical phenomenon: At small distances, the wave functions of both electrodes (tip and sample) overlap through the vacuum barrier, which allows electrons to pass from one electrode to the other. In a one-dimensional approximation (based on the WKB approximation) with a trapezoidal barrier of width z, the transmission probability τ for an electron can be written as[51,58]:

$$\tau(z,V,E) = \exp(-2\kappa z), \quad \kappa = \sqrt{\frac{2m}{\hbar^2}\left(\Phi + \frac{eV}{2} - E\right)}, \tag{2.1}$$

where m is the mass of the electron, and E the energy of the electron relative to the Fermi energy of the sample, Φ is the average work function of tip and sample, $\hbar$ the reduced Planck constant, and V the applied voltage bias, which is assumed to be $V < \Phi/e$. In a typical STM setup, κ reaches values of the order of $10\,\mathrm{nm}^{-1}$, meaning that the tunneling current changes by one order of magnitude when the distance of tip and sample changes by only 100 pm.

To obtain the tunneling current, the electronic states of tip and sample have to be taken into account. To enable the tunneling of an electron from the tip into the sample, an occupied state in the tip and an unoccupied state in the sample at corresponding energies need to be available. In 1960, Bardeen proposed a model for tunneling[59] following Fermi's golden rule. Based on this model, Tersoff and Hamann gave the following expression for the tunneling current[60]:

$$I = \frac{2\pi e}{\hbar} \sum_{\mu,\nu} f(E_\mu, T)\,[1 - f(E_\nu + eV, T)] \cdot |M_{\mu\nu}|^2\, \delta(E_\mu - E_\nu), \tag{2.2}$$

where $f(E,T)$ is the Fermi function at a temperature T, which is assumed to be the same for tip and sample; and $M_{\mu\nu}$ is the tunneling matrix element between states ψ_μ of the tip and ψ_ν of the sample. Here, the difficulty lies in the determination of the tunneling matrix element.

In the limit of small temperatures and small voltages and with the assumption of a spherical tip, Tersoff and Hamann derived an expression for the tunneling matrix element applicable to STM[61]. They found out that the tunneling current of an STM is a probe of the local density of states (LDOS) of the sample at the Fermi energy at the center of the tip.

In general, however, also finite temperatures and the density of states (DOS) of the tip need to be considered. Going back to the simple model of a one-dimensional barrier, the matrix element can be approximated by the transmission probability τ, as shown in Reference 51. The tunneling current then depends on the temperature T, the distance z, and the LDOS of both tip and sample (ρ_T and ρ_S respectively), and can be written as[51]:

$$I(V,z,T) = \frac{4\pi e}{\hbar} \int_{-\infty}^{\infty} \tau(z,V,E)\rho_T(E-eV)\rho_S(E)\,[f(E-eV,T) - f(E,T)]\,dE \tag{2.3}$$

For low voltages ($|eV| \ll \Phi$), the energy and voltage dependence of the tunneling factor τ can be neglected. When keeping the distance z constant, the following expression for the tunneling current is obtained, which can also be expressed in terms of convolutions $[(f*g)(x) = \int_{-\infty}^{\infty} f(\tau)g(x-\tau)d\tau]$:

$$\begin{aligned} I(V,T) &\propto \int_{-\infty}^{\infty} \rho_T(E-eV)\rho_S(E)\,[f(E-eV,T) - f(E,T)]\,dE \\ &= \Big(\rho_S(E) * [\rho_T(-E)f(-E,T)]\Big)(eV) - \Big([\rho_S(E)f(E,T)] * \rho_T(-E)\Big)(eV) \end{aligned} \tag{2.4}$$

In this way, the tunneling current $I(V)$ for arbitrary LDOSs of tip and sample can be calculated very fast using modern calculation applications like Matlab[62].

2.1.2 Scanning Tunneling Spectroscopy

Since $I(V)$ strongly depends on the LDOS of both tip and sample, the measurement of $I(V)$ spectra is used to obtain information about these. In this method, called electron tunneling spectroscopy (or scanning tunneling spectroscopy (STS), if applied in an STM), $dI/dV(V)$ or even $dI^2/d^2V(V)$ spectra are often recorded instead of $I(V)$. In STM, normal-conducting metals with very flat DOS, like W or PtIr, are usually used for the tip. The energy dependence of ρ_T can then be neglected, and in the limit of zero temperature, $dI/dV(V)$ essentially depends on the sample's LDOS $\rho_S(E)$ only – in accordance with Tersoff and Hamann[61]. However, it can still be challenging to extract the LDOS from such spectra, especially when it comes to constant-current dI/dV[63]. Corresponding spectra must therefore be interpreted with caution.
The measurement of the dI/dV is nevertheless an established method to probe the sample's LDOS, e. g., molecular orbitals of single molecules. Esaki and Stiles were the first to demonstrate this technique in 1965 [64] by measuring the energy band structure of bismuth via electron tunneling spectroscopy.
In addition to the LDOS measurement, many different phenomena can be observed when it comes to inelastic electron tunneling spectroscopy (IETS), as will be shown in the next section 2.1.3.

Instead of numerically calculating the dI/dV (or d^2I/dV^2) from recorded $I(V)$ curves, it can be measured directly via standard lock-in technique as described, e. g., in Reference 65. The bias voltage is then modulated by a small modulation voltage V_M with high frequency f (values of 700 to 1000 Hz are typically used in the scope of this thesis). The obtained current signal is analyzed by the lock-in amplifier, which ***locks in*** to the chosen modulation frequency, meaning that it amplifies the amplitude of the AC component with frequency f, while blocking other frequencies. Finally, the output signal of the lock-in amplifier is proportional to the dI/dV or differential conductance. Since the lock-in amplifier acts as a frequency filter, a much better signal to noise ratio is usually obtained via this technique compared to numerical derivation.

2.1.2.1 Broadening in Scanning Tunneling Spectroscopy

The measured features in a dI/dV curve may be broadened because of different reasons. First, when using the lock-in technique, the finite modulation amplitude leads to broadening. This instrumental broadening is modeled by convoluting the unbroadened spectrum with an instrumental function $\chi_{\text{lock-in}}$[66,67] (see Figure 2.1a):

$$\chi_{\text{lock}-\text{in}}(V) = \begin{cases} \frac{2}{\pi V_M^2}\sqrt{V_M^2 - V^2} & ,|V| \leq V_M \\ 0 & ,|V| > V_M, \end{cases} \tag{2.5}$$

The full width at half maximum (FWHM) is $\Delta V_{\text{lock}-\text{in}} = \sqrt{3}V_M$. Therefore, the modulation voltage V_M must be chosen small enough so that the lock-in instrumental broadening does not interfere with the measurement.
Secondly, there will be broadening due to electronic noise in the STM setup. I model this effect

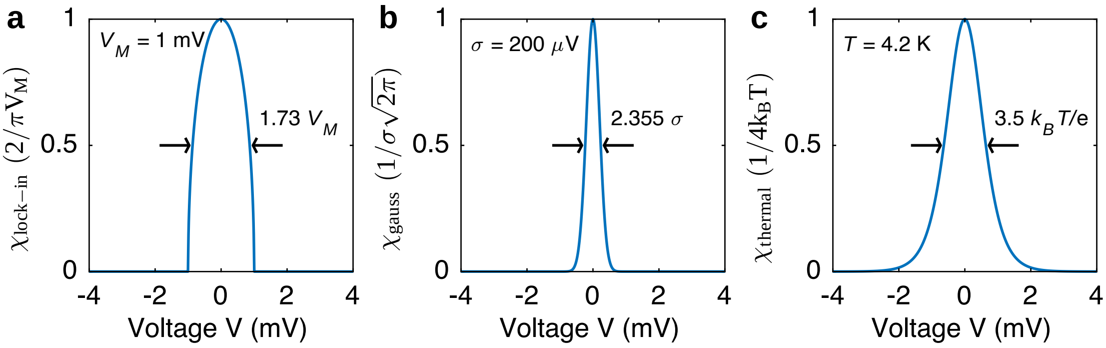

Figure 2.1: Broadening functions for (a) lock-in instrumental broadening, (b) electronic broadening, and (c) thermal broadening, as described in the text.

by convoluting the unperturbed signal with a Gaussian function (see Figure 2.1b):

$$\chi_{\mathrm{gauss}}(V) = \frac{1}{\sigma\sqrt{2\pi}} \exp\left(-\frac{V^2}{2\sigma^2}\right), \tag{2.6}$$

where σ is the standard derivation. A similar approach has been used, e. g., in References 25, 68. With the STM setups used in the scope of this thesis, values down to $\sigma \approx 100\,\mu\mathrm{V}$ are achieved, which relates to a FWHM of $\Delta V_{\mathrm{gauss}} = 2\sqrt{2\ln(2)}\sigma \approx 236\,\mu\mathrm{V}$.
Finally, thermal broadening has to be considered. At finite temperatures $T > 0$, the Fermi-Dirac distribution of the occupied states lead to a broadening, which can be modeled by convolution with the thermal-broadening function χ_{thermal} [66] (see Figure 2.1c):

$$\chi_{\mathrm{thermal}}(V) = \frac{1}{4k_BT\left[\cosh\left(\frac{eV}{2k_BT}\right)\right]^2}, \tag{2.7}$$

where k_B is the Boltzmann constant. Thus, at a temperature of 4.2 K, a broadening with a FWHM of $\Delta V_{\mathrm{thermal}} = 3.5 k_BT/e \approx 1.3\,\mathrm{mV}$ is obtained.
When using modulation voltages smaller than approximately $700\,\mu\mathrm{V}$, the broadening of the dI/dV is limited by the thermal broadening at 4.2 K. However, the thermal broadening can be neglected if superconducting electrodes with a sufficiently large gap parameter are used ($2\Delta \gg k_BT$) [69], as will be shown in Section 2.2.4. In either way, the thermal broadening is already included when calculating the tunneling current via Equation 2.4.
A similar discussion of lock-in and thermal broadening on dI/dV spectra can also be found, e. g., in References 70, 71. The effect of lock-in and thermal broadening on inelastic d^2I/dV^2 spectra has already been discussed in 1973 by Klein et al.[72].

A model function of the dI/dV signal is obtained by calculating the tunneling current via Equation 2.4, numerical derivation, and subsequent convolution with the broadening functions $\chi_{\mathrm{lock-in}}$ and χ_{gauss}. I have used this model function to simulate measured dI/dV spectra, and also fitted it to them to extract experimental parameters.

2.1.3 Inelastic Electron Tunneling Spectroscopy

So far, only elastic electron tunneling has been considered. However, an electron may also tunnel via an inelastic process where it loses some of its energy, e. g., to a phonon with energy $\hbar\omega$, as depicted in Figure 2.2a. In this case, the electron ends up in a state of the sample that is $\hbar\omega$ lower in energy than in case of elastic tunneling. In the most simple picture of two metal electrodes at zero temperature, the inelastic process comes into play, when the bias voltage reaches $V_\omega = \frac{\hbar\omega}{e}$, since the electron can only tunnel into unoccupied states of the sample. Consequently, a new transmission channel opens up at voltages $V \geq V_\omega$, which may increase the differential conductance of the contact. Therefore, inelastic electron tunneling processes induce characteristic signatures, which are observable in STS.
I will focus my discussion on IETS of molecular vibrational modes, especially in STM. In addition, however, IETS has also been used to measure, e. g., phonons[73–75], plasmons[75, 76], magnons[77–79], and spin excitations[80].

IETS of molecular vibrations was demonstrated for the first time in 1966 by Lambe and Jaklevic[81] with metal-oxide-metal tunnel junctions . They observed resonances in the d^2I/dV^2 signal, which were attributed to vibrational excitations of molecules contained in the oxide layer. In 1998, Stipe et al.[53] transferred the technique of IETS to STM (STM-IETS). They measured vibrational modes of single acetylene molecules adsorbed on a Cu(100) surface. However, only some of the vibrational modes could be observed, while others were hidden. This puzzle has been solved by a theoretical study of Lorente and Persson[82] published in 2000. They showed that the increase of the conductance via the opening of an inelastic-tunneling channel can be canceled out by an elastic contribution to the tunneling current, in which a virtual vibration is emitted and readsorbed. In this way, some vibrational modes are not observable in STM-IETS, while others may even come with a decrease of the conductance. In general, each vibrational mode can be assigned a factor η that gives the corresponding relative change of the conductance.

Figure 2.2b,c shows a simulated dI/dV and d^2I/dV^2 spectrum, respectively, assuming a constant DOS in both electrodes and an excitation energy of $\hbar\omega = 2\,\mathrm{meV}$ with a conductance gain of $\eta = 10\,\%$. Typically, much smaller values of η are observed, however, I chose a larger value for clarity. In the dI/dV spectrum (b), only a small step is observable, while in the d^2I/dV^2 spectrum (c) a peak shows up at $V_\omega = \frac{\hbar\omega}{e}$ and a dip at $-V_\omega$. In conventional IETS measurements, the d^2I/dV^2 signal is therefore evaluated, because it provides a more distinct sensing signal. After all, the small steps in the dI/dV spectrum might be obfuscated, since in reality the DOS is not absolutely constant and in addition, the measurement signal is contaminated by noise.

To further improve the sensitivity in IETS, it is possible to resonantly enhance the signal of the inelastic tunneling processes. This concept was first proposed theoretically by Persson and Baratoff[83] in 1987. The underlying idea is that the effective conductance gain does not only depend on the cross-section of the inelastic process, but also on the number of empty states available for elastic and inelastic tunneling electrons. Namely, if the LDOS of the sample at the Fermi edge is increased with respect to the LDOS at $E = \hbar\omega$, e. g., by a molecular orbital of an adsorbed molecule, the contribution of the inelastic tunneling processes will be enhanced in

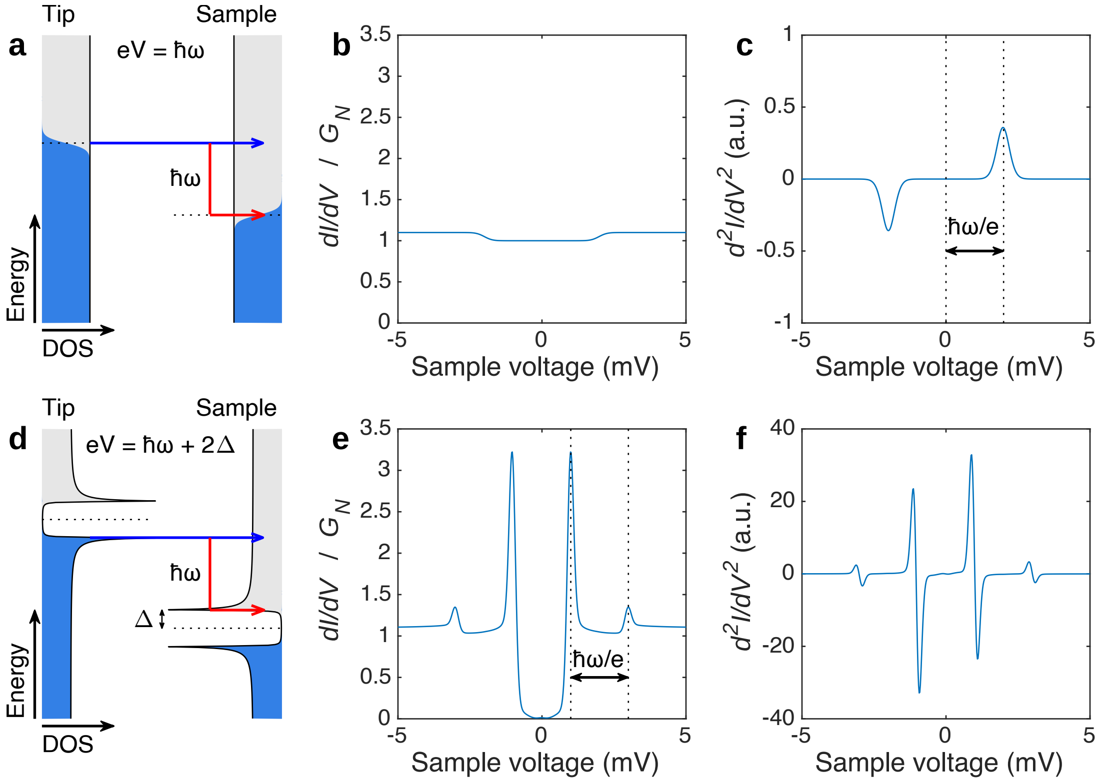

Figure 2.2: Depictions of (a–c) conventional IETS and (d–f) IETS resonantly enhanced via superconducting electrodes. (a,d) Energy diagrams showing a direct elastic tunneling process (blue arrow) and a corresponding inelastic tunneling process (red arrow) with an excitation energy of $\hbar\omega$. The corresponding transmission channel opens up at a sample voltage of $eV = \pm\hbar\omega$ or $eV = \pm(\hbar\omega + 2\Delta)$, respectively, where Δ is the superconducting gap parameter of tip and sample. Consequently, in conventional IETS, a small step is observable in the dI/dV at that voltage (b), while in d^2I/dV^2 it is a peak (or dip at negative voltage) (c). In the case of superconducting electrodes however, peaks are already observable in dI/dV at $eV = \pm(\hbar\omega + 2\Delta)$ (d). The DOS and the spectra were calculated using the following parameters (see Sections 2.1.2 and 2.2.1): $\eta = 10\,\%$, $\hbar\omega = 2\,\mathrm{meV}$, $\Delta = 0.5\,\mathrm{meV}$, $\Gamma = 10\,\mathrm{\mu eV}$, $\sigma = 100\,\mathrm{\mu eV}$, $T = 1\,\mathrm{K}$.

comparison with the elastic contribution. This effect was demonstrated in experiment, e. g., by Guo et al.[84].

Here, however, I will focus on the use of superconducting electrodes. As will be discussed in Section 2.2, the DOS of a superconductor is characterized by a small gap of width 2Δ around the Fermi energy enclosed by two sharp coherence peaks. These coherence peaks can also serve to enhance the inelastic tunneling signal. This technique was first demonstrated in STM by Heinrich et al.[85] in 2013, where they observed excited spin states of Fe–octaethylporphyrin–chloride molecules on a Pb(111) surface with a Pb-covered tip. Before, it was already demonstrated, e. g., in carbon-nanotube quantum-dots by Grove-Rasmussen et al.[86]. As will be shown in Section 2.2.4, the use of superconducting electrodes furthermore allows a significant increase in spectral resolution.

Figure 2.2d–f shows a corresponding energy diagram and calculated dI/dV and d^2I/dV^2 curves. Except for the superconducting DOS (calculated via Equation 2.11), the same parameters were used as in Figure 2.2a–c. With superconducting electrodes, the inelastic excitation can be observed as peaks in the dI/dV curve at $V = \pm(\hbar\omega + 2\Delta)/e$ (Figure 2.2e). Thus, the d^2I/dV^2 signal is of minor interest.
As will be shown in Section 5.3 and following, I went even one step further and used YSR resonances (see Section 2.3) to enhance the signal of inelastic excitations.

For a more detailed description of STM-IETS and its recent advances, the reader is referred to a review by You et al.[87].

2.2 Superconductivity

Superconductivity is a macroscopic quantum state in which a conductor has no electrical resistance at all. Its existence was discovered by Kamerlingh Onnes in Leiden 1911 [88, 89] by measuring the resistance of mercury at low temperatures, shortly after he succeeded in liquefying helium[90]. The phenomenon of superconductivity occurs with various materials below a certain temperature, i. e. the critical temperature T_C. The elements with the highest critical temperatures are[91]: Nb (9.25 K), Tc (8.2 K), Pb (7.2 K), La (6 K) and V (5.4 K).
I chose Pb as material for both electrodes of the STM, because Pb single crystals are available in high purity, and it is comparatively easy to prepare atomically clean and flat surfaces on them.

In the last hundred years, more and more superconducting compounds with higher and higher critical temperatures have been discovered[92]. Today, even room-temperature superconductivity has been achieved in carbonaceous sulfur hydride under laboratory conditions and high pressure[93]. Other high temperature superconductors have long been important for many technical applications[94]. Superconductors are used, e. g., in magnet coils to generate strong magnetic fields[95], in superconducting quantum interference devices (SQUIDs)[96] as high precision magnetic field sensors, or for efficient power transmission[97, 98]. Furthermore, superconductors are the basis for the most advanced approaches to quantum computing[99–103].

In the course of this chapter, fundamental properties of conventional superconductors are discussed. It starts with the Bardeen-Cooper-Schrieffer (BCS) theory (Section 2.2.1) with focus on the quasiparticle DOS, which exhibits the superconducting gap. Then, the influence of the temperature on the gap (Section 2.2.2) and the BdG approach to superconductivity (Section 2.2.3) are addressed. Afterwards, tunneling between superconductors is discussed (Section 2.2.4). The chapter concludes with the two-band superconductivity of Pb (Section 2.2.5).
For a more in-depth introduction to superconductivity, the reader is referred to some of the many textbooks dealing with the subject (References 104–106).

2.2.1 BCS Theory

In 1957, Bardeen, Cooper and Schrieffer published a theory of superconductivity[107,108], also known as BCS theory. It was the first microscopic theory that could explain the observed phenomenon and applies to the conventional superconductors, to which Pb also belongs.

The BCS theory states that under certain circumstances, the interaction between electrons resulting from virtual exchange of phonons becomes positive, overcomes the Coulomb repulsion, and finally leads to the formation of so called Cooper pairs. The latter were previously proposed by Cooper[109] in 1956 based on preceding work concerning electron-phonon interaction by Fröhlich[110]. The BCS theory thereby assumes a sufficiently weak coupling of the electrons and, strictly speaking, therefore only applies to so called weak-coupling superconductors. Pb however is among the strong-coupling superconductors, which deviate from the BCS theory. A framework to describe strong-coupling superconductors was published by Scalapino et al.[111,112] based on Eliashberg theory[113]. For the scope of this thesis, however, those deviations will be neglected.

In the most common case, a Cooper pair consists of two electrons with opposing spin. Hence, it is in a singlet state with total spin $S = 0$. If, in addition, the orbital angular momentum is also zero ($l = 0$), the material is referred to as an s-wave superconductor, to which all elemental superconductors belong. Furthermore, the two electrons in a Cooper pair have a momentum of the same magnitude but with opposing direction. Thus, a Cooper pair can be written as $\{+\mathbf{k}_\uparrow, -\mathbf{k}_\downarrow\}$, where $\mathbf{k}$ is the wave vector.

Since Cooper pairs have an integer spin, they act like bosons. Thus, they condense into the same energy state, as described by the Bose-Einstein statistics. In consequence, the entirety of Cooper pairs is described by a single macroscopic wave function ψ (see, e. g., Reference 105):

$$\psi(\mathbf{r},t) = \psi_0(\mathbf{r},t)\exp\left(\mathrm{i}\varphi(\mathbf{r},t)\right), \tag{2.8}$$

which is essentially defined by two parameters only: the Cooper pair density $n_C = |\psi_0|^2$ and the phase φ. These parameters are indeed of macroscopic nature, as demonstrated by, e. g., flux quantization[114–116] and the Josephson effect[105,117].

As a major consequence, the BCS theory predicted the formation of an energy gap in the DOS symmetrically located around the Fermi energy E_F. It separates the superconducting ground state from quasiparticle excitations. The width of the gap is described by the superconducting order parameter Δ, which depends on the normal state DOS at the Fermi energy $\rho_N(E_F)$, the coupling potential V and the Debye frequency ω_D (Reference 104, p. 56, Equation 3.34):

$$\Delta_{\mathrm{BCS}} = \frac{\hbar\omega_D}{\sinh\left[\frac{1}{\rho_N(E_F)V}\right]} \approx 2\hbar\omega_D \exp\left(\frac{-1}{\rho_N(E_F)V}\right) \quad, \rho_N(E_F)V \ll 1. \tag{2.9}$$

An energy of Δ has to be expended per electron to break a Cooper pair, leading to single particle excitations.

In a superconductor, a single excited electron can be transformed into an excited hole of opposing

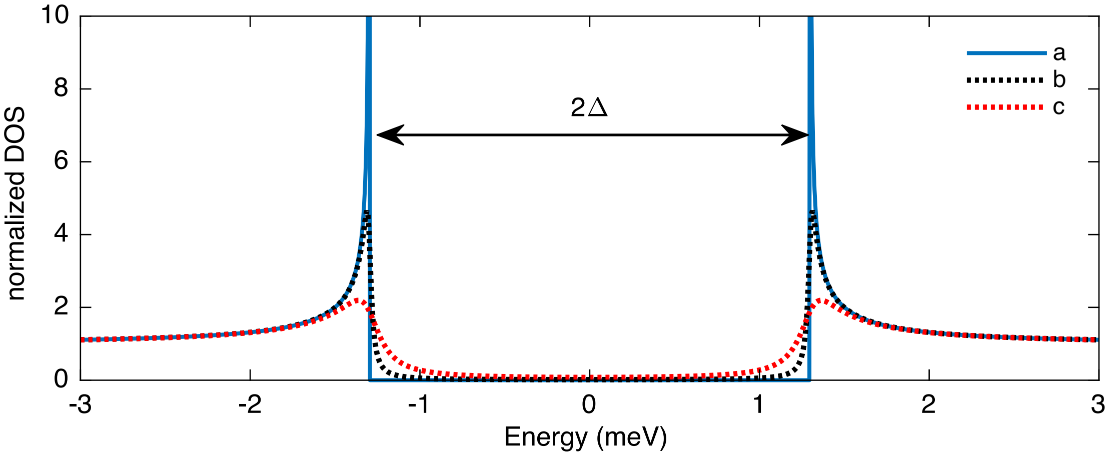

Figure 2.3: The DOS of Pb ($\Delta = 1.3\,\text{meV}$) as calculated by BCS theory. Curve (a) was calculated via Equation 2.10, and the curves (b) and (c) via Equation 2.11 using Dynes' parameters of $\Gamma = 20\,\mu\text{eV}$ and $\Gamma = 100\,\mu\text{eV}$, respectively.

momentum and spin and a Cooper pair, and vice versa. This process is essentially equivalent to the Andreev reflection, which will be briefly explained in Section 2.2.3. In consequence, superconductors feature single particle excitations that are better described as superpositions of electrons and holes, so called Bogoliubov quasiparticles[118].

In 1960, Giaever[119] was the first to measure the superconducting energy gap by electron tunneling. He used an aluminum/aluminum-oxide/lead contact and measured $I(V)$ curves down to temperatures of 1.6 K where Pb is superconducting, but Al is still normal conducting. This experimental finding was an important verification of the BCS theory.

In BCS theory, the quasiparticle DOS is derived as[107]:

$$\rho_{\text{BCS}}(E) = \rho_N(E) \cdot \Re\left(\frac{|E|}{\sqrt{E^2 - \Delta^2}}\right), \tag{2.10}$$

where $\rho_N(E)$ is the DOS in the normal-conducting state.
In 1978, Dynes et al.[120] introduced an additional parameter Γ (thereon referred to as Dynes' parameter), which accounts for quasiparticle-lifetime broadening. The quasiparticle DOS then reads:

$$\rho_{\text{BCS}}(E) = \rho_N(E) \cdot \Re\left(\frac{\text{sign}(E) \cdot (E - \mathrm{i}\Gamma)}{\sqrt{(E - \mathrm{i}\Gamma)^2 - \Delta^2}}\right) \tag{2.11}$$

In Figure 2.3 the DOS of Pb is plotted as calculated using Equations 2.10 and 2.11. The DOS has an energy gap of 2Δ centered around the Fermi energy ($E_F = 0$), which is enclosed by two peaks, the so called coherence peaks. In the original BCS DOS (Equation 2.10) singularities occur at $E = \pm\Delta$, which are eradicated by the introduction of Dynes' parameter. Furthermore, Dynes' parameter leads to a broadening of the coherence peaks and a finite DOS inside the gap in accordance with experimental observations[120].

Therefore, I use Equation 2.11 to calculate the superconducting DOS, e. g., for model fits to experimental dI/dV spectra (see, e. g., Section 2.2.4). Besides Δ, then also Γ becomes a fit parameter.

2.2.2 Temperature Dependence of the Gap

The superconducting order parameter Δ depends on the temperature T, the applied magnetic field B and the current density j ($\Delta = \Delta(T, B, j)$). There exists a critical value for all three parameters, at which superconductivity is fully suppressed. Here, I will only discuss the temperature dependence. No magnetic fields were applied, and the dependence on the current density is negligible in tunneling experiments.

According to the BCS theory, the critical temperature T_C is directly related to the order parameter at zero temperature Δ_0[104, 107]:

$$\Delta_0 = 1.764 \cdot k_B T_C \tag{2.12}$$

Pb deviates a little bit from this relation ($\Delta_0/k_B T_C \approx 2.1$), since it is a strong coupling superconductor and the BCS theory assumes weak coupling.
The principle course of $\Delta(T)$, however, is accurately predicted by BCS theory. While an analytic expression for the order parameter close to the critical temperature was obtained[104, 107]:

$$\Delta(T) \approx 3.2 k_B T_C \sqrt{1 - \frac{T}{T_C}}, \tag{2.13}$$

the general dependence of $\Delta(T)$ can be calculated numerically, as carried out by Mühlschlegel[121] in 1959. Figure 2.4a shows a corresponding curve. First measurements of the temperature dependence of the superconducting gap were published by Giaever and Megerle[122] in 1961, which essentially confirm the result.
According to this curve, the gap parameter Δ of Pb is reduced by approximately 8 % at 4.2 K. However, at a temperature of 2.5 K it deviates only less than 1 % from Δ_0. It might therefore be advantageous to reduce the temperature of the STM below 4.2 K.

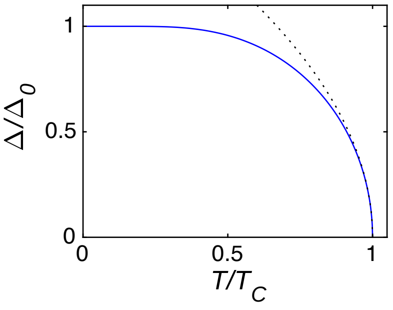

Figure 2.4: Dependence of the gap parameter Δ on the temperature T. The values for the blue curve are taken from Reference 121. The dotted line, shows the relation of Equation 2.13.

2.2.3 Bogoliubov-de Gennes Theory

In the following, I will discuss the Bogoliubov-de Gennes (BdG) method, which offers an alternative approach to superconductors. It was proposed by De Gennes in 1966[123]. The reader is referred to References 124 and 125 for a more detailed discussion.
The BdG method allows the quasiparticle band structure of a superconductor to be calculated. Furthermore, excitation spectra of YSR states can be calculated, as will be discussed in Section 2.3.3. Here, I will introduce the general idea, guided by Reference 124.

First, I have to introduce the concept of Andreev reflections[126]. An incident spin-up electron with energy $E < \Delta$ cannot simply traverse from a normal conductor into a superconductor. Instead, it *drags* a spin-down electron with energy $2E_F - E$ with it into the superconductor to form a Cooper pair. In other words, the incident spin-up electron is reflected into a spin-down hole (vacancy in the spin-down electron band), which flows away from the interface. Vice versa, a hole can be reflected into an electron. Thus, Andreev reflections couple electrons and holes of opposite spin.

In the BdG approach, electrons and holes of opposite spin are coupled via the implementation of a pairing potential $\Delta e^{-\mathrm{i}2E_F t/\hbar}$. Without the coupling, the wave functions of single electrons u' and holes v' obey the time-dependent Schrödinger equation (Reference 124, p. 9):

$$Hu' = \mathrm{i}\hbar\frac{\partial u'}{\partial t} \qquad -H^*v' = \mathrm{i}\hbar\frac{\partial v'}{\partial t} \tag{2.14}$$

H is the standard one-electron Hamiltonian (and H^* its complex conjugate):

$$H = \frac{(\mathbf{p} - e\mathbf{A})^2}{2m} + eV, \tag{2.15}$$

with scalar potential V, vector potential $\mathbf{A}$, particle mass m, and momentum $\mathbf{p}$. Corresponding dispersion curves for u' and v' are shown in Figure 2.5a.

The coupled system is then described by the following equation, where electrons and holes of opposite spin mix via the pairing potential (Reference 124, p. 9, Equation 2.2):

$$\begin{bmatrix} H & \Delta e^{-\mathrm{i}2E_F t/\hbar} \\ \Delta^* e^{+\mathrm{i}2E_F t/\hbar} & -H^* \end{bmatrix} \begin{Bmatrix} u' \\ v' \end{Bmatrix} = \mathrm{i}\hbar\frac{\partial}{\partial t} \begin{Bmatrix} u' \\ v' \end{Bmatrix} \tag{2.16}$$

Actually, one would need a four dimensional system of linear equations to fully describe the system of both spin-up and spin-down electrons and holes. However, since spin-up electrons only couple to spin-down holes and vice versa, the problem can be reduced to the two dimensional set of equations shown here (see, e. g., Reference 125, Section 1.5.1).
In general, the pairing potential Δ can be complex and dependent on the wave vector $\mathbf{k}$. For the simple case of an s-wave superconductor, Δ is assumed to be constant and real ($\Delta^* = \Delta$). The additional time dependency $e^{-\mathrm{i}2E_F t/\hbar}$ of the pairing potential is needed to account for the energy change from E to $E - 2E_F$, which occurs when switching from electrons to holes and vice versa. However, this time dependency can be eliminated by a gauge transformation with

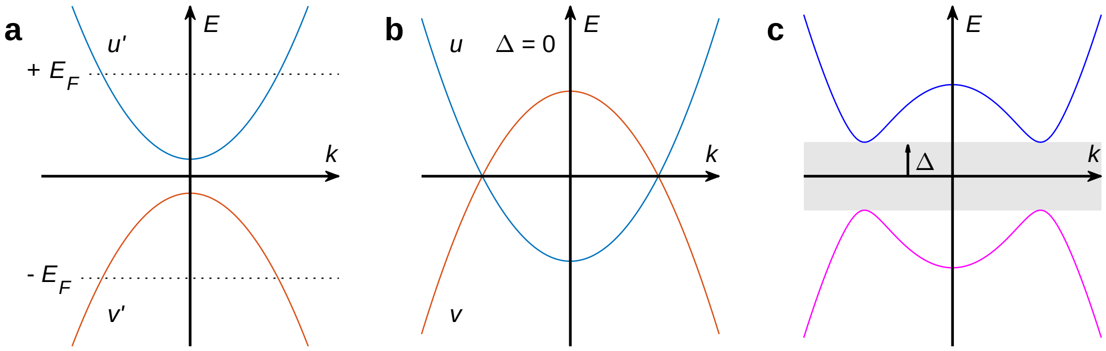

Figure 2.5: Dispersion curves of the energy states of single electrons u' and holes v' according to the standard Hamiltonian (a), and according to the BdG equation with $\Delta = 0$ (b) and $\Delta \neq 0$ (c). In the last case, an energy gap of 2Δ opens up and the electron and hole states mix into two bands of Bogoliubov quasiparticles.

$u = u' e^{+\mathrm{i}E_F t/\hbar}$ and $v = v' e^{-\mathrm{i}E_F t/\hbar}$. As a result, the standard form of the equilibrium BdG equation is obtained (Reference 124, p. 11, Equation 2.4):

$$\begin{bmatrix} H - E_F & \Delta \\ \Delta^* & -(H^* - E_F) \end{bmatrix} \begin{Bmatrix} u \\ v \end{Bmatrix} = \mathrm{i}\hbar \frac{\partial}{\partial t} \begin{Bmatrix} u \\ v \end{Bmatrix} \tag{2.17}$$

Now, I want to focus on the solution of the BdG equation. In the case of $\Delta = 0$, the solution is obvious, since the matrix Hamiltonian on the left in Equation 2.17 is diagonal. Then, $\{u, 0\}^{\mathrm{T}}$ and $\{0, v\}^{\mathrm{T}}$ are the eigenfunctions with the eigenvalues $\varepsilon = \pm(\varepsilon_k - E_F)$, where $\varepsilon_k = \frac{\hbar^2 k^2}{2m} + eV$ is the eigenvalue of the single particle Hamiltonian H (Figure 2.5b).

For $\Delta \neq 0$, the matrix Hamiltonian needs to be diagonalized first. Consequently, the eigenfunctions become mixtures of the electron and hole components, also known as Bogoliubov quasiparticles. The corresponding eigenvalues are found to be (Reference 124, p. 13, Equation 2.9):

$$E = \pm\sqrt{(\varepsilon_k - E_F)^2 + \Delta^2} \tag{2.18}$$

Figure 2.5c shows corresponding dispersion curves. A gap of width 2Δ has opened up symmetrically around zero energy, separating the quasiparticle states. The quasiparticle states themselves are mixtures of electron and hole components, with equal composition where they are closest to the gap.

Furthermore, the DOS of the superconductor can be calculated from the solution of the BdG equation, which reproduces the BCS DOS as shown in Equation 2.10 (see, e. g., Reference 125, Section 1.7). The DOS is the derivative of the k-space volume Ω with respect to the energy of the states. Thus, with the dispersion relation of Equation 2.18 and $E_F = 0$,

$$\rho(E) = \frac{\partial \Omega}{\partial E} = \frac{\partial \Omega}{\partial \varepsilon_k} \frac{\partial \varepsilon_k}{\partial E} = \rho_N(E) \cdot \frac{\partial}{\partial E} \left(\sqrt{|E|^2 - \Delta^2} \right) = \rho_N(E) \cdot \frac{|E|}{\sqrt{E^2 - \Delta^2}}, \tag{2.19}$$

where $\rho_N(E) = \frac{\partial \Omega}{\partial \varepsilon_k}$ is the DOS in the normal-conducting state.

2.2.4 Tunneling between Superconductors

As discussed in Section 2.2.1, conventional superconductors exhibit an energy gap in their DOS symmetrically around the Fermi energy and enclosed by the coherence peaks. When tunneling into a superconductor at small junction conductances ($G \ll G_0 = \frac{2e^2}{h}$, i. e. the conductance quantum), this gap can be directly observed in dI/dV measurements. At higher conductances ($G \approx G_0$), additional phenomena like multiple Andreev reflections (MAR)[127,128] and the Josephson supercurrent[117,129] occur. Here, however, I will limit my discussion to small junction conductances.

As shown in Section 2.2.3, single particle excitations in superconductors are better described in terms of Bogoliubov quasiparticles. Nevertheless, in this section, I will discuss the tunneling processes in terms of single electrons (and holes) for better illustration.

When a superconducting sample is probed with a normal-conducting tip (ρ_T assumed to be constant), the superconducting DOS of the sample ρ_S can directly be observed in STS, as discussed in Section 2.1.2. Figure 2.6a shows an energy diagram of a respective contact. For a single electron to tunnel from the Fermi level of the tip into the superconductor, a sample voltage of $V \geq \Delta_S/e$ is needed to span the energy gap of the sample Δ_S. In this way, the energy gap of the sample is reproduced in STS. However, at finite temperatures, the Fermi distribution of occupied states in the tip leads to a broadening of the spectrum.

Figure 2.7a shows a corresponding calculated spectrum. In comparison with the sample DOS (dotted line), the spectrum is broadened significantly at a temperature of 4.2 K.

Such spectra can be calculated by inserting the BCS DOS (Equation 2.11) for ρ_S (and ρ_T, if the tip is superconducting too) into Equation 2.4. As discussed in Section 2.1.2, the corresponding

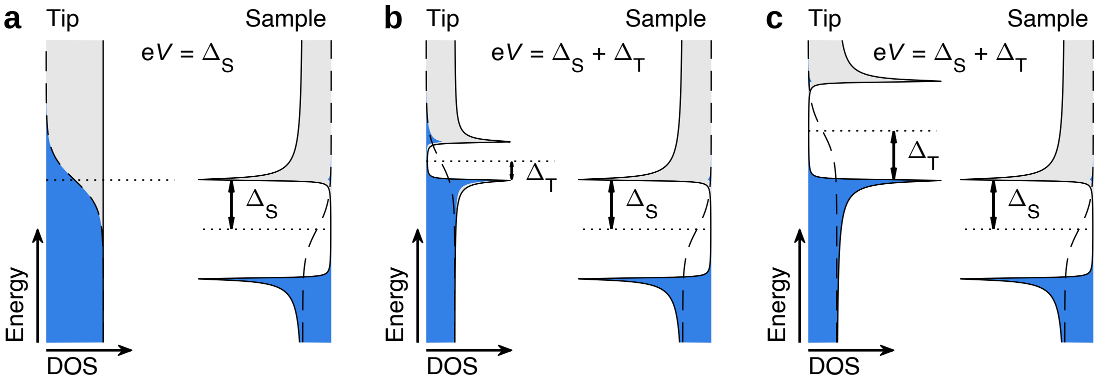

Figure 2.6: Energy diagrams of tunneling contacts with superconducting electrodes. The DOS of tip and sample are shown as solid curves with the blue area indicating the states that are filled according to the Fermi distribution (dashed curves). The respective Fermi level is marked by a dotted line. For the calculation of the DOS, the same parameters as in Figure 2.7 have been used respectively. (a) Tunneling contact with a normal-conducting gap, which leads to a broadened gap of width $2\Delta_S$ in STS as shown in Figure 2.7a. (b) Both tip and sample are superconducting, but the tip has a smaller gap. A corresponding spectrum is shown in Figure 2.7b. (c) Tip and sample have the same gap parameter, which leads to spectra as shown in Figure 2.7c,d.

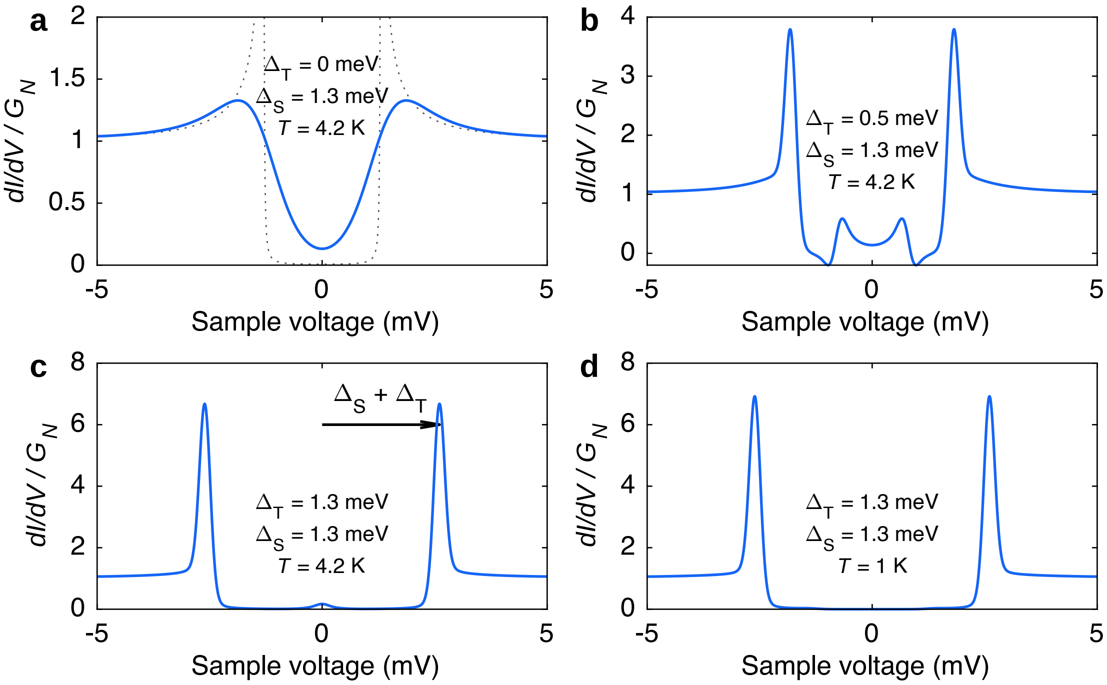

Figure 2.7: Calculated STS spectra of the superconducting gap. (a) Superconducting sample and normal-conducting tip ($\Delta_T = 0$). Additionally, the DOS of the sample is shown as a gray dotted line. (b) Both electrodes are superconducting, but have different gap parameters, which leads to additional peaks. (c) Same gap parameters for both electrodes. The temperature is set to $T = 4.2\,\mathrm{K}$, while (d) shows the same contact at $T = 1\,\mathrm{K}$. For all spectra, the same values are used for the other model parameters: $\Gamma = 10\,\mu\mathrm{eV}$, $\sigma = 100\,\mu\mathrm{eV}$, and $V_M = 100\,\mu\mathrm{V}$.

dI/dV signal can then be calculated by including the lock-in and electronic broadening. In this way, a model function is obtained (Figure 2.7), which can also be fitted to real data.

The thermal broadening can be suppressed by using a superconducting tip. Now, both the gap of the tip Δ_T and of the sample Δ_S must be overcome to tunnel a single electron, as shown in the energy diagrams in Figure 2.6b,c. Thus, a larger gap of width $2(\Delta_T + \Delta_S)/e$ is observed in the corresponding dI/dV spectra (Figure 2.7b-d). However, the spectral features are much sharper in comparison with the spectrum with a normal-conducting tip.

At smaller voltages $|V| < (\Delta_S + \Delta_T)/e$, only thermally excited electrons (or holes) can tunnel. This behavior is demonstrated for the case of an asymmetric junction, where the gap of the tip is much smaller than that of the sample (Figure 2.6b). At a temperature of $T = 4.2\,\mathrm{K}$, the coherence peak of the tip above the Fermi level is populated by some thermally excited electrons, which can tunnel into the unoccupied coherence peak of the sample at a voltage of $V = (\Delta_S - \Delta_T)/e$. Consequently, two smaller peaks inside the gap can be observed in the corresponding dI/dV spectrum (Figure 2.7b).

In the case of a symmetric gap (Figure 2.6c) tunneling of thermally excited single particles is possible at zero voltage, which is then observed as a small peak in the spectrum at $V = 0$ (Figure 2.7c). However, this peak vanishes at lower temperatures as shown in Figure 2.7d.

Apart from that, the width of the spectral features did not change in comparison to Figure 2.7c. Conclusively, already at $T = 4.2\,\mathrm{K}$, the thermal broadening is almost completely suppressed by the use of superconducting electrodes with a gap parameter of $\Delta \approx 1.3\,\mathrm{meV}$.

2.2.5 Two-Band Superconductivity of Pb

A single superconducting gap is mostly assumed for Pb throughout this thesis. Strictly speaking, however, Pb has two different gaps. Here, I will briefly address this peculiarity.

The BCS theory assumes a spherical Fermi surface and an isotropic superconducting gap. However, this premise does not hold true in reality. It has been already known from early tunneling experiments that Pb exhibits an anisotropic energy gap with two different gap parameters[130–133]. It was originally assumed that the cause lies in the anisotropic phonon density of states of Pb[134]. Later on, when highly anisotropic superconductors like MgB_2 were discovered, it has been realized that different gap parameters originate in disjunct Fermi sheets with different electron-phonon couplings[135]. In 2007, Floris et al.[136] were the first to calculate the superconducting properties of Pb by DFT. They reproduced the experimental findings and showed that the two gaps of Pb are indeed linked to its two Fermi sheets.
Finally, in 2015, Ruby et al.[68] measured the two gaps of Pb with STM. They observed different intensities of the coherence peaks linked to the two gaps, depending on the crystallographic orientation of the sample, which is due to selective tunneling into the two bands. They furthermore showed that the weighting of the two gaps changes when the STM tip is moved over a single Pb adatom. On a pristine Pb(100) surface, for example, they observed that the smaller gap Δ_1 is roughly twice as dominant than the larger gap Δ_2. However, the situation changes above a single Pb adatom where the larger gap becomes more prominent.
In the early tunneling experiments, the gap parameters were determined to $\Delta_1 \approx 1.21\,\mathrm{meV}$ and $\Delta_2 \approx 1.38\,\mathrm{meV}$[132,133]. The data from Ruby et al.[68], however, suggest slightly higher values of $\Delta_1 \approx 1.27\,\mathrm{meV}$ and $\Delta_2 \approx 1.42\,\mathrm{meV}$.

Unfortunately, with the provided STM setup, I was not able to resolve the coherence peaks of the two gaps independently, which are only separated by $\approx 150\,\mu\mathrm{V}$. Rather, I observed a single gap with an effective gap parameter Δ lying between Δ_1 and Δ_2. Its exact value thereby depends on the weighting of the two gaps. Consequently, I observed small changes of the effective gap parameter, when measuring above an adatom, step edge, or molecule compared to the gap on the pristine Pb(100) surface.
The poly-crystalline STM tip features only one gap, whose value might vary from tip to tip[68].

2.3 Yu-Shiba-Rusinov States

As already outlined in the Introduction (Chapter 1), Yu-Shiba-Rusinov (YSR) bound states are a phenomenon that occurs when magnetic impurities interact with a superconducting substrate. The magnetic moment of the impurity induces a pair-breaking potential for the Cooper pairs of the substrate, leading to quasiparticle excitations inside the superconducting gap. These excitations are observable as peaks in dI/dV spectra, symmetrically positioned around the Fermi energy, but typically asymmetric in height.

This section gives a short introduction to YSR states including an explanation of their most important properties. For more detailed information, the reader is referred to a review article by Heinrich, Pascual, and Franke[137].

2.3.1 Historical Background and Previous Studies

YSR states were theoretically predicted in the late 1960s by Yu[1], Shiba[2], and Rusinov[3]. Although it was already known that magnetic impurities alter the DOS of a superconductor[138], it took some time until YSR states were experimentally investigated. In 1997, Yazdani et al.[33] were the first to study YSR states in an STM. They observed excitations within the superconducting gap in STS measured in the vicinity of single magnetic Mn and Gd adatoms on a Nb(110) surface. However, at a temperature of 3.8 K and with a normal-conducting gold tip, the spectral energy resolution was rather limited. At the same time, the first three-dimensional and self-consistent calculation of the YSR in-gap states was carried out by Flatté and Byers[139] in terms of a Green's function approach. They explained the observed height asymmetry of the YSR peaks by particle-hole asymmetry in the normal state of the superconductor.
It took ten more years for the next STM study of YSR states: In 2008, Ji et al.[34] studied single atoms and dimers of Mn and Cr on Pb thin films. In comparison to the work of Yazdani et al., they increased the spectral resolution drastically by operating at temperatures down to 0.4 K and by using a superconducting Nb tip. They also were the first to observe multiple pairs of YSR resonances in their spectra, which were attributed to different angular-momentum scattering channels.
The next groundbreaking work in this field was published in 2011 by Franke, Schulze, and Pascual[35]. They studied MnPc molecules on a Pb(111) surface at 4.5 K with a Pb tip. They demonstrated experimentally that in a system of a localized magnetic moment on a superconductor, two different ground states are possible, which are connected by a quantum phase transition. These ground states are determined by the interplay of Kondo screening and superconducting pair-breaking. Depending on the coupling strength of the impurity to the substrate, the so called Kondo-screened state (singlet) or the free spin state (doublet) represents the ground state of the system.
From there on, many studies on YSR states have been published, especially driven by the discovery of zero-energy end-states in chains of ferromagnetic iron atomic chains on Pb(110) in 2014 [11].

In most of the STM studies, 3d transition metal atoms[11–15,23,26,34,39,40] or metal-organic molecules[24,35,37,140–144] on Pb single crystals were investigated. However, also Nb(110)[30,33,145,146] and $NbSe_2$[21,25,28,147,148] were used as substrates. Even more exotic systems like Fe atoms on oxygen-reconstructed Ta(100)[19,42,149], Re(0001)[18,150] or $FeTe_{0.55}Se_{0.45}$[43,151] were examined. Ménard et al.[22] studied long-range magnetic bound states of Fe atoms embedded in a 2H–$NbSe_2$ crystal. In a later study[152], they even found dispersive YSR states on the edge of Co-Si islands on Si(111) covered by a monolayer of Pb. Furthermore, systems like, e. g., Fe doped $NbSe_2$ [153], Cr atoms on β-Bi_2Pd [27], and Gd atoms on ultra-thin Bi layers on Nb(110) [154] were investigated. Huang et al. have recently studied a YSR system on V(100) extensively[29,38,41,155,156], where the nature of the impurities is still unknown.

The single atom impurities studied are especially the 3d transition metals Fe[11–14,18,19,21,28,42,145,148–150], Mn[23,26,30,33,34,39,145,150], Co[15,150], and Cr[27,34,40,145,146]. In addition, magnetic molecules have been studied, mostly metal phthalocyanines (MPcs). Next to MnPc[35,37,140,147,157] also iron phthalocyanine (FePc)[147], cobalt phthalocyanine (CoPc)[25,147], and copper phthalocyanine (CuPc)[158], but also ammonia decorated MnPc (NH_3-MnPc) on Pb(111)[24] and vanadyl phthalocyanine (VOPc) on Pb(111)[142]. Furthermore, YSR states have been observed for other metal-organic complexes like iron porphin (FeP)[141], Fe-5,10,15,20-tetrapyridyl-porphyrin (FeTPyP)[143], and Fe-tetraphenyl porphyrin (FeTPP)[144] [all on Pb(111)].

In addition to the STM studies listed above, YSR states have also been investigated in terms of quantum dots[159–165] and molecular break junctions[166].

The above overview of previous publications is intended to provide a rough outline and does not claim to be exhaustive. To the best of my knowledge, however, I am the first to investigate YSR states on molecules that are originally paramagnetic: H_2Pc and PbPc.

2.3.2 Classical and Quantum Spin Model

This section provides a brief discussion of the classical model and the quantum spin model of YSR states and the properties that follow. It was guided by Reference 137. A more detailed description is given in Reference 167.

In the simplest case, the magnetic impurity has a spin $S_{\text{imp}} = 1/2$ that is described classically. The overall system, consisting of superconducting substrate and impurity, can then assume two different states: a singlet state ($S = 0$) where the impurity spin is screened by an electron from the substrate bound to the impurity, and a doublet state ($S = 1/2$) corresponding to a free, unscreened impurity spin. One of both states serves as the ground state, which can be excited to the other. Consequently, a single pair of resonances appears inside the superconducting gap of the substrate, symmetric in energy with respect to the Fermi level. Figure 2.8a shows a corresponding diagram. The resonances result from quasiparticle excitations from the ground state to the excited state. The total spin of the system is then changed by $\Delta S = \pm 1/2$, whereby the system switches from the singlet state to the doublet state, or vice versa.
In the classical model, the excitation energy, i. e. YSR energy, can be expressed as follows (Reference 137, Equation 1):

$$E_{\text{YSR}} = \Delta \frac{1-\alpha^2}{1+\alpha^2}, \quad \text{where } \alpha = \pi \rho_N(E_F) \cdot J S_{\text{imp}}, \tag{2.20}$$

with the coupling strength α depending on the impurity spin S_{imp}; $\rho_N(E_F)$, which is the DOS of the sample in the normal-conducting state at the Fermi energy E_F; and the exchange coupling J. Figure 2.8b shows a calculated curve of $E_{\text{YSR}}(\alpha)$ (solid line). A dotted line depicts the position of the second resonance, which appears at $-E_{\text{YSR}}$, since – because of the coupling of electrons and holes in superconductors – the system can either be excited by adding or by removing an electron.

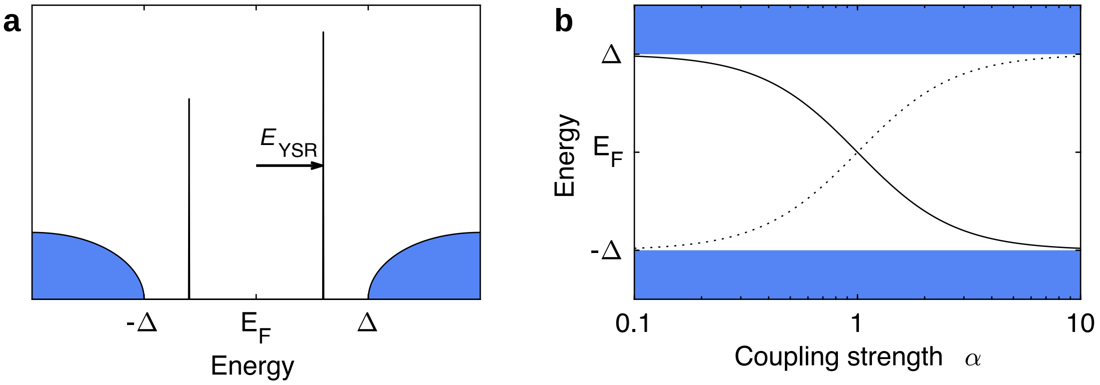

Figure 2.8: (a) Sketch of the quasiparticle excitation spectrum of the sample, showing YSR resonances as a pair of peaks inside the gap. (b) Energy of the YSR state E_{YSR} as a function of the coupling strength α (solid line). In addition, the position of the hole-like excitation is shown as a dotted line. The blue area depicts the quasiparticle continuum of the sample outside the superconducting gap.

The qualitative description in the quantum spin model is very similar. The singlet state is then described as a Kondo screened state, similar to the Kondo effect[168] in normal metals: The impurity spin interacts with the quasi-particle reservoir of the sample via antiferromagnetic exchange coupling ($J > 0$). The case of ferromagnetic coupling is omitted here, but is discussed, e. g., in Reference 167. In this model, the coupling strength is typically expressed in terms of the Kondo temperature T_K. Analogous to the classical model, the Kondo screened state is formed for strong coupling ($k_B T_K \gg \Delta$). In addition to the YSR states, a Kondo resonance can then be observed outside of the superconducting gap[35]. For weak coupling ($k_B T_K \ll \Delta$), the impurity spin remains unscreened and the Kondo peak is masked by the superconducting gap.

At an intermediate coupling strength, the levels of the screened and unscreened state cross and a quantum phase transition occurs. As calculated by numerical renormalization group theory[169,170], it happens at a Kondo temperature of $k_B T_K \approx 0.3\,\Delta$. At the quantum phase transition, the YSR energy crosses zero and becomes negative (Figure 2.8b) as the screened state becomes the new ground state. This level crossing is accompanied by an asymmetry inversion of the spectral weights of the electron- and hole-like excitations, as observed in experiment[35,37,142]. The different spectral weights of electron- and hole-like excitations, also referred to as peak height asymmetry, arise from a particle-hole asymmetry in the substrate, which is either caused by the local Coulomb interaction[167] or by an asymmetry in the normal-state conductance of the superconductor[36,139].

As mentioned earlier, even multiple pairs of YSR resonances can be observed[34]. It has been shown that each pair of resonances is linked to a different impurity orbital[39,40,171]. Consequently, only one pair of YSR resonances is expected for impurities with only one orbital with an unpaired electron ($S = 1/2$).

2.3.3 YSR States in the BdG Theory

In this section, the YSR states in an s-wave superconductor are discussed in terms of the BdG approach. I will limit my discussion on the deduction of the LDOS at the site of the impurity. A more detailed elaboration can be found, e. g., in Reference 125, Section 3.2. In addition, Flatté and Byers[139,172] did a three-dimensional, self-consistent calculation of impurities in superconductors using a similar formalism. Here, I will show a simplified version that allows me to calculate dI/dV spectra featuring YSR states.

First, the Hamiltonian for an s-wave superconductor with a single-site impurity is introduced (see Reference 125, p. 70):

$$\mathcal{H} = \mathcal{H}_0 + \mathcal{H}_{\text{imp}} \tag{2.21}$$

$$\mathcal{H}_0 = \sum_{\mathbf{k},\sigma} \xi_{\mathbf{k}} c^\dagger_{\mathbf{k}\sigma} c_{\mathbf{k}\sigma} + \Delta \sum_{\mathbf{k}} \left(c^\dagger_{\mathbf{k}\uparrow} c^\dagger_{-\mathbf{k}\downarrow} + c_{-\mathbf{k}\downarrow} c_{\mathbf{k}\uparrow} \right) \tag{2.22}$$

$$\mathcal{H}_{\text{imp}} = \sum_{\sigma} \left(\sigma J S + W \right) c^\dagger_{0\sigma} c_{0\sigma}, \tag{2.23}$$

where $c^\dagger_{\mathbf{k}\sigma}$ ($c_{\mathbf{k}\sigma}$) is the creation (annihilation) operator for an electron of spin $\sigma \in \{\uparrow, \downarrow\}$ and wave vector $\mathbf{k}$, and $\xi_{\mathbf{k}} = \varepsilon_{\mathbf{k}} - E_F$ (see Section 2.2.3). $\mathcal{H}_0$ is the Hamiltonian of the unperturbed superconductor, which is equivalent to the BdG equation (Equation 2.17). $\mathcal{H}_{\text{imp}}$ on the other hand describes the scattering induced by an impurity with spin S, where J (W) is the antiferromagnetic (nonmagnetic) scattering potential.

The scattering at the impurity acts as a perturbation on the superconducting state. In the following, this interaction will be analyzed in terms of a Green's function formalism. I start with the homogeneous Green's function of the unperturbed superconducting substrate, which reads (see Reference 172, Equation 12):

$$G_0(E) = \begin{pmatrix} g(E) & f(E) \\ f^*(-E) & -g^*(-E) \end{pmatrix}, \tag{2.24}$$

where $g(E)$ and $f(E)$ are the normal and anomalous Green's functions, respectively (see Reference 172, Equations 38,39):

$$g(E) = -\pi \rho_N(E) \frac{E + \mathrm{i}\Gamma}{\sqrt{\Delta^2 - (E + \mathrm{i}\Gamma)^2}} \qquad f(E) = -\pi \rho_N(E) \frac{\Delta}{\sqrt{\Delta^2 - (E + \mathrm{i}\Gamma)^2}} \tag{2.25}$$

The Green's function matrix is written in spin-up electron and spin-down hole space, similar to the BdG equation (Equation 2.17). It is identical for spin-down electrons and spin-up holes. Furthermore, the Green's function simplifies for a flat normal-conducting DOS $\rho_N(E) = \text{const.}$ and close to the Fermi energy, because then $-g^*(-E) = g(E)$ and $f^*(-E) = f(E)$.

The impurity spin however acts differently on spin-up and spin-down electrons. Thus, the impurity scattering matrix depends on the electron spin σ (see Reference 125, p. 71, Equation 3.6):

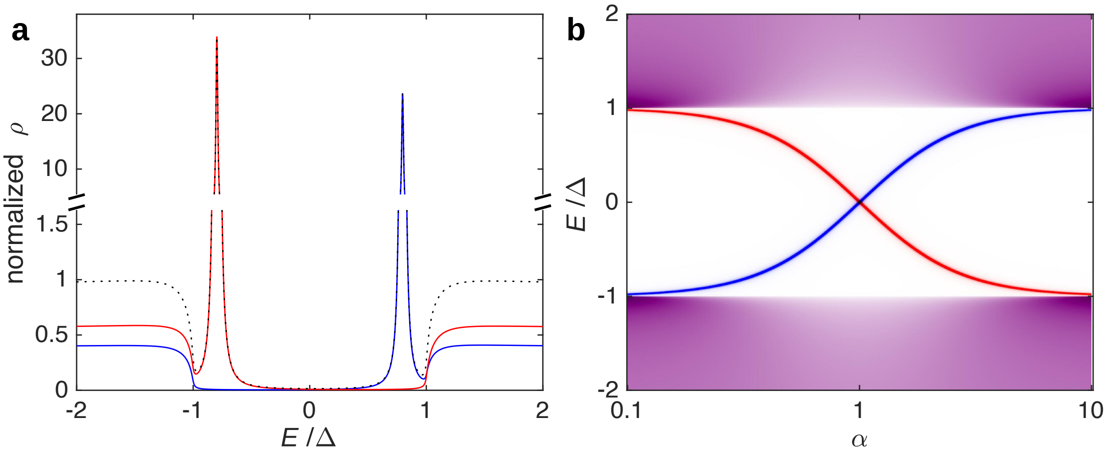

Figure 2.9: Calculated DOS featuring YSR states. The spin-up (spin-down) component is shown in blue (red). Areas where both components overlap appear purple. The DOS is normalized so that it takes the value 1 far outside the gap. (a) Single spectrum calculated with following parameters: $\alpha = 3$, $\beta = 0.3$ and $\Gamma/\Delta = 0.01$. The total DOS is shown as a black dotted curve. (b) DOS with YSR resonances in dependence of the coupling strength α, with the other parameters set to $\beta = 0$ ($W = 0$) and $\Gamma/\Delta = 0.001$.

$$\Sigma_\sigma = \begin{pmatrix} \sigma JS + W & 0 \\ 0 & \sigma JS - W \end{pmatrix} \tag{2.26}$$

With this approach, the Green's function of the coupled system can be calculated as:

$$G_\sigma(E) = \left(G_0^{-1}(E) - \Sigma_\sigma\right)^{-1} \tag{2.27}$$

Finally, the spin-dependent LDOS is obtained by taking the imaginary part of the (1,1) component of G_σ:

$$\rho_\sigma(E) = -\frac{1}{\pi}\Im\left(G_\sigma^{(1,1)}(E)\right) \tag{2.28}$$

The total LDOS is the sum of both spin components $\rho = \rho_\uparrow + \rho_\downarrow$.

Figure 2.9a shows an exemplary calculated spectrum. The spin-up and spin-down components are shown separately (blue and red, respectively). Since YSR resonances are fully spin-polarized, each of the two resonances occurs at one spin polarity only. The position of the YSR peaks depends on the coupling strength $\alpha = \pi\rho_N JS$, as demonstrated in Figure 2.9b. In analogy to α, the nonmagnetic scattering potential W translates to $\beta = \pi\rho_N W$. If $\beta = 0$, both YSR resonances have the same spectral weight, whereas if $\beta \neq 0$, there is a peak height asymmetry. The behavior shown in Figure 2.9b reproduces the relation of Equation 2.20 shown in Figure 2.8b.

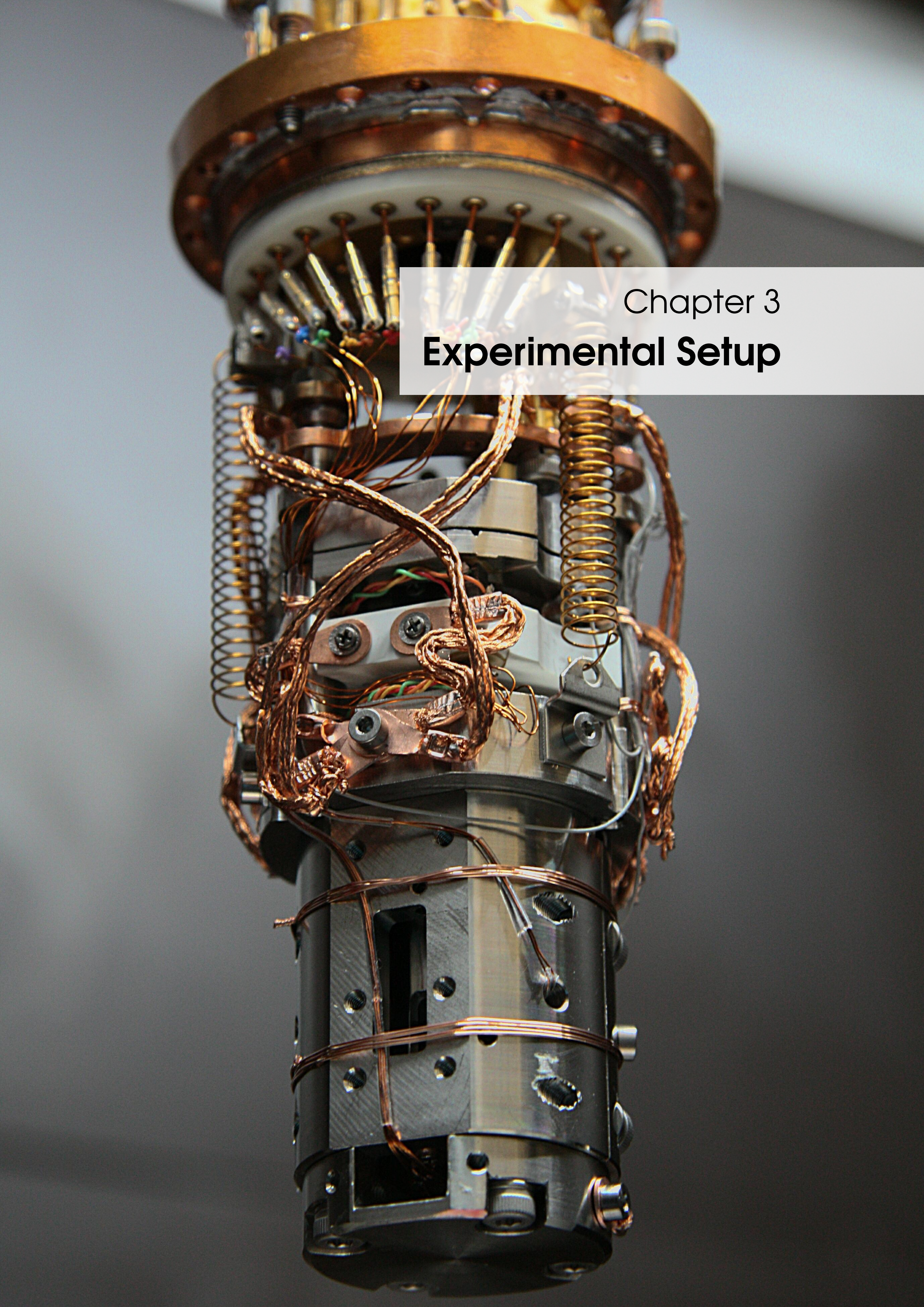

Chapter 3

Experimental Setup

Previous page:
STM from Unisoko used in the mK setup. The photograph was taken during maintenance when the cryostat and UHV enclosure were removed.

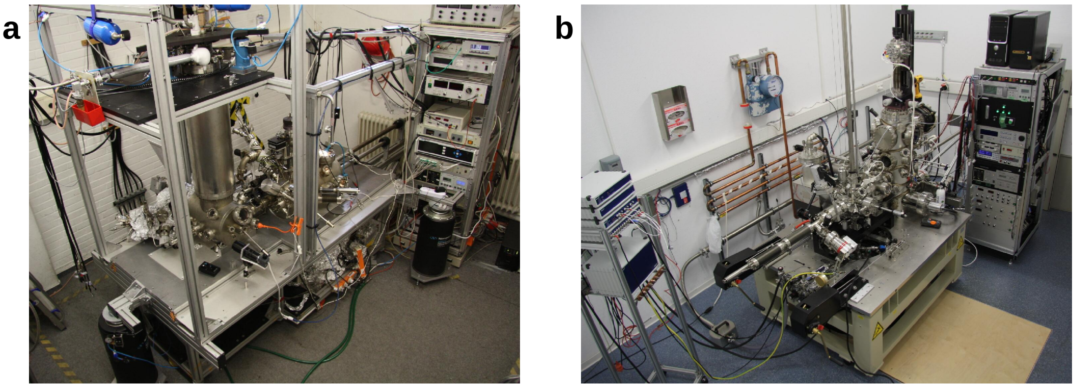

Figure 3.1: STM setups: (a) *4K* and (b) *mK*.

To operate an STM at ultra-low temperatures in UHV, a variety of laboratory equipment is necessary. In addition to the experimental setups, the preparation techniques and the system to be examined are described in this chapter.

3.1 Laboratory Setup

The experiments were mainly conducted at two different STM setups, which will be referenced as *4K* and *mK* and are shown in Figure 3.1a and b, respectively. The *4K* setup is home-built (for a detailed description, see Reference 173), including the STM itself, similar to an original design by Gaisch et al.[174]. The *mK* setup on the other hand is a commercially available STM system from *Unisoko Co., Ltd.* (USM1300[175]) with some custom modifications like a home-built preparation chamber.

Both setups consist of multiple connected vacuum chambers, including a load lock chamber to introduce tips, samples and evaporators into the system; a preparation chamber, suitably equipped to prepare tip and sample; and an STM chamber, where the STM is located. In the STM chamber a base pressure of about 4×10^{-10} mbar is achieved. The preparation chamber of the *mK* setup is furthermore equipped with a compact electron-energy analyzer ESA 150 from *STAIB Instruments* used for Auger electron spectroscopy.

The STM is mounted at the bottom of (*4K*) or surrounded by (*mK*) a helium bath cryostat. With the helium bath alone, the STM reaches a temperature of 4.5 K (*4K*) or 4.2 K (*mK*), which can be further reduced in different ways. In the *4K* setup, a temperature of 2.3 K is reached by reducing the boiling point of helium via pumping on the cryostat. In the *mK* setup, the helium from the cryostat can be expanded through a needle valve to achieve a temperature of about 1.6 K. In addition, even lower temperatures of down to 350 mK can be reached by condensation of He-3 from a built-in reservoir. During these operation modes of the *mK* setup, the STM is thermally insulated from the warmer helium bath via an intermediate vacuum chamber, which is otherwise filled with a small amount of helium gas, acting as thermal exchange gas.

Unlike the *4K* setup, the *mK* setup also has a three axis magnet, which is built into the cryostat and allows the application of magnetic fields of up to 9 T in z-direction and 2 T in both x- and y-direction to the STM.

3.2 Data Acquisition

The *4K* STM is operated via an SPM1000 electronic and XPMPro software from *RHK Technology*. In the mK setup, a Nanonis SPM Control System v5 (electronics and software) from *SPECS Surface Nano Analysis GmbH* are used, which is also equipped with a built-in lock-in amplifier. In the *4K* setup, an SR830 lock-in amplifier from *Stanford Research Systems* is used for that purpose. In both setups, the tunneling current is amplified by a DLPCA-200 variable gain transimpedance amplifier from *FEMTO Messtechnik GmbH*. To enable high voltage-resolution in STS, both setups are equipped with home-built switchable voltage dividers that reduce the applied sample voltage in ratios of 1:1, 1:10, or 1:100.
The acquired measurement data were processed and analyzed using Matlab[62] and Gwyddion[176].

3.3 Sample and Tip Preparation

In the scope of this thesis, almost exclusively Pb(100) single crystals were used as samples and Pb wires for the tips. The crystals of a purity of 99.999% were obtained from *MaTeck Material Technologie & Kristalle GmbH*. The STM tips were made out of Pb wire (0.5 mm diameter, 99.998% purity), which was notched by hand and then torn apart to obtain a clean and sharp tip. The tips were further cleaned via Ar^+ ion sputtering in the preparation chamber before installation in the STM. The Pb crystals were also cleaned in the preparation chamber via ion sputtering and subsequent annealing at 200 to 250 °C. Thereby, special care must be taken not to reach the Pb melting temperature of 327 °C. Melting tests were therefore conducted beforehand, and the sample's temperature was monitored via a pyrometer during annealing. Afterward, the molecules of interest were deposited onto the surface via molecular-beam epitaxy. Home-built

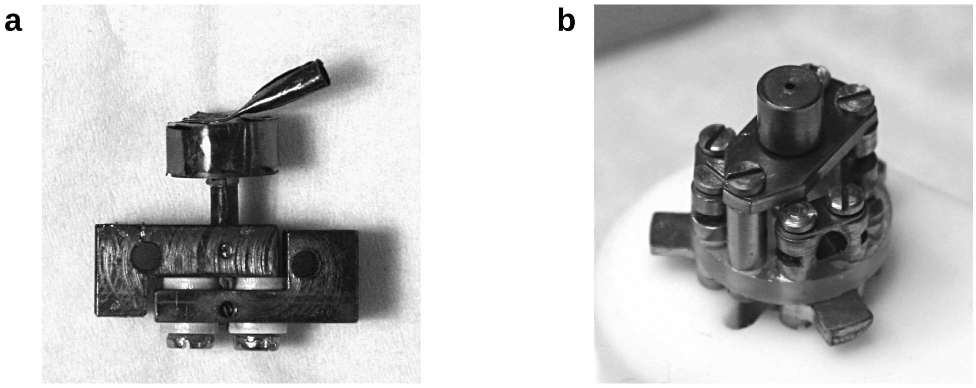

Figure 3.2: Home-built crucibles used for molecule evaporation in (a) the *4K* and (b) the *mK* setup.

crucibles, as shown in Figure 3.2, were used for this purpose. The crucibles were thoroughly cleaned in ultrasonic bath and subsequent degassing in vacuum at high temperatures. Finally, they were filled with the molecules of interest, which were then also degassed in the preparation chamber prior to the evaporation onto the sample.

3.4 Phthalocyanine Molecules

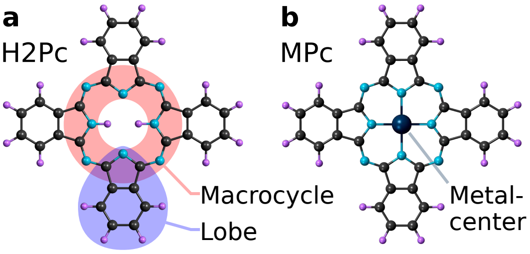

Figure 3.3: Structure models of (a) H_2Pc and (b) MPc. C, N, and H atoms are depicted in gray, cyan, and purple color, respectively. The inner pyrrolic H atoms of H_2Pc render the molecule twofold symmetric, while MPc is fourfold symmetric.

The molecules I studied are (metal-)phthalocyanines, especially H_2-phthalocyanine (H_2Pc) (Chapter 4.1) and lead phthalocyanine (PbPc) (Chapter 5), but also, e. g., manganese phthalocyanine (MnPc) and aluminum phthalocyanine (AlPc) (Appendix A). H_2Pc is a planar aromatic organic molecule composed of four isoindole units, which are linked by nitrogen atoms. The formula is $(C_8H_4N_2)_4H_2$, whereby two additional H atoms are located in the center of the molecule, each bound to a N atom. MPc is obtained by replacing both pyrrolic H atoms by a single metal atom, which leads to a rich variety of metal-organic complexes. Figure 3.3 shows structure models of H_2Pc and MPc. I will refer to each isoindole unit as a *lobe* of the molecule, while *macrocycle* denotes the inner ring-like structure of alternating C and N atoms.

Phthalocyanine molecules exhibit an extended delocalized π-electron system. The resulting optical properties are the basis of a large variety of applications[177,178], such as dyes and pigments[179], organic solar cells[180], photodynamic cancer treatment[181], and many more. Consequently, phthalocyanines are among the most studied types of molecules, especially in nanosciences, where there is an unmanageable number of publications about them. Some surface-science studies on phthalocyanines are listed in a review by Gottfried from 2015 [182].

Because of their chemical stability, phthalocyanines are suitable for molecular-beam epitaxy, and furthermore, they are commercially available from, e. g., *Sigma-Aldrich*. Consequently, phthalocyanines are ideal candidates for STM studies.

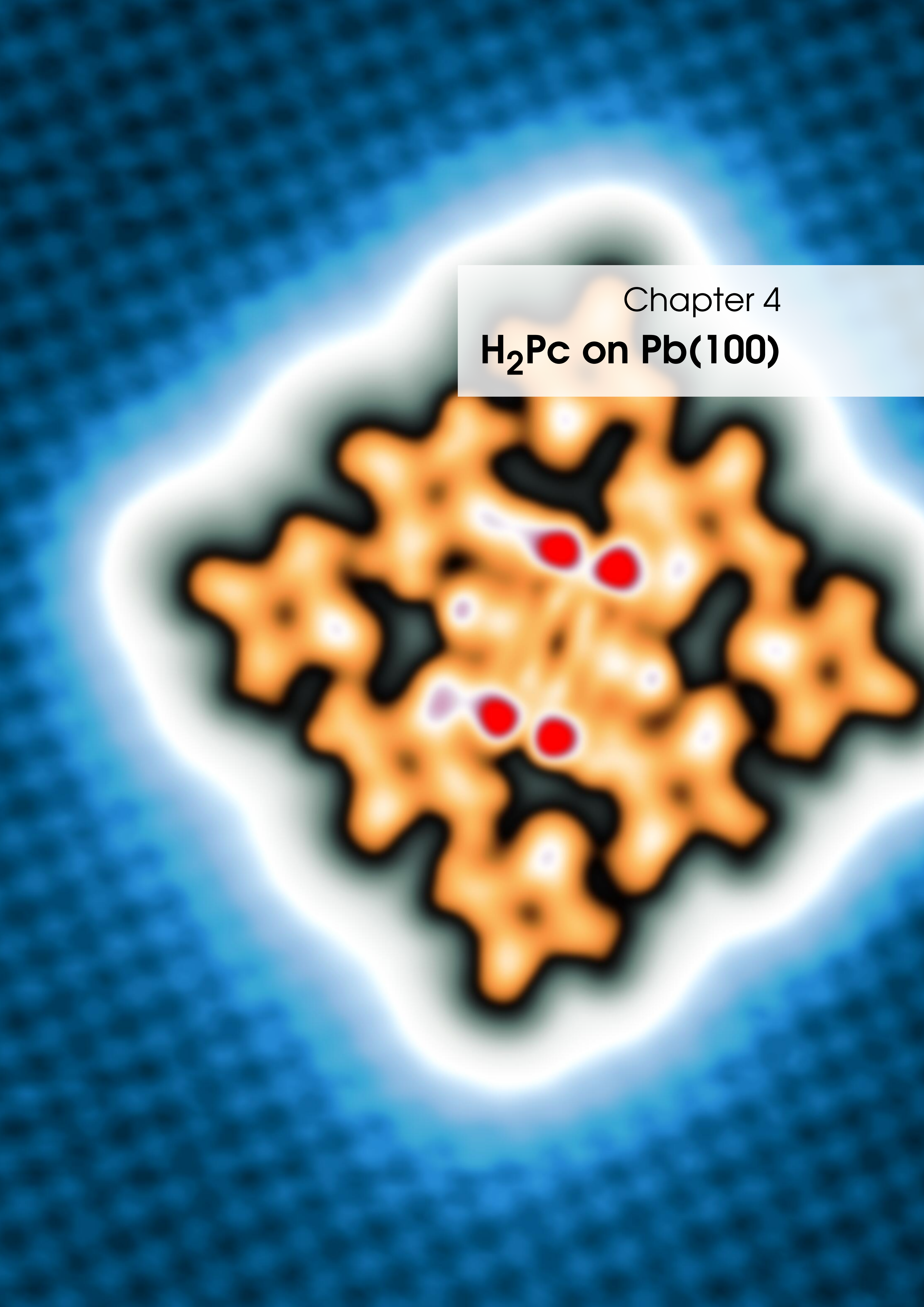

Chapter 4

H_2Pc on Pb(100)

Previous page:
Topograph of an enneamer of $\mathrm{H_2Pc}$ molecules on Pb(100). It was measured at a sample voltage of $V = -10\,\mathrm{mV}$ and a setpoint of $I = 500\,\mathrm{pA}$. The same topograph is revisited in Figure 4.13.

Although H_2Pc molecules are diamagnetic in gasphase, they can acquire a net magnetic moment upon cluster assembly on the surface. This phenomenon is revealed by the observation of YSR states on manually assembled H_2Pc enneamers on Pb(100). Furthermore, the underlying intermolecular interactions are uncovered.
Most of the findings have been published in an article at ACS Nano[45], which is reproduced in the following Section 4.1 and can be accessed online:

https://pubs.acs.org/articlesonrequest/AOR-696SGUUMYZKQKFHDBN9S

The corresponding Supporting Information is reproduced in Section 4.2 thereafter. The layout of text and figures of the article and the Supporting Information has been adapted to this thesis without changing their contents.
Finally, in Section 4.3 the phenomenon of enhanced differential conductances measured centrally above two neighboring molecules is discussed, that was observed and interpreted in the scope of the H_2Pc investigations.

Author Contributions

The reproduced manuscript (Section 4.1) and Supporting Information (Section 4.2) are a joint work of Jan Homberg, Alexander Weismann, Richard Berndt, and Manuel Gruber. The author contributions are as follows:
All authors conceived the experiment. J.H. acquired the STM data with support by A.W. Model development and data analysis were carried out by A.W., M.G., and J.H. All authors contributed to the manuscript.

4.1 Inducing and Controlling Molecular Magnetism through Supramolecular Manipulation

Reproduced with permission from *ACS Nano* 2020, 14, 12, 17387–17395. Copyright © 2020 American Chemical Society.

4.1.1 Abstract

Diamagnetic H_2Pc are probed on superconducting Pb(100) using a low-temperature STM. In supramolecular arrays made with the STM, the molecules acquire a spin as detected via the emergence of YSR resonances. The spin moments vary among the molecules and are determined by the electrostatic field that results from polar bonds in the surrounding phthalocyanine (Pc) molecules. The moments are further finely tuned by repositioning the hydrogen atoms of the inner macrocycle of the surrounding molecules.

4.1.2 Introduction

Magnetic molecules on surfaces have attracted considerable interest, in particular, in view of tuning spin-dependent electron transport through molecular junctions[183–185]. The interaction between a molecule and a substrate can significantly alter the molecular spin through charge transfer, extreme cases being the creation or quenching of spin magnetic moment[186–192]. The charge transfer can be modified by charges close to the molecule[187,193].

The interaction between a localized spin and Cooper pairs of a superconductor leads to the emergence of YSR states[1–3,33], which has been shown for, e. g., MPc complexes[24,25,35,137,140,142,147]. In low-temperature STS, YSR resonances are observed as pair(s) of peaks, symmetrically located around the Fermi energy E_F within the gap of the superconductor.

Here, we show the emergence of a spin moment in initially diamagnetic H_2Pc molecules within a self-assembled monolayer on Pb(100) using YSR resonances for spin detection. The spin moments are found to significantly vary from molecule to molecule. The magnitude of the induced moment is determined by the electrostatic field that results from polar bonds in the surrounding Pc molecules. Each molecule generates an approximate quadrupole field, which can be inverted by repositioning the hydrogen atoms of the inner macrocycle of the molecule. We fabricated supramolecular arrays and selectively swapped hydrogen atoms to tune the magnetic moment with a precision of ~0.01 Bohr magneton.

4.1.3 Results and Discussion

Single Molecules on Pb(100). H_2Pc (Figure 4.1a) at first glance does not lend itself to spintronics and YSR physics. The molecule adsorbs flat on Pb(100) in two orientations (Figure 4.1b) and exhibits no magnetic moment due to its closed electron shell and the absence of charge transfer. Correspondingly, low bias differential-conductance (dI/dV) data acquired with superconducting Pb tips are virtually identical on the molecules and the substrate and show coherence peaks at $\pm 2\Delta$[68], Δ being the superconducting order parameter (Figure 4.1c).

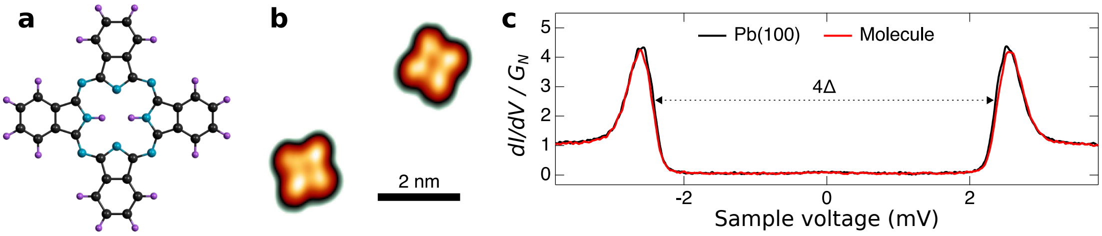

Figure 4.1: (a) Model of H_2Pc. Gray, blue, and purple spheres represent C, N, and H atoms, respectively. (b) STM topograph ($V = 30\,\text{mV}$, $I = 60\,\text{pA}$) of two H_2Pc molecules on Pb(100). (c) dI/dV spectra acquired using a superconducting tip atop a single molecule (red) and on Pb(100) (black).

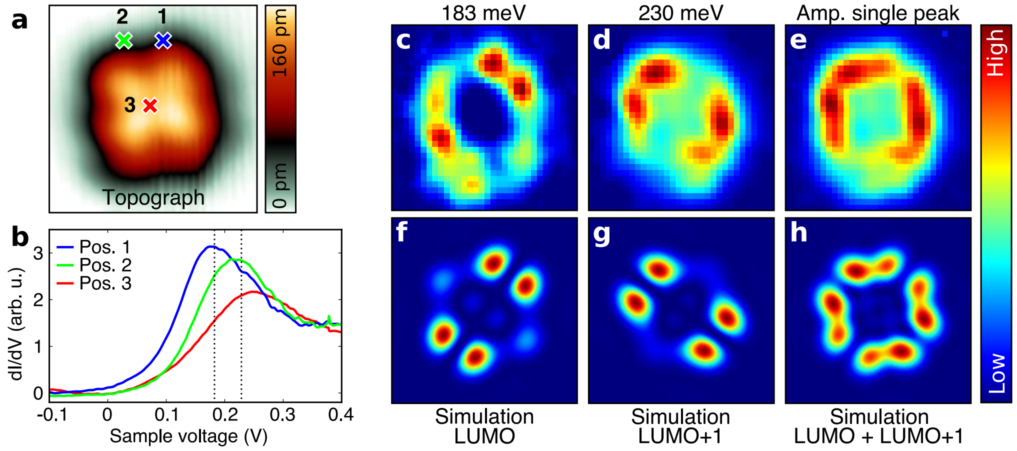

Figure 4.2: (a) Constant-current topograph of a single H_2Pc molecule ($V = 10\,\mathrm{mV}$, $I = 100\,\mathrm{pA}$, 3.5 nm wide). (b) Background-subtracted dI/dV spectra measured at the positions indicated in (a). The vertical dashed lines are located at 183 and 230 meV. dI/dV spectra such as shown in (b) acquired over a grid of 32×32 points above the H_2Pc imaged in (a) were fitted using two approaches. (i) Data were fit with two Lorentzians of variable widths and amplitudes centered around fixed energies of 183 and 230 meV, respectively. (c) and (d) display the amplitudes of the Lorentzians. (ii) The fit function is a single Lorentzian, whose amplitude is shown in (e). (f–h) Simulated dI/dV maps of the LUMO, LUMO+1 and of their sum (see text and Supporting Information 4.2.2.2). Experimental dI/dV were obtained from measured I(V,x,y) data (feedback opened at $I = 1\,\mathrm{nA}$ and $V = -400\,\mathrm{mV}$) by energetic and spatial smoothing prior to numerical differentiation.

Next, we focus on the LUMO of single individual H_2Pc molecules on Pb(100), as they play an important role in the magnetism induced in supramolecules discussed below. The dI/dV spectrum acquired atop the center of a single molecule (red curve in Figure 4.2b) exhibits a broad resonance centered at ≈0.2 V. At first glance, this resonance could be ascribed to the LUMO of H_2Pc on Pb(100). However, we find the resonance energy to depend on the lateral position (Figure 4.2a,b), which we attribute to two distinct effects.

First, the spectrum contains contributions from LUMO and LUMO+1 orbitals, which are close in energy (splitting of ≈38 meV in our gas-phase DFT calculations). To separate these components, dI/dV spectra acquired on a 32×32 grid (Figure 4.2a) were fit with two Lorentzians. Fixed energies of 183 and 230 meV were used for all spectra, but the widths and amplitudes were allowed to vary. The spatially resolved amplitudes of the Lorentzians are represented with colors in Figure 4.2c,d. The amplitude distribution at low energies (Figure 4.2c) appears to be rotated by 90° compared to the higher energy pattern (Figure 4.2d). Such a rotation between LUMO and LUMO+1 is indeed expected from our DFT calculations. For further comparison, we simulated dI/dV maps within the Bardeen approach and considered tunneling matrix elements between a spherical wave function modeling the tip and the LUMO and LUMO+1 (see Supporting Information 4.2.2.2). The simulated dI/dV maps of the LUMO and LUMO+1 (Figure 4.2f,g) qualitatively match the experimental amplitude distributions (Figure 4.2c,d). In particular, the positions of the highest intensities (red areas) are quite well reproduced. For completeness, instead of using two Lorentzians, we fit the same dI/dV spectra with a *single* Lorentzian. The resulting amplitude distribution (Figure 4.2e), which exhibits maxima at the rim of the molecule, is qualitatively reproduced by a simulated dI/dV map that takes the LUMO and LUMO+1 into account (Figure 4.2h). We conclude that the large dI/dV resonance at $\approx$0.2 V has contributions from both the LUMO and LUMO+1. In turn, the peak energy varies according to the relative weight of these orbitals.

A second cause of a spatial variation of the resonance energy was previously described by Pavliček et al.[194]. At the center of the molecule, the tunneling matrix element between the s-wave tip and the rapidly oscillating molecular wave function vanishes because of symmetry. However, a molecular vibrational mode can break the symmetry such that a dI/dV resonance occurs at the voltage corresponding to the sum of the LUMO and vibration energies. Indeed, spectra acquired over the center of the molecule (red curve in Figure 4.2b) display a peak at $\approx$250 meV, i. e., above the LUMO+1 energy. Our simulated dI/dV maps (Figure 4.2f–h) do not take this mechanism into account and consequently do not show this resonance at the center.

Self-Assembled Monolayer of H_2Pc. In contrast to individual H_2Pc molecules on Pb(100), some molecules in self-assembled islands observed at larger coverage display additional protrusions with various apparent heights (purple areas in Figure 4.3a). Differential-conductance spectra acquired atop these protrusions reveal the signatures of YSR resonances (e. g., red and blue curves in Figure 4.3b). Compared to the coherence peaks of the substrate, these resonances are closer to E_F and have larger amplitudes that are different at positive and negative voltages. The asymmetries and the energies of the YSR resonances vary with the intensity of the purple protrusions in Figure 4.3b indicating that these protrusions have a magnetic origin. The aggregation of H_2Pc molecules into a self-assembled layer apparently leads to the emergence of magnetism. Intriguingly, only half of the assembled molecules carry a magnetic moment, and their magnetic properties scatter.

Figure 4.3: (a) Topograph (20 nm wide, $I = 50$ pA, $V = 10$ mV) of a self-assembled H_2Pc layer on Pb(100). Superimposed models depict individual molecules. Arrows indicate crystallographic axes of the Pb(100) substrate. (b) dI/dV spectra of protrusions [purple areas in (d)] of different heights (blue and red) and of Pb(100) (black). The peaks of the red and blue curves lie in the superconducting gap, are larger and asymmetric about $V = 0$, which is typical of YSR resonances. The inset shows a zoom around 2.5 mV.

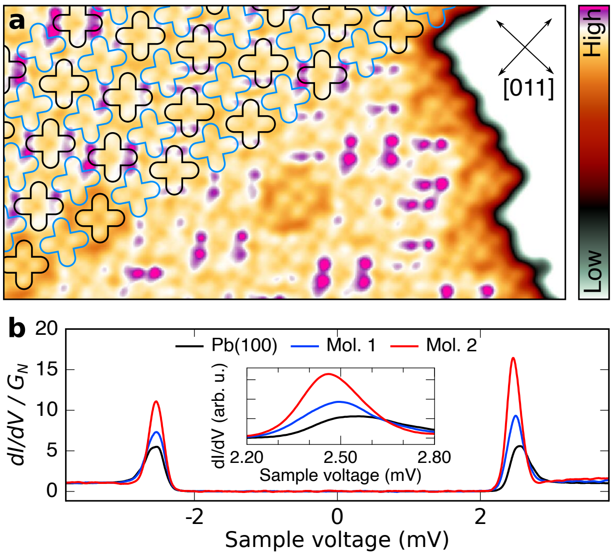

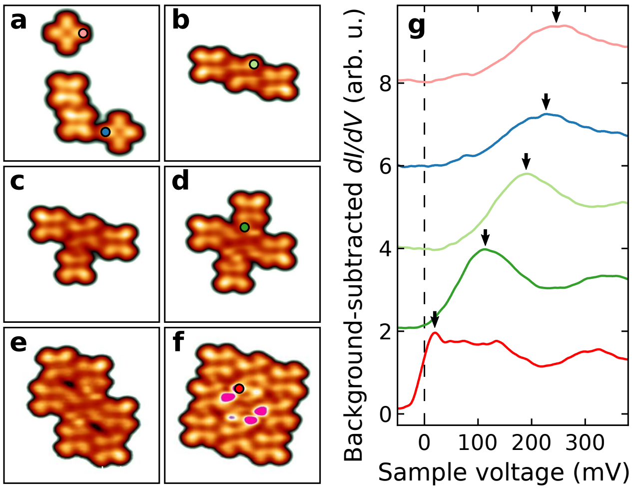

Figure 4.4: (a–f) Constant-current STM topographs (70 pA, 10 mV, image width 8 nm) illustrating the construction of a 3 × 3 supramolecule. (g) Background-subtracted dI/dV spectra acquired over the points marked in (a–f). The spectra are vertically offset for clarity. The fourth spectrum from the top was scaled by a factor of 0.6. As the number of neighbors of the central molecule increases, the first unoccupied resonance (marked by a black arrow) progressively shifts toward the Fermi level.

Construction of Supramolecules. To understand the unanticipated results, we constructed – similar to experiments on Ag(100) and Cu(100)^{187,195} – arrays of 3×3 molecules, which are the smallest structures replicating the results observed from the self-assembled monolayer. Manipulation with the STM was used as illustrated in Figures 4.4a–f. Eight classes (A, A*, B, B*, C, C*, D, D*; see below) of supramolecules with different lattice vectors and molecular orientations were constructed and studied. The self-assembled monolayer (Figure 4.3a) may be viewed as a periodic repetition of A and A* supramolecules. The center and corner (edge) molecules of a supramolecule A are oriented as depicted by the black (blue) contours (Figure 4.3a). The investigated supramolecules are of type A if not otherwise specified. The central molecule of this enneamer (Figure 4.4f) exhibits protrusions (purple) similar to those observed in the self-assembled monolayer. Figure 4.4g displays dI/dV spectra acquired over a lobe of the central molecule at different steps of the construction sequence. The energy of the LUMO/LUMO+1 resonance, located at approximately 250 meV for a single molecule (and depending on the lateral position as described above), decreases as further neighbors are added to the cluster. For a 3×3 supramolecule (red spectrum in Figure 4.4g), the resonance on the central molecule crosses the Fermi level.

To gain further insight in the electronic states properties of the supramolecule, we acquired dI/dV spectra on a 64×64 grid. Figure 4.5a shows a map of the dI/dV signal at 16 meV. The intensity is the highest at the rim of the central molecule. The resemblance of the central part of the map with the simulated dI/dV map of the LUMO of a single molecule (Figure 4.2f) suggests that, at 16 meV, the dI/dV signal mainly originates from the LUMO of the central molecule. The LUMO+1 of this molecule is mainly probed at 42 meV (Figure 4.5b). Compared to the 16 meV map, the pattern appears to be rotated by 90°. In contrast, the dI/dV signal at 180 mV is largest at the rim of the surrounding molecules, while the central molecule exhibits low conductance. These observations show that the lowest unoccupied supramolecular orbital (LUSO) essentially corresponds to the LUMO of the central molecule.

Figure 4.5d shows the dI/dV spectra acquired over the center of every molecule within the supramolecule (black curves). To determine approximate LUMO energies, each spectrum was

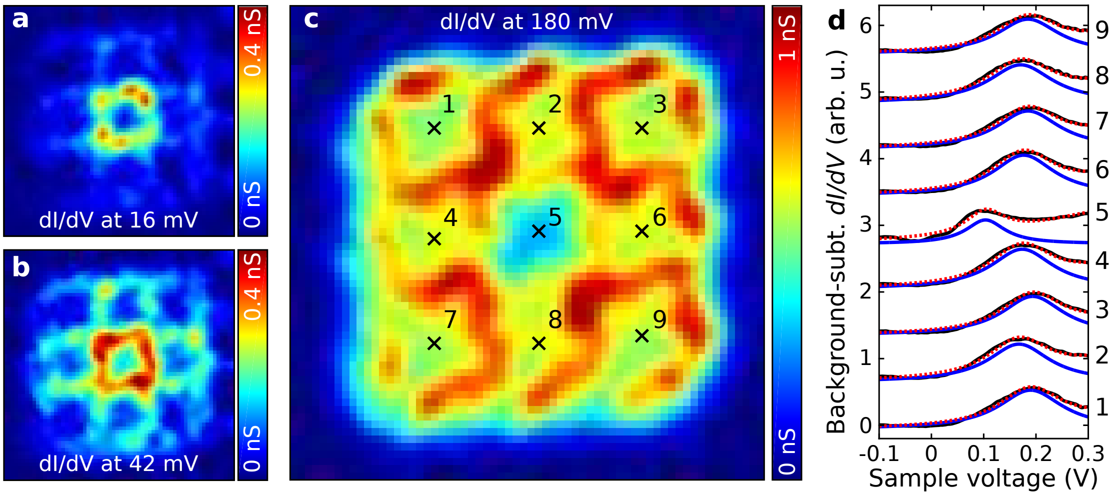

Figure 4.5: Grid of 64×64 I-V curves was acquired over a supramolecule (feedback loop opened at $I = 200\,\text{pA}$ and $V = -400\,\text{mV}$). Corresponding dI/dV maps at (a) 16, (b) 42, and (c) 180 mV. (d) Background-subtracted dI/dV spectra obtained at the center of each molecule [see (c) for locations] along with a fit (dotted red curve) with the sum of two Lorentzians (the first one is shown as a blue curve). The spectra are vertically shifted in steps of 0.7 for clarity.

fit with the sum of two Lorentzians. The first Lorentzian (blue curves in Figure 4.5d) is attributed to the LUMO and LUMO+1 of the investigated molecule. The second Lorentzian (not shown) accounts for spectral features at higher voltages including vibrational excitation at higher energies. As the dI/dV spectra of Figure 4.5d were acquired over the molecular center, the influence of neighboring molecules is minimized. The peak energies (peaks of the blue curves) therefore correspond to the sum of the respective LUMO energies and the vibrational energy of the modes breaking the orbital symmetry, which we assume to be constant for all molecules. In the present example, the blue curves in Figure 4.5d peak at 190, 168, 194, 174, 104, 177, 185, 171, and 185 mV for molecules 1 to 9. These values are indicative of the relative variation of the LUMO energy on the different molecules.

Magnetism of Supramolecules. Similar to molecules in the self-assembled layer, the central molecule of a 3 × 3 cluster exhibits apparent protrusions (purple areas in Figure 4.6a). Differential-conductance spectra acquired over these protrusions (orange curve in Figure 4.6b) exhibit the characteristic features of YSR resonances. The superconducting gap appears to be effectively reduced compared to that of the substrate (dashed lines in Figure 4.6b), the peak heights below and above the Fermi level are different, and – in the present case – their amplitudes are significantly larger than those of the coherence peaks of the substrate (blue curve in Figure 4.6b). The supramolecule shown in Figure 4.6a consequently carries a magnetic moment, and thus reproduces the main observations from the self-assembled layer.

The dI/dV image in Figure 4.6c reveals that the YSR resonance is limited to the central molecule and displays a 2-fold symmetry, similar to the LUMO of the Pc molecule. DFT calculations (substrate initially neglected) show that the LUSO (Figure 4.6d) resembles the dI/dV map

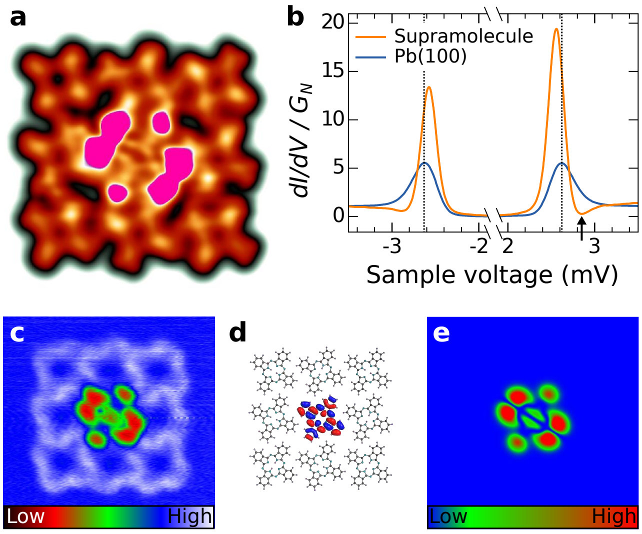

dI/dV @ 2.85 mV

LUSO

Simulated *dI/dV* LUSO

Figure 4.6: (a) Constant-height STM current image (6 nm wide, $V = 5\,\text{mV}$) of a 3×3 array exhibiting protrusions over the central molecule (purple region). (b) dI/dV spectra acquired over the protrusion (orange) exhibiting YSR resonances and on Pb(100) (blue). The two solid black lines indicate the peak positions expected without YSR resonances. (c) Constant-height dI/dV image [2.85 mV, arrow in (b)] mapping the YSR resonances. The inset shows the corresponding color scale. (d) Isocontour of the supramolecule LUSO from gas-phase DFT calculations along with molecular models. Blue and red colors represent different signs of the wave function. (e) Simulated dI/dV image of the LUSO shown in (d).

and the LUMO of H_2Pc on the central molecule. A simulated dI/dV map taking into account the tunneling matrix element between an s-wave tip and the LUSO (Figure 4.6e) matches the experimental data even better (Figure 4.6c). We emphasize that the LUSO does not directly contribute to the signal of Figure 4.6c. At the sample voltage of 2.85 mV used (arrow in Figure 4.6b), the YSR resonance reduces dI/dV compared to the substrate spectrum, whereas a direct LUSO contribution would increase it. The dI/dV reduction after the resonance can result in negative differential conductance (see, e. g., Figure 4.16 of the Supporting Information). Numerical simulations (not shown) suggest that a negative dI/dV cannot solely result from the BCS density of states of the tip and sample. Rather in-gap states are involved.

The similar lateral distributions of the YSR resonance and the LUSO suggest that the LUSO is at the origin of the magnetic moment. *Single* H_2Pc molecules on Pb(100) are *neutral* as reflected by positive energy of the LUMO. The LUSO energy of a *supramolecule*, however, decreases with the number of constituents (Figure 4.4), and crosses the Fermi level (red curve in Figure 4.4g) leading to a charge transfer, which in turn results in an unpaired electron and hence a magnetic moment. A Kondo resonance on single CuPc complexes on Ag(100) was observed to disappear upon the construction of similar supramolecules[187]. This was attributed to a LUMO shift caused by electrostatic interactions of charged CuPc, in contrast to the present case of neutral H_2Pc. Alternatively, while shifts of molecular orbitals induced by neighboring neutral molecules have been reported previously[196], these shifts did not lead to induced magnetism.

Origin of the LUSO Energy Shift. To understand the energy difference between the LUMO of an isolated molecule and the LUSO, we expanded the DFT wave functions of the supramolecule into linear combinations of H_2Pc orbitals localized on each molecule and derived an effective tight-binding Hamiltonian of the supramolecule in this basis (see Supporting Informa-

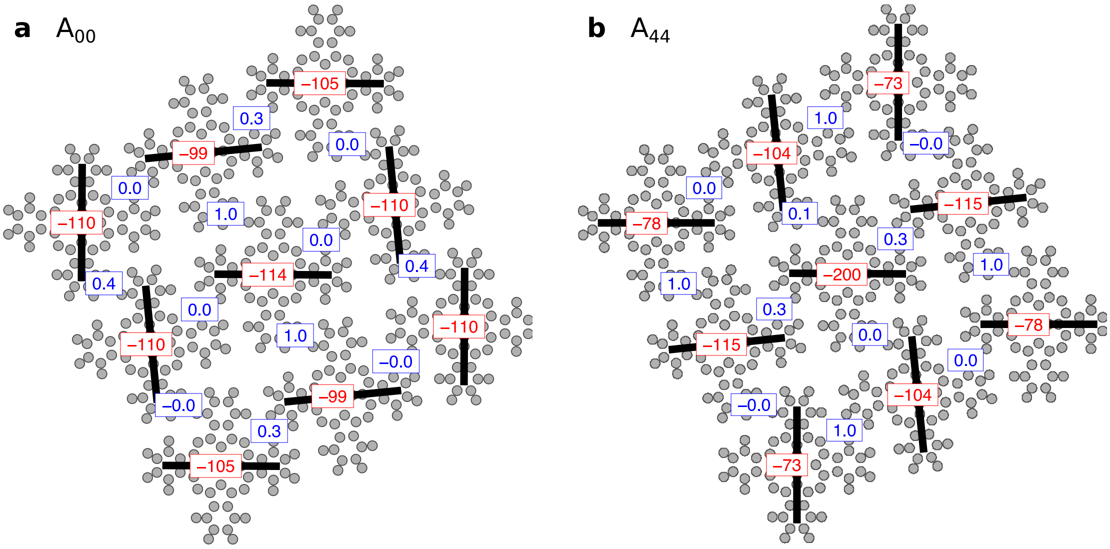

Figure 4.7: On-site energies (red) of LUMOs in supramolecules (a) A_{00} and (b) A_{44} relative to the LUMO energy of the isolated molecule (see Supporting Information 4.2.2.3). The hopping matrix elements between the LUMOs of neighboring molecules are indicated in blue. Gray disks represent atoms of the H_2Pc molecules. Black bars indicate the axes defined by the pyrrolic hydrogen atoms.

tion 4.2.2.3). Figure 4.7 shows tight-binding parameters extracted from calculations of two supramolecules with different positions of the inner pyrrolic hydrogen atoms of the eight surrounding molecules. We use the axis defined by these H atoms to label the configurations as A_{XY}, where X (Y) is the number of side (corner) molecules whose axis is pointing toward the central molecule. We observe that the hopping matrix elements (values in blue in Figure 4.7) are relatively small, which indicates a negligible hybridization between LUMOs of neighboring molecules. The hybridizations to neighboring highest occupied molecular orbitals (HOMOs) and LUMOs+1 are negligible as well (Supporting Information 4.2.2.3). The orbitals of a H_2Pc supramolecule can therefore be approximated by orbitals of the individual molecules shifted in energy due to intermolecular interactions.

The energy shift is given by the on-site energy (values in red in Figure 4.7). For instance, the central molecule LUMO of a A_{00} cluster is shifted by $-114\,\mathrm{meV}$ (Figure 4.7a) relative to the LUMO of an isolated molecule. For the A_{44} supramolecule, the energy shift of the central LUMO is even larger ($-200\,\mathrm{meV}$, see Figure 4.7b). While these shifts are inferred from gas-phase calculations, they are similar to the experimentally observed LUMO downshift ($\approx 200\,\mathrm{meV}$).

We performed a similar analysis on other orbitals, including the HOMO and LUMO+1 (Supporting Information 4.2.2.3). For a given molecule in a supramolecule, the energy shifts of the HOMO, LUMO and LUMO+1 have similar magnitudes, which is evidence of an electrostatic origin. To further elucidate the electrostatic interactions, we compared the supramolecular Mulliken charge distribution to that of an isolated molecule. We find three main contributions to the downshift of the LUSO based on an analysis of 42 calculated supramolecules with differ-

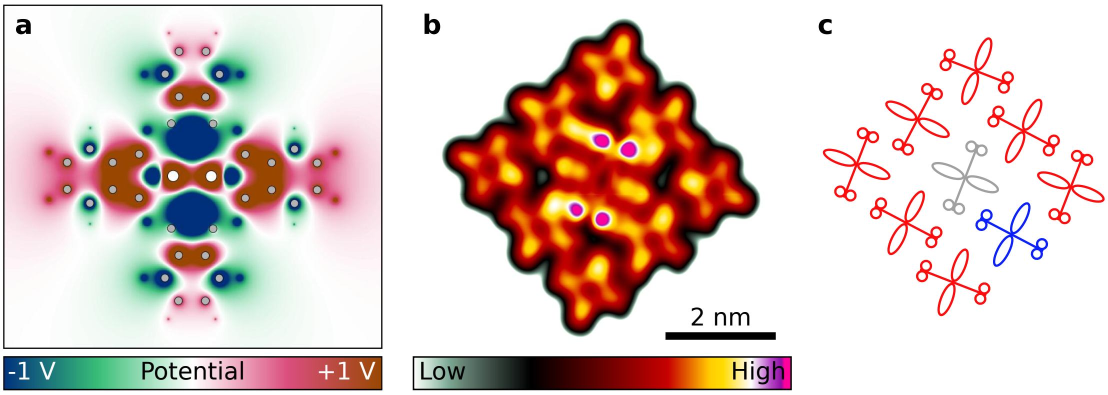

Figure 4.8: (a) Electrostatic potential of a neutral H_2Pc molecule calculated using atomic Mulliken charges obtained from gas-phase DFT calculation of a single molecule. Gray and white disks, respectively, represent C and inner H atoms. (b) Constant-current STM topograph ($V = -10\,\text{mV}$, $I = 100\,\text{pA}$) of a supramolecule on Pb(100). The lobes carrying a pyrrolic H appear higher. (c) Illustration of the tautomer configuration, where broad long (split) arms represent the isoindole groups bearing (void of) an inner H atom. Molecules with pyrrolic H pointing toward (away from) the central molecule are depicted in red (blue).

ent tautomer configurations, i. e., different positions of the two central hydrogen atoms of each molecule (Supporting Information 4.2.2.4): (i) the LUMO of each molecule shifts by $\approx -40\,\text{meV}$ per nearest neighbor, (ii) although individual H_2Pc molecules are neutral, they contain polar bonds leading to a quadrupole-like electrostatic field (Figure 4.8a) which can shift the orbital energies of nearest (next-nearest) molecules by $\approx \pm 10\,\text{meV}$ ($\approx \pm 4\,\text{meV}$). (iii) The polarization of neighboring molecules (Figure 4.9) causes electrostatic fields inducing an additional shift of up to $\pm 10\,\text{meV}$.

Figure 4.8a shows the electric potential of a single H_2Pc in the gas phase calculated from the Mulliken charges. Outside of the molecule, it is essentially quadrupolar, similar to the field reported previously for naphthalocyanine molecules[197]. Adjacent molecules located on areas with positive potential (red) exhibit a lower LUMO energy. The orientation of the quadrupole-like potential is dictated by the positions of the inner hydrogen atoms, which can be recognized in high-resolution STM images. The isoindole groups bearing pyrrolic hydrogen atoms appear higher[56,198,199]. For instance, the lower and upper groups of the upper molecule in Figure 4.8b appear slightly higher than the left and right parts. Close inspection of the data enables this identification for every molecule. For simplicity, the tautomer configuration is visualized in Figure 4.8c, where broader arms represent the benzopyrrole groups with pyrrolic H atoms. It may be worth mentioning that the tautomer configuration of the central molecule is inferred from the orientation of the purple LUMO-related protrusions.

The electrostatic polarizations of molecules in a cluster are shown in Figure 4.9. Colors indicate Mulliken charge differences compared to equivalent atoms of isolated molecules. The largest contributions are due to polarized C–H bonds, which generate electrostatic dipole fields.

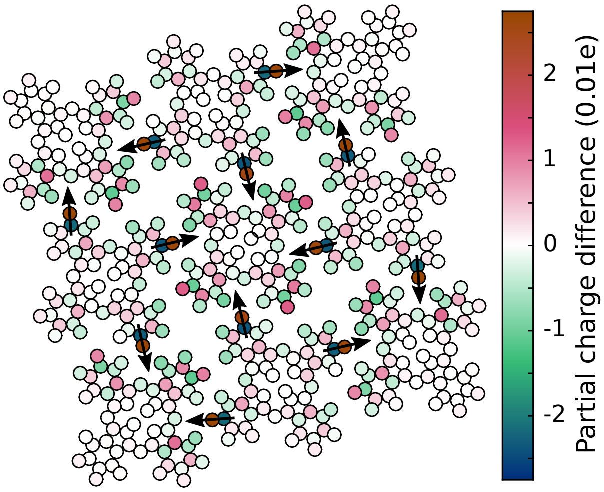

Figure 4.9: Electrostatic polarization upon supramolecular assembly. Black circles indicate atoms of H_2Pc molecules. Colors represent partial charge differences, which were obtained by subtracting the charges of equivalent atoms in isolated H_2Pc molecules from the Mulliken charges of the supramolecules. The largest polarization is found within C-H bonds where the respective C and H atoms form dipoles (arrows). The dipoles vary with the type of supramolecule (compare A and A* in Supporting Information Figure 4.25). The calculations were done for supramolecule A_{44}.

We included the previously mentioned three contributions in a phenomenological model that predicts the orbital-energy shift of each molecule inside a supramolecule for an arbitrary tautomer configuration (Supporting Information 4.2.2.4). The screening by the metal substrate is expected to reduce these shifts. This was taken into account by including image charges in the substrate and leads to a good agreement between our model and the energies from dI/dV spectra. In summary, the gas-phase calculations show that the lowest (highest) energy of the LUSO is obtained when the axes through the two pyrrolic H atoms of all surrounding molecules point toward (away from) the central molecule. In total, out of the 512 possible tautomer configurations for a supramolecule, the LUSO energy may be tuned to at least 25 different values.

Tuning of the Magnetic Moment via Tautomerization. Tautomerization of the pyrrolic H rotates the electrostatic stray field of the molecule by 90° and thereby modifies the LUMO energies of neighboring molecules. Molecules within the cluster may be selectively tautomerized by electron injection ($V \geq 400\,\mathrm{mV}$)[198,199].

We converted a supramolecule into various tautomer configurations (Figure 4.10(a) and Supporting Information 4.2.1.5), and acquired dI/dV spectra. From A_{00} to A_{44}, the LUSO energy decreases (not shown) and the YSR resonance continuously shifts toward E_F (Figure 4.10b), while the peak-height asymmetry increases. Similar measurements were performed on another supramolecule, where three further configurations are addressed (Supporting Information 4.2.1.5). We note that a shift of the YSR energy was previously induced by changing the tip-molecule distance. The effect was attributed to varying coupling between the localized spin and

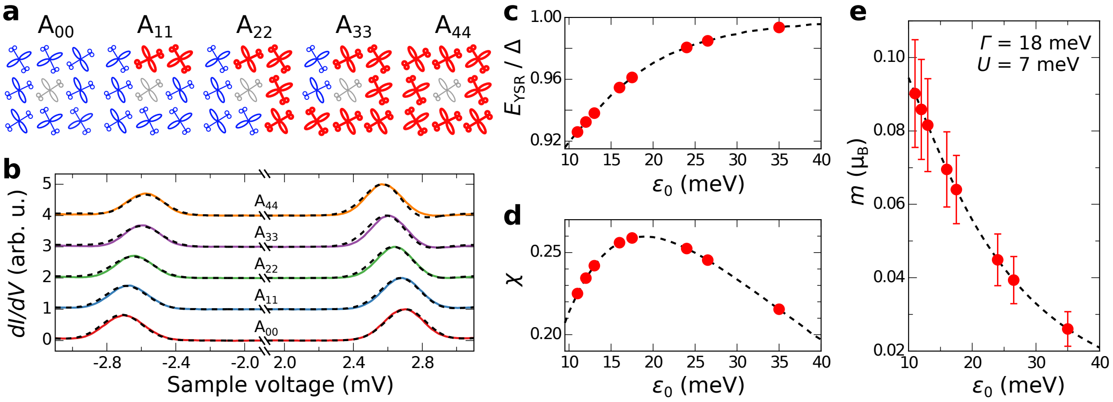

Figure 4.10: (a) Tautomer configurations realized in a supramolecule. (b) Corresponding experimental differential-conductance spectra acquired on the central molecule (solid lines) along with simulated spectra (dashed lines). The latter were obtained by calculating the spectral function, convolving the spectral function with the density of states of the superconducting tip and a Gaussian of standard deviation of $120\,\mu$V. The parameters $U = 7\,$meV, $\Gamma = 18\,$meV, and $\Delta = 1.39\,$meV were used for all simulated spectra, while $\epsilon_0 \in [11, 13, 17.5, 24, 35]\,$meV. The values ϵ_0 were obtained from experimental high-bias spectra (Supporting Information 4.2.1.4) and were allowed to vary by $\pm 1\,$meV to better match the experimental YSR resonances. (c) Normalized YSR energy E_{YSR}/Δ vs. ϵ_0 (curve). Symbols show the experimentally determined ratio E_{YSR}/Δ and ϵ_0. (d) Peak-height asymmetry χ of the YSR resonance vs. ϵ_0 calculated using the parameters of (c). (e) Calculated magnetic moment m vs. ϵ_0 (curve). Symbols represent the estimated magnetic moment for, from left to right, A_{44}, A_{40}, A_{33}, A_{30}, A_{22}, A_{11}, A_{10}, and A_{00}. The bars show uncertainties of m resulting from the uncertainties of $\pm 1\,$meV and $\pm 3\,$meV for U and Γ, respectively. (c, d) and (e) include data from a different supramolecule (Supporting Information 4.2.1.5), which have been simulated using the same parameters U, Γ, and Δ.

the substrate[141,142,155]. In the present case, the different YSR energies are the result of different magnetic moments of the supramolecule controlled through static configurations of the pyrrolic hydrogen atoms.

Determination of the Magnetic Moment. To address the relationship between YSR, magnetic moment, and LUSO energies, we used a Bogoliubov-de Gennes (BdG) approach to model single spin-up and spin-down orbitals at the energies $\epsilon_0 - U/2$ and $\epsilon_0 + U/2$, which hybridize with a superconducting substrate with a pairing energy Δ[200]. U describes the effective splitting of the spin-up and spin-down orbitals, which is assumed to be constant for all supramolecules. The hybridization V to the substrate broadens the orbitals to a half-width at half-maximum (HWHM) $\Gamma = |V|^2\pi\rho$, where ρ is the density of states of the substrate in the normal-conducting state. From this model, we calculated spectral functions within a Green function approach. Using the experimental LUSO energy as ϵ_0 (Supporting Information 4.2.1.4) and a single set of parameters $U = 7\,$meV and $\Gamma = 18\,$meV, the calculations reproduce the experimental spectra well (dashed black lines in Figure 4.10b and Supporting Information 4.2.1.5). Figure 4.10c displays the extracted normalized YSR energies E_{YSR}/Δ as a function of ϵ_0 (red circles). As ϵ_0 decreases, which corresponds to an increased filling of the LUSO, the YSR moves to E_F and the magnetic moment grows (U is kept fixed). For completeness, we mention that an evolution of YSR states with the shift of energy levels was observed on quantum dots coupled to a superconductor[201]. Besides the YSR energies E_{YSR}, the model also reproduces the asymmetry $\chi = (A_+ - A_-)\,/\,(A_+ + A_-)$ of the peak heights A_+ and A_- at positive and negative bias, respectively (Figure 4.10d). χ is closely related to the spin polarization of the molecular orbital.

Next, we estimated the magnetic moments of the different H configurations of the supramolecule from the extracted model parameters. The magnetic moment, given by the difference in occupation of the two orbitals, decreases as ϵ_0 increases (Figure 4.10e). We find small moments ($< 0.1\,\mu_{\mathrm{B}}$) as can be expected from the small effective energy splitting U (7 meV). Figure 4.10e also shows that the magnetic moment can be fine-tuned on the order of $0.01\,\mu_{\mathrm{B}}$ by choosing tautomer configurations.

The large number of possible configurations of a supramolecule in a self-assembled layer with random tautomer configurations rationalizes the scatter of the apparent heights and the dI/dV data (Figure 4.3). These moments are possibly magnetically coupled, although our measurements are not sensitive to this coupling.

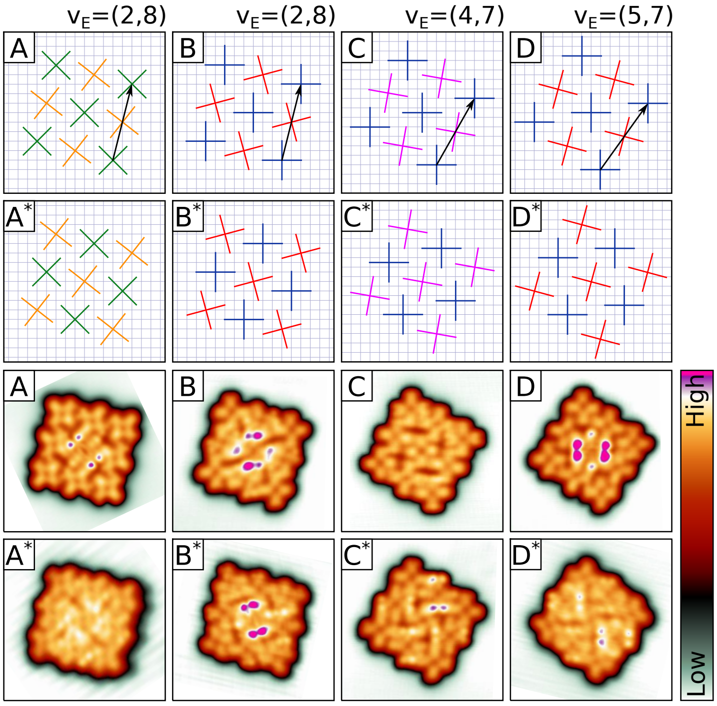

Figure 4.11: Schematics of the H_2Pc enneamers constructed on Pb(100) and corresponding constant-current STM topographs. The Pb(100) lattice is depicted by square meshes in the eight upper panels. Different orientations of the molecular lobes are marked by colors. Green, orange, red, blue, and violet crosses correspond to angles of 45°, 50°, 15°, 0° and −10°, respectively, relative to a ⟨011⟩ direction of the Pb(100) substrate. The topographs were acquired with the following tunneling parameters: A: 100 pA, −10 mV; A*: 50 pA, 10 mV; B: 70 pA, 6 mV; B*: 54 pA, 25 mV; C: 168 pA, 6 mV; C*: 100 pA, 6 mV; D: 68 pA, 6 mV; D*: 63 pA, 30 mV.

Different Types of Supramolecules. Since the electrostatic field surrounding a molecule is highly directional, its effect on a neighboring molecule strongly depends on their relative orientations. We constructed eight types of 3×3 supramolecules on Pb(100) (Figure 4.11). Within the accuracy of the STM images, each cluster comprises two groups of molecules that exhibit characteristic angles between the molecular lobes and $\langle 011 \rangle$ directions in the surface plane. For example, in cluster A the lobes of the central and corner (edge) molecules, represented by green (orange) crosses in Figure 4.11, are rotated by 45° (50°) relative to the $\langle 011 \rangle$ directions. In configurations B–D, the orientations of the molecules are as indicated by the crosses in Figure 4.11. Clusters A*–D* are obtained by exchanging the two groups of molecules in the respective clusters A–D.

The second parameter we use to distinguish the constructed supramolecules is the vector $\mathbf{v}_\mathrm{E}$ that connects two corner molecules of a cluster along the corresponding edge. It is expressed in units of the nearest-neighbor distance of the Pb(100) lattice (0.35 nm). We find $\mathbf{v}_\mathrm{E} = (2, 8)$ for A and B, $\mathbf{v}_\mathrm{E} = (4, 7)$ for C, and $\mathbf{v}_\mathrm{E} = (5, 7)$ for D. Molecular orientations and distances were determined for all configurations. For cluster A, we also determined the adsorption sites of all molecules from atomically resolved STM topographs (Supporting Information 4.2.1.1).

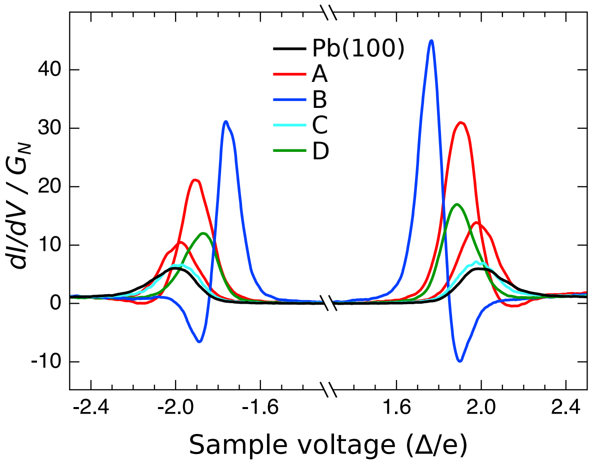

Figure 4.12: dI/dV spectra were measured on supramolecules of types A, B, C, and D (red, blue, yellow, and green curves, respectively). A spectrum measured on the Pb(100) substrate (black) is shown for reference. All spectra are normalized with regard to the conductance G_N of the junction in the normal-conducting state. The sample voltage is normalized by Δ/e where Δ is the pairing energy of the Pb(100) substrate and e the elementary charge. Different tips were employed to acquire the data set, which may imply different effective resolutions. Two spectra are shown for type A supramolecules. Their differences are assigned to different tautomer configurations.

The magnetic properties of the enneamers other than type A have been studied in less detail. Clear YSR resonances were observed on supramolecules A, B, B* and D, where they lead to protrusions in the STM topographs (purple areas in Figure 4.11). In contrast, we did not resolve YSR resonances in enneamers A*, C, C*, and D*. No attempt was made to systematically change the tautomer configurations of these clusters, which might modify this result. Figure 4.12 shows examples of differential conductance spectra recorded on different supramolecules. Interestingly, the YSR resonance is significantly closer to the Fermi level on supramolecule B than on A.

4.1.4 Conclusions

In conclusion, our results highlight the impact of intermolecular interactions on the magnetic properties of adsorbed molecules. Via these interactions the magnetic moments may be tuned, which may be useful for exploring spin induced states at tunable moments on superconductors. As to molecular spintronics, related effects may strongly affect the magnetotransport properties.

4.1.5 Methods

The Pb(100) substrate was prepared by cycles of Ar^+ sputtering and annealing up to 530 K. H_2Pc molecules were deposited from a Knudsen cell onto the Pb crystal held at room temperature. The experiments were performed in ultra-high vacuum at temperatures of 1.6, 2.3, and 4.5 K. The differential-conductance dI/dV was measured using a lock-in amplifier with a modulation voltage of $55\,\mu$V at frequencies between 600 and 900 Hz.

To subtract the background of a spectrum $G_{\mathrm{mol}}(V)$, an additional spectrum $G_{\mathrm{Pb}}(V)$ was acquired over the bare substrate as a reference[202]. Both spectra were then divided by their respective values at a sample voltage V_{Ref}, which was chosen in a region void of spectroscopic features (e. g., $V_{\mathrm{Ref}} = -200\,\mathrm{mV}$). The background-subtracted spectrum is obtained by subtracting the normalized reference spectrum from the normalized spectrum of interest: $G_{\mathrm{BS}}(V) = G_{\mathrm{mol}}(V)/G_{\mathrm{mol}}(V_{\mathrm{Ref}}) - G_{\mathrm{Pb}}(V)/G_{\mathrm{Pb}}(V_{\mathrm{Ref}})$.

4.1.6 Acknowledgments

We acknowledge discussions with C. Ast, N. Lorente, N. Pascual and R. Žitko and funding from the European Union's Horizon 2020 program (grant No. 766726) and the Deutsche Forschungsgemeinschaft (SFB 677).

4.2 Supporting Information: Inducing and Controlling Molecular Magnetism through Supramolecular Manipulation

4.2.1 Supporting Experimental Data

4.2.1.1 Details on Supramolecules

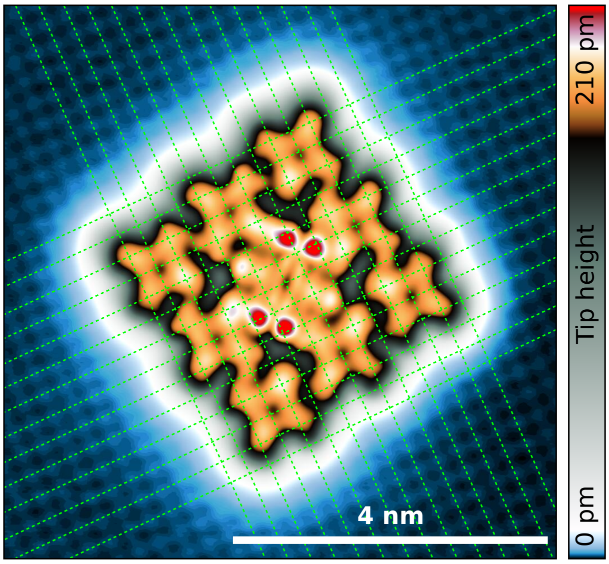

Figure 4.13: Epitaxy of the molecules within a cluster on a Pb(100) substrate. Constant-current topograph of a supramolecule A measured at $V = -10\,\mathrm{mV}$ and $I = 500\,\mathrm{pA}$. Dashed green lines interpolate the Pb lattice that is resolved around the cluster. The centers of all molecules are located atop Pb atoms.

Figure 4.13 shows a high-resolution STM topograph of a supramolecule A along with atomic resolution of the Pb(100) surface. The intersections between the dashed green lines indicate the positions of the surface Pb atoms. Within the uncertainty of the experiment, the centers of all molecules are located atop Pb atoms. We assume that the commensurability between the corner molecules and the Pb(100) lattice observed in Figure 4.13 is preserved for all configurations A–D and A*–D*. The systems comprising a supramolecule and the Pb(100) substrate are chiral. Below, however, we do not distinguish between the enantiomers.

A* is the least stable configuration investigated. In contrast to the other configurations, we were not able to directly construct a cluster A* through the assembly of nine molecules. Instead, we first built a cluster A, added three more molecules at one edge to form a 3×4 cluster and then removed three molecules from the opposite edge (Figure 4.14 a–c). This procedure resulted in a cluster of type A*. However, it switched to configuration A during a subsequent acquisition of a topograph with $I = 100\,\mathrm{pA}$ and $V = 10\,\mathrm{mV}$ (Figure 4.14d). Besides the change in the orientations of the molecules, protrusions are visible over the lower half of the central molecule (imaged after the transition). These protrusions indicate the presence of YSR resonances in configuration A, which were presumably absent in configuration A*. It may be worth mentioning that similar cooperative in-plane rotational switching of multiple phthalocyanine molecules has been reported in Reference 203.

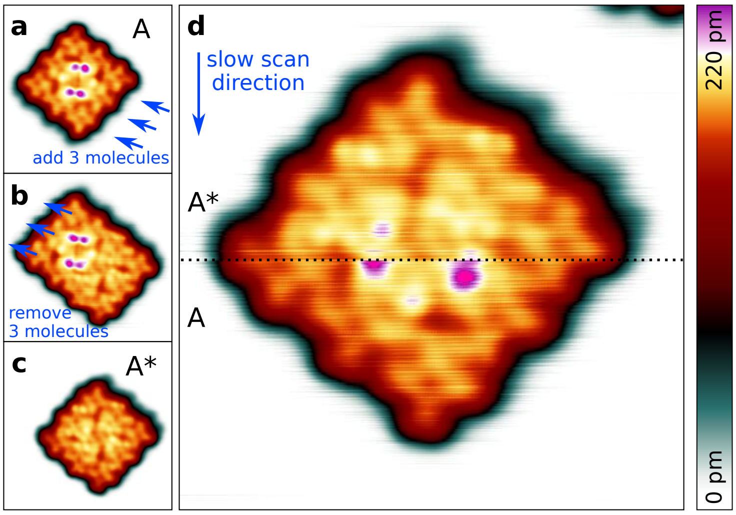

Figure 4.14: Assembly of an A* supramolecule. Sequence of constant-current topographs displaying some steps of the construction of a supramolecule A*. The sequence starts from (a) a cluster A to which three further molecules [arrows in (a)] are added to produce (b) a 4 × 3 cluster. (c) A cluster A* is obtained by removing the three upper left molecules [indicated in (b) with arrows]. (d) Clusters A* are less stable than type A and switch to configuration A during scanning. A dotted vertical line separates the upper part of the topograph, acquired before the A* to A transition, from the lower part, which was imaged after the transition. The topographs were acquired with a sample voltage of 10 mV and tunneling currents of 50 pA (a–c) and 100 pA (d). The widths of the images are 10 nm for (a–c) and 8 nm for (d).

The 4 × 3 cluster shown in Figure 4.14b may be viewed as a combination of A and A* supramolecules. Indeed, such supramolecules can be obtained by removing the three top left or three bottom right molecules. In analogy, the self assembled layer of H_2Pc on Pb(100), discussed in the main manuscript, is composed of A and A* supramolecules. The molecules marked in black in Figure 4.3a of the main manuscript exhibit YSR resonances and are located in environments that resemble an A cluster. Similarly, molecules without YSR resonance (blue) are surrounded by an A*-like neighbor shell.

4.2.1.2 Supplementary Topographs

The measurements described below have been taken on two manually assembled H_2Pc type A clusters. The tautomer configurations of the molecules within the supramolecule were modified by placing the STM tip above a molecular lobe and increasing the sample voltage to 600 mV at $I = 200\,\text{pA}$. Tautomerization events lead to two-level fluctuations of the apparent height of the molecule. Once the tautomer of interest was obtained, the voltage was quickly reduced. This operation was repeated on each molecule of the supramolecule to obtain a desired tautomer configuration. Figures 4.15a–b show different configurations of two supramolecules measured with two different tips. YSR resonances were measured on each of these configurations (Figure 4.10 of the main text and Figure 4.19).

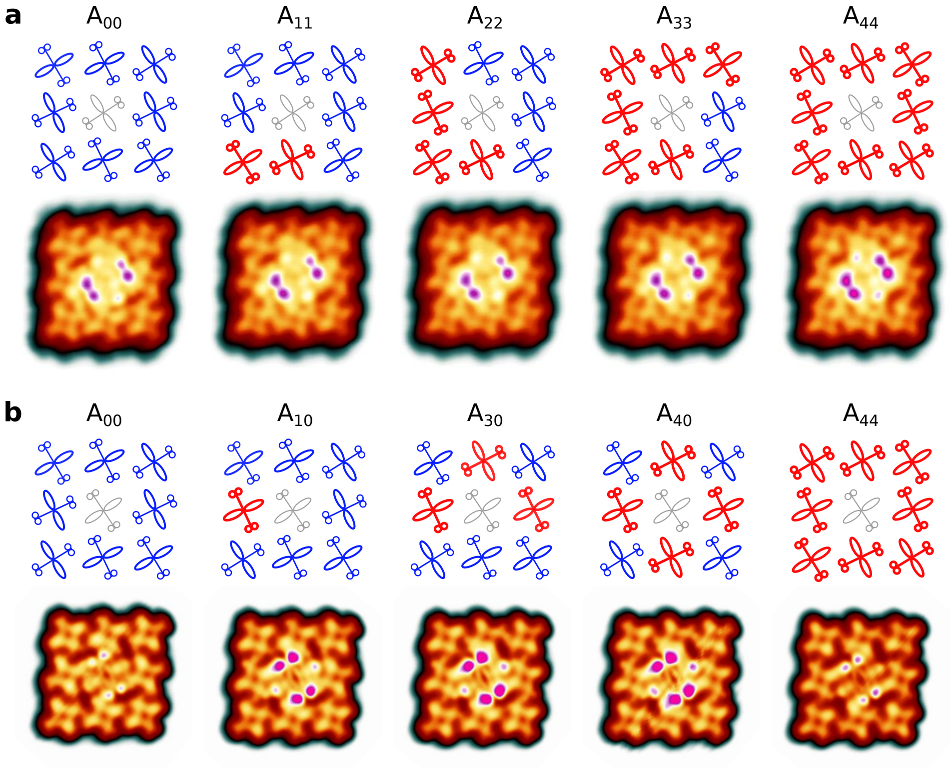

Figure 4.15: Different tautomer configurations realized in two supramolecules. (a–b) Schematics and STM topographs ($V = 10\,\mathrm{mV}$, $I = 100\,\mathrm{pA}$) of tautomer configurations. The configurations were prepared on two different supramolecules and with two different tips. The topographs of A_{00} and A_{44} in (b) have been measured at a sample voltage of $V = -10\,\mathrm{mV}$. Therefore, the protrusions on the central molecules are less prominent.

The configurations of the supramolecule are illustrated by schematics in Figure 4.15. Ovals correspond to the lobes of the molecules to which the inner hydrogen atoms are bonded. The molecules are colored in gray for the central molecules, in red when the axis defined by the two ovals is passing through the central molecule and in blue otherwise. As discussed below, the distinction between red and blue molecules is useful to predict the LUSO and YSR-resonance energies of the central molecule.

4.2.1.3 Influence of the Tautomerization of the Central Molecule

Figures 4.16a and b show topographs of the same supramolecule A acquired before and after tautomerization of the central molecule. The tautomerization effectively rotates the protrusions (purple) that are related to YSR resonances by 90°. This rotation is expected because the spatial distribution of YSR resonances is linked to the LUMO of the central molecule (approximately corresponding to the LUSO), which rotates upon tautomerization.

Apart from this rotation, the tautomerization of the central molecule has little effect on the YSR resonances as displayed in Figure 4.16c (red and blue curves). The peaks of both tautomers are

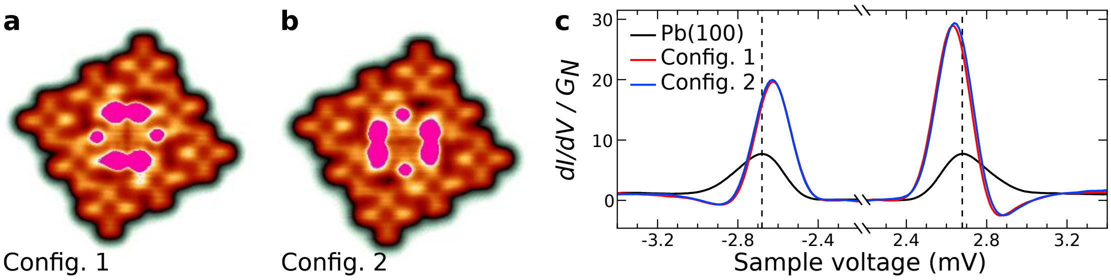

Figure 4.16: STM topographs (8 nm wide) of a cluster A (a) before and (b) after tautomerization of the central molecule. (c) Differential conductance spectra acquired atop the central molecules [purple areas in (a,b)] before (red) and after (blue) its tautomerization, along with a dI/dV spectrum acquired over Pb(100) (black) under identical conditions. All spectra are normalized to the conductance G_N in the normal state of substrate and tip. The dashed black lines indicate the positions of the Pb coherence peaks.

closer to the Fermi level than the two coherence peaks of the substrate (dashed lines) and their heights are asymmetric.
The YSR peaks of configuration 1 are slightly (≈10 µV) closer to the Fermi level than observed for configuration 2. We attribute this difference to the asymmetries of the LUSO and the electrostatic potential induced by the neighbors. Indeed, the rotation of the LUSO modifies the volume integral of the electrostatic potential multiplied by the LUSO density (Equation 4.37), which affects the LUSO energy. In turn, the LUSO energy change corresponds to an evolution of the YSR energy.

4.2.1.4 Identification of Orbitals

Single H_2Pc Molecule. Figures 4.17a and b show that the peak position of the resonances at ≈0.2 V depends on the spatial location over the molecule. As an alternative to fits with two Lorentzians (main manuscript), we fitted spectra recorded on a grid with single Lorentzians and display the resulting peak positions in Figure 4.17c. The peak occurs at lower voltages at the

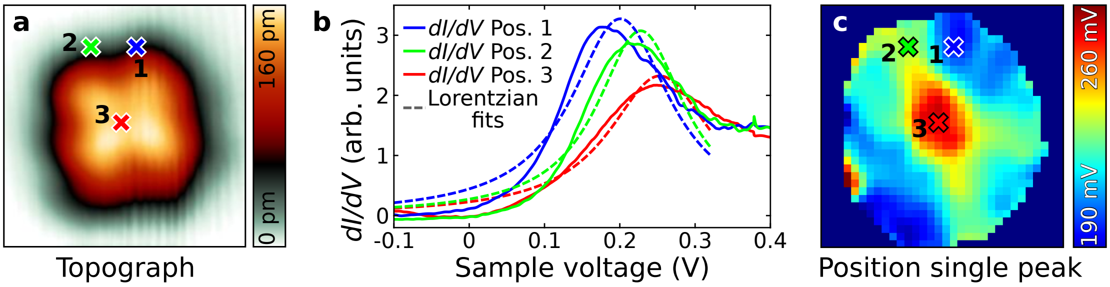

Figure 4.17: Spatial dependence of dI/dV spectra. (a) Topograph of a single H_2Pc molecule. The crosses indicate the locations where dI/dV spectra were recorded. (b) Background subtracted dI/dV spectra measured at the positions indicated in (a) along with fits using a single Lorentzian. (c) Map of the peak positions obtained from the fits.

lobes of the molecule and shifts upwards by up to 70 mV at the center of the molecule. We tentatively attribute this shift to vibration assisted tunneling as described by Pavliček et al.[194]. At the center of the molecule, the overlap between the LUMO and an s-wave tip vanishes by symmetry and the expected conductance is zero. Vibrations of the molecules, however, break the LUMO symmetry. The apparent shift of the orbital (≈70 mV) therefore may be interpreted as the energy required to excite a molecular vibration.

Supramolecule. As described in the main manuscript, the supramolecular orbitals can be approximated by molecular orbitals of individual molecules. For instance, the spatial distribution of the LUSO is very close to that of the LUMO applied on the central molecule. The two denominations are hereafter equivalently employed.
Figure 4.18 shows a dI/dV spectrum, measured atop the center of a supramolecule A (see inset). Similar to the case of the single molecule, the LUSO and the LUSO+1 energies are not resolved but the orbitals are spatially separated. However, the positions with maximum weight of the LUSO are close to the rim of the molecule (see purple areas in Figure 4.18) where the spectrum contains contributions from neighbors. In addition, the spectrum exhibits YSR resonances, which are broadened by the voltage modulation (2.5 mV amplitude).

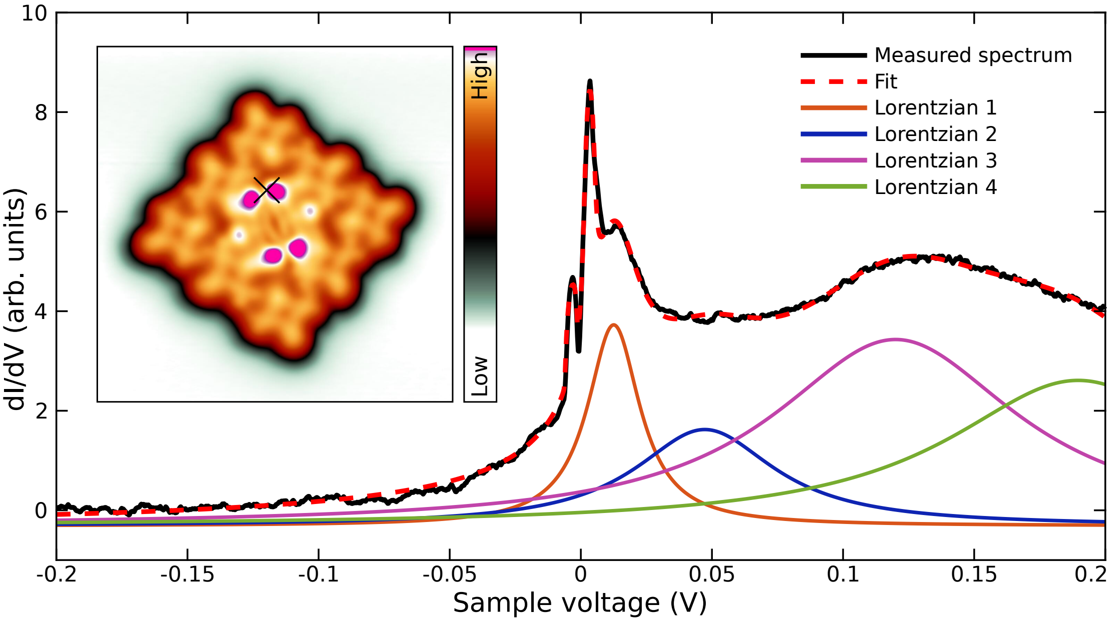

Figure 4.18: Identification of the LUSO and estimation of charge transfer. Background-subtracted dI/dV spectrum (black line) from the center of a supramolecule A shown in the topograph (width: 8 nm) in the inset. The spectrum was measured at the position indicated by a cross (voltage modulation 2.5 mV, feedback loop opened at $I = 500\,\text{pA}$ and $V = -200\,\text{mV}$). The red dashed line shows the sum of six Lorentzians convolved with the instrument response function $f_{\text{lock-in}}$. Two Lorentzians, which are not shown, account for the YSR peaks. The other Lorentzians are displayed as solid lines. The resonance in orange, attributed to the LUSO, is centered at (12.5 ± 0.2)meV and has a half width at half maximum $\Gamma = (12.2 \pm 0.6)$meV.

To determine the different contributions to the spectrum, we fit the data with the sum of six Lorentzians convoluted with a function that describes the broadening caused by the voltage modulation used for lock-in detection[67]

$$f_{\text{lock-in}}(V) = \begin{cases} \frac{2}{\pi V_M^2}\sqrt{V_M^2 - V^2} & ,|V| \leq V_M \\ 0 & ,|V| > V_M, \end{cases} \tag{4.29}$$

where V is the sample voltage and V_M the voltage modulation amplitude. Six Lorentzians are used to model two YSR peaks and four molecular orbitals.

The overall fit (dashed red curve in Figure 4.18) reproduces the experimental spectrum (black curve). The red and blue curves are attributed to LUSO and LUSO+1 located at (12.5 ± 0.2) mV and (47.3 ± 1.1) mV , respectively, while the purple and green curves correspond to contributions from neighboring molecules. The difference conforms to an energy splitting of 35 meV between the LUSO and LUSO+1, in line with the 47 meV splitting observed for a single molecule.

The orange curve (Figure 4.18), associated to the LUSO, crosses the Fermi level. Approximately 25 % of the peak area is below the Fermi level. As each orbital can accommodate two electrons, the position of the LUSO indicates a charge transfer of ≈0.5 e from the substrate to the supramolecule.

4.2.1.5 YSR Resonances for Additional Tautomer Configurations

Figure 4.19 shows dI/dV spectra of different tautomer configurations. These measurements are complementary to that shown in Figure 4.10 of the main manuscript. Although the datasets were acquired on different supramolecules and with different tip apices, the spectra can be simulated with the same parameters ϵ_0, Γ and Δ, showing the reproducibility of the measurements. We nonetheless slightly modified the Gaussian broadening from a standard deviation of $120\,\mu$V to $155\,\mu$V, which essentially reflects a small change in energy resolution.

The YSR energies and the asymmetries extracted from the fits to the experimental data are shown in Figures 4.19c–f (red points). For $\Gamma = 18$ meV and $U = 7$ meV, the model predicts a particular evolution of E_{YSR} and χ as a function of the average energy of the spin-up and spin-down orbitals ϵ_0 (solid black curves in Figure 4.19). A small deviation from these values, e. g., $U = 10$ meV or $\Gamma = 30$ meV, leads to a significant change in the evolution of E_{YSR} and χ (dashed black lines in Figure 4.19), which highlights the sensitivity of these parameters to the properties of the YSR resonances.

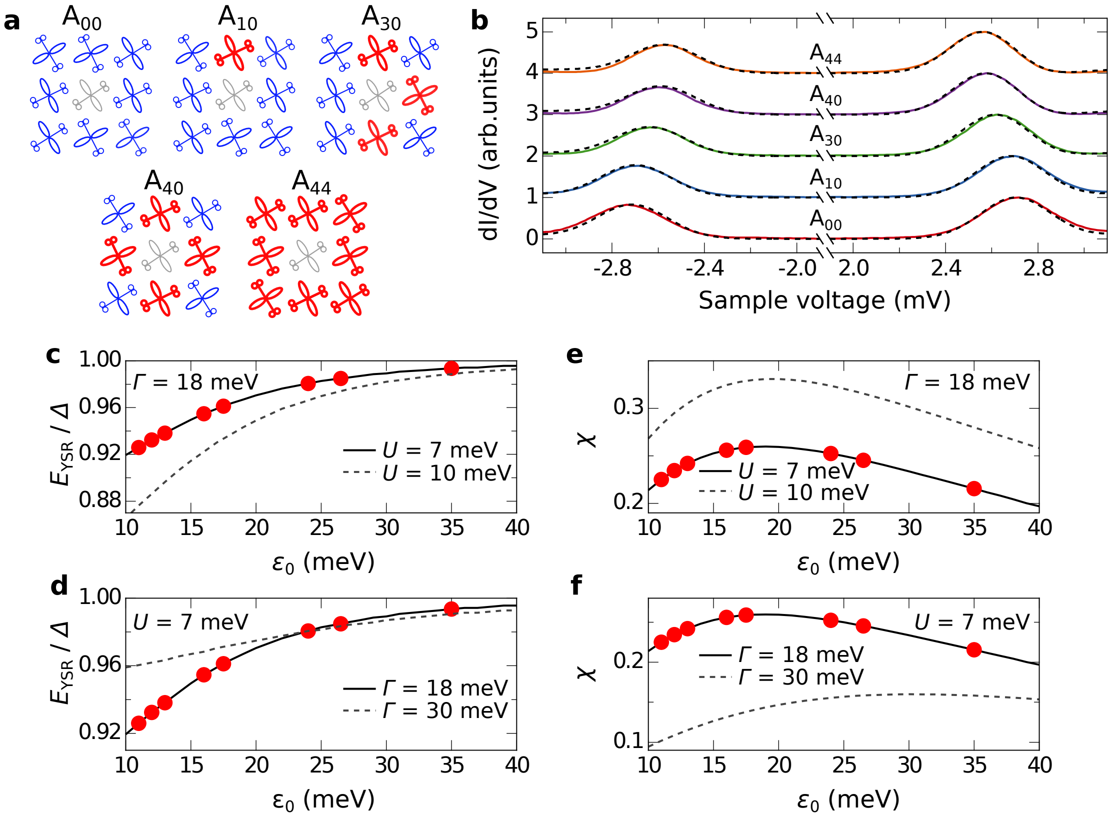

Figure 4.19: Fine tuning of YSR resonances by changing the tautomer configuration. (a) Model of the tautomer configurations realized on a supramolecule. (b) Corresponding experimental dI/dV spectra acquired on the central molecule (solid colored lines) along with simulated spectra (dashed black lines). The spectra were simulated as described in the caption to Figure 4.10 of the main manuscript using the same parameters with the exception of the standard deviation of the Gaussian broadening of $155\,\mu$V. LUSO energies for the different configurations are $\epsilon_0 \in [11, 12, 16, 26.5, 35]\,$meV. (c,d) Normalized YSR energy E_{YSR}/Δ as a function of ϵ_0 obtained with the model described in Reference 200 for $U = 7\,$meV and $\Gamma = 18\,$meV (solid black curves). The red symbols show the experimentally determined ratio E_{YSR}/Δ and ϵ_0 (including data from Figure 4.10 of the main manuscript). The dashed black line in (c) [(d)] was calculated with $U = 10\,$meV and $\Gamma = 18\,$meV [$U = 7\,$meV and $\Gamma = 30\,$meV]. (e,f) Peak-height asymmetry χ of the YSR resonance as a function of ϵ_0 calculated using the parameters of (c,d).

4.2.2 Density Functional Theory Related Modeling

We performed gas-phase density functional theory (DFT) calculations of individual molecules and supramolecules. We then employed an effective tight binding Hamiltonian to decompose the supramolecular orbitals into a combination of molecular orbitals. Based on the DFT and tight-binding analyses, we have identified several sources of intermolecular interaction. These sources of interaction are simulated in a simplified phenomenological model, which essentially reproduces the DFT and experimental results.

4.2.2.1 DFT Calculations

DFT calculations were performed using the PBE[204] functional and the def2svp[205] basis set using Gaussian 09. First, the structure of a single H_2Pc molecule in the gas phase was optimized using Grimme's description of dispersion forces[206]. The input file for the supramolecular cluster calculations was constructed by placing 9 single molecules, each of them with the structure obtained from the single-molecule calculation, as depicted in Figure 4.11 of the main manuscript. The orientations of the two groups of molecules defined in Figure 4.11 as well as the tautomer configurations were adjusted to the experimental results of the considered supramolecule. The DFT calculation was then performed for the supramolecule without further structure optimization.

4.2.2.2 Simulation of *dI/dV* Maps

The simulated dI/dV maps shown in the manuscript correspond to the transition matrix element M squared evaluated for different positions (x_{tip}, y_{tip}) of the tip using a modified Bardeen approach[207]:

$$M(x_{tip}, y_{tip}) = \frac{\hbar^2}{2m} \int_\Sigma \left(\psi^*_{tip} \nabla \psi_{sample} - \psi_{sample} \nabla \psi^*_{tip}\right) dS, \tag{4.30}$$

where $\hbar$ and m are the reduced Planck constant and the electron mass. The integral is carried out over a plane Σ between the tip and the molecule. The wave function of the tip ψ_{tip} is assumed to be spherical:

$$\psi_{tip} = \frac{a}{r} \exp\left(-kr\right), \tag{4.31}$$

where a is a constant, $k = \sqrt{2m\phi}/\hbar$ (ϕ is the work function of the tip), r the distance between the tip apex at $(x_{tip}, y_{tip}, z_{tip})$ and a point of interest in space (x, y, z). In our calculations, ψ_{sample} is substituted by the wave function of the molecular orbitals of interest (e. g. LUMO).

4.2.2.3 Effective Tight Binding Hamiltonian from DFT

The DFT calculations of the single molecules (supramolecules) provide Kohn-Sham energies ϵ_i (E_j) and wave functions ϕ_i (Ψ_j), which are represented in a localized basis of atomic orbitals.

The indices j and i respectively enumerate the (supra-) molecular orbitals (MO). Both sets of ϕ_i and Ψ_j orbitals are orthonormal:

$$\sum_x \phi_i^* (x) \phi_{i'} (x) = \delta_{ii'}, \qquad \sum_x \Psi_j^* (x) \Psi_{j'} (x) = \delta_{jj'}, \tag{4.32}$$

where x is a combined position and atomic-orbital coordinate. The supramolecular wave functions can be expressed as a linear combination of single molecular wave functions. The coefficients are obtained by projection:

$$V_{(k,i),j} = \sum_x \left[\hat{R}_k \phi_i^* (x) \right] \Psi_j (x), \tag{4.33}$$

where the matrix $\hat{R}_k$ shifts and rotates the states of the single molecules, so that the atom positions coincide with those of molecule $k \in [1, 9]$ in the supramolecule. In the analysis below, we used $i \in \{\text{HOMO, LUMO, LUMO+1}\}$ to expand the 9 highest occupied and 18 lowest unoccupied supramolecular orbitals, resulting in $\hat{V}$ being a 27×27 matrix. This subset of i represents an almost complete basis set (for the subspace of interest), as $\sum_{k,i} \left| V_{(k,i),j} \right|^2 > 0.99$ for all j, and is therefore expected to reliably describe the supramolecular DFT solutions of interest. The considered tight-binding Hamiltonian H in a single MO basis reads:

$$\hat{H} = \hat{V}^\dagger \hat{D} \hat{V}, \tag{4.34}$$

where $\hat{D}$ is a matrix containing the energies E_j on its diagonal. The matrix $\hat{H}$ contains on-site energies (diagonal elements) and hopping matrix elements (off-diagonal elements). The former ones are hereafter expressed relative to the energies ϵ_i of the unperturbed MO and therefore represent the molecule-dependent energy changes of the considered MO i due to the interaction with neighbors.

The obtained matrix $\hat{H}$ is illustrated for two configurations of a supramolecule, namely A_{44} and A_{00} that respectively exhibit the maximum and minimum energy shift of the central molecule LUMO. In the A_{44} configuration, the HOMO, LUMO and LUMO+1 of the central molecule are all shifted by approximately -200 meV (numbers in red panels in Figure 4.20). The energy shifts of the HOMO, LUMO and LUMO+1 are virtually identical for each molecule in the cluster, which suggests an electrostatic origin. In contrast, the hopping matrix elements (numbers in blue panels in Figure 4.20) vary with the molecular orbitals involved and depend on their relative symmetry. However, the overall magnitude of the off-diagonal elements is small (<1.5 meV) compared to the shift of the on-site energy (up to -200 meV). From this we conclude that the hybridization between the molecules is negligible and that the shift of the LUMO on the central molecule mainy stems from the electrostatic stray field of the neighboring molecules. It should be noted that there are also non-zero matrix elements up to 16 meV between the HOMO and the LUMO or LUMO+1 on the same molecule. Due to the large energy difference between the HOMO and the LUMO ($\epsilon_{\text{LUMO}} - \epsilon_{\text{HOMO}} \approx 1.4$ eV), these intramolecular inter-orbital matrix elements cause a negligible change (< 0.2 meV) of E_j and an admixture of $\approx$1% of ϕ_{HOMO} to the unoccupied supramolecular states. However, these matrix elements contribute to an induced electrostatic dipole moment, which is absent from the isolated molecule.

Similar observations are made for the A_{00} configuration as shown in Figure 4.21. The on-site

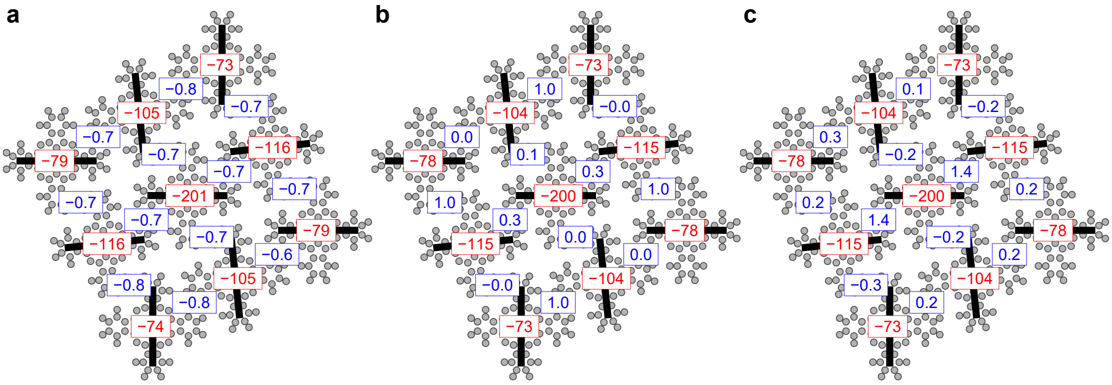

Figure 4.20: Tight-binding parameters (in meV) of the A_{44} cluster. Gray disks represent atoms of the H_2Pc molecules. On-site energies (red) of (a) HOMO, (b) LUMO, and (c) LUMO+1 relative to the respective energies of the isolated molecule. The hopping matrix elements of the same MO between neighboring molecules are indicated in blue. Black bars indicate the axes defined by the pyrrolic hydrogen atoms.

energies, however, are different. For instance, the energy shift of the central molecule MO is approximately -115 meV for A_{00} in contrast to -200 meV observed for configuration A_{44}. This difference can be rationalized by different stray fields acting on the central molecule as detailed in Section 4.2.2.4.

In summary, the tight-binding projection shows that the DFT wave functions of the supramolecule are essentially single molecular wave functions rigidly shifted in energy. This shift depends on the position of a molecule inside the cluster and the tautomer configuration of the surrounding molecules.

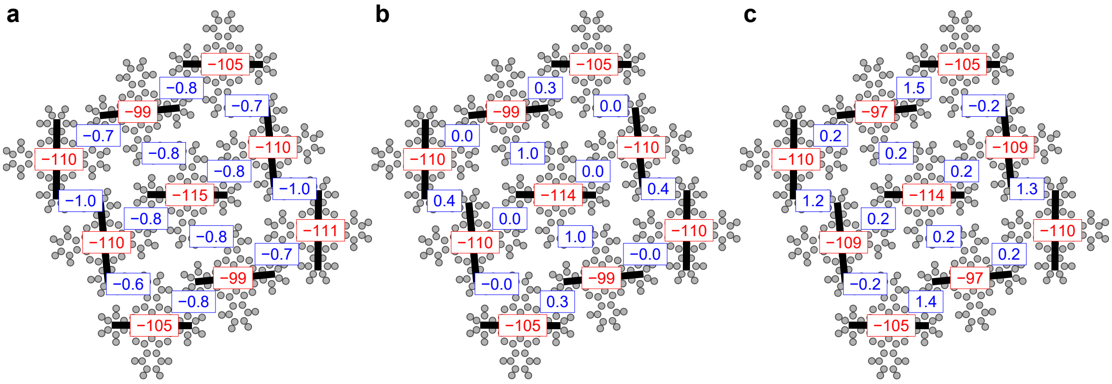

Figure 4.21: Tight-binding parameters (in meV) of the A_{00} cluster. Same as Figure 4.20 but for tautomer configuration A_{00}, which causes the smallest reduction of the on-site energy on the central molecule.

4.2.2.4 Phenomenological Intermolecular Interaction Model

The tight-binding projections indicate a rigid energy shift of all orbitals on a molecule, that may be due to an electrostatic interaction. The charge distribution, as calculated by DFT, is analyzed in the following. While the single molecule is neutral, polar bonds inside the molecule produce an electrostatic stray field with a quadrupole moment in lowest order of the multipole expansion. The quadrupole field is linked to the positions of the pyrrolic hydrogen atoms and can be inverted upon tautomerization. Furthermore, inside the cluster, the electrostatic field of neighboring molecules induces an electrostatic polarization by charge redistribution. Below, we tentatively reproduce the energy shifts of all molecules, as obtained from the tight-binding projections, by the stray fields originating from DFT-derived static and induced charges. The electrostatic screening by the electrons of the substrate, absent in the DFT calculations, is accounted for in the model by including image charges. This leads to a good agreement between the interaction model and LUMO energies extracted from the experiments.

Description of the Model. We express the LUMO energy E_i of molecule i within a cluster as

$$E_i\left(\vec{t}\right) = E^{\text{single}} + Q_i\left(\vec{t}\right) + P_i\left(\vec{t}\right) + V_i. \tag{4.35}$$

The numbering scheme of the molecules is shown in Figure 4.5 of the main manuscript. The tautomer configuration is described by a vector $\vec{t}$. E^{single} is the LUMO energy of an isolated H_2Pc molecule. Q_i accounts for the quadrupole-like electrostatic potential generated by unperturbed H_2Pc molecules and is directly linked to their tautomer configuration. P_i takes into account the polarization of the molecules that leads to a small charge redistribution and further LUMO energy shifts. V_i captures tautomerization-independent effects via three parameters:

$$V_i = \begin{cases} V_{\text{corner}} & , i \in \{1,3,7,9\} \\ V_{\text{edge}} & , i \in \{2,4,6,8\} \\ V_{\text{center}} & , i = 5. \end{cases} \tag{4.36}$$

The determination of the parameters is detailed in the subsections below. To test the reliability of the model, we compare estimates of the LUMO energies from the model with that from DFT calculations and experiments. The blue squares in Figure 4.22 show the LUMO energy reductions (see Section 4.2.2.3) for the nine molecules of a supramolecule A in five different tautomer configurations. Estimates of the corresponding energies, calculated using Equation 4.35, are shown as blue crosses. The agreement is quite good. The model essentially captures all the molecule- and configuration-dependent energy reductions and the deviations from DFT results are limited to a few meV. We further tested the phenomenological model to DFT results from 30 different tautomer configurations of A-type clusters and 12 calculations for A* enneamers. The energy differences between the predictions of the model and DFT are displayed with histograms in Figures 4.23a and b. For configuration A (A*), the maximum deviation is 4 meV (2.5 meV) and the maximum relative difference (not shown) is 4.5 % (2.5 %). In summary, the model provides estimates for the LUMO energies despite its simplicity.

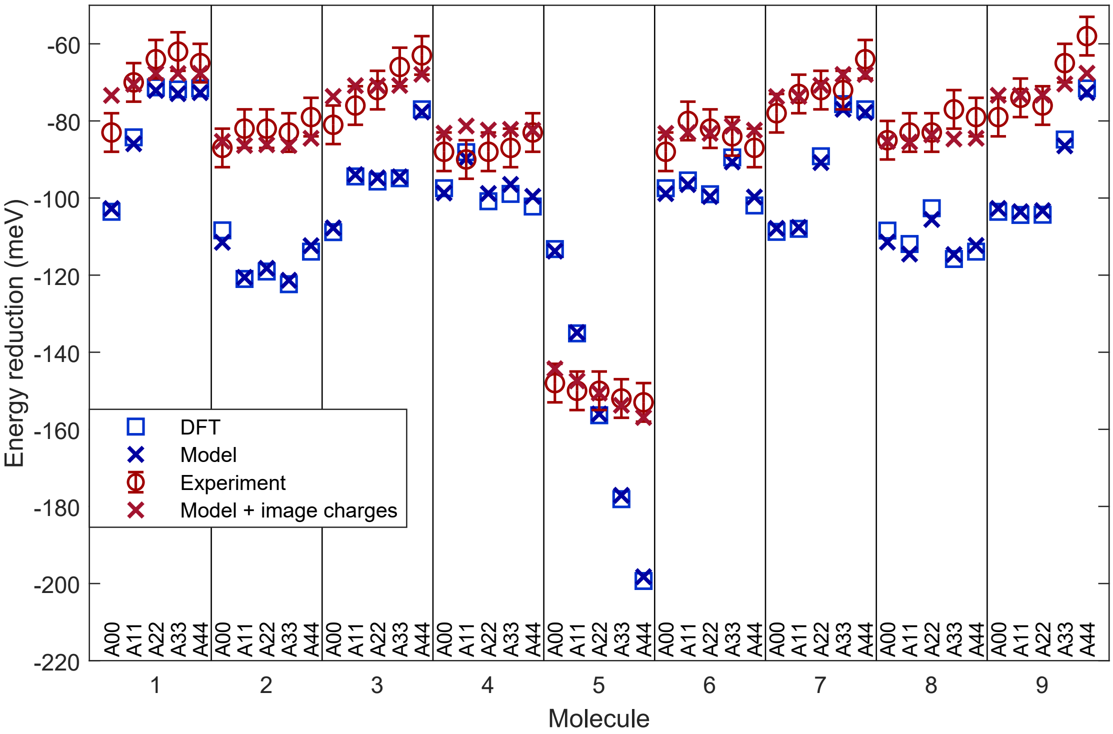

Figure 4.22: Reduction of the LUMO energy due to intermolecular interaction. The LUMO energy reduction is shown for each of the molecules (numbers 1 to 9) of type A cluster in five characteristic tautomer configurations (A_{00} to A_{44}). Blue squares, blue crosses, red circles, and red crosses show the results of gas-phase DFT calculations (Section 4.2.2.3), Equation 4.35, experiments (Figure 4.5 of the main manuscript), and Equation 4.35 including the effect of image charges in the substrate. The experimental data were extracted from dI/dV spectra acquired over the centers of the respective molecules. It is assumed that the energy of vibrational excitation is identical for all molecules. An estimated uncertainty of ±5 meV of the experimental results is indicated. The following parameters have been used for the models. Blue crosses: $V_{\text{corner}} = -77\,\text{meV}$, $V_{\text{edge}} = -122\,\text{meV}$, $V_{\text{center}} = -152\,\text{meV}$, $k = 0.82$. Red crosses: $V_{\text{corner}} = -66\,\text{meV}$, $V_{\text{edge}} = -85\,\text{meV}$, $V_{\text{center}} = -144\,\text{meV}$, $k = 0.82$, $d_{\text{image}} = 3.2\,\text{Å}$.

The experiments were carried out on a Pb(100) substrate. While DFT calculations and the model (blue squares and crosses in Figure 4.22) essentially reproduce the experimental molecule-to-molecule and the configuration-to-configuration energy reductions (red circles), there are some discrepancies. In particular for molecule 5, at the center of the supramolecule, the LUMO energy changes much less than the gas-phase DFT predictions. This is actually to be expected because electrostatic intermolecular interactions are to some extent screened on the metal substrate, which reduces the corresponding energy shifts. We take the screening into account by placing image charges in the substrate at a distance d_{image} from the molecules and by allowing the V_i to change. The best agreement between the model and the experimental data is found for $d_{\text{image}} = 3.2\,\text{Å}$ (red crosses and circles in Figure 4.22). On the surface, V_{corner}, V_{edge}, and V_{center} increase (i. e. are less negative) by 9, 37, and 8 meV, respectively. The histogram in Figure 4.23c shows the deviation of the LUMO energy reduction between the model with image charges

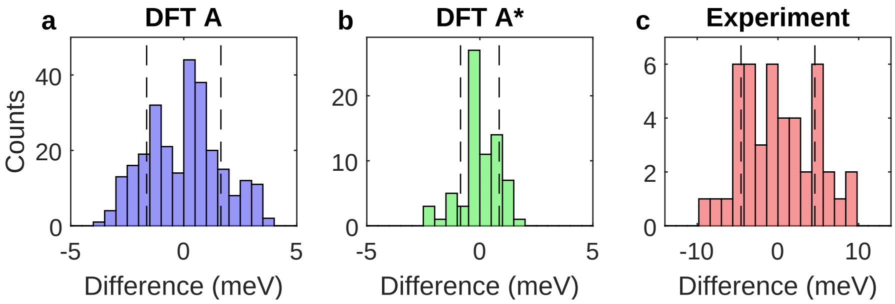

Figure 4.23: Reliability of LUMO energies from the model. Histograms of the deviations of the LUMO energy reductions of the model from the DFT calculations and the experiments. (a,b) Model vs. DFT for supramolecules A and A*. (c) Model vs. experimental results on supramolecule A. The histograms are based on (a) 270, (b) 108, and (c) 45 molecules. The model calculations in (c) take image charges into account. Dashed lines indicate differences of one standard deviation.

and experimental data from 45 molecules. The largest deviation is 9.6 meV and the standard deviation reads 4.6 meV. In other words, the model predicts the energy reductions with a error margin of ≈10 %. This agreement suggests that the energy contributions discussed for the gas phase clusters are still present on the surface albeit reduced by screening.

Nearest Neighbor Interaction. The variable V_i was adjusted to better fit the DFT or the experimental results. We find that, to a good approximation, V_i is proportional to the number of nearest neighbors (NN) and hence reckon that it originates from a nearest neighbor interaction (Figure 4.24). This interaction significantly reduces the LUMO energy of the considered molecule by 33 to 40 meV per nearest neighbor.

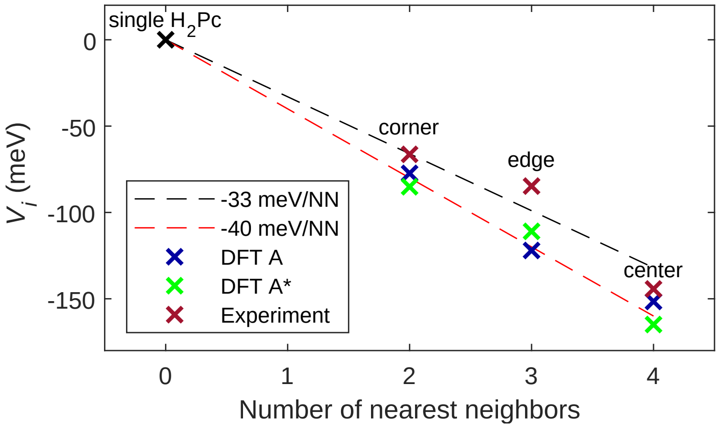

Figure 4.24: Nearest neighbor interaction. Parameters V_i adjusted to fit DFT results of configurations A and A* (blue and green crosses) and experimental results on cluster A (brown crosses) shown as a function of the number of nearest neighbors. The dashed lines exhibit slopes of -33 meV/NN (black) and -40 meV/NN (red).

Electrostatic Interaction from Unperturbed H_2Pc Molecules. As described in the main manuscript, the inhomogeneous charge distribution of H_2Pc leads to a sizable electrostatic potential Φ. For a molecule i, the sum of the electrostatic potentials of the neighbors changes the LUMO energy by:

$$Q_i = -k \int_V d\vec{r} \cdot |\Psi_i(\vec{r})|^2 \cdot \sum_{n \neq i} \Phi_n(\vec{r}), \tag{4.37}$$

where Φ_n is the electrostatic potential induced by the unperturbed molecule n, $|\Psi_i(\vec{r})|^2$ is the LUMO electron density of molecule i, and V the volume of integration. The factor k scales the electrostatic interaction. It takes for instance into account that the molecule of interest i partially screens the electrostatic potential generated by its neighbors. In the following, the value is fixed to $k = 0.82$, which leads to the best agreement.

By evaluating Equation 4.37 for all tautomer configurations we construct the matrix $\hat{Q}$. The element $Q_{i,j}$ is half of the LUMO energy change of molecule i upon tautomerization of molecule j. The vector $\vec{Q}$ describes the energy changes of the nine molecules of a cluster with tautomer configuration $\vec{t}$:

$$\vec{Q}\left(\vec{t}\right) = \frac{1}{2}\left(\vec{Q}_{\mathrm{T}_{00}} + \vec{Q}_{\mathrm{T}_{44}}\right) + \hat{Q} \cdot \vec{t}. \tag{4.38}$$

$\vec{t}$ is a nine-component vector with the $t_i \in \{-1, 1\}$ indicating the orientation of the pyrrolic hydrogen atoms in molecule i. $\vec{Q}_{\mathrm{T}_{00}}$ ($\vec{Q}_{\mathrm{T}_{44}}$) with $\mathrm{T} \in \{\mathrm{A}, \mathrm{A}^*\}$ is the LUMO energy reduction in the configuration for which none of (all) the axes through the pyrrolic hydrogen atoms pass through the central molecule, which corresponds to $t_i = -1$ ($t_i = 1$) for all molecules.

Electrostatic Interaction due to Charge Redistribution. The polarizability of the molecules and the overlap of the wave functions lead to a charge redistribution over the supramolecule. Figure 4.25 shows the induced charge difference on every atom of the molecules for a cluster A and A*. The largest changes occur on edge (corner and central) molecules at peripheral C and H atoms for type A (A*) cluster and lead to the formation of dipoles pointing toward neighboring molecules. Interestingly, for cluster type A, the dipoles point toward the central molecule thereby decreasing the corresponding LUMO energy. In contrast, the induced dipoles lead to a LUMO energy increase of the central molecule for cluster type A*. The orientation of the dipoles is consistent with the presence and absence of YSR resonances for supramolecules A and A*, respectively.

The change in the electrostatic potential, due to the charge redistribution, is computed using Equation 4.37, where the potentials Φ_n result from the change in charges (Figure 4.25) instead of the static charges. In analogy to $\vec{Q}$, the vector $\vec{P}$ that describes the LUMO energy changes due to charge redistribution reads

$$\vec{P}\left(\vec{t}\right) = \frac{1}{2}\left(\vec{P}_{\mathrm{T}_{00}} + \vec{P}_{\mathrm{T}_{44}}\right) + \hat{P} \cdot \vec{t}. \tag{4.39}$$

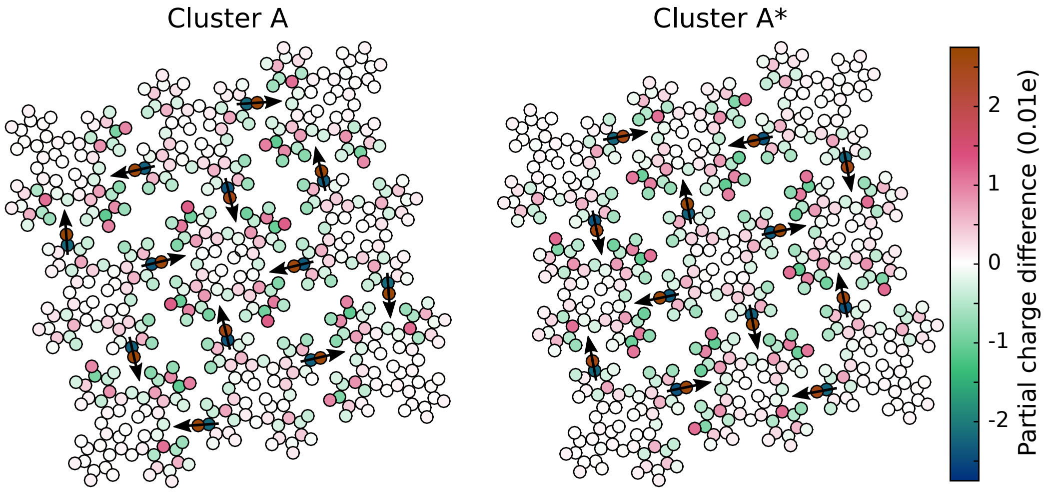

Figure 4.25: Charge redistribution upon assembly. The black circles represent atoms of the H_2Pc molecules and the color within the circles encode the partial charge difference (see colorscale). The partial charge differences are obtained from the Mulliken charges of the supramolecules to which the charges of unperturbed H_2Pc is subtracted for each molecule. The largest difference is found on the edge (central and corner) molecules in cluster A_{44} (A^*_{44}), where the respective C and H atoms form dipoles (arrows).

Discussion. Figure 4.26 shows a representation of the matrices $\hat{Q}$ and $\hat{P}$ for a supramolecule A. The central coarse compartment indicates the impact of the tautomerization of a molecule j on the LUMO energy of molecule 5. The largest contributions Q_{5j} are observed for $j = 2, 4, 6, 8$, i. e.

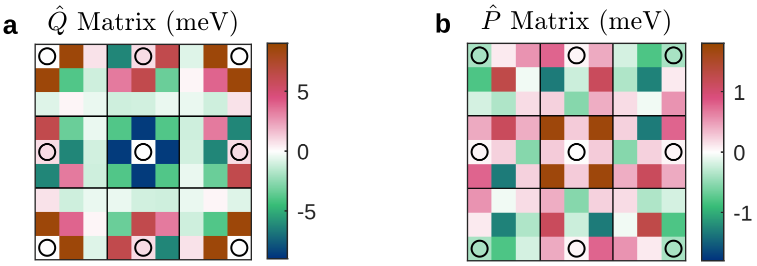

Figure 4.26: Electrostatic-interaction matrices $\hat{Q}$ and $\hat{P}$ for type A cluster (without image charges). The color scale encodes the values (a) Q_i and (b) $P_{i,j}$, which correspond to half of the LUMO energy variation of molecule i caused by the tautomerization of molecule j. The coarse compartments (surrounded by a thick solid line) focus on the entries affecting the energy of a given molecule i. The numbering scheme goes from left to right and top to bottom. For instance, the upper-right compartment, indicates the contributions on molecule 3. Within a compartment, the 9 squares distinguish the molecules j, with the same numbering scheme. The squares with $i = j$ are marked with a black circle. As an example, the brown square in the first column and second row in (a) indicates that the tautomerization of molecule $j = 4$ leads to an increase of the molecule $i = 1$ LUMO energy by $\approx 2 \times 8.6\,\text{meV}$ due to the change in the quadrupole-like field.

Cluster	Q_5	P_5	V_5	ΔE_5
A_{00}	5	-5	-144	-144
A_{44}	-10	-3	-144	-157
A^*_{00}	4	2	-	-
A^*_{44}	-6	4	-	-

Table 4.1: LUMO energy shifts (in meV) of the central molecule inferred from the model with image charges. Q_5, P_5 and V_5 denote the energy shifts on molecule 5 due to the quadrupole-like field of the unperturbed neighbors, the induced charges and the nearest neighbor interaction, respectively. $\Delta E_5 = Q_5 + P_5 + V_5$ correspond to the total energy shift. Q_5 and P_5 were evaluated using Equations 4.38 and 4.39 (including image charges), respectively. Note that we do not have enough experimental data to accurately estimate V_5 for the model involving image charges.

the nearest neighbors of molecule 5. For P_{5j}, tautomerization of the corner molecules induces the largest shifts, i. e. tautomerization of the next-nearest neighbors. We recall that $\hat{P}$ accounts for induced charges due to the polarizability of the molecules. The largest effect of the next nearest neighbors may be rationalized as follow. The tautomerization of a corner molecule affects the induced charges on its neighbors, i. e. edge molecules. In turn, the induced charges of the edge molecules modify the electrostatic potential acting on the central molecule. The importance of nearest and next nearest neighbors for respectively $\hat{Q}$ and $\hat{P}$ is observed for all molecules i. The chirality of the supramolecules (Figure 4.11 of the main manuscript) reduces the symmetry of matrices $\hat{Q}$ and $\hat{P}$. For instance, tautomerization of molecule $j = 1$ increases the LUMO energy of molecule $i = 4$ (see reddish square in the first column and fourth row in Figure 4.26a), while that of $j = 7$ decreases it (green square, first column, sixth row), although both j molecules are located at corners and are nearest neighbors of i.

Table 4.1 shows the amplitudes of the different contributions (including image charges) to the LUMO energy of the central molecule for four configurations of a supramolecule. The largest contribution arises from V_5, which depends on the number of nearest neighbors. This explains why the central molecule of a cluster systematically experiences the largest energy shift, possibly accompanied by YSR resonances when the shift is sufficient to cross the Fermi level.

The change of the tautomer configuration from A_{00} to A_{44} leads to a decrease of the LUMO energy by 13 meV. The decrease is driven by Q_5 (-15 meV variation), while the change in P_5 is in the other direction and tends to increase the LUMO energy. Therefore, the changes in LUMO and YSR energies for cluster type A discussed in the main text are essentially dictated by Q_5 and hence by the quadrupole field of the unperturbed neighbors.

Figure 4.25 shows that the induced charges within the supramolecule lead to dipoles. For cluster type A, the nearest neighbors of the central molecule exhibit dipoles pointing toward the center. This leads to an energy decrease of the central molecule by approximately 5 meV (P_5 value in Table 4.1), taking into account the screening of the field by the substrate. In contrast, for type A* supramolecules, the dipoles are located on the central molecule and point toward its neighbors. Accordingly, this shifts the LUMO energy of the central molecule upwards (positive P_5 value in Table 4.1).

4.3 Intermolecular State Enhancement

This section reports on an intriguing finding made during the H_2Pc investigations. Namely, after the assembly of two or more H_2Pc molecules (for a description of the assembly, see Section 4.1.3), enhanced conductances have been observed centrally above two neighboring molecules at specific sample voltages.

Figure 4.27 shows two examples: an H_2Pc trimer (a–d) and an enneamer (e–h). A significantly larger differential conductance is observed centrally above two neighboring molecules compared to the rest of the molecules, as shown by dI/dV maps (c,g) measured at 155 mV and 100 mV, respectively. Figure 4.28 shows exemplary dI/dV spectra measured on the trimer. A ridge of peaks at positive sample voltages was observed on the molecules. I attribute the first and most intense resonance to the LUMO/LUSO. The additional features at higher voltages may be due to vibronic excitations, but also higher orbitals could be involved. As shown in Section 4.1.3, the LUMO and LUMO+1 of an isolated H_2Pc appear as a single broad peak at approximately 200 mV. The peaks in the spectra measured on a molecule and between neighbors differ only in amplitude, but otherwise exhibit the same energy and shape. This characteristic indicates that the enhanced LDOS in between the molecules is related to the (supra)molecular orbitals.

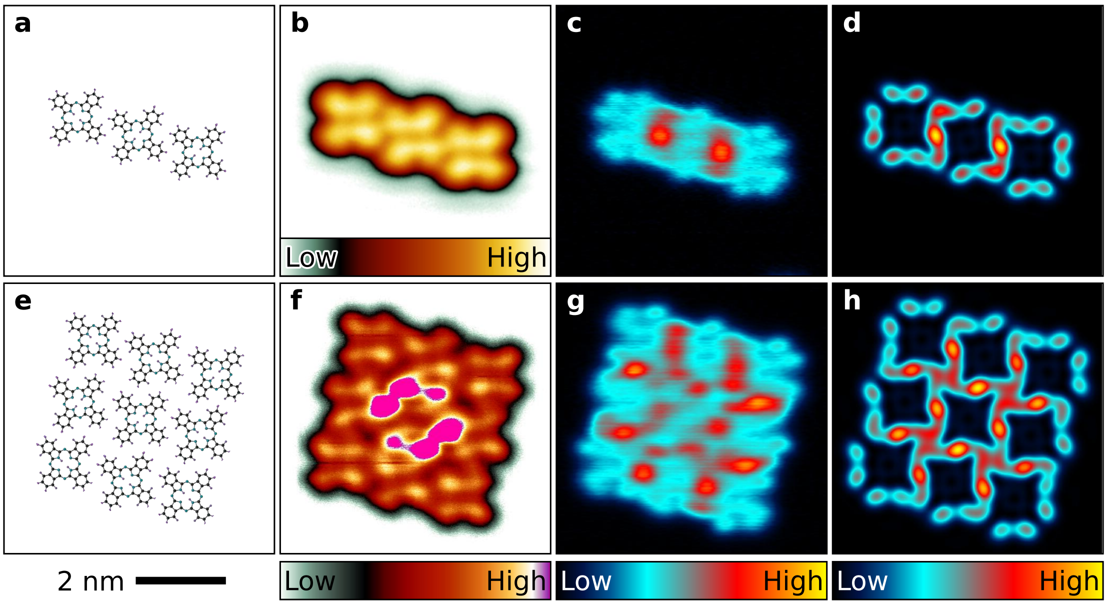

Figure 4.27: (a,e) Structure models, (b,f) topographs, (c,g) constant-height dI/dV maps, and (d,h) simulated dI/dV maps of (a–c) an H_2Pc trimer and (e–h) an enneamer, respectively. Intermolecular state enhancement is visible in both cases (c, g). This phenomenon is reproduced by the simulated dI/dV maps (d,h). For the trimer, LUSO to LUSO+5; and for the enneamer, LUSO to LUSO+17 were taken into account for the calculations. The topograph in (f) was measured in constant-height mode. The measurement parameters were as follows: (b) $V = 10\,\mathrm{mV}$, $I = 57\,\mathrm{pA}$; (c) $V = 155\,\mathrm{mV}$, $V_M = 14.1\,\mathrm{mV_{PP}}$, $f = 828.3\,\mathrm{Hz}$; (f) $V = 10\,\mathrm{mV}$; (g) $V = 100\,\mathrm{mV}$, $V_M = 14.1\,\mathrm{mV_{PP}}$, $f = 828.3\,\mathrm{Hz}$;

Figure 4.28: dI/dV spectra taken at the positions marked by crosses in the inset. The inset shows the same dI/dV map of an H_2Pc trimer as Figure 4.27c. Structure models of the molecules are superimposed. The LUMO/LUSO of the molecule(s) appears as a resonance at ≈200 mV, whereby it is clearly enhanced in the spectrum taken centrally above two neighboring molecules (red). The black curve was measured on the pristine substrate for reference. All spectra were recorded with a voltage modulation of $V_M = 14.1\,\mathrm{mV_{PP}}$ at a frequency of $f = 828.3\,\mathrm{Hz}$ at a constant tip height set at $V = 1\,\mathrm{V}$ and $I = 200\,\mathrm{pA}$.

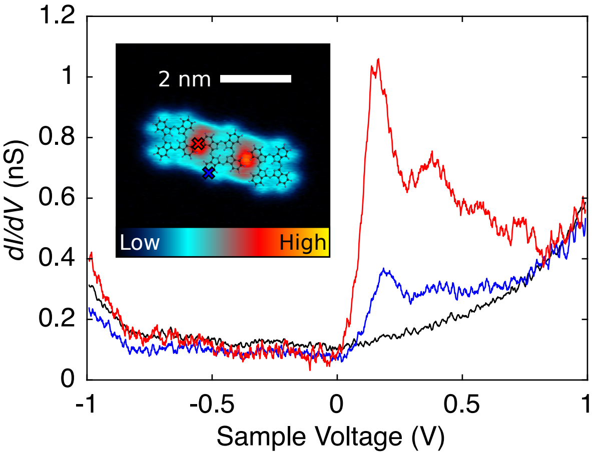

As shown before (see Sections 4.1.3 and 4.2.2), dI/dV maps can be simulated from molecular orbitals calculated by DFT in gasphase. Figure 4.27d,h shows corresponding calculated maps. The LUSO up to LUSO+5 (LUSO+17) were taken into account in case of the trimer (enneamer), which are essentially equivalent to the entirety of LUMOs and LUMOs+1 of all the molecules. In the simulation, the intermolecular enhancement of the differential conductance is reproduced by the superposition of the orbitals. In conclusion, I propose that the intermolecular state enhancement comes from overlapping LUMOs from neighboring molecules.

A similar intermolecular state enhancement was previously observed by K. Scheil et al.[208]. They studied monolayers of NDI-cyclophane molecules on Ag(111) and observed a highly enhanced differential conductance in between neighboring molecules at approximately 700 mV. Supported by DFT calculations, they explained this observation by Ag adatoms from the substrate that are incorporated into the self-assembled structure.

In the present case of H_2Pc however, the incorporation of substrate atoms is excluded, since the molecules are assembled manually on the pristine substrate and no adatoms are left after subsequent disassembly. Thus, the present case demonstrates that seemingly similar phenomena can have very different causes, which must be investigated thoroughly.

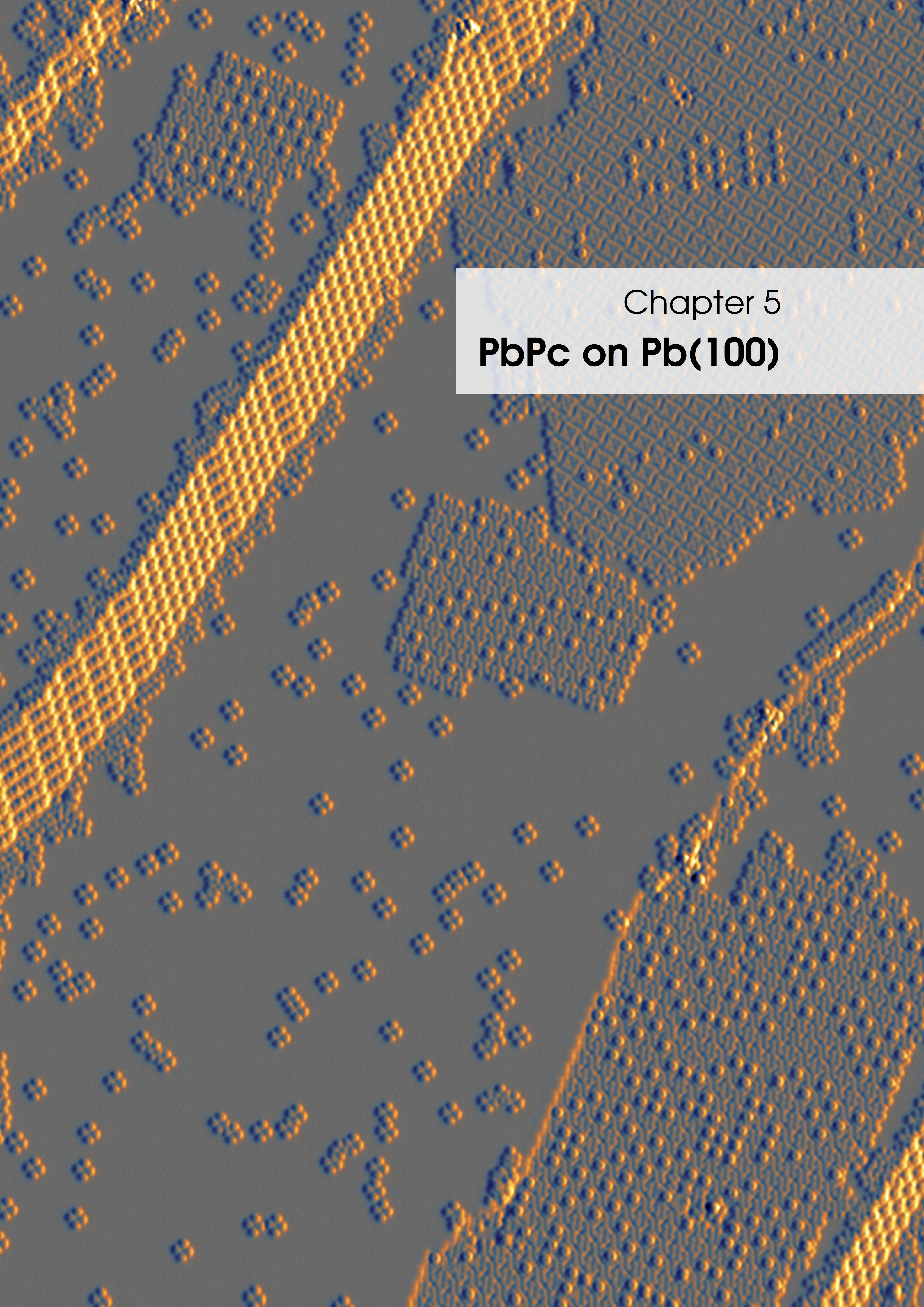

Chapter 5

PbPc on Pb(100)

Previous page:
Topograph of a Pb(100) surface with adsorbed PbPc molecules. Instead of the z position, the tunneling current is shown, which is approximately proportional to the gradient of the z position (fast scan direction from right to left). The sample voltage was set to $V = 100\,\mathrm{mV}$ with a setpoint of $I = 57\,\mathrm{pA}$. The section shown measures approximately $100\,\mathrm{nm} \times 140\,\mathrm{nm}$.

More pronounced YSR states with much lower YSR energies than on H_2Pc were found on PbPc on Pb(100). Although a similar mechanism underlies the formation of the YSR states, the in-depth study of this system reveals a different kind of intermolecular interaction. Furthermore, the very sharp and intense YSR resonances are utilized as probes for molecular vibrations.
Similar to H_2Pc, PbPc is diamagnetic in gasphase but becomes paramagnetic upon cluster assembly on the surface. In contrast to H_2Pc, PbPc is four-fold symmetric, rendering the LUMO which carries the YSR state two-fold degenerate. Although PbPc lacks tautomerization and an electrostatic quadrupole moment, an even larger variation of the YSR energies was observed, which is caused by different molecular neighbors. Since PbPc is a non-planar molecule with the Pb atom sitting on one side of the molecular plane, it can orient itself in two different ways: with the Pb atom pointing away or toward the substrate. In this way, PbPc on Pb(100) is a system with another degree of freedom compared to H_2Pc.

5.1 Adsorption Geometry

PbPc molecules were deposited onto a Pb(100) substrate at room temperature as described in Chapter 3. A coverage of less than one monolayer has been reached in both setups (*4K* and *mK*). I will refer to the samples prepared in the *4K* and *mK* setup as sample 1 and sample 2, respectively. As will be shown in this section, the molecules form ordered islands, which vary in geometry and composition. In Figure 5.1 respective topographs of the samples are shown.

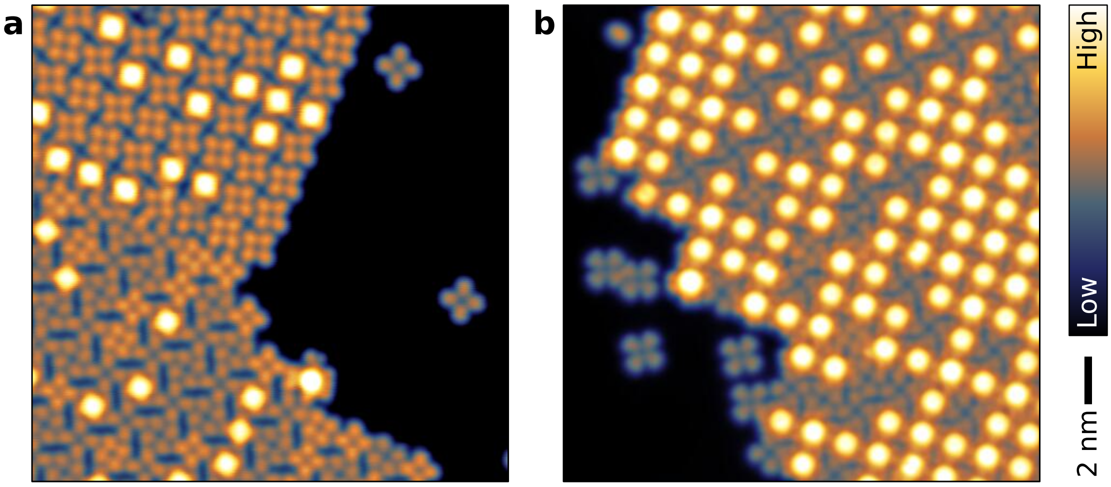

Figure 5.1: Topographs of (a) sample 1 and (b) sample 2. The PbPc (and H_0Pc) molecules self assemble into ordered islands. In addition, isolated H_0Pc molecules are found. Two different domains are shown in (a), while on sample 2 only one type of domain was found (b). Scan parameters: (a) $I = 200\,\mathrm{pA}$, $V = -10\,\mathrm{mV}$; (b) $I = 100\,\mathrm{pA}$, $V = 100\,\mathrm{mV}$.

5.1.1 Observed Types of Molecules

The ordered islands essentially consist of three different types of molecules. Since PbPc is a non-planar molecule with the Pb atom sitting on one side of the molecular plane, it can orient itself in two different ways: with the Pb atom pointing away or toward the substrate, similar to, e. g., tin phthalocyanine (SnPc)[209–212]. I will refer to it as PbPc↑ and PbPc↓ molecules, respectively. In addition, some of the molecules lose the Pb atom during the preparation process and become empty Pc molecules. To differentiate those molecules from ordinary phthalocyanine (H_2Pc), I will refer to them as H_0Pc. Although H_0Pc would not be stable as a pure substance, it may well persist adsorbed on the substrate. While PbPc↑ and PbPc↓ molecules were only found inside ordered islands or attached to step edges or defects, some isolated H_0Pc molecules were found on the pristine Pb(100) surface. I suspect that while PbPc is only physisorbed, H_0Pc is chemisorbed to the substrate because of its radical nature, which greatly reduces its surface diffusion rate.

While PbPc↑ molecules are easily recognizable in topographs by their protruding Pb atom, the differences of PbPc↓ and H_0Pc molecules are rather subtle. In topographs, PbPc↓ molecules appear slightly higher than H_0Pc and seem to have a smaller depression in its center. Furthermore, H_0Pc molecules were obtained by deliberate demetallation of PbPc↑ molecules, as will be shown in Section 5.8, or by dehydrogenation of H_2Pc molecules. In return, H_0Pc molecules were transformed into PbPc↑ molecules by metallation. I have also tried to metallize PbPc↓ molecules as well, without success. Furthermore, I eventually observed isolated H_0Pc molecules becoming H_2Pc by capturing hydrogen that was released from the STM tip. STS measurements of the molecular orbitals of all three types of molecules are shown in Section 5.9.

5.1.2 Geometric Structure of the Ordered Islands

Concerning the geometry of the ordered islands, I observed two different types of domains, which I refer to as domain A and B. Both domains can be seen in the topograph shown in Figure 5.1. Depictions of the geometries are shown in Figure 5.2. In both domains, the molecules are arranged in a $\left(\begin{smallmatrix}5 & 3\\ -3 & 5\end{smallmatrix}\right)$ superstructure on the square Pb(100) lattice with two molecules per unit cell, similar to H_2Pc (Figure 4.3a). This checkerboard like pattern is composed of two groups of molecules with different angular orientations of the molecules within the surface plane. The orientation angles are different for the two domains, resulting in a total of four groups of molecules (A1, A2, B1 and B2). In domain A, the molecules enclose an angle of 46° (A1) and 54° (A2) to the $\langle 110\rangle$ surface direction, while in domain B the orientation angles are 21° (B1) and 1° (B2). The angular orientation of the different groups of molecules was determined by measuring the orientation of 32 to 45 single molecules each. Figure 5.2 shows a corresponding histogram.
It is noteworthy that domain A of PbPc has essentially the identical geometry as the self-assembled monolayer of H_2Pc (Figure 4.3a), which corresponds to the H_2Pc enneamers of type A/A* (Figure 4.11). Furthermore, the geometry of PbPc domain B corresponds to H_2Pc enneamers of type B/B* (Figure 4.11).

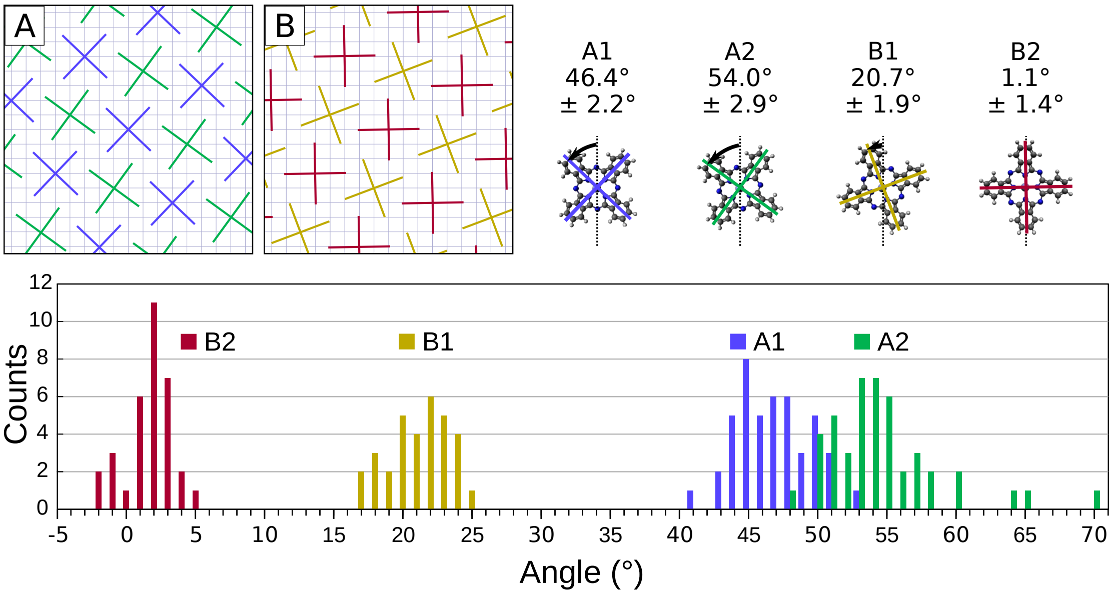

Figure 5.2: Adsorption geometry of PbPc on Pb(100). Models of domain A and B are shown on the top left. The molecules form a $\begin{pmatrix} 5 & 3 \\ -3 & 5 \end{pmatrix}$ superstructure on the Pb(100) lattice (depicted as a square grid). The four groups of molecules (depicted in different colors) differ in their angular orientation. Those angles have been determined by measuring the orientation of a total of 32 (B1), 33 (B2), 45 (A1) or 45 (A2) molecules each. A corresponding histogram is shown on the bottom. The scatter of the values is at least partly due to measurement inaccuracy, which is approximately ±2° in the best case. However, some spread – e. g., the clear outliers in A2 at >60° – can only be explained by a deviation of the actual orientation of the molecules.

5.1.3 Composition of Different Domains

While both domains were observed on sample 1, on sample 2 only islands of domain A were found. Furthermore, the different samples showed different compositions of domain A as listed in Table 5.1. On sample 1, domain A was mainly composed of PbPc↓, one third PbPc↑ and only very view H_0Pc. However, on sample 2 nearly no PbPc↓ have been observed and domain A consisted of more than three quarters of PbPc↑. Domain B on sample 1, on the other hand, was composed of H_0Pc mainly.

Domain	PbPc↑	PbPc↓	H_0Pc
A (sample 2)	77% (347)	2% (10)	21% (93)
A (sample 1)	34% (142)	63% (262)	3% (12)
B (sample 1)	16% (145)	12% (113)	72% (649)

Table 5.1: Compositions of the domains on both samples. The numbers in brackets give the total number of molecules that have been counted. For each domain, areas within ordered islands at different spots of the sample have been evaluated.

The differences between sample 1 and 2 could perhaps be explained by a different crystal temperature during molecule deposition, which would lead to different dynamics during island growth. Since the deposition was conducted approximately half an hour after the final annealing, the crystal may not have cooled down completely to room temperature by then, depending on the thermal coupling of the sample to the manipulator. Unfortunately, the temperature of the crystal could not be measured during the evaporation of the molecules.

5.2 YSR States on PbPc

Although PbPc is diamagnetic in itself, YSR states are observed on PbPc↑ molecules inside ordered islands on Pb(100). Isolated PbPc↑ molecules do not show any YSR states, neither do PbPc↓ or H_0Pc molecules, independent of their surroundings. On PbPc↑ however, YSR states emerge in a similar way as on H_2Pc: On isolated molecules, a LUMO resonance is observed at $U \approx 140\,\mathrm{mV}$. With additional neighboring molecules, the LUMO shifts to lower energy and becomes partially populated. This effect finally leads to the emergence of YSR states.

Figure 5.3 shows corresponding measurements. dI/dV spectra taken on an isolated PbPc↑ molecule and one inside an ordered island are presented in (a). The LUMO of the molecule inside the island is shifted toward the Fermi edge by more than 100 meV. As shown in (c), YSR states are observed on such molecules, while none are detected on isolated PbPc↑. Furthermore, the lateral distribution of YSR state intensity (d) resembles the lateral distribution of the LUMO (b). The highest intensity is measured in a ring shaped area above the Pb atom of the molecule. But there is also a significant intensity observed on the macrocycle and the lobes. This lateral distribution is consistent with results from DFT calculations[213] of the LUMO of PbPc. The LUMO of PbPc is doubly degenerate and includes hybridized p_x and p_y orbitals of the Pb atom, which in combination give rise to the ring shape. As for H_2Pc, I therefore claim that the YSR state is carried by the LUMO.

Although the mechanism of YSR state emergence is very similar for PbPc and H_2Pc, there are also distinct differences. First, a wider range of YSR energies is observed for PbPc, starting from $E_{\mathrm{YSR}} \approx \Delta$ down to $E_{\mathrm{YSR}} < \frac{\Delta}{2}$. For H_2Pc the observed YSR energies were restricted to $E_{\mathrm{YSR}} \gtrsim 0.9\Delta$. Secondly, the variation of YSR energies on H_2Pc was explained by the different orientation of the quadrupole moments of neighboring molecules. Since PbPc molecules do not have such quadrupole moments, the mechanism behind the YSR energy variation must be different. As I will show, it is due to a different composition of molecular neighbors (PbPc↑, PbPc↓, H_0Pc).

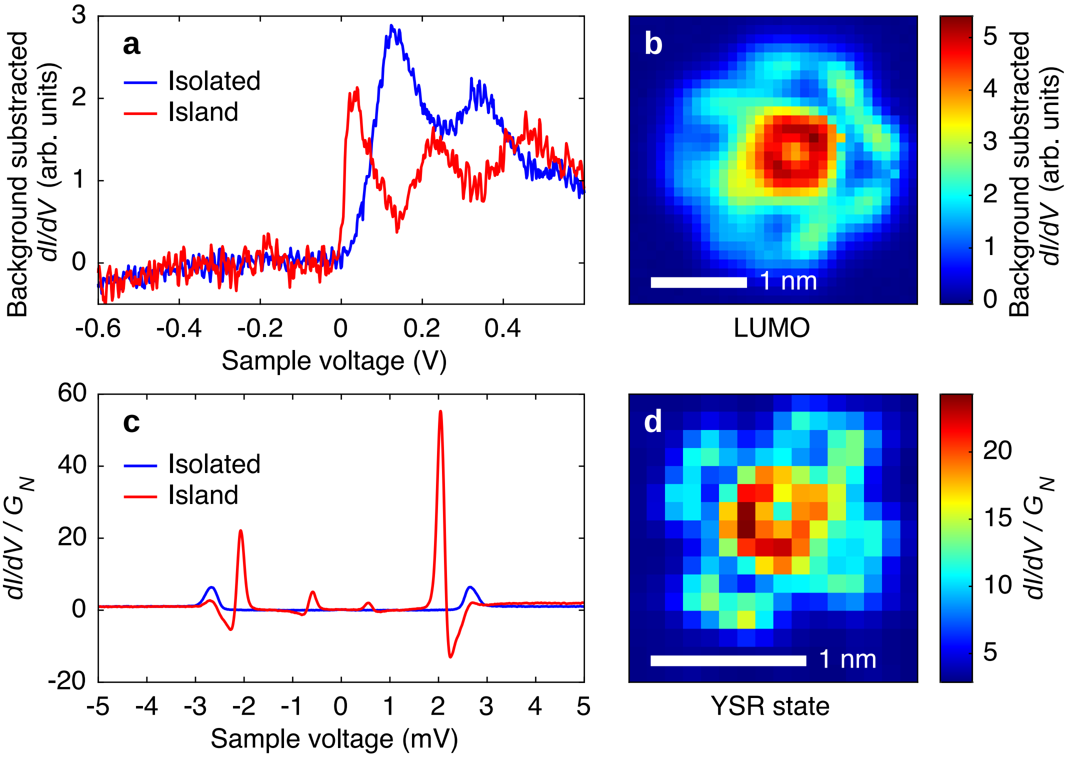

Figure 5.3: (a,c) dI/dV spectra taken on an isolated PbPc↑ molecule (blue curve) and on a PbPc↑ molecule inside an ordered island (red curve). The spectra in (a) were measured at a fixed tip position ($V = 1\,\mathrm{V}$, $I = 100\,\mathrm{pA}$) with a voltage modulation of $V_M = 14.1\,\mathrm{mV}$ at a frequency of $f = 772.8\,\mathrm{Hz}$. A spectrum measured on the pristine Pb(100) substrate was subtracted for background correction. I assign the first resonance observable at positive voltage (at 140 and 30 mV, respectively) to the LUMO of the molecule. The additional resonances at higher voltages are most likely due to vibronic excitations. (b) Map of the LUMO peak height of an isolated PbPc↑. A 32×32 grid of I/V spectra was taken, which were then numerically derived, normalized and background subtracted, similar to the spectra shown in (a). The values of the resulting spectra at $V = 135\,\mathrm{mV}$ are shown, which are laterally smoothed by a Gaussian filter. The spectra in (c) were measured at a fixed tip position ($V = 6\,\mathrm{mV}$, $I = 100\,\mathrm{pA}$) with a voltage modulation of $V_M = 113\,\mu\mathrm{V_{PP}}$ at a frequency of $f = 939.4\,\mathrm{Hz}$. Furthermore, they are normalized to the normal state conductance G_N, which was determined from the constant differential conductance at $V < -3.5\,\mathrm{mV}$. While the spectrum measured on the isolated PbPc↑ (blue curve) resembles the spectrum on the superconducting substrate, pronounced YSR resonances are observed on PbPc↑ inside an ordered island (red curve). (d) Map of the YSR peak height of a PbPc↑ molecule inside an ordered island. A 16×16 grid of dI/dV spectra was taken and normalized to the normal conductance, like the spectra in (c). The value of the spectral amplitude at $V = 2.35\,\mathrm{mV}$ is shown.

5.2.1 Characterization of YSR Spectra

Hundreds of dI/dV measurements on many different molecules have been conducted in total, some of which show YSR resonances. However, a smooth transition from spectra of molecules without YSR states, which resemble the unchanged superconducting gap of the substrate, to molecules with YSR states is observed. At YSR energies close to Δ, the YSR peaks and the coherence peaks are merged in dI/dV spectra. Only at YSR energies significantly smaller than Δ, the YSR peaks and the coherence peaks can be observed separately. In some borderline cases, it is hard to determine whether there are YSR states. However, there are two characteristic spectral properties that indicate the presence of YSR states:

1. The voltage $\pm V_P$ of the main spectral peaks becomes smaller. Without YSR states, the main peaks are the coherence peaks and $eV_P = \Delta_T + \Delta_S$. With pronounced YSR states, the main peaks are the YSR peaks and $eV_P = \Delta_T + E_{\mathrm{YSR}}$. The energy of the respective peak in the DOS of the sample is given as $E_P = eV_P - \Delta_T$. In most cases, however, I do not exactly know the superconducting gap of the tip Δ_T. Instead, I measured the gap on the pristine substrate and took the mean value for Δ, assuming $\Delta_T \approx \Delta_S$. In the following, I will use the reduced peak energy $\tilde{E}_P = E_P/\Delta = eV_P/\Delta - 1$ as characteristic parameter. Without a YSR state, I expect $\tilde{E}_P = 1$ and with a pronounced YSR state $\tilde{E}_P = \tilde{E}_{\mathrm{YSR}} = E_{\mathrm{YSR}}/\Delta$.

2. The existence of an asymmetry $\chi = (P^+ - P^-)/(P^+ + P^-)$ of the peak heights at positive and negative sample voltage (P^+ and P^-, respectively) is an indication of YSR states, since YSR peaks are typically asymmetric in height. Without YSR states, no asymmetry is expected ($\chi = 0$). However, a slope in the spectral background can lead to a net asymmetry even without YSR states. To eliminate this effect, I extracted the slope of the spectral background from the deconvoluted DOS of the sample and calculated the intrinsic asymmetry χ^*. This procedure is detailed in Appendix C.

In the following, I will use $\tilde{E}_P$ and χ^* to characterize the dI/dV spectra.

5.2.2 Variation of the YSR Energy

Figure 5.4 shows a plot of $\tilde{E}_P$ vs. χ^* for many different spectra taken on PbPc↑ molecules. On the pristine substrate there is $\tilde{E}_P = 1$ and $\chi^* = 0$. For isolated PbPc↑ molecules, I obtained essentially the same result (black symbols), which demonstrates the absence of YSR states in this case. For PbPc↑ molecules inside ordered islands, however, $\tilde{E}_P$ decreases, while χ^* increases. Here, distinct differences among the four different groups of molecules (A1, A2, B1 and B2) are observed. The most pronounced YSR states by far have been observed on A1 molecules, while A2 molecules only show weak signs of YSR states, if any. The differences of the molecular groups in domain B are less pronounced. In general, however, B2 molecules show YSR states with smaller energies compared to B1 molecules.

In conclusion, the adsorption geometry of PbPc and its neighboring molecules seems to have a significant influence on the emergence and energy of the YSR states. In fact, there is a striking

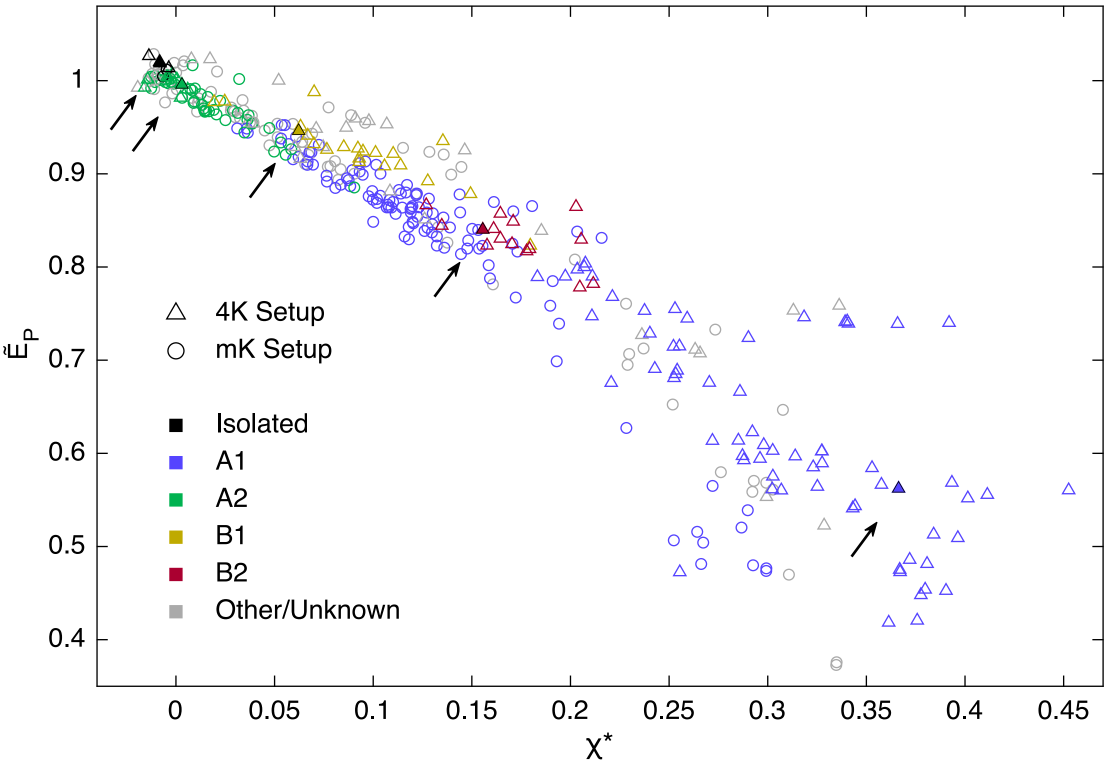

Figure 5.4: Plot of the reduced peak energy $\tilde{E}_P$ vs. the intrinsic asymmetry χ^* for spectra taken on PbPc↑ molecules. Data from both setups (*4K* and *mK*) are shown. Different molecular configurations are highlighted by colors. For molecules of groups A1, A2, B1 and B2, only those are considered that were completely surrounded by neighboring molecules. Data points from molecules at the edge of ordered islands are classified under ’Other’. Some exemplary spectra are shown in Figure 5.5. The corresponding data points (filled triangles) are marked by arrows.

similarity to the case of H_2Pc (Section 4.1.3). As noted in Section 5.1, the geometry of domains A and B of PbPc corresponds to the geometry of H_2Pc enneamers of type A/A* and B/B* (Figure 4.11), respectively. YSR states have been observed for enneamers of type A, B and B*, while no YSR states have been observed for type A*. Indeed, concerning the geometry, the central molecule of an H_2Pc enneamer of type A* corresponds to PbPc group A2, where the weakest or no YSR states have been observed either.

As detailed in Section 4.1.3, DFT calculations of H_2Pc enneamers have shown that there is an electrostatic polarization of the lobes of neighboring molecules. The largest polarization was found within C-H bonds pointing towards neighboring molecules (Figure 4.9). Those dipoles are pointing from one molecular group to the other, leading to different LUMO energy shifts for the groups. The DFT calculations furthermore showed that this effect is accompanied by a charge transfer between the two molecular groups.

I assume that the very same effect occurs in the case of PbPc, leading to different LUMO energies for the molecular groups, which finally leads to different YSR energies. Furthermore, the polarization and intermolecular charge transfer will be different for different geometries. The

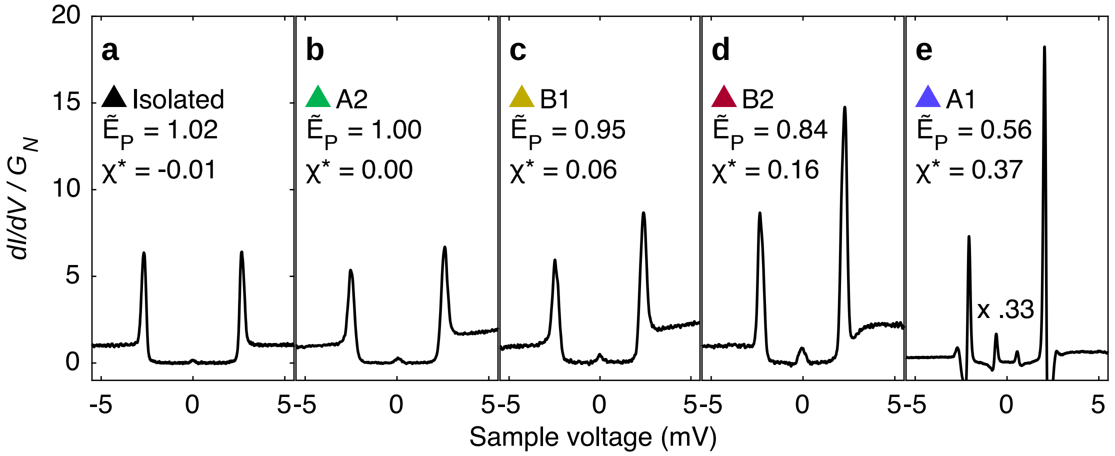

Figure 5.5: *dI/dV* spectra taken on different PbPc↑ molecules. While no YSR states are observed on isolated PbPc↑ molecules (a), YSR signatures of varying distinctness are observed inside ordered islands (b–e), with the most pronounced emerging on molecules of group A1 (e). The spectrum in (e) is scaled with a factor of 0.33. All spectra were measured at a constant tip position ($V = 6\,\mathrm{mV}$, $I = 100\,\mathrm{pA}$) with a voltage modulation of $V_M = 113\,\mu\mathrm{V_{PP}}$ at frequencies between 770 Hz and 940 Hz. The values obtained for $\tilde{E}_P$ and χ^* are listed. Corresponding data points are marked in Figure 5.4.

fact that I observed different YSR energies for the molecular groups in domain B compared to domain A is therefore not at all surprising.

Figure 5.6 shows a topograph (a) and a simultaneously measured *dI/dV* map (b) of an ordered island of domain A. A sample voltage of $V = 2.6\,\mathrm{mV}$ was chosen, which is just outside of the coherence peak (similar to the *dI/dV* map of an H_2Pc enneamer shown in Figure 4.6c). The emergence of a YSR state leads to a decrease of the differential conductance at that voltage (blue areas in Figure 5.6b). In this way, the YSR states are mapped across the full scan area. Pronounced YSR states are mainly observed on PbPc↑ molecules of group A1, while on PbPc↑ molecules of group A2 usually only a very weak YSR signature is detected.

On other molecules, like the isolated H_0Pc in the top left corner, the differential conductance is increased (yellow and red areas in Figure 5.6b). This effect may be due to the nearby LUMO of the respective molecule. However, there is another possible explanation: On molecules without a YSR state, I observed a slightly larger superconducting gap. E. g., for isolated PbPc↑ molecules, I observed values of up to $\tilde{E}_P \approx 1.06$ (Figure 5.4). This apparent change of the superconducting gap is an effect of the two-band superconductivity of Pb[68] as detailed in Section 2.2.5. As a result, the coherence peak is closer to the sample voltage, which might as well explain the increased differential conductance.

The shape of the YSR distribution seems to be rather twofold symmetric on some of the molecules, similar to what has been observed on H_2Pc. I assume that this effect is caused by an anisotropic neighborhood, which breaks the fourfold symmetry and therefore lifts the degeneracy of the LUMO of PbPc. The YSR state is then carried by the lower orbital, which has a twofold symmetry similar to the LUMO of H_2Pc.

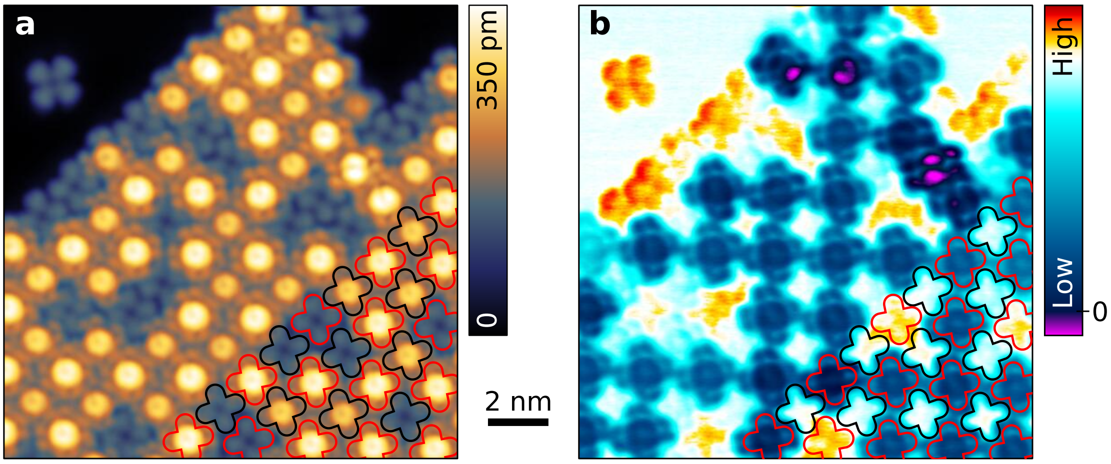

Figure 5.6: (a) Topograph of an ordered island (domain A) of PbPc molecules measured at $V = 2.6\,\mathrm{mV}$ and $I = 50\,\mathrm{pA}$. (b) dI/dV map of the same location, measured simultaneously. Areas with the same differential conductance as on the pristine substrate appear white. Areas with an increased (decreased) differential conductance are colored in yellow and red (blue). A decreased differential conductance indicates YSR states. On some molecules, even negative differential conductance is observed (purple spots). In (a,b), the outlines of some molecules are shown for clarification in the bottom right corner. The outlines of molecules of group A1 (A2) are shown in red (black).

As shown in Figure 5.4, I did not only observe large variations of the YSR states among different groups of molecules, but also within a single group of molecules. For group A1 for example, I observed YSR energies between $0.95\,\Delta$ and $0.4\,\Delta$. In the following, I will show that this variation is due to different neighboring molecules. As detailed in Section 5.1, the ordered islands are composed of PbPc↑, PbPc↓ and $\mathrm{H_0Pc}$) molecules. Consequently, a PbPc↑ molecule can have any combination of the three different types of molecules as nearest and next nearest neighbors (NN and NNN, respectively).

To analyze the influence of the different molecular neighbors on the peak energy $\tilde{E}_P$, I set up a model and fitted it to the experimental data. The model describes $\tilde{E}_P$ as a function of the molecular neighbors. Starting with an offset value $\tilde{E}_{P,0}$ for a molecule with no neighbors, a constant value $\epsilon(t, d)$ is added for each neighboring molecule n depending on its type t_n (PbPc↑, PbPc↓ or $\mathrm{H_0Pc}$) and distance d_n (NN or NNN):

$$\tilde{E}_{P,\mathrm{model}} = \tilde{E}_{P,0} + \sum_n \epsilon(t_n, d_n) \tag{5.40}$$

Thus, the model contains seven parameters in total.

In Table 5.2 the fit results for the model parameters are given. As expected, each additional molecular neighbor reduces the peak energy. However, the influence varies significantly among the different types of molecules. PbPc↓ molecules have by far the strongest impact on the peak

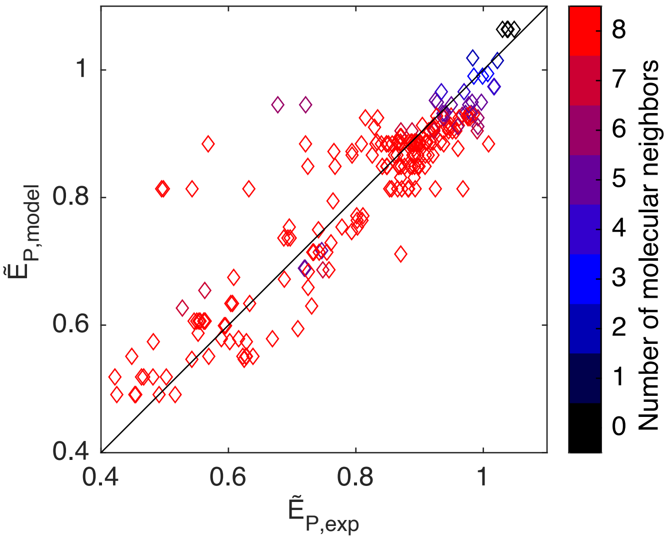

Figure 5.7: Plot of the peak energy $\tilde{E}_{P,\text{model}}$ from the model vs. the experimental peak energy $\tilde{E}_{P,\text{exp}}$. Data points from PbPc↑ molecules of group A1 and from isolated PbPc↑ molecules are shown. The model parameters have been fitted to the data. Most of the data points are close to the line $\tilde{E}_{P,\text{model}} = \tilde{E}_{P,\text{exp}}$ (black line), which shows that the model matches the experiment fairly well.

Type t	NN	NNN
PbPc↑	-0.025 ± 0.022	-0.020 ± 0.016
PbPc↓	-0.102 ± 0.024	-0.048 ± 0.022
H_0Pc	-0.042 ± 0.024	-0.000 ± 0.018

Table 5.2: Fits for the model parameters $\epsilon(t, d)$, describing the reduction of the peak energy $\tilde{E}_{P,\text{model}}$ per nearest (NN) and next nearest neighbor (NNN) broken down by the type of molecule. A peak energy of $\tilde{E}_{P,0} = 1.064 \pm 0.057$ is obtained from the fit for a molecule without any neighbors. The 95 % confidence intervals from the fit are given.

energy $\tilde{E}_P$. Therefore, the lowest YSR energy is to be expected for PbPc↑ molecules that are completely surrounded by PbPc↓ molecules only.

Figure 5.7 shows a plot of the model peak energy $\tilde{E}_{P,\text{model}}$ vs. the peak energy $\tilde{E}_{P,\text{exp}}$ from experiment. The model describes the experimental data fairly well, which shows that the energy variation is indeed mainly caused by the variation of molecular neighbors.

A possible explanation for the different effect of the molecular neighbors on the YSR energy is the electric dipole moment of PbPc. PbPc has a dipole moment perpendicular to the molecular plane, which is pointing in the direction of the Pb atom[214,215]. However, very different absolute values of the dipole moment have been reported, e. g., 1.0 Debye[214] or 0.06 Debye[215]. Troels Markussen obtained a value as large as 0.66 eÅ = 3.2 Debye from on-surface DFT calculations of PbPc↑ (see Section 5.4.1). To obtain the dipole moment of the charged molecule, he shifted the Mulliken charges obtained from structural relaxation in order to make the molecule charge neutral. The dipole moments of neighboring molecules interact with the dipole moment of the PbPc↑ molecule carrying the YSR state. An anti-parallel alignment would be favorable and thus, the dipole moment of neighboring PbPc↓ molecules could lead to an additional downshift of the LUMO. Earlier experiments with PbPc on Pb(111) [216] suggest in fact that PbPc↓ may have an even larger absolute dipole moment than PbPc↑, which would fit to my observations.

5.2.3 Fitting YSR Spectra with BdG Model Calculations

All dI/dV spectra of the superconducting gap, including possible YSR resonances, measured on PbPc↑ molecules have been fitted with a model function. This procedure allows me to obtain estimates for the coupling parameters $\alpha = \pi\rho_0 JS$ and $\beta = \pi\rho_0 W$. These parameters can then be related to the reduced peak energy $\tilde{E}_\mathrm{P}$ and the intrinsic asymmetry χ^*, which have been determined for all spectra as discussed before (Section 5.2.1).

Figure 5.8 shows two exemplary dI/dV spectra and corresponding fits. Positive values between about 0.3 and 0.8 are obtained for both α and β. The very same spectra can be reproduced with negative values for both α and β. Without loss of generality, however, I limit my analysis to positive values of α. Usually antiferromagnetic exchange coupling ($J > 0$) is assumed[137] anyway, because only then values of $|E_\mathrm{YSR}| \ll \Delta$ are obtained in the quantum spin model[169].

The model is obtained by calculating the tunneling current via Equation 2.4, numerical derivation and subsequent convolution with the broadening functions accounting for the lock-in and electronic broadening of the setup, as discussed in Section 2.1.2. A BCS DOS with constant $\rho_\mathrm{N}(E)$ is assumed for the tip (Equation 2.11). The DOS ρ_S of the sample on the other hand may contain YSR resonances. However, it is possible that the tunneling current flows partially trough transmission channels without any YSR resonances. Therefore, I use the Bogoliubov-de Gennes (BdG) approach as discussed in Section 2.3.3 to calculate the DOS ρ_BdG of the sample containing YSR states and allow for an additional mixing with a BCS DOS ρ_BCS, such that $\rho_\mathrm{S} = (1-m)\cdot\rho_\mathrm{BdG} + m\cdot\rho_\mathrm{BCS}$, where $m \in [0,1]$ is the mixing parameter.

This model already reproduces the essential characteristics of the observed spectra, even when assuming a constant normal-conducting DOS for the sample $\rho_\mathrm{S,N}(E) = \rho_0$. Corresponding fits are shown as orange curves in Figure 5.8. They slightly deviate from the measurements. Especially the negative differential conductance outside of the YSR resonances tends to be exaggerated.

The fit results can be further improved by considering non-constant $\rho_\mathrm{S,N}(E)$. This approach is furthermore motivated by the observation of the LUMO resonance close to the Fermi edge and the possible presence of a Kondo resonance, which might overlap with the superconducting gap[35]. The normal-conducting DOS of the sample is therefore modeled by the combination of a Lorentzian (accounting for the LUMO) and a Fano line-shape (accounting for a possible Kondo resonance).

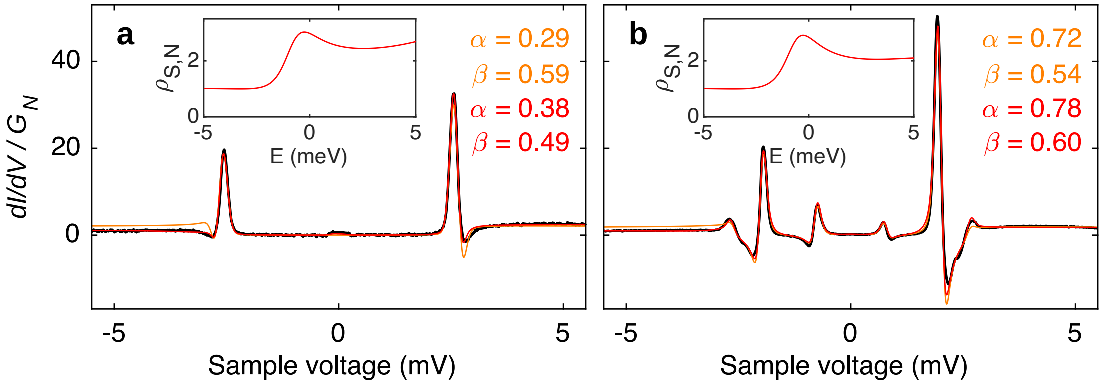

Figure 5.8: Two exemplary dI/dV spectra measured on PbPc↑ molecules inside an ordered island of (a) type B1 and (b) type A1. The measured spectra (black curves) are overlayed by fits with constant and non-constant $\rho_{\mathrm{S,N}}(E)$ (orange and red curves, respectively). The corresponding $\rho_{\mathrm{S,N}}(E)$ used in the second fit is shown in the insets. Similar values for α and β are obtained from the fits.

$$\rho_{\mathrm{S,N}}(E) = \left[\rho_N + A_F \cdot \Im\left(e^{\mathrm{i}\phi} \cdot \frac{\Gamma_F}{E - \varepsilon_F + \mathrm{i}\Gamma_F}\right)\right] \cdot \left[1 + A_L \frac{\Gamma_L^2}{(E-\varepsilon_L)^2 + \Gamma_L^2}\right] \tag{5.41}$$

Here, ρ_N is a constant background, A_F (A_L) is the amplitude, Γ_F (Γ_L) the width and ε_F (ε_L) the position of the Fano (Lorentzian) peak; ϕ defines the Fano shape. The width of the Fano (Lorentzian) peak is limited by a minimal value of 1 meV (5 meV) to avoid direct interference with the YSR resonances. Corresponding fits are shown as red curves in Figure 5.8. The respective $\rho_{\mathrm{S,N}}(E)$ are shown in the insets.

Similar values for α and β are obtained from the fits with constant and non-constant $\rho_{\mathrm{S,N}}(E)$, suggesting that the fit results for those coupling parameters are not very much altered by the addition of a non-constant $\rho_{\mathrm{S,N}}(E)$ to the model. The extended model with non-constant $\rho_{\mathrm{S,N}}(E)$ is used for the following analysis.

Figure 5.9 shows all the obtained data points for $\tilde{E}_{\mathrm{P}}$ vs. α, β and χ^* respectively. Similar values of $\alpha \approx 0.3 \ldots 0.7$ and $\beta \approx 0 \ldots 0.6$ are obtained for most of the spectra. Deviations therefrom are mainly observed with large $\tilde{E}_{\mathrm{P}}$ where the YSR peaks mix with the coherence peaks and the fits become less robust. Both parameters seem to slightly increase with decreasing $\tilde{E}_{\mathrm{P}}$. An increase in α in particular seems to correlate with stronger YSR states, as demonstrated by the color code in (c).

Another model calculation has been conducted to verify the results from the fits. YSR DOSs have been calculated via the BdG approach assuming a constant $\rho_{\mathrm{S,N}}(E)$. α and β have been varied simultaneously from 0 to 0.8 and 0.6, respectively. As a calculation result the reduced YSR energy $\tilde{E}_{\mathrm{YSR}}$ and the peak height asymmetry χ^* have been obtained. The overall results of

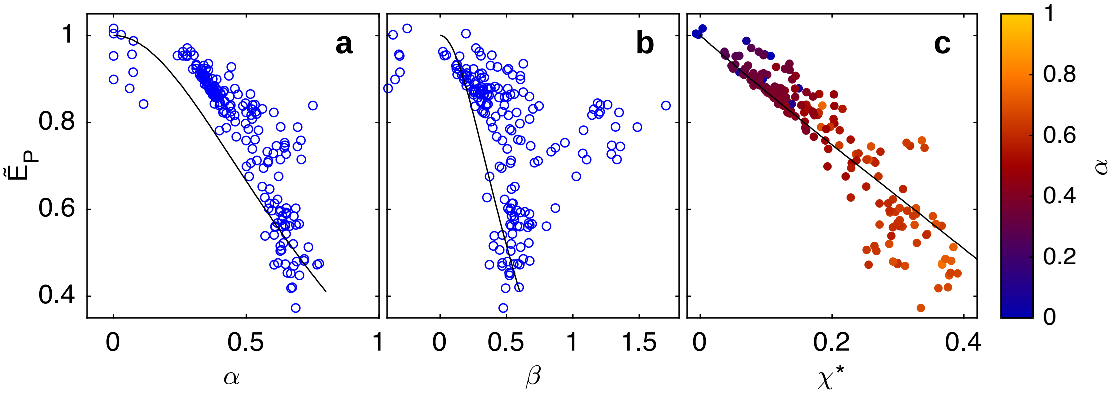

Figure 5.9: Plots of the reduced peak energy $\tilde{E}_\mathrm{P}$ vs. the coupling parameters α (a) and β (b), as well as the intrinsic asymmetry χ^* (c). Circles/dots represent data points obtained from fits to the experimental data. Only data points with a mixing parameter of $m < 0.15$ have been evaluated. The black curves have been calculated from a separate model calculation of YSR spectra, in which the values for α and β are varied simultaneously from 0 to 0.8 and 0.6, respectively.

this model calculation are shown as black curves in Figure 5.9. The observations from experiment are fairly reproduced.

5.3 Resonance-enhanced Vibrational Spectroscopy of Molecules on a Superconductor

The sharp and intense YSR resonances on PbPc are utilized as a probe for vibrational excitations in IETS. A manuscript featuring most of the findings has been accepted for publication in Physical Review Letters[217]. The manuscript is reproduced in the following. The corresponding Supplemental Material is subject of Section 5.4 thereafter. The layout of text and figures has been adapted to this thesis without changing their contents.

Author Contributions

The reproduced manuscript (Section 5.3) and Supplemental Material (Section 5.4) are a joint work of Jan Homberg, Alexander Weismann, Troels Markussen, and Richard Berndt. The author contributions are as follows:
J.H., A.W., and R.B. conceived the experiment. J.H. acquired the STM data with support by A.W. Model development and data analysis were carried out by A.W. and J.H. T.M. carried out the DFT calculations and wrote the corresponding part of the Supplemental Material (Section 5.4.1). R.B. wrote the manuscript with contributions from all authors. J.H. created all figures with input from R.B. and A.W., except those in Section 5.4.1 which were contributed by T.M.

5.3.1 Abstract

Molecular vibrational spectroscopy with the scanning tunneling microscope is feasible but usually detects few vibrational modes. We harness sharp YSR states observed from molecules on a superconductor to significantly enhance the vibrational signal. From a lead phthalocyanine molecule 46 vibrational peaks are resolved enabling a comparison with calculated modes. The energy resolution is improved beyond the thermal broadening limit and shifts induced by neighbor molecules or the position of the microscope tip are determined. Vice versa, spectra of vibrational modes are used to measure the effect of an electrical field on the energy of YSR states. The method may help to further probe the interaction of molecules with their environment and to better understand selection rules for vibrational excitations.

5.3.2 Main

The vibrational modes of a molecule are sensitive probes of molecular bonds and their response to external parameters. They may serve as fingerprints for identification and as indicators of geometric changes. Molecular vibrations can also help elucidating processes at surfaces. In 1998, the unequivocal observation of vibrational features in data recorded with the STM was reported[53]. Like in the case of molecules in metal-oxide-metal junctions[81], the tunneling current I is modified when inelastic processes like molecular vibrations are excited. Unfortunately, the

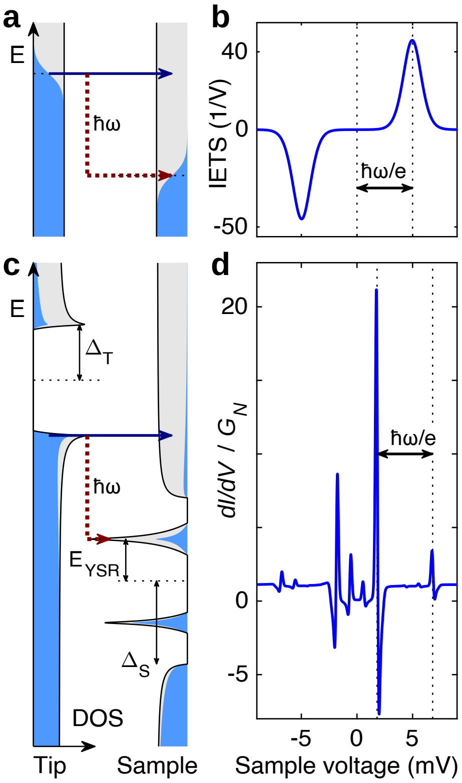

Figure 5.10: (a) Schematic energy diagram of elastic (blue solid) and inelastic (red dashed) tunneling processes between normal-conducting tip and sample electrodes with energy independent DOS. Both Fermi distributions (occupied states shaded in blue) are broadened by temperature. The sample voltage V is chosen to match the energy of a vibrational excitation, $eV = \hbar\omega$. (b) Second derivative d^2I/dV^2 of the current I scaled with dI/dV for the scenario in (a) (parameters $\eta = 10\%$, $\hbar\omega = 5\,\text{meV}$, $T = 4.2\,\text{K}$). The inelastic process gives rise to a broad peak/dip at $\pm\hbar\omega/e$. (c) Related diagram for a superconducting tip (energy gap $2\Delta_\text{T}$) and sample ($2\Delta_\text{S}$). A paramagnetic impurity induces sharp YSR states, separated by $\pm E_\text{YSR}$ from the Fermi level $E_F = 0$ of the sample (dotted line). V is chosen to satisfy $eV = \hbar\omega + E_\text{YSR} + \Delta_\text{T}$. (d) Calculated spectrum of dI/dV scaled by the conductance G_N outside the gap [η, $\hbar\omega$, and T as in (b)]. The YSR states lead to two predominant asymmetric peaks with different amplitudes at $V = \pm(E_\text{YSR} + \Delta_\text{T})/e$. Tunneling of thermally excited electrons (*e. g.* from the upper coherence peak of the tip to the YSR state) produces minor peaks in the gap at $\pm(\Delta_\text{T} - E_\text{YSR})/e$. Inelastic transitions (red dashed) to the YSR states produce pairs of peaks at $\pm(\hbar\omega + E_\text{YSR} + \Delta_\text{T})/e$. Their relative intensities reflect those of the YSR resonances. Their widths are much smaller than in (b) because they are not dictated by thermal broadening.

net effect on the current is usually on the order of few percent at best because the additional inelastic current is partially compensated by a reduction of the elastic current[82]. Consequently, only few molecular vibrations lead to observable signals, which typically are best discerned in d^2I/dV^2, the second derivative of I with respect to the sample voltage V. A notable exception are data from C_{60} adsorbed to superconducting lead, where 9 modes were observed[218]. Vibronic transitions may also lead to larger changes of the tunneling conductance but detailed spectra of various modes have not been reported[219–221]. In addition, vibrational features may be resolved in single-molecule fluorescence spectroscopy with the STM[222, 223].

Here, we show that sharp resonances in the density of states of paramagnetic molecules on superconductors may be used to simultaneously increase the signal amplitude and the spectral resolution of inelastic tunneling spectroscopy. The measurement concept may be introduced using energy diagrams of STM junctions (Figure 5.10) between (a) two normal conductors and (b) a superconducting tip and sample. In the former case, a vibrational mode of energy $\hbar\omega$ may be excited through inelastic tunneling transitions when $V > \hbar\omega$. This leads to a minute stepwise change of the $I(V)$ slope that becomes more readily discernible in $d^2I/dV^2(V)$. A model spectrum is displayed in Figure 5.10c. It was calculated assuming a fairly large relative change of conductance ($\eta = 10\ \%$) due to the inelastic processes. The peak width in d^2I/dV^2 is

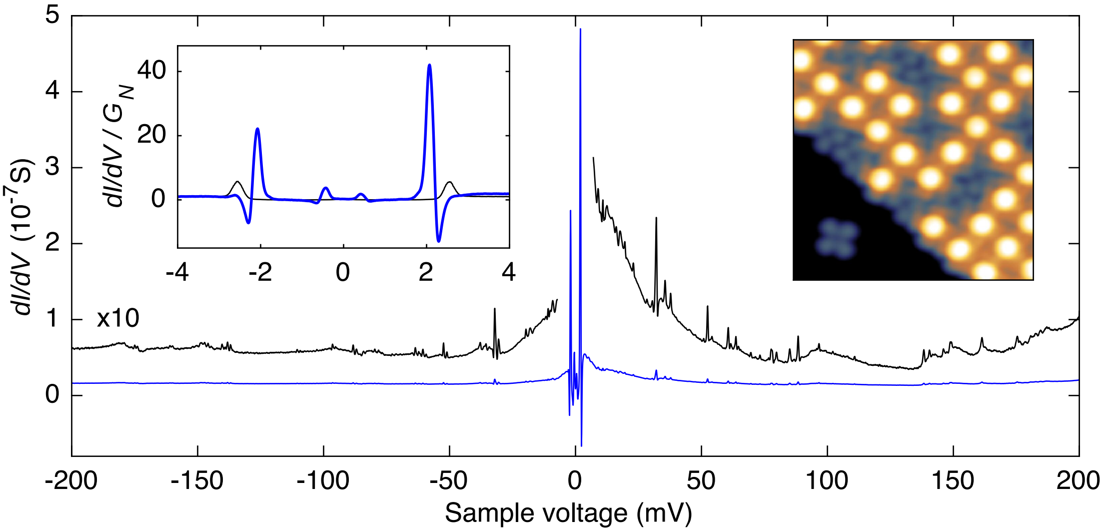

Figure 5.11: dI/dV spectrum of PbPc on superconducting Pb(100). The spectrum (lower blue line) was recorded above the Pb center of a molecule within a molecular island. The most prominent spectral features are YSR resonances at ±2 mV (see also left inset). A magnified view (multiplied by 10, black upper line) reveals a wealth of additional peaks that are due to vibration excitations. The inset to the right shows a constant-current image of molecules assembled into an island with a square mesh. Some molecules (blueish clover shaped patterns) lost their Pb ion. The majority is intact with the Pb atom imaged as a bright protrusion. The main spectrum is an average of 20 spectra recorded with an initial current of 4 nA at $V = 200\,\mathrm{mV}$ and a voltage modulation of $0.5\,\mathrm{mV_{PP}}$. The blue spectrum (thick line) in the inset was measured with parameters 500 pA at 5 mV and $0.05\,\mathrm{mV_{PP}}$ modulation while the black (thin) curve shows $dI/dV(V)/G_N$ on a molecule without YSR states for reference.

determined by the thermally broadened Fermi distributions so long as other instrumental effects can be neglected. In the superconducting case (Figure 5.10c), the LDOS of tip and sample exhibit coherence peaks and gaps around the Fermi energies. Moreover, sharp resonances within the superconducting gap of the sample may be induced by paramagnetic impurities. These YSR states are located at the energies $\pm E_{\mathrm{YSR}}$ around the sample Fermi energy $E_F = 0$ and strongly affect the current[23,33,144]. In the model calculation of Figure 5.10d, the YSR peak height exceeds the background (conductance G_N outside the gap) by a factor of ≈20. In some experiments, we achieved values of up to ≈50. When such a resonance is the final state of a transition the inelastic current is enhanced by the same ratio. As a result, inelastic transitions prominently appear in differential conductance (dI/dV) spectra (Figure 5.10d) as asymmetric peaks that replicate the YSR resonances. The relative change of dI/dV due to a vibrational excitation is thus moved from the scale of a few percent[53,218] to values up to ≈80 % and the detection limit is improved by approximately one order of magnitude.

We investigated PbPc on superconducting Pb(100). The experiments were performed in ultrahigh vacuum with scanning tunneling microscopes operated at 2.3 and 4.2 K. The Pb(100) substrate was prepared in vacuo by repeated cycles of $\mathrm{Ar^+}$ bombardment and annealing at about 530 K. PbPc molecules were sublimated from a Knudsen cell onto the Pb substrate held at room temperature. The differential-conductance dI/dV was measured using a lock-in amplifier with modulation voltages between 50 and 500 μV_{PP} at a frequency of 831 Hz.

DFT calculations were carried out for the free PbPc molecule as well as PbPc molecules adsorbed on Pb(100). We also calculated the inelastic tunneling spectrum, d^2I/dV^2, using DFT combined with the non-equilibrium Green's function method with electron-phonon coupling taken into account using a current conserving lowest order expansion method. All calculations were performed using QuantumATK[224, 225]. In the Supplemental Material (Section 5.4) we detail the calculation methods and results.

After deposition of PbPc at ambient temperature, the molecules arrange in a square mesh with two rotational domains and lie flat on the substrate as displayed in the right inset of Figure 5.11. The unit cell contains two molecules which are rotated by 8° (domain A) or 20° (domain B) with respect to each other. Although some molecules (blueish clover shaped patterns) loose the Pb ion a majority stays intact with the ion either below or above the macrocycle.

The main experimental observation is the dI/dV spectrum (blue lower line) recorded above a Pb center. It appears flat over a wide voltage range and exhibits tall YSR resonances at ± 2 mV (left inset). Like in the case of H_2Pc[45], we find YSR states for arrays of PbPc but not for isolated molecules. A magnified view (black upper line) reveals 46 clear features positioned symmetrically around zero bias. They ride on a background that may be approximated by a superposition of a broad Lorentz-shaped resonance and the spectral signature of bulk phonons we observe on pristine Pb(100). Based on the analyzes presented below, we attribute the features to the excitation of molecular vibrations. The YSR resonance amplitudes depend on the bias polarity and so do the related inelastic features.

Figure 5.12a displays the low energy part of the dI/dV spectrum shifted by $E_{\mathrm{YSR}} + \Delta_T$, with $2\Delta_T$ being the excitation gap of the tip. This shift has been applied to all experimental spectra shown as a function of energy (as opposed to sample voltage). Figure 5.12b shows a calculated spectrum of d^2I/dV^2. 29 features are marked in the experimental data by vertical lines. We find an excellent agreement with the calculated peak energies shifted by +1.0 meV. This leads us to propose a tentative assignment of the experimental peaks to vibrational modes. Data up to 200 meV are presented in Supplemental Figure 5.17. As expected the differences between measurement and calculation are slightly larger at high energies. Nevertheless, the similarity between the calculated and measured spectra remains as indicated in Figure 5.12c. All 46 experimental modes (blue circles) match with calculated ones (green lines).

The Supplemental Material (Section 5.4) presents an overview and animations of the calculated vibrational modes of a PbPc monolayer on Pb(100). Our DFT calculations with different functionals showed that the vibrational energies are robust (Supplemental Figure 5.16). The surface unit cell comprises two molecules supporting 2×171 modes, many of them being almost degenerate pairs. As expected for an array of interacting dipoles, the modes of the monolayer are blueshifted compared to those of a single adsorbed molecule (Supplemental Figure 5.23), which in turn are red shifted from gasphase results because of the interaction with image charges[226, 227].

In the calculated d^2I/dV^2 spectra we observe 74 peaks with intensities above an arbitrary threshold of 500 nA/V^2 corresponding to an effective cross-section of $\eta \approx 0.07\%$. Several of the

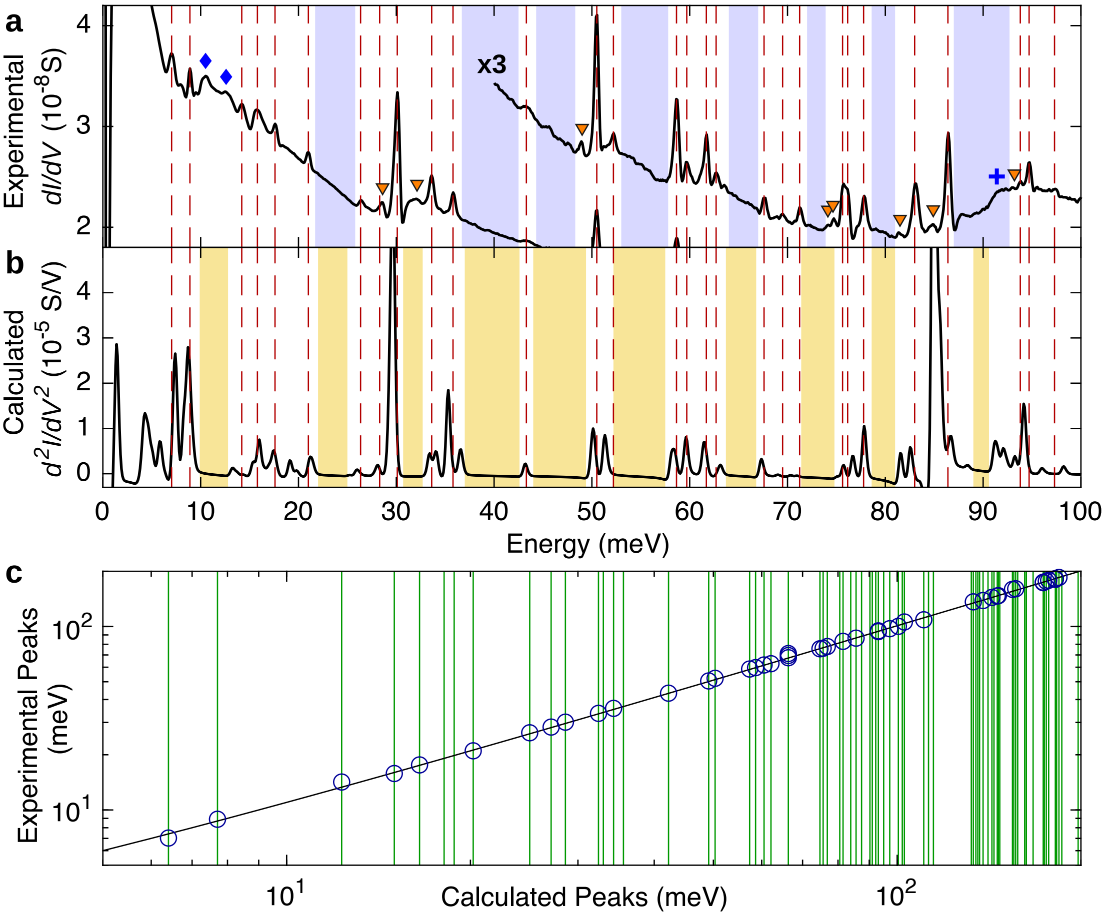

Figure 5.12: Comparison of experimental and calculated spectra. (a) Low energy part of the dI/dV data from Figure 5.11 shifted by the resonance position $E_{\mathrm{YSR}} + \Delta_{\mathrm{T}}$. Vertical dashed lines indicate peaks. Left of intense peaks, small copies are observed (orange triangles) due to thermally excited charge carriers in the tip. In addition to molecular vibrations, bulk phonons, which are also visible also on pristine Pb(100), affect the spectrum at low energies. Two broader peaks (blue diamonds) were omitted from the mode assignment for this reason. A step at ≈90 meV (blue cross) coincides with a multi-peak structure in the calculated d^2I/dV^2. (b) Calculated spectrum of d^2I/dV^2. Except for a 1.0 meV shift, most of the calculated peak energies match the experimental ones thus enabling a tentative peak assignment. Shaded areas indicate gaps in the vibrational spectra. (c) Comparison of calculated peak energies (green vertical lines) with corresponding measured energies (vertical coordinate of blue circles). Logarithmic axes are used to mimic constant relative uncertainties. The black line indicates the relation $E_{exp} = E_{calc} + 1\,\mathrm{meV}$.

corresponding modes (e. g., 15, 63, 123, 205, and 239 at 6.3, 34.3, 83.9, 132.3, and 154.4 meV) exhibit the same B_1 symmetry as the two degenerate lowest unoccupied molecular orbitals (LUMOs), which are the most transmitting transport channels and, therefore, determine the electron transport[228]. Most of the intense modes correspond to experimental peaks, but some calculated modes are close in energy and thus not individually resolved in dI/dV. Presently, a more detailed analysis of the intensities is precluded by the fact that they drastically depend on the functional used and the resulting orbital energies.

At first glance it may seem surprising that electron transport through YSR states may be directly compared to transport channels involving the LUMOs. However, spatial mapping of the YSR state shows detailed similarities with the LUMOs[45]. Still some characteristics of YSR states must be considered in analyzing the experimental data, as the interaction with the tip and an electric field can change their energy and line shape. Our measurements on PbPc (Supplemental Figure 5.20) and published results show that the YSR states shift, broaden, and loose intensity when the tip is brought closer to the sample[25,141]. Taking this shift of the resonances into account we find distinct shifts of vibrational modes.

Figure 5.13 presents applications of the energy resolution of our method. Panel (a) shows the evolution of mode energies with the tip-sample separation. The modes near 18 and 30 meV exhibit red-shifts on the order of 0.1 meV while the modes near 58 and 86 meV undergo blue-shifts of similar magnitude. The displacement patterns of the corresponding vibrational modes reveal some similarities. The red-shifting modes (37/38, 55/56) involve mainly vertical atomic displacements while the blue-shifting modes (81/82, 123) are predominantly horizontal. We tentatively attribute the blue shift to the attractive force exerted by the STM tip that increases the distance between the molecule and the substrate and thereby partially reverts the adsorption-induced red-shift of horizontal modes. In addition, the tip softens the potential along the surface normal and thereby induces a red-shift of vertical modes.

Next, we reverse the roles of YSR states and vibrational excitations. As the voltage between the tip and the sample may gate the molecule, the energy and peak height asymmetry of YSR states could be bias dependent. In contrast to elastic tunneling processes, which probe YSR states at voltages close to zero, the vibration induced copies of the YSR resonances appear at higher voltages and therefore provide access to a possible gating effect. Figure 5.13c shows the spectra of three vibrational excitations at positive (red solid line) and negative (blue dotted line) voltages. Each excitation gives rise to a pair of peaks at both polarities, the peak closer to zero bias being due to thermally excited electrons (holes) in the coherence peaks of the tip above (below) E_F. Towards higher excitation energies the peaks separate in a linear fashion (Figure 5.13d, circles). To calculate inelastic tunneling spectra, the bias dependent density of states of the sample around E_F is obtained using a Green's function approach that takes into account a constant potential scattering W and an exchange coupling J, which depends linearly on the voltage. The observed shift may be understood as follows. At $V < 0$, the LUMO is lowered relative to E_F of the sample, its occupation increases, the YSR state moves deeper into the superconductor gap, and finally the peak height asymmetry is enhanced.

The interaction between a molecule and its local environment may also be addressed. Figure 5.13b and Supplemental Figure 5.19 show spectra of PbPc molecules surrounded by PbPc molecules on nearest neighbors (NN) and next nearest neighbors (NNN) sites (green dotted). When the Pb ions are removed from either NN-molecules (blue dashed) or both, NN and NNN-molecules (red solid line), the vibrational modes observed on the center PbPc undergo small but clearly resolved shifts. Three segments from spectra in Figure 5.13b illustrate diverse evolutions.

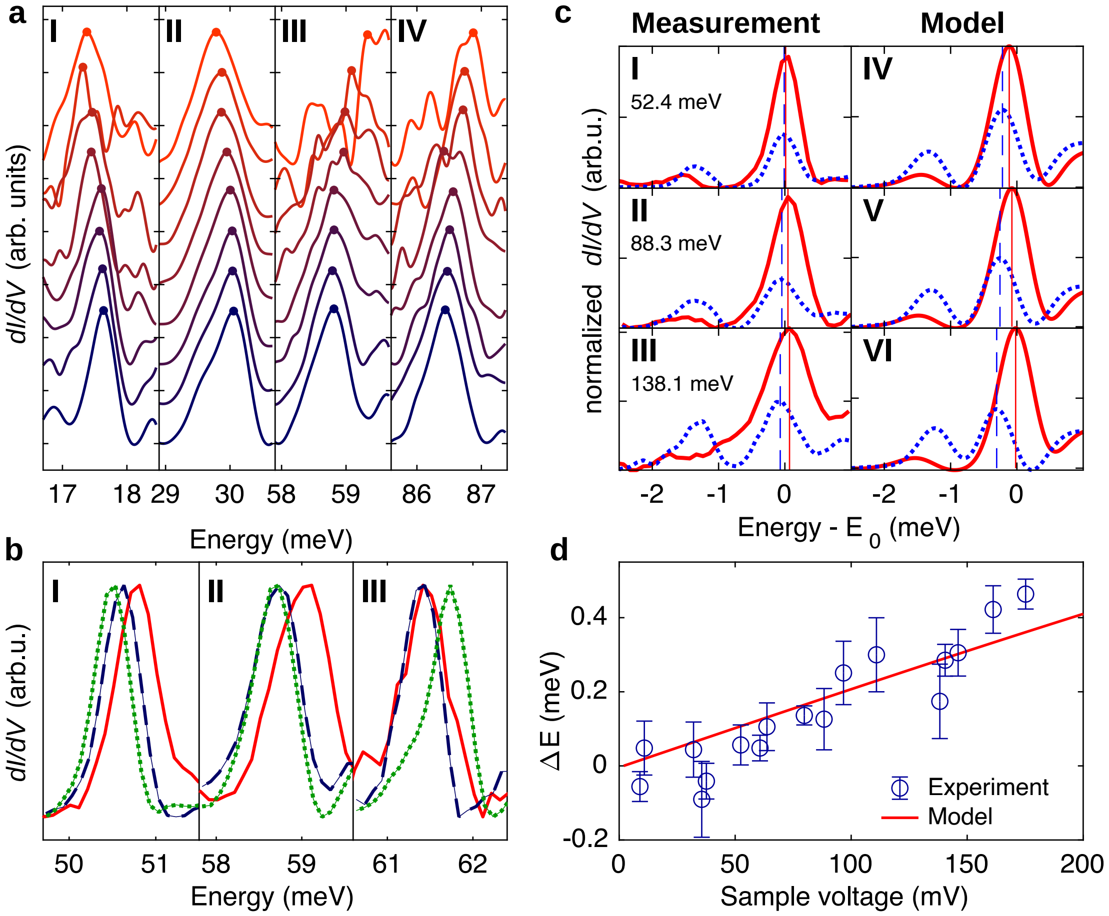

Figure 5.13: Spectral changes caused by tip, neighbors, and bias polarity. (a) dI/dV spectra of a PbPc molecule recorded over a range of tip heights. For the bottom spectrum, the current feedback was disabled at $V = 200\,\mathrm{mV}$ and $I = 500\,\mathrm{pA}$ and the tip was brought 128 pm closer to the sample. From spectrum to spectrum the tip-sample separation was reduced by further 16 pm. A sinusoidal modulation of $0.5\,\mathrm{mV_{PP}}$ was used. (b) dI/dV spectra of PbPc molecules in different environments. The green dotted spectrum was recorded on a molecule with PbPc on nearest neighbor (NN) and next nearest neighbor (NNN) sites. The blue dashed (red solid) curve shows data where Pb was absent from NN (NN and NNN) molecules. (c) Left column: Experimental dI/dV data of excitations at 52.5, 88.3 and 138.1 meV measured at positive (red solid) and negative (blue dotted) V. $E_0 = E_{\mathrm{YSR}} + \Delta_T + \hbar\omega$. The main peaks are due to tunneling from the occupied (unoccupied) coherence peak of the tip to the unoccupied (occupied) YSR state at $V > 0$ ($V < 0$). Thermally excited charge carriers lead to a minor peak in each spectrum. The positions of the main peaks (dashed vertical lines) do not exactly coincide and separate with $|V|$ in a linear fashion. The relative heights of the major and minor peaks also change. Right column: dI/dV calculated with a model that considers a voltage dependence of the YSR states reproduces the experimental data. (d) Polarity induced differences of peak positions evaluated from various excitations. A model presented in the Supplemental Material reproduces the observed linear relation (Equation 6). Experimental parameters are identical to those in Figure 5.11.

In summary, taking advantage of YSR states, the detection limit of vibrational spectroscopy with the STM is improved and the energy resolution is pushed beyond the thermal limit. Such resonances may be expected from molecules that carry a spin, be it due to intrinsic molecular properties or charge transfer involving the environment. While modeling of the vibrational mode energies is fairly accurate, the inelastic intensities will require further attention.

5.4 Supplemental Material for Resonance-enhanced Vibrational Spectroscopy of Molecules on a Superconductor

5.4.1 DFT and DFT-NEGF Calculations

5.4.1.1 Structural Relaxation of PbPc on Pb(100)

For the DFT calculations we use a DoubleZetaPolarized basis set and the exchange-correlation functional is described within the generalized gradient approximation (GGA) using the PBE functional[204].

The relaxed structure is shown in Figure 5.14. Panel A is a top view illustrating the unit cell containing two PbPc molecules rotated by 23°. Panel B shows a side view of the PbPc monolayer on the Pb(100) surface and an idealized STM tip, which is comprised of a similar Pb(100) surface but with five additional tip atoms. The PbPc monolayer lays almost flat on the Pb(100) surface except the central Pb atom pointing upward. The distance between the flat part of the molecule and the surface is approximately 3.7 Å. The STM tip is positioned right above the Pb atom in the PbPc molecule with a distance of 4.0 Å.

Structural relaxation is performed for the molecules as well as first metal layers plus metal tip atoms until the maximum force is less than 0.05 eV/Å using a $2 \times 2 \times 1$ Monkhorst Pack k-point sampling.

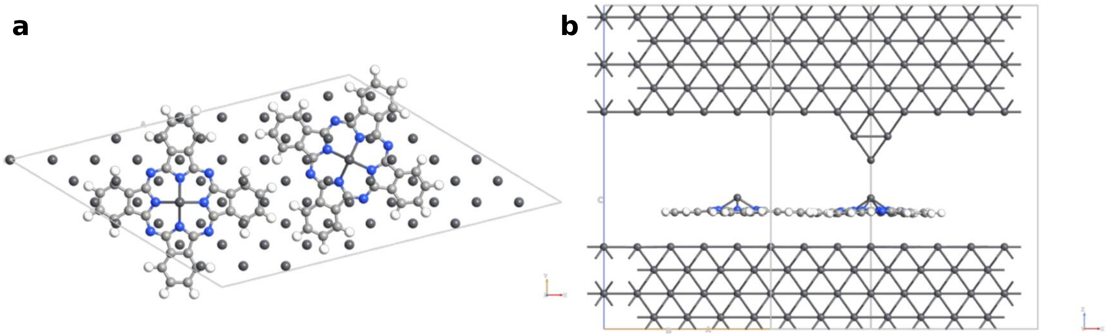

Figure 5.14: Calculation cell for the PbPc monolayer on Pb(100). (a) Top view of the unit cell containing two PbPc molecules rotated by 23°. (b) Side view showing the Pb(100) substrate and tip structure. The tip is positioned directly over the Pb atom of the PbPc molecule. The closest distance between the tip and PbPc molecule is 4.0 Å and the distance from the molecule to the substrate is approximately 3.7 Å.

5.4.1.2 Inelastic DFT-NEGF Calculations

To calculate the inelastic signals we use a lowest order expansion (LOE) method[229, 230] going beyond the original wide band approximation[231].

We first calculate the dynamical matrix taking only atoms in the PbPc molecules into account. Although the LOE method allows for scattering with a finite momentum transfer, we limit our calculations to only considering incoming and outgoing electrons with transverse momentum $\mathbf{k}_{||} = 0$ interacting with phonon also having zero momentum $\mathbf{q} = 0$. From the dynamical matrix $\mathbf{D}$ we obtain the phonon frequencies ω_λ and eigenvectors $\mathbf{u}_\lambda$ for a particular phonon band index λ:

$$\mathbf{D}\mathbf{u}_\lambda = \omega_\lambda^2 \mathbf{u}_\lambda, \tag{5.42}$$

where the phonon mode vectors are normalized, i. e. $\mathbf{u}^T \cdot \mathbf{u} = 1$. We further define mass-scaled phonon mode vectors according to

$$\mathbf{v}_\lambda(\alpha) = \mathbf{u}_\lambda(\alpha)\sqrt{\frac{\hbar}{2M_\alpha \omega_\lambda}}, \tag{5.43}$$

where M_α is the mass of the atom with index α.

The electron-phonon coupling matrix for phonon mode λ is

$$M_\lambda^{\mu\nu} \quad = \quad \langle \phi_\nu | \mathbf{v}_\lambda \cdot \nabla H(r) | \phi_\mu \, \rangle, \tag{5.44}$$

where $|\phi_{\mu,\nu}\,\rangle$ denote the LCAO basis orbitals, the derivative of the Hamiltonian is taken with respect to atomic coordinates and restricted to atoms in the PbPc molecules for simplicity. The calculation of the inelastic signals follows the description in References 229,230 and is performed using the InelasticTransmissionSpectrum in QuantumATK.

5.4.1.3 Magnetic PbPc on Pb(100)

Since the occurrence of YSR states requires a magnetic moment, we have investigated whether a magnetic configuration can be identified in calculations. For the PBE calculations presented above, this is not the case. Both the free molecule, free monolayer (i. e. the molecules in Figure 5.14 without the Pb substrate and tip) as well as the PbPc monolayer on Pb(100) give a non-magnetic ground state. In this case, the orbital dominating the transport is the LUMO, which is evident from a projected density of states (PDOS) plot shown in Figure 5.15a. The spin-resolved PDOS for the PbPc molecule is defined as

$$D^\sigma(E) = \sum_i \sum_{\mu \in \mathrm{PbPc}} w_i |\langle \phi_\mu | \psi_i^\sigma \rangle| \delta(E - \epsilon_i^\sigma) \tag{5.45}$$

where the sum over i runs over all spin σ (up or down) eigenstates $|\psi_i^\sigma\rangle$ in the system with eigenvalues ϵ_i^σ including k-point summation and corresponding weight factors w_i. The μ-sum

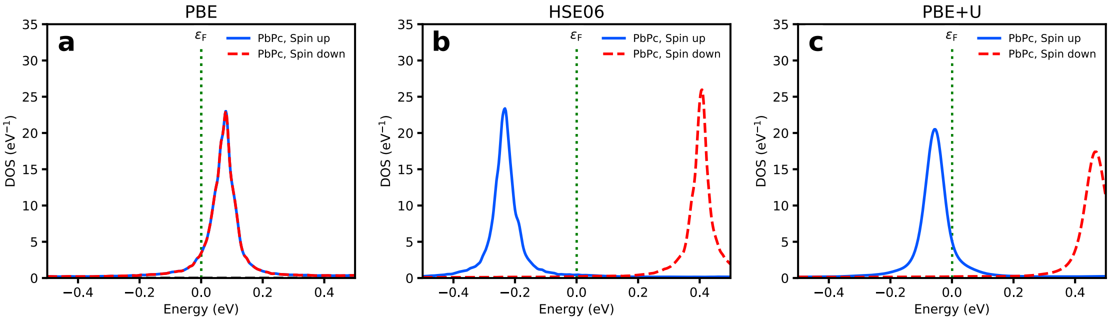

Figure 5.15: PDOS of the PbPc molecule under the tip calculated with PBE (a), HSE06 (b), and PBE+U (c). The spin splitting observed with HSE06 and PBE+U is in qualitative agreement with the experimental observation of YSR states.

runs over basis orbitals centered on atoms belonging to the PbPc molecule under the tip. In the calculations, the δ-function is replaced by a Gaussian with a width of 0.005 eV.

Interestingly, using the hybrid functional HSE06[232,233], the calculated ground state of PbPc molecules on Pb(100) is magnetic as shown in Figure 5.15b, where a splitting of the spin up and down orbitals close to the Fermi energy is clearly seen. Without the Pb substrate both a single PbPc molecule and the PbPc monolayer come out as non-magnetic with HSE06, showing that the magnetic state of PbPc on Pb(100) is caused by molecule-substrate interaction.

Since inelastic NEGF calculations using hybrid functionals are not yet available in QuantumATK (and, to the best of our knowledge, in other codes), we have also performed DFT+U[234] calculations in order to simulate the magnetic configuration. Figure 5.15c shows the PDOS from such a PBE+U calculation, where a Hubbard U energy term has been added to the p-orbitals on carbon and nitrogen with a U value of 4 eV. The purpose of PBE+U calculations is not to obtain a one-to-one correspondence with the HSE06 result, but rather a qualitative check of the inelastic PBE calculations. A comparison of PBE and PBE+U inelastic calculations is shown below.

5.4.1.4 PBE and PBE+U Inelastic Calculations

Figure 5.16 shows the calculated transmission spectrum (left column) and the IETS signal (right column). The transmission spectrum is obtained using the DFT-NEGF method[225]. The IETS signal is here calculated as $\mathrm{IETS}(V) = \left(\frac{d^2I}{dV^2}\right) / \left(\frac{dI}{dV}\right)$. Since we focus on the peak positions, we use a very low temperature of $T = 1\,\mathrm{K}$ for the IETS calculations to reduce the thermal broadening of the peaks. Panel A shows the transmission spectrum calculated with the PBE functional. The transmission around the Fermi energy ($E = 0\,\mathrm{eV}$) is dominated by the spin degenerate LUMO orbital. The corresponding IETS spectrum is displayed in panel C and compared with the experimental results in the main manuscript. Panel B presents the transmission spectrum obtained with the PBE+U functional, where a Hubbard U has been added to carbon and nitrogen p orbitals. The transmission spectrum closely resembles the PDOS shown in Figure 5.15c with a spin-up HOMO orbital closest to the Fermi energy and a spin-down LUMO 0.5 eV above the

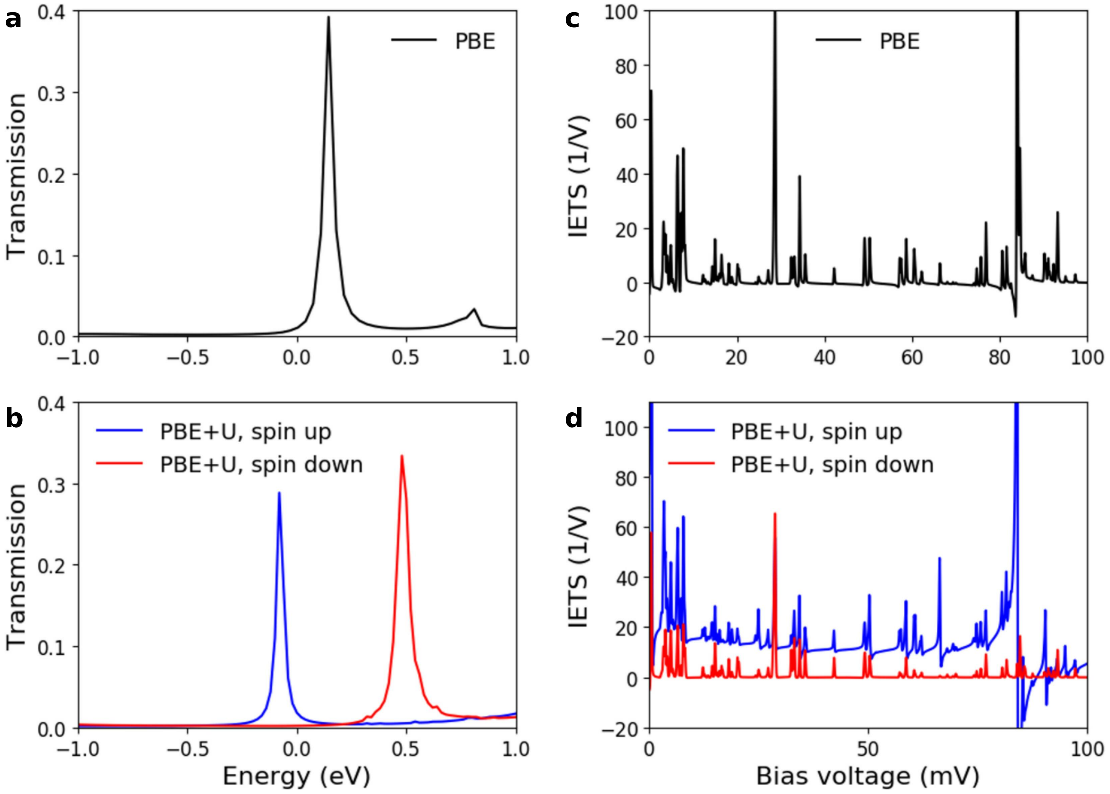

Figure 5.16: Transmission spectrum and IETS as obtained using the PBE functional (a) and (c) giving a non-magnetic molecular configuration, and using PBE+U (b) and (d) with a magnetic ground state configuration. For the IETS calculations, we use the same vibrational modes and energies obtained with PBE and focus only on the effect of the different electronic states.

Fermi energy. The IETS spectrum for the PBE+U calculation is shown in panel (d). For this calculation, the same vibrational modes and energies have been used as for the PBE calculation. Although there is a notable difference in relative peak intensities between the PBE and PBE+U calculations, the two calculations give qualitatively similar results. In particular, the vibrational modes giving rise to the largest IETS signals appear to be identical in the two calculations. Notice that the spin up HOMO, being almost resonant with the Fermi energy, gives rise to significant peak asymmetries and Fano-like shapes, in agreement with References 229, 230.

Despite the theoretical uncertainty about the magnetic configuration of the PbPc molecules, the qualitative comparison between the PBE and PBE+U IETS spectra shows that the coupling of the vibrational modes to the frontier orbitals is qualitatively similar. This justifies the use of the calculated PBE IETS signal when comparing to the experimental results.

5.4.2 Supplemental Experimental Data

5.4.2.1 Data from the Range 100 mV < |V| < 200 mV

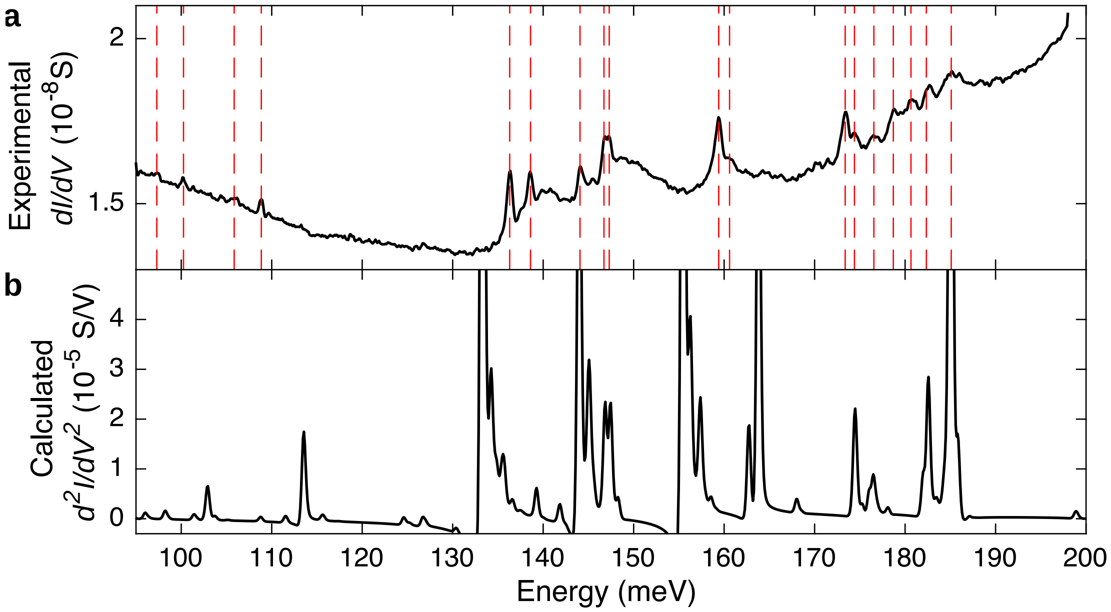

Figure 5.17: Experimental and calculated spectra at elevated energies. (a) dI/dV data shifted by the resonance position $E_{\mathrm{YSR}} + \Delta_{\mathrm{T}}$. Vertical lines indicate some of the observed peaks. (b) Calculated spectrum of dI^2/dV^2 shifted by 1.0 meV to higher energies. Based on a tentative peak assignment, we find deviations of less than 7 meV between the experimental and calculated energies. However, the relation between measured and calculated peaks is less obvious than at low energies.

5.4.2.2 *dI/dV*-Spectra of Molecules with and without YSR States

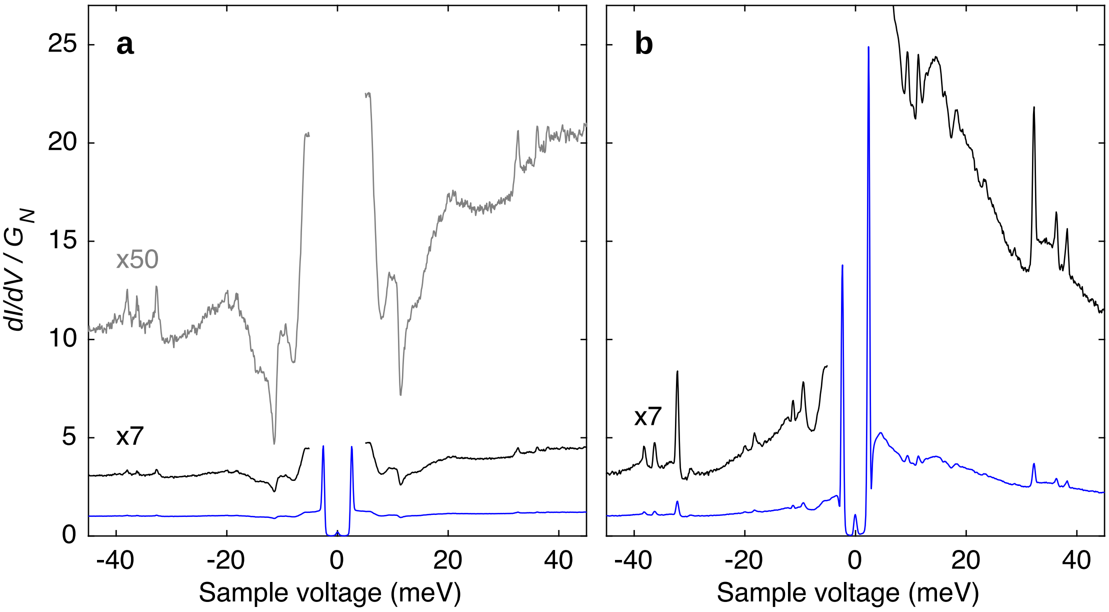

Figure 5.18: $dI/dV(V)$ spectra, normalized to the normal state conductance, of molecules (a) without and (b) with YSR states. Panel (a) shows a spectrum recorded on an isolated molecule on the pristine Pb(100) substrate. Spectral signatures at $V \approx \pm 10\,\mathrm{mV}$ and $\pm 6\,\mathrm{mV}$ are strong coupling features originating from Pb phonons. No YSR states are present, the coherence peaks have identical amplitudes and vibrational signatures are barely discernible at large magnifications ($\times 50$). In panel (b) a spectrum recorded over a molecule inside the monolayer reveals YSR states, whose vibrational copies have much larger amplitude and their peak-height asymmetry resembles those of the YSR states.

5.4.2.3 Interaction with Neighbor Molecules

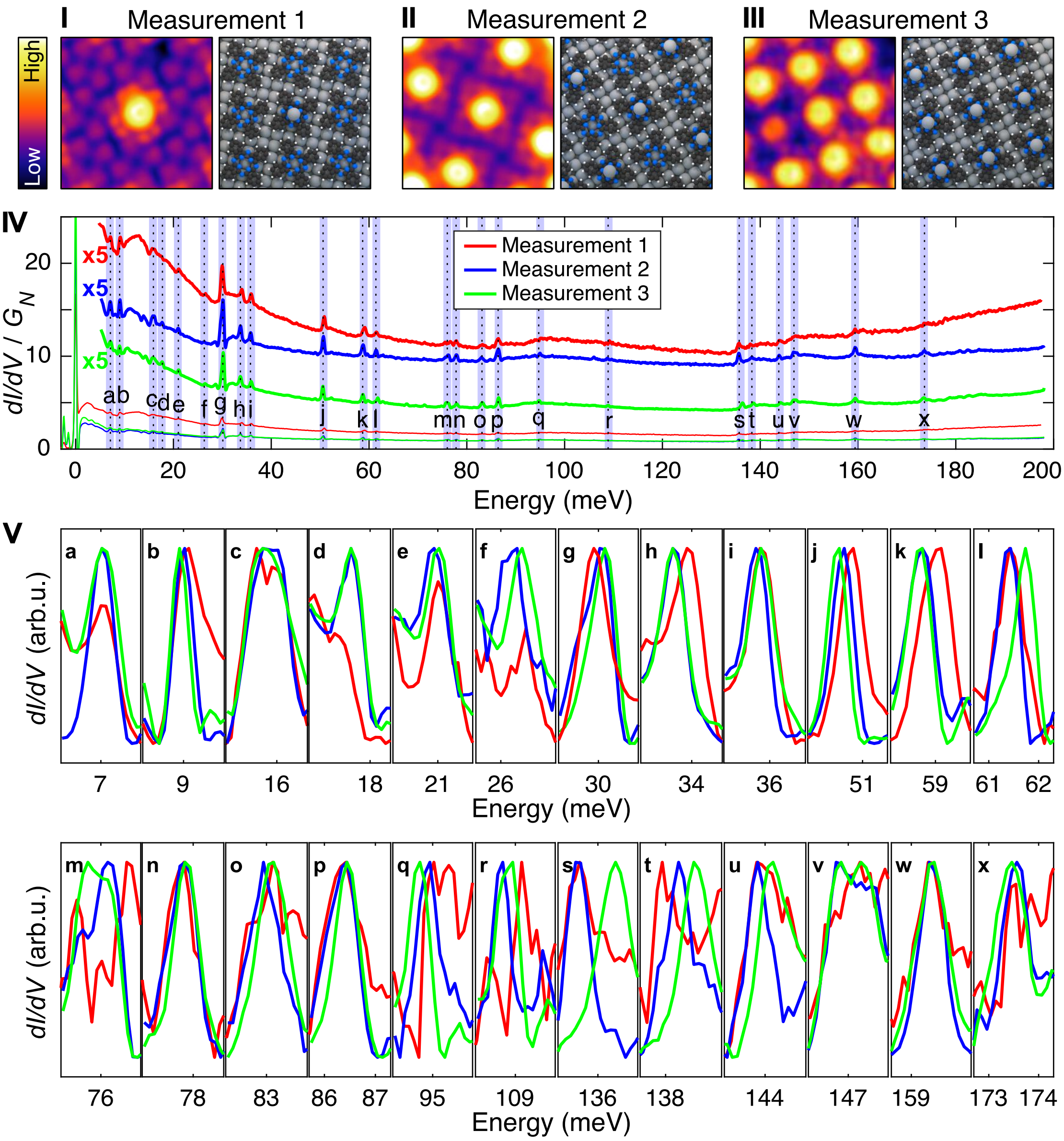

Figure 5.19: Topographs and structure models of a PbPc molecule surrounded by (I) Pc without Pb ion, (II) PbPc on NNN sites and (III) PbPc on NN and NNN sites. (IV) dI/dV spectra of the central molecules in (I – III) normalized with the conductance G_N at large energies. Vertical lines indicate the peaks observed from the molecule in (I). (V) Close-up views of peaks indicated by blue shaded areas in (IV). Some modes continuously shift to higher (g, n, p, t) or lower (b, j, q) energies as the number of PbPc neighbors increases. Others (h, k) exhibit a red-shift for NNN PbPc that is no further increased by the addition of NN PbPc. The modes in (l) and (s) exhibit a blue-shift only if Pb is present in NN molecules. The modes in (a, c, w) are unaffected by Pb in NN or NNN molecules.

5.4.2.4 Interaction with the STM Tip

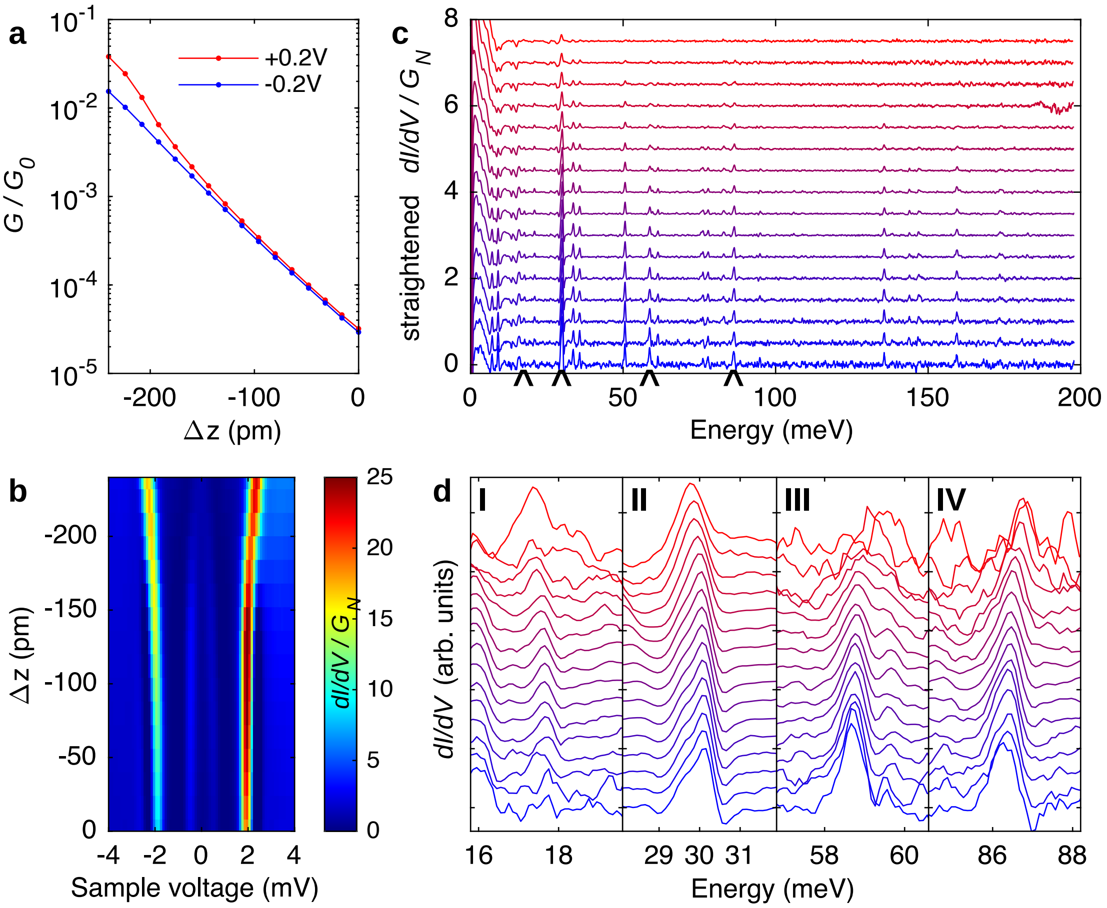

Figure 5.20: Vibrational excitations at different tip distances. (a) Evolutions of the conductance at $V = \pm 0.2\,\mathrm{V}$. The STM current feedback was disabled at $I = 500\,\mathrm{pA}$, which defines $\Delta z = 0$. (b) Low-bias range of 16 dI/dV spectra recorded above the center of a PbPc molecule. From spectrum to spectrum the tip-sample separation was reduced by 16 pm. The YSR peaks shift from $\approx \pm 1.9$ (bottom spectrum) to $\approx \pm 2.4\,\mathrm{mV}$ during the tip approach. (c) dI/dV spectra from (a) normalized with the conductance G_N at large voltages and straightened by removing background features (bulk phonon spectrum and Lorentzian). Only data at $V > 0$ is shown. The spectra have been shifted by the energy of the relevant YSR peak so that the abscissa shows excitations energies. The top spectrum (red) was recorded at the largest tip-sample separation. Spectra are vertically shifted in steps of $0.5\,G_N$. (d) Subsections of the untreated spectra showing vibrational peaks at various energies. The data are also presented in Figure 5.13a of the manuscript, where they are normalized to similar peak heights.

5.4.2.5 Structure of the PbPc Layer

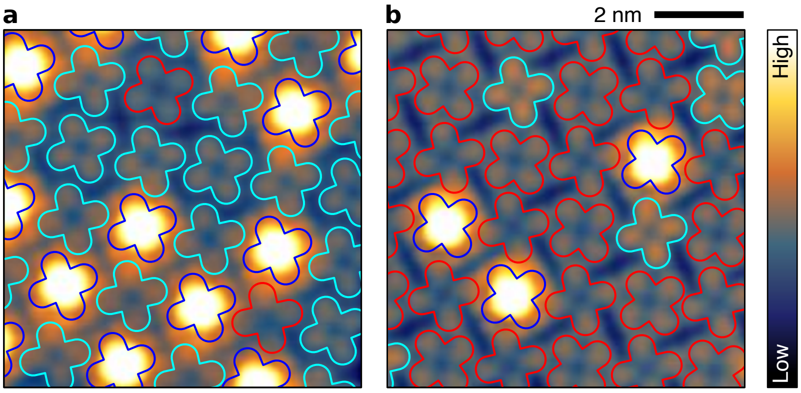

Figure 5.21: Constant-current topograph of PbPc on Pb(100). (a) and (b) show two different domains. The outlines of the molecules are indicated by lines. PbPc may adsorb with the Pb ion pointing away from the substrate (dark blue lines) or between the substrate and the molecular frame (cyan). In addition, Pc molecules without Pb ion are found (red). The Pb ions may also be intentionally removed by manipulation with the STM tip. YSR resonances are only observed from the first class of molecules. (a) $V = 6$ mV, $I = 100$ pA (b) $V = -6$ mV, $I = 100$ pA.

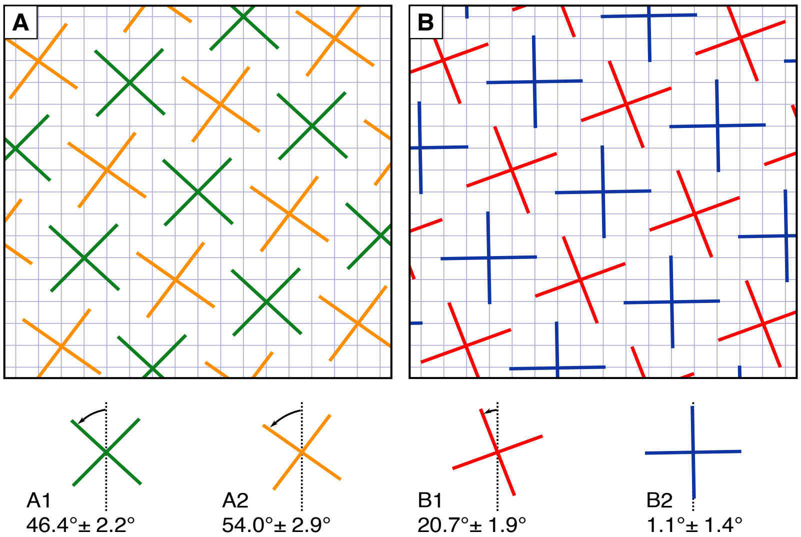

Figure 5.22: Schematics of the adsorption geometries. (A) and (B) show the two domains from Figure 5.21. The Pb(100) lattice is depicted as a square pattern with a mesh size corresponding to 350 pm. Phthalocyanine molecules are indicated by crosses. In both configurations, the molecules are centered atop of a Pb atom and form a ((3 5)(5 3)) superstructure with two molecules per unit cell. Colors indicate groups of molecules with different orientations. Angles and their standard deviations were measured from at least 32 molecules per group. The molecules in (A) are oriented with their long axes approximately a $\langle 001 \rangle$ substrate direction. The orientations of the two groups differ by $\approx 8°$. In (B), half of the molecules (blue) have one of their long axes oriented along a $\langle 011 \rangle$ substrate direction, the other half (red) is rotated by $\approx 20°$.

5.4.3 Modeling of YSR Enhanced Vibrational Features in *dI/dV* Spectra

To analyze the gating effect on YSR states presented in Figure 5.13c of the manuscript, we calculated spectral line shapes from a set of vibrational mode energies $\hbar\omega_\nu$ and their cross-sections η_ν as presented below.

We model the YSR states as a part of the local density of states (LDOS) of the sample using Bogoliubov-de Gennes and Green's function formalisms. The starting point is the homogeneous Green's function of the unperturbed superconducting substrate:

$$G_0(E) = \begin{pmatrix} g(E) & f(E) \\ f^*(-E) & -g^*(-E) \end{pmatrix}, \tag{5.46}$$

where $g(E)$ and $f(E)$ are the normal and anomalous Green's functions, respectively[172]:

$$g(E) = -\pi\rho_{S,N}(E)\frac{E+\mathrm{i}\Gamma}{\sqrt{\Delta_S^2-(E+\mathrm{i}\Gamma)^2}} \qquad f(E) = -\pi\rho_{S,N}(E)\frac{\Delta_S}{\sqrt{\Delta_S^2-(E+\mathrm{i}\Gamma)^2}} \tag{5.47}$$

Here, $\rho_{S,N}(E)$ is the LDOS of the sample in the normal-conducting state, Δ_S the superconducting gap of the sample and Γ a broadening parameter similar to Dynes' parameter. The Green's function matrix is written in spin up electron and spin down hole space. It is identical for spin down electrons and spin up holes. Next, the impurity spin, which acts differently on up-spin and down-spin electrons of the substrate, is included. The respective impurity scattering matrix depends on the electron spin $\sigma \in \{1, -1\}$:

$$\Sigma_\sigma = \begin{pmatrix} \sigma JS + W & 0 \\ 0 & \sigma JS - W \end{pmatrix}, \tag{5.48}$$

where JS and W describe spin dependent and spin independent scattering potentials, respectively. The Green's function of the coupled system reads:

$$G_\sigma(E) = \left(G_0^{-1}(E) - \Sigma_\sigma\right)^{-1} \tag{5.49}$$

leads to the spin-dependent LDOS:

$$\rho_\sigma(E) = -\frac{1}{\pi}\Im\left(G_\sigma^{(1,1)}(E)\right) \tag{5.50}$$

The LDOS of the sample is the sum of both spin components $\rho_S = \rho_{\mathrm{YSR}}(E) = \rho_\uparrow(E) + \rho_\downarrow(E)$. Assuming a constant $\rho_{S,N}(E) = \rho_0$ within the energy range $-\Delta \ldots \Delta$, it contains YSR states at energies

$$\pm E_{\mathrm{YSR}} = \Delta\frac{\pi^2\rho_0^2(J^2S^2 - W^2) - 1}{\sqrt{(\pi^2\rho_0^2(J^2S^2 - W^2) - 1)^2 + 4\pi^2\rho_0^2 J^2S^2}}. \tag{5.51}$$

For the density of states of the tip we use the BCS result extended by a Dynes' parameter Γ:

$$\rho_T = \rho_{\mathrm{BCS}}(E) = \rho_{T,N}(E) \cdot \Re\left(\frac{\mathrm{sign}(E)\cdot(E-\mathrm{i}\Gamma)}{\sqrt{(E-\mathrm{i}\Gamma)^2-\Delta_T^2}}\right) \tag{5.52}$$

$\rho_{T,N}(E)$ is the tip DOS in the normal-conducting state and assumed to be constant for simplicity.

The elastic tunneling current $I_{el}(V)$ is obtained from the DOS of tip and sample:

$$\begin{aligned} I_{el}(V) &= c\int_{-\infty}^{\infty} \rho_t(E-eV)\rho_s(E)\,[f(E-eV,T)-f(E,T)]\,dE \\ &= \Big(\rho_s(E) * [\rho_t(-E)f(-E,T)]\Big)(eV) - \Big([\rho_s(E)f(E,T)] * \rho_t(-E)\Big)(eV) \end{aligned} \tag{5.53}$$

$f(E,T)$ is the Fermi distribution at a temperature T and c is proportional to the tunneling transmission.

For inelastic tunneling, the energy of the final state is lower by the energy $\hbar\omega_\nu$ of the relevant vibrational mode ν:

$$\begin{aligned} I_\nu(V) = c\,\eta_\nu \int_{-\infty}^{\infty} dE\Bigg(&\rho_t(E-eV+\hbar\omega_\nu)\ \overbrace{f(E-eV+\hbar\omega_\nu,T)}^{\to\,0,\ \text{for } -eV+\hbar\omega_\nu \gg k_BT}\ \rho_s(E)[1-f(E,T)] \\ &- \rho_s(E)f(E,T)\rho_t(E-eV-\hbar\omega_\nu)\underbrace{[1-f(E-eV-\hbar\omega_\nu,T)]}_{\to\,0,\ \text{for } eV+\hbar\omega_\nu \gg k_BT}\Bigg) \end{aligned} \tag{5.54}$$

Next, the contributions of all vibrational modes, weighed by cross-sections η_ν, are added to arrive at the inelastic tunneling current:

$$I_{\mathrm{inel}}(V) = \sum_\nu I_\nu(V) \tag{5.55}$$

Finally, the dI/dV spectrum is calculated by numerical derivation $\frac{d}{dV}(I_{\mathrm{el}}(V) + I_{\mathrm{inel}}(V))$.

To account for electronic broadening, the spectrum is furthermore convoluted with a Gaussian with a standard derivation $\sigma \approx 150\,\mu$eV. Broadening caused by the voltage modulation V_m for lock-in detection is taken into account by convolution with the broadening function $\Re(2\sqrt{V_m^2 - V^2}/(\pi V_m^2))$.

The best match of the experimentally observed linearly increasing separation between the vibrational features at negative and positive bias was obtained using a constant potential scattering $\pi\rho_0 W = 0.42$ and an exchange coupling $\pi\rho_0 JS = 0.57 - 0.88 \cdot V/\mathrm{V}$.

5.4.4 Calculated Vibrational Modes

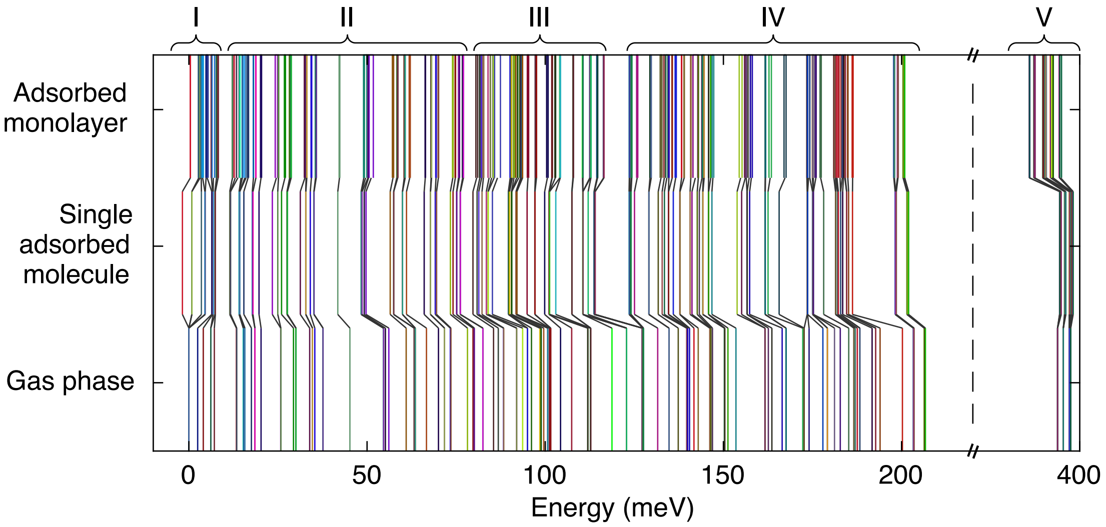

Figure 5.23: Energies of vibrational excitations from gas phase, single adsorbed molecule and adsorbed monolayer calculations. Different groups of vibrational modes are identified: (I) frustrated modes and bending modes, (II) higher order bending modes and horizontal rotation of the lobes, (III) lobe squeezing and shearing modes with vertical C-H bending, (IV) C-C and N-C stretching/breathing modes with horizontal C-H bending and (V) C-H stretching modes.

Table 5.3: Properties of calculated vibrations. The unit cell of the calculation contains two PbPc molecules with 57 atoms each, resulting in 342 modes. Modes with energies up to 200 meV are listed below. The symmetry of the vibrations and the dominant direction were analyzed for the molecule below the tip. The dominant direction of motion is indicated by h = exclusively horizontal, hm = mainly horizontal, v = exclusively vertical, vm = mainly vertical, or m = mixed. The symmetry of the vibrations is given by Mulliken symbols denoting the irreducible representations of the point group C_{4v} of the molecule. Intensities were determined from calculated peak heights in d^2I/dV^2 spectra.

ID	Energy (meV)	Symmetry (Mulliken)	Dominant Direction	Intensity (10^{-8} S/V)
1	0.40	E	h	1547.41
2	0.41	E	h	1479.81
3	2.66	A_2	h	65.45
4	2.87	A_2	hm	164.19
5	3.15	E	m	444.59
6	3.16	E	vm	292.41
7	3.32	E	m	582.47
8	3.61	E	v	534.36
9	3.69	E	vm	337.80
10	4.04	B_2	v	452.65
11	4.74	E	vm	401.50
12	4.91	E	vm	373.28
13	4.92	E	m	141.37
14	5.34	A_2	vm	116.36
15	6.25	B_1	v	1314.74

Table 5.3: (continued)

ID	Energy (meV)	Symmetry (Mulliken)	Dominant Direction	Intensity (10^{-8} S/V)
16	6.42	E	v	901.97
17	6.50	E	v	886.28
18	7.22	A_1	v	1120.99
19	7.69	E	v	1497.28
20	7.82	E	v	1103.18
21	8.11	B_2	v	519.00
22	8.27	E	v	52.64
23	12.16	E	m	98.83
24	12.30	E	m	85.88
25	12.69	B_2	h	63.62
26	13.32	E	vm	17.36
27	13.39	E	vm	17.15
28	14.10	B_1	hm	18.95
29	14.32	A_2	v	286.07
30	14.93	E	m	354.95
31	14.98	B_1	m	93.22
32	15.01	E	m	340.83
33	15.47	B_1	m	99.77
34	15.94	E	m	72.75
35	15.99	E	m	48.87
36	16.08	E	m	46.19
37	16.46	A_1	v	456.80
38	16.74	A_1	v	155.78
39	18.08	E	m	184.50
40	18.15	E	m	174.32
41	18.79	E	vm	53.75
42	18.82	E	vm	55.72
43	20.10	B_1	vm	325.67
44	20.39	B_1	vm	209.98
45	24.22	A_2	h	29.17
46	24.89	B_2	m	113.49
47	25.07	B_2	m	24.90
48	25.21	A_2	h	23.33
49	26.79	B_2	m	47.47
50	27.10	B_2	m	225.42
51	28.19	A_1	hm	184.36
52	28.37	E	v	557.24
53	28.46	E	v	1011.44
54	28.51	E	v	720.44
55	28.65	E	v	3169.52
56	28.74	E	v	1905.46
57	32.40	A_1	vm	479.16
58	32.70	A_1	vm	122.93
59	32.86	E	m	39.46
60	32.92	E	m	101.67
61	33.07	E	m	233.48
62	33.12	E	m	247.46
63	34.29	B_1	vm	1899.25
64	34.47	E	vm	9.43
65	35.50	E	m	228.30
66	35.57	E	m	275.47
67	35.70	E	hm	68.21

Table 5.3: (continued)

ID	Energy (meV)	Symmetry (Mulliken)	Dominant Direction	Intensity (10^{-8} S/V)
68	35.77	E	hm	24.50
69	42.16	A_1	v	264.99
70	42.35	A_1	v	18.85
71	49.02	E	v	509.65
72	49.16	E	v	477.65
73	49.27	B_1	v	241.43
74	49.93	A_2	v	41.72
75	50.26	A_2	v	133.06
76	50.26	A_2	v	649.08
77	50.36	E	v	5.43
78	50.48	A_1	v	146.09
79	50.58	B_1	v	6.02
80	51.75	E	v	2.42
81	57.10	B_2	h	499.60
82	57.45	B_2	h	427.78
83	58.34	E	v	63.83
84	58.36	E	v	56.26
85	58.60	E	v	385.83
86	58.62	E	v	386.43
87	60.42	E	h	314.38
88	60.44	E	h	283.98
89	60.66	E	h	199.33
90	60.72	E	h	70.58
91	61.82	B_2	v	77.45
92	62.12	B_2	v	197.01
93	66.29	B_1	h	339.99
94	66.39	B_1	h	51.27
95	67.95	E	h	15.31
96	68.00	E	h	14.37
97	68.08	E	h	5.43
98	68.13	E	h	3.97
99	69.27	A_2	h	30.68
100	69.42	A_2	h	4.05
101	69.93	A_1	h	20.60
102	70.09	A_1	h	9.46
103	73.98	A_2	hm	29.99
104	74.15	A_2	hm	35.04
105	74.70	A_2	vm	309.53
106	74.84	A_2	vm	0.50
107	75.65	E	m	244.02
108	75.66	E	m	255.48
109	75.87	E	m	4.44
110	75.90	E	m	2.92
111	76.82	E	m	550.61
112	76.83	E	m	582.38
113	77.03	E	m	18.04
114	77.06	E	m	18.78
115	80.53	E	v	660.75
116	81.01	E	v	7.84
117	81.52	B_1	v	739.86
118	81.77	A_1	h	114.36
119	82.07	A_1	h	49.48

Table 5.3: (continued)

ID	Energy (meV)	Symmetry (Mulliken)	Dominant Direction	Intensity (10^{-8} S/V)
120	82.23	B_2	hm	20.85
121	82.54	B_2	hm	141.10
122	82.76	B_2	hm	6.21
123	83.94	B_1	m	14246.69
124	84.55	E	v	1276.58
125	84.64	E	v	1212.17
126	85.29	E	vm	16.96
127	85.54	A_1	v	230.30
128	85.76	E	v	208.93
129	85.79	E	v	204.43
130	87.43	A_1	v	80.49
131	90.15	E	m	267.62
132	90.18	E	m	278.96
133	90.47	B_1	v	324.83
134	90.48	E	hm	5.55
135	90.53	E	hm	6.10
136	91.05	E	vm	216.48
137	91.06	E	vm	228.09
138	91.42	A_1	v	175.55
139	91.74	E	v	60.61
140	92.23	E	v	179.38
141	92.28	E	v	184.62
142	92.83	A_1	v	79.27
143	93.07	A_2	v	211.41
144	93.16	E	v	412.66
145	93.19	E	v	468.96
146	93.23	E	v	443.22
147	93.51	A_1	v	2.44
148	93.56	B_2	v	31.04
149	93.63	E	v	11.14
150	93.65	E	v	8.87
151	94.98	B_1	h	117.96
152	95.35	B_1	h	18.20
153	97.20	E	h	82.70
154	97.23	E	h	78.84
155	97.53	E	h	13.09
156	97.56	E	h	12.71
157	100.40	A_1	h	106.89
158	100.81	A_2	h	20.84
159	101.83	E	v	189.13
160	101.90	E	v	174.98
161	101.92	E	v	200.48
162	102.01	E	v	149.03
163	102.71	A_2	h	77.07
164	102.92	A_2	h	5.80
165	104.07	E	v	3.32
166	104.10	E	v	2.58
167	104.16	E	v	4.82
168	104.29	E	v	2.88
169	107.75	E	h	38.32
170	107.80	E	h	27.83
171	107.83	E	h	22.59

Table 5.3: (continued)

ID	Energy (meV)	Symmetry (Mulliken)	Dominant Direction	Intensity (10^{-8} S/V)
172	107.91	E	h	3.91
173	110.43	E	v	34.47
174	110.50	E	v	35.09
175	110.56	E	v	36.42
176	110.61	E	v	37.51
177	112.47	B_2	h	991.49
178	112.54	B_2	h	771.82
179	112.65	E	vm	8.29
180	112.75	E	vm	65.50
181	112.79	E	v	2.67
182	112.86	E	v	0.21
183	114.46	B_2	v	19.41
184	114.58	E	v	34.79
185	114.63	E	v	37.14
186	114.74	A_2	v	36.61
187	116.33	E	v	1.70
188	116.40	E	v	1.48
189	116.45	B_2	v	1.43
190	116.50	E	v	0.62
191	123.54	A_1	h	119.92
192	123.65	E	h	5.83
193	123.70	E	h	23.66
194	123.76	E	h	5.17
195	124.14	E	h	3.56
196	124.19	E	h	13.06
197	124.26	E	h	20.63
198	124.32	E	h	3.15
199	125.65	B_2	h	164.52
200	125.97	B_2	h	66.39
201	129.37	E	h	56.75
202	129.42	E	h	48.17
203	129.73	E	h	10.46
204	129.75	E	h	7.32
205	132.27	B_1	h	23108.16
206	132.71	A_2	h	28.64
207	133.22	B_2	h	2396.57
208	133.62	A_2	h	33.09
209	133.84	E	h	595.09
210	134.41	E	h	512.73
211	134.66	E	h	320.22
212	134.73	E	h	323.36
213	135.57	E	h	112.11
214	135.68	E	h	107.51
215	136.45	A_1	h	53.50
216	136.78	A_1	h	21.35
217	138.24	E	h	296.66
218	138.31	E	h	292.81
219	138.95	E	h	18.89
220	139.04	E	h	14.06
221	140.79	A_2	h	215.77
222	140.93	A_2	h	206.47
223	141.45	A_1	h	71.19

Table 5.3: (continued)

ID	Energy (meV)	Symmetry (Mulliken)	Dominant Direction	Intensity (10^{-8} S/V)
224	142.81	A_2	h	81.41
225	142.92	E	h	4637.10
226	143.00	E	h	5050.88
227	143.92	B_2	h	908.89
228	144.08	E	h	1132.39
229	144.16	E	h	1051.70
230	144.54	E	h	171.04
231	144.58	E	h	156.25
232	144.61	E	h	126.90
233	145.83	E	h	983.25
234	145.87	E	h	1159.49
235	146.43	E	h	1163.05
236	146.47	E	h	1030.99
237	146.83	A_2	h	145.08
238	147.29	A_2	h	415.26
239	154.44	B_1	h	19307.37
240	155.24	B_2	h	3324.53
241	155.93	B_2	h	53.14
242	156.36	E	h	827.95
243	156.37	E	h	839.22
244	156.44	E	h	390.37
245	156.90	A_2	h	187.93
246	157.56	E	h	120.20
247	157.58	E	h	107.90
248	158.11	A_2	h	38.71
249	161.69	E	h	990.57
250	161.77	E	h	756.17
251	161.78	E	h	259.51
252	161.83	E	h	12.04
253	162.79	B_1	h	10083.63
254	163.46	E	h	43.90
255	167.01	A_1	h	269.48
256	167.59	A_1	h	32.73
257	173.42	E	h	775.85
258	173.43	E	h	805.29
259	173.55	A_1	h	24.12
260	173.58	E	h	414.89
261	173.62	E	h	288.06
262	174.17	E	h	103.64
263	174.24	E	h	87.02
264	174.26	E	h	82.05
265	174.97	E	h	13.26
266	175.00	E	h	415.10
267	175.01	E	h	61.50
268	175.47	E	h	710.48
269	175.86	E	h	95.62
270	176.03	E	h	10.37
271	177.11	A_1	h	132.37
272	177.46	A_1	h	0.02
273	180.99	E	h	425.00
274	181.01	E	h	467.34
275	181.43	A_2	h	44.86

Table 5.3: (continued)

ID	Energy (meV)	Symmetry (Mulliken)	Dominant Direction	Intensity (10^{-8} S/V)
276	181.53	B_1	h	2211.79
277	181.60	E	h	384.70
278	181.63	E	h	50.61
279	181.65	E	h	44.57
280	182.09	A_2	h	5.30
281	182.46	B_2	h	207.14
282	183.00	E	h	31.17
283	183.32	E	h	332.24
284	183.38	E	h	243.86
285	183.68	E	h	33.86
286	183.69	E	h	64.38
287	184.01	E	h	8923.23
288	184.12	E	h	7932.17
289	184.15	E	h	822.16
290	184.25	E	h	32.71
291	184.85	A_2	h	1591.26
292	184.97	A_2	h	19.98
293	186.13	A_1	h	71.30
294	186.40	A_1	h	13.36
295	197.79	B_1	h	47.61
296	197.86	E	h	45.13
297	197.92	E	h	33.68
298	198.06	A_1	h	32.23
299	198.81	B_1	h	0.83
300	198.89	E	h	1.08
301	198.91	E	h	1.10
302	199.08	A_2	h	8.40

5.4.5 Experimental Vibration Energies

Table 5.4: Experimental vibration energies. In Figure 5.12a of the main manuscript and in Figure 5.17a, a spectrum revealing a total of 46 inelastic excitations is shown. Here, we list the observed energies and estimated effective cross-sections η of the corresponding vibrational modes. Both were obtained by simulating the measured spectrum as described above. In addition, the assigned calculated modes are listed.

Energy (meV)	η (%)	Assigned calculated mode #	Energy (meV)	η (%)	Assigned calculated mode #
7.1	0.35	15-17	77.8	0.3	111-112
9.0	0.6	19-20	83.0	0.6	117-121
14.2	0.15	23-27	86.4	0.95	123-129
15.8	0.25	29-32	93.8	0.1	142-143
17.7	0.25	37-38	94.7	0.3	144-146
21.0	0.2	43-44	97.3	0.1	151-154
26.4	0.15	46-47	100.1	0.1	157-158
28.3	0.15	50	105.9	0.05	165-168
30.1	2.7	55-56	108.7	0.2	169-172
33.6	0.7	57-58	136.3	0.7	205-212
35.8	0.6	63	138.6	0.4	217-218
43.4	0.05	69	144.1	0.35	225-226
50.5	1.1	71-73	146.7	0.55	233-234
52.2	0.1	75-78	147.2	0.5	235-236
58.7	0.6	81-82	159.4	0.6	239-240
59.7	0.15	85-86	160.6	0.15	242-247
61.7	0.5	87-90	173.4	0.4	257-258
62.7	0.1	91-92	174.4	0.2	260-261
67.6	0.15	93-94	176.5	0.15	268
69.5	0.05	95-98	178.7	0.2	271
71.2	0.15	99-102	180.7	0.2	272-274
75.6	0.4	105-106	182.4	0.2	276-277
76.1	0.4	107-108	185.1	0.15	283-289

5.5 Mapping Vibrational Excitations

The enhanced sensitivity on vibrational modes in the STM allows me to laterally map the intensity of individual vibrational excitations across a molecule. Figure 5.24 shows maps of 20 different excitations, which were measured by two different techniques (I and II). In addition, displacement amplitudes of the assigned calculated modes are shown (III). Before the discussion of the observations, the measurement techniques are explained.

In the first measurement (I), a 16×16 grid of dI/dV spectra was taken on a PbPc↑ molecule of group A1. The grid covers an area of about $8\,\mathrm{nm} \times 8\,\mathrm{nm}$. Each spectrum spans a voltage range from $-200\,\mathrm{mV}$ to $200\,\mathrm{mV}$ in increments of $0.1\,\mathrm{mV}$ (4000 points per spectrum). The spectra were taken at a constant tip position, with the feedback loop opened before each spectrum with a setpoint of $I = 5\,\mathrm{nA}$ at a sample voltage of $V = 200\,\mathrm{mV}$. The voltage was modulated with an amplitude of $V_M = 0.5\,\mathrm{mV_{PP}}$ at a frequency of $f = 831\,\mathrm{Hz}$.
The intensity of the excitation peaks depends not only on the lateral distribution of the vibrational modes, but also on the intensity of the coherence/YSR peak (primary peak) in the respective spectrum. To correct for that effect, the measured heights of the excitation peaks above the spectral background have been divided by the height of the primary peak in the respective spectrum. The height of the primary peak essentially gives the YSR peak intensity as shown in Figure 5.3d. In this way, maps of the effective cross-section η are obtained.

The second measurement (II) is based on dI/dV maps taken at selected voltages on another PbPc↑ molecule of group A1. The scans were taken in constant-current mode at a setpoint of $I = 5\,\mathrm{nA}$ and a voltage modulation of $V_M = 0.5\,\mathrm{mV_{PP}}$ at a frequency of $f = 831\,\mathrm{Hz}$. To reduce the influence of the feedback loop inertia, a slow scan speed of $3\,\mathrm{nm\,s^{-1}}$ was chosen. Furthermore, I overlayed forward and backward scan and used an average value for the analysis. For each vibrational excitation, one dI/dV map was measured at the voltage of the excitation peak itself and an additional map was measured at a voltage smaller by $1\,\mathrm{mV}$ to obtain the background level. Figure 5.24II shows the quotient of peak to background measurements.

Especially the second technique based on constant-current dI/dV maps is vulnerable to topographic artifacts[63]. This effect probably explains the deviations observed between measurements (I) and (II) at small voltages (a, b and h). At higher voltages, however, the results of both techniques seem to be fairly consistent.

In addition to the experimental intensity maps, the absolute values of the displacement amplitudes of the assigned calculated modes are shown (III). Most excitations have been assigned to two or more modes (see Table 5.4), in which case, the mean value is taken.

For many excitations, distinct patterns are observed experimentally. Furthermore, there is some agreement with the calculated modes. In every case, where there is a significant displacement of the Pb atom, the highest intensity is also observed in the center of the molecule (a,b,d,h). In contrast, e. g., in (c) or (r), high intensity is observed on the lobes of the molecule, which corresponds to a high displacement of the atoms in the lobes. In (k), a ring like intensity pattern is observed, which matches the calculated distribution of the displacement amplitudes. However,

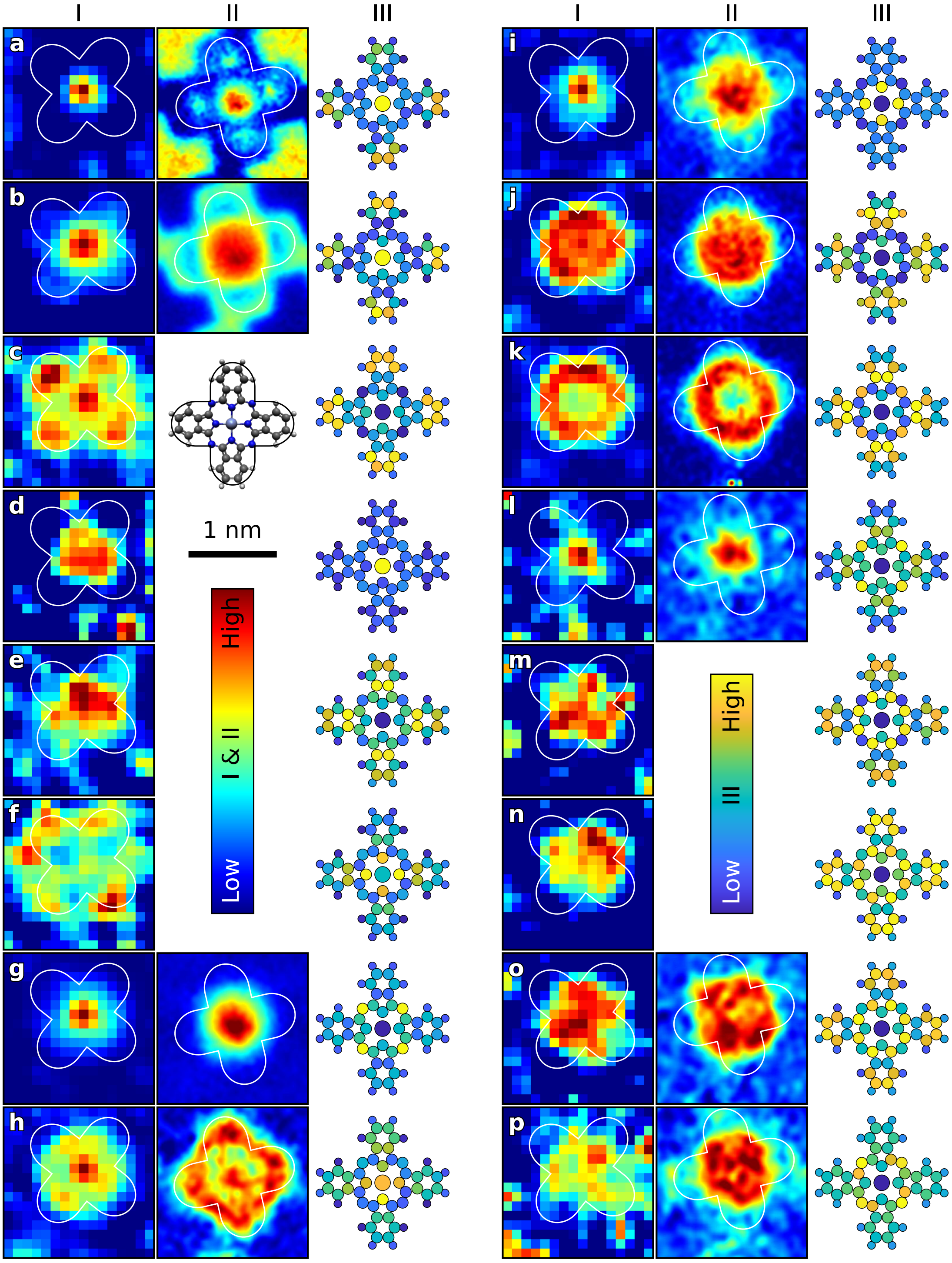
I
II
III
I
II
III
a
b
c
d
e
f
g
h
i
j
k
l
m
n
o
p
1 nm
High
I & II
Low
High
III
Low

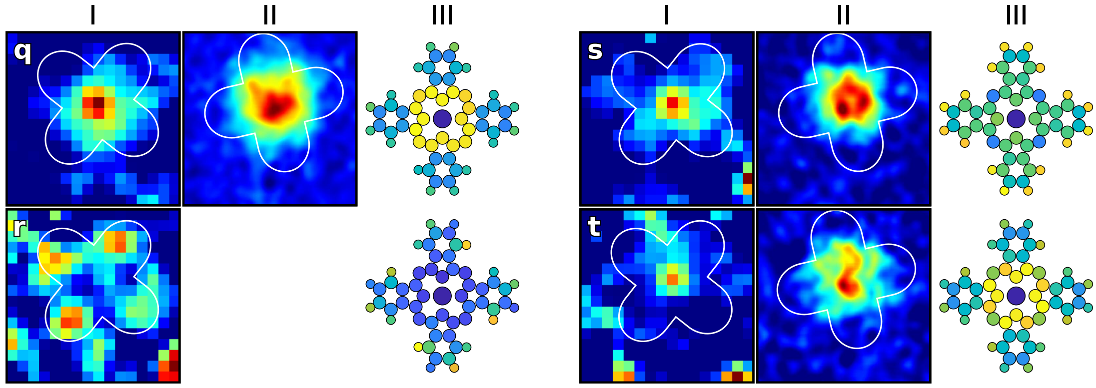

Figure 5.24: (a-t) Intensity maps of 20 different vibrational excitations. Two different measurement techniques have been used as detailed in the text: (I) a dI/dV grid measurement and (II) measurements of constant-current dI/dV maps at selected voltages. In (I) the intensities are normalized to the primary peak height, which is essentially the intensity of the YSR resonance. In (II) maps measured at the voltage of the excitation peak are divided by maps measured at a slightly smaller voltage. In this way, the relative height of the excitation peaks is obtained. All maps have been smoothed by Gaussian filters. The outline of the molecule is superimposed as a white line on each map. A scale depiction of a PbPc molecule with corresponding outline is shown in the center of the left page. The energies of the excitations in meV are as follows:

a	7.1	f	26.4	k	58.8	p	82.9
b	9.1	g	30.0	l	61.5	q	86.3
c	15.9	h	33.8	m	75.6	r	106.3
d	17.4	i	35.8	n	76.4	s	135.5
e	21.2	j	50.5	o	77.9	t	159.4

(III) Mean amplitudes of the displacement vectors for each atom of the assigned calculated modes. The displacement vectors were scaled by the square root of the atomic masses.

there is less agreement between the observed intensity pattern and the calculated displacements in other cases.

In conclusion, it has been demonstrated that YSR enhanced STM-IETS enables the measurement of the lateral distribution of vibrational excitations. Furthermore, there is some agreement with the calculation results. However, my evaluation of the calculated modes is rather simplistic and there is plenty of room for more sophisticated calculations to come.

5.6 Cluster Assembly

Single PbPc molecules can be moved on the Pb(100) substrate by manipulation with the STM tip, similar to H_2Pc. This technique allows the manual assembly of PbPc supramolecules in analogy to the H_2Pc supramolecules shown in Chapter 4. The following reports on the assembly of a 3 × 3 supramolecule and the observations thereby.

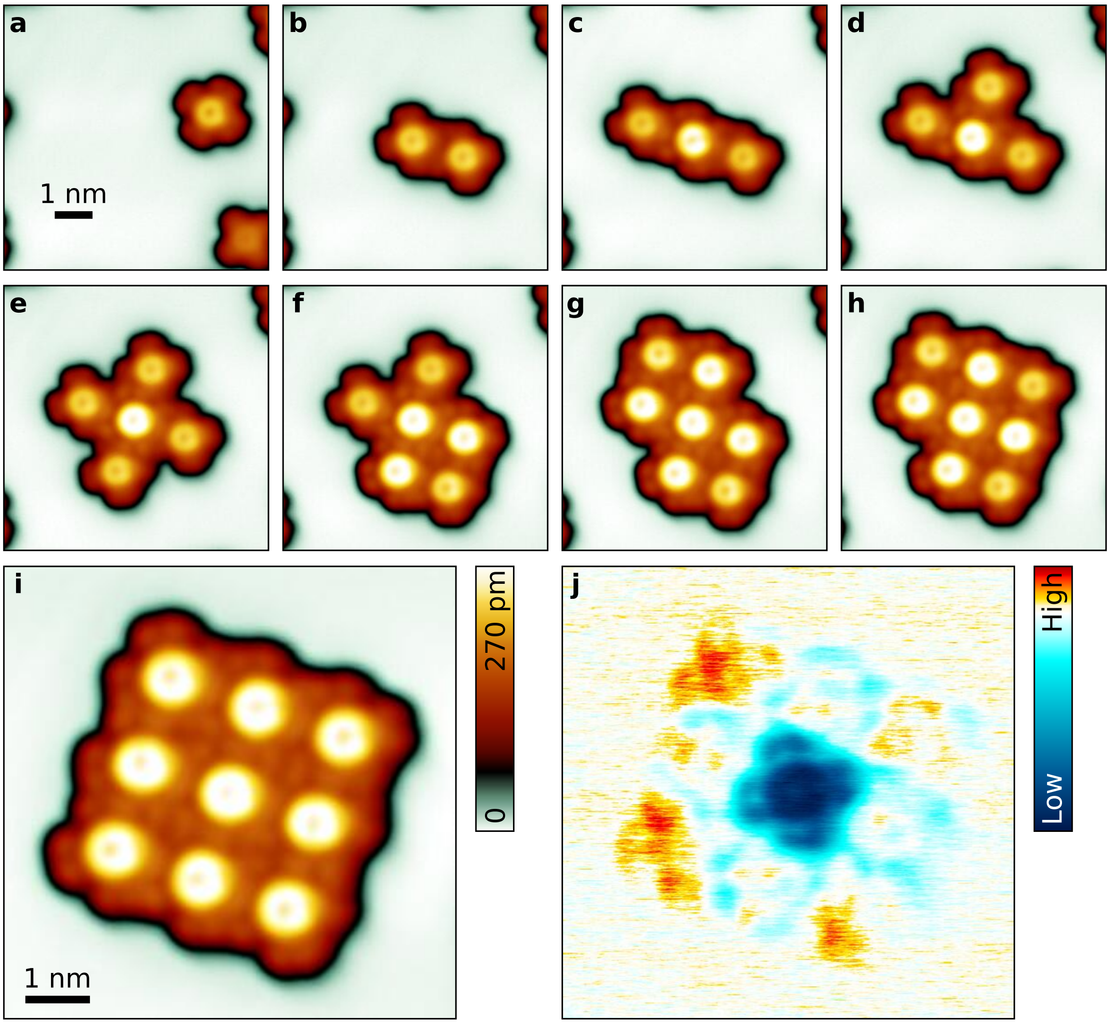

Figure 5.25: (a–i) Topographs of the step-wise assembly of a PbPc enneamer. The topographs were taken at a setpoint of $I = 50\,\text{pA}$ and a sample voltage of $V = -10\,\text{mV}$. (j) dI/dV map of the enneamer taken in constant-current mode with a setpoint of $I = 300\,\text{pA}$ at a sample voltage of $V = 2.6\,\text{mV}$. YSR states lead to a reduction of the differential conductance, since the voltage is very close to the coherence peak. A similar measurement is shown in Figure 5.6 and discussed in detail in the corresponding section.

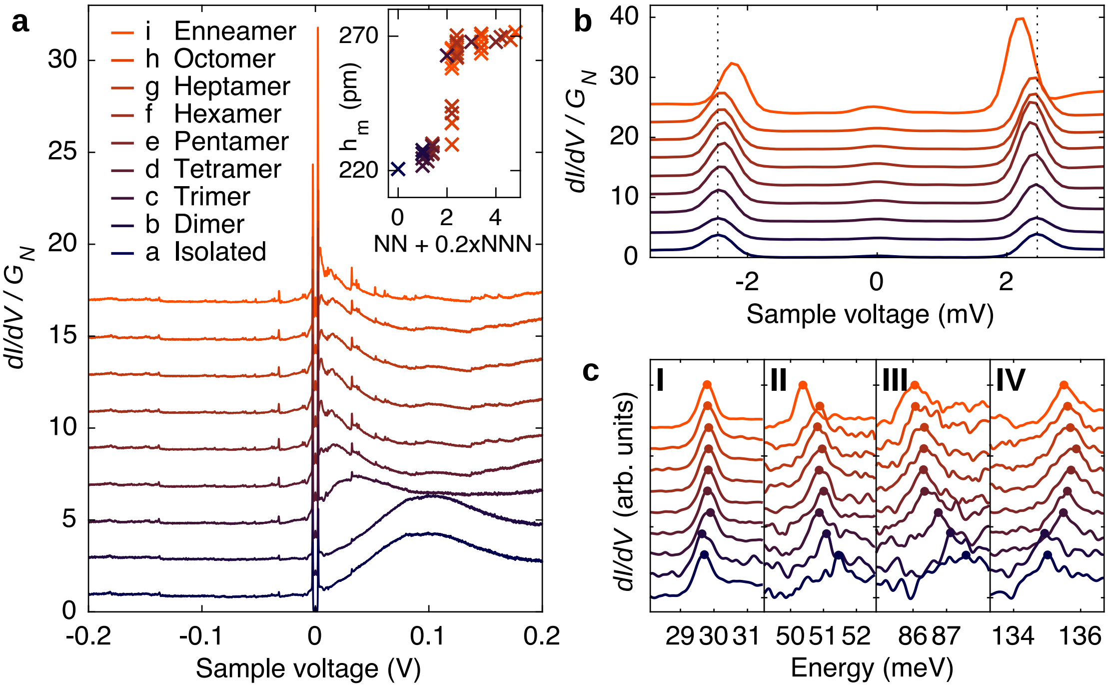

Figure 5.26: (a) dI/dV spectra taken on the central molecules of the assembled clusters shown in Figure 5.25 a-i. The spectra were taken at a fixed tip position ($I = 5\,\mathrm{nA}$, $V = 200\,\mathrm{mV}$) with a voltage modulation of $V_M = 0.5\,\mathrm{mV_{PP}}$ at a frequency of $f = 831\,\mathrm{Hz}$. The inset shows the maximal apparent height h_m of all the molecules measured at $V = -10\,\mathrm{mV}$ vs. the number of NN plus the number of NNN multiplied by 0.2. (b) Details of the spectra at small voltages, showing the superconducting gap and the emergence of YSR states. As a reference, the peak positions of the spectra measured on the isolated molecule (bottom curve) are marked by dotted vertical lines. (c) Peaks of four different vibrational excitations. The energy (x axis scale) is equal to the sample voltage minus the position of the coherence/YSR peak. The spectra in (c) are individually scaled to level up the peak heights. The spectra in (a–c) are shifted vertically by increments for clarity.

In Figure 5.25 topographs of the successive assembly of a supramolecule are shown (a to i). The geometry of the enneamer (i) is the same as for H_2Pc supramolecules of type A (Figure 4.11). Just like with H_2Pc, a YSR state emerges on the central molecule. A corresponding dI/dV map of the cluster (j) shows the lateral distribution of it. In contrast to the H_2Pc supramolecule however, the four molecules on the edges of the cluster also show weak signs of YSR states.

In Figure 5.26 dI/dV spectra are shown that were taken on the central molecule of the cluster at the single steps of assembly. The entire spectra are shown in (a), while (b) and (c) focus on selected sections of the same spectra. Various spectroscopic features have been observed as discussed in detail before.

In (a), LUMO resonances are visible positioned at ≈100 mV in the spectra taken on the isolated molecule and the dimer (bottom curves). On the trimer, the LUMO resonance is already shifted to ≈30 mV and on the subsequent supramolecules, it is located at even smaller voltages. The

inset shows the maximal apparent height h_m of all the molecules observed in the topographs shown in Figure 5.25 a to i vs. the number of NN plus the number of NNN multiplied by 0.2. The arbitrary factor of 0.2 accounts for the minor influence of NNN compared to NN. The apparent height rises from 220 pm for the isolated molecule to 270 pm for molecules surrounded by others. The height does not increase linearly with the number of NN, but instead a sudden jump of the apparent height is observed at NN = 2. The rise of the apparent height can be explained by the downshift of the LUMO. The threshold value of NN = 2 matches the observation of the LUMO energy, which is already close to the Fermi level for the central molecule of the trimer.
As shown in (b), YSR states arise meanwhile as evidenced from the decreasing peak energies and the emerging peak height asymmetry. While the spectra measured on the isolated molecule and the dimer (bottom curves) do not differ virtually, the spectrum on the trimer already shows YSR state specific characteristics. I therefore suspect that two neighbor molecules are sufficient to obtain YSR states on PbPc$\uparrow$ molecules on Pb(100).

In addition, vibrational excitations have been observed. Figure 5.26c shows the evolution of four selected excitation peaks upon cluster assembly. Some peaks, like the one at 30 meV (I), stay approximately at the same energy. Others, however, undergo an energy shift to smaller (II and III) or larger (IV) energies. The largest energy shifts are of the order of 1 meV and most of the shifts occur during the first steps of the assembly when the NN molecules are added. However, the peak at 51 meV (II) undergoes an additional abrupt shift to smaller energies at the very last construction step. Interestingly, the YSR characteristics got significantly more pronounced at the last construction step as well (Figure 5.26b). However, additional measurements are needed to show whether these effects are linked and reproducible.
The peaks at 51 meV (II) and 86 meV (III) have been assigned to vertical modes, while the peak at 135 meV (IV) has been assigned to horizontal modes. The observations suggest that vertical (horizontal) modes undergo a red (blue) shift when adding neighboring molecules. The same behavior was observed when approaching the STM tip to a molecule (Section 5.3). While the approaching STM tip stretches the molecule in the vertical direction, neighboring molecules may compress it horizontally. In both cases, the intramolecular bond lengths of the molecule are vertically increased and horizontally decreased leading to a red shift of vertical and a blue shift of horizontal modes, according to the Badger rule[235]. Furthermore, the molecule could be slightly lifted from the substrate due to intermolecular interaction, contributing to the increase in apparent height. However, almost the same amount of increase as on the central molecule was also observed on the edge and corner molecules, which renders a significant lift of the molecule in real space unlikely.

5.7 YSR Peak Heights

The sensitivity of YSR state enhanced IETS crucially depends on the relative height of the YSR resonances with respect to the normal state conductance. It is therefore desirable to obtain large YSR peak heights. To my knowledge, the reasons for different peak heights have not been systematically investigated to date. However, there are certain factors that are discussed in detail below.

First, the YSR states by themselves can have different intensities in the DOS of the sample. Such a YSR DOS $\rho_{\mathrm{YSR}}(E)$ can be modeled via the Bogoliubov-de Gennes (BdG) approach, as detailed in Section 2.3.3. The central parameters of the model are $\alpha = \pi\rho_0 JS$ and $\beta = \pi\rho_0 W$, where J and W are the exchange coupling and nonmagnetic scattering potential, respectively. ρ_0 is the normal-conducting DOS of the sample at the Fermi edge.
I have calculated $\rho_{\mathrm{YSR}}(E)$ for a wide range of parameters and obtained varying YSR peak heights and energies. Figure 5.27a shows the sum of the peak heights at positive and negative energy P_Σ vs. the reduced YSR energy $\tilde{E}_{\mathrm{YSR}}$. In fact, all data points lie on a single curve $P_\Sigma(\tilde{E}_{\mathrm{YSR}})$, which is fairly accurately reproduced by following equation:

$$P_\Sigma = P_{\Sigma,\Delta} + a \cdot \left(1 - \tilde{E}^2_{\mathrm{YSR}}\right)^{0.7}, \tag{5.56}$$

where $P_{\Sigma,\Delta}$ is the combined relative peak height for $E_{\mathrm{YSR}} = \pm\Delta$ and a is an arbitrary scaling factor. $P_{\Sigma,\Delta}$ is the minimal value and equal to the sum of the height of the coherence peaks. $P_\Sigma(\tilde{E}_{\mathrm{YSR}})$ increases for decreasing $|E_{\mathrm{YSR}}|$ and reaches its maximum at $E_{\mathrm{YSR}} = 0$.
The broadening of the peaks that is introduced by the Dynes' parameter Γ, leads to a scaling of the curve but does not change the qualitative progression.

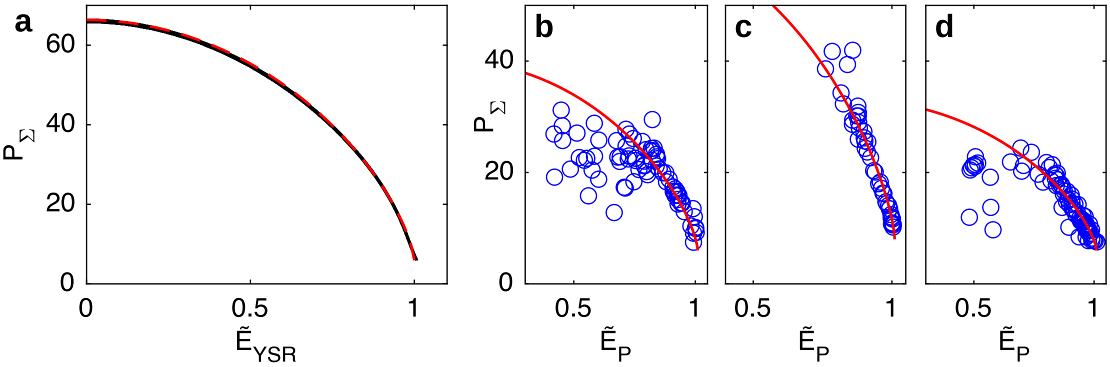

Figure 5.27: (a) Sum of YSR peak heights P_Σ with respect to the reduced YSR energy $\tilde{E}_{\mathrm{YSR}} = E_{\mathrm{YSR}}/\Delta$. YSR density of states have been calculated via the BdG approach for a wide range of parameters ($0.03 < \rho_0 JS < 3.1$ and $-0.5 < \rho_0 W < 0.5$). The combined relative height of the YSR peaks has been plotted as a black curve. It only depends on the YSR energy E_{YSR} and follows approximately Equation 5.56 (dashed red line). (b–d) Observed sum of peak heights P_Σ vs. the reduced peak energy $\tilde{E}_{\mathrm{P}}$ for three different data sets. For each data set, only spectra measured on PbPc↑ molecules at similar conductance and instrumental broadening are considered. The red curves are fits according to Equation 5.56.

When evaluating the experimental data, it must be considered that other parameters influence the peak heights. In particular the electronic and instrumental broadening and the junction conductance play a role. Therefore, I have limited my analysis to data sets where these parameters have similar values. Figure 5.27b-d shows plots of the sum of the peak heights P_Σ observed in dI/dV spectra vs. the peak energy $\tilde{E}_\mathrm{P}$ for three different data sets. In all three cases, the data points mostly follow the progression described by Equation 5.27 as indicated by the red curves. Higher YSR peaks are generally observed at smaller YSR energies. However, the peak heights tend to spread at smaller YSR energies, which suggests that there is another parameter influencing the peak heights, which has not been identified yet.

Another parameter that has direct impact on the YSR peak heights in dI/dV spectra is the distribution of the tunneling current to different transmission channels. In general, there are multiple transmission channels from tip to substrate and not all of them involve the molecular orbital carrying the YSR state, but instead can go directly into the substrate or via other molecular orbitals. Such *current leakage* will lower the YSR peak heights. This interrelation may be one of the reasons for the large YSR peak heights observed in PbPc: Nearly all of the tunneling current flows via the LUMO of PbPc carrying the YSR state.

Lastly, the instrumental and electronic broadening of the dI/dV spectra has a significant influence on the YSR peak heights. At higher energy resolution, much larger peak heights can be observed. E. g., coherence peak heights of up to $16\,G_N$ have been reported in Pb-Pb junctions at $0.3\,\mathrm{K}$[236]. I therefore tried to improve the energy resolution of the experimental setups and set the voltage modulation for the lock-in measurements as small as possible. The sensitivity of YSR enhanced IETS experiments, however, does not only depend on the YSR peak heights, but also on the signal to noise ratio. In this regard, a higher modulation amplitude is beneficial. In the end a compromise must be made, which is why I chose a relatively high modulation voltage of $V_M = 0.5\,\mathrm{mV_{PP}}$ for most of my IETS measurements of molecular vibrations.

5.8 (De-)Metallation

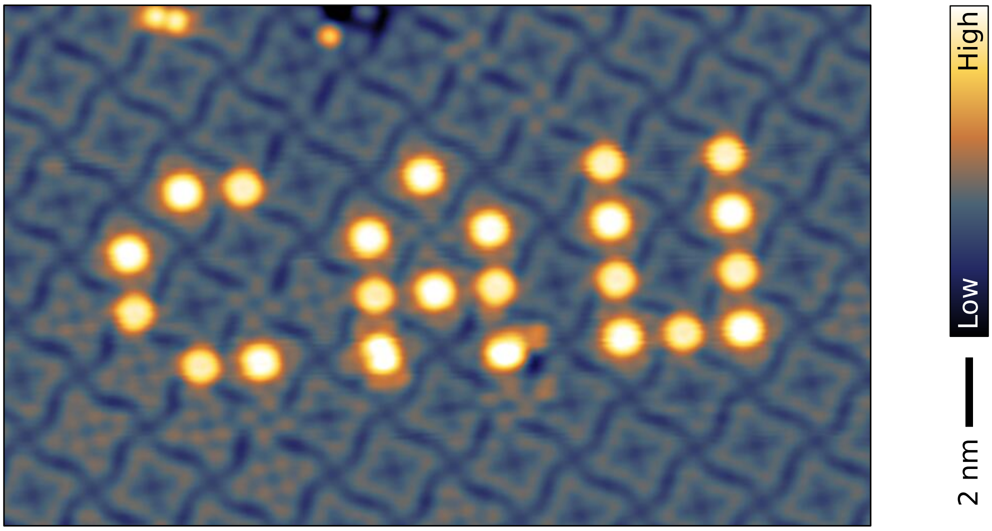

Figure 5.28: Topograph ($I = 55\,\mathrm{pA}$, $V = 10\,\mathrm{mV}$) of an artificial structure made by single molecule manipulation. The letters 'CAU' have been written by deliberately (de-)metallizing single H_0Pc (PbPc) molecules in an ordered layer. The PbPc↑ molecules have different apparent heights as those of group B1 appear slightly higher than those of group B2.

As already shown by Alexander Sperl, single PbPc (H_0Pc) molecules can be deliberately demetallized (metallized) by manipulation with the STM tip[56,57]. I succeed in reproducing this technique and utilized it, e. g., to investigate the dependence of vibrational modes on different neighboring molecules (see Figure 5.19).

To demetallize (metallize) a PbPc (H_0Pc) molecule, the STM tip has to be positioned centrally above the molecule. Then, the sample voltage is set to $2\,\mathrm{V}$ ($-1\,\mathrm{V}$) and the tip is brought closer to the molecule until a sudden drop in the tunneling current is observed, which typically happens at a maximal current of about $200\,\mathrm{nA}$ ($3\,\mu\mathrm{A}$).

To demonstrate the reliability of this manipulation technique, the letters 'CAU' have been written by (de-)metallizing multiple molecules in an ordered island as shown in Figure 5.28.

5.8.1 Manipulation of the STM Tip

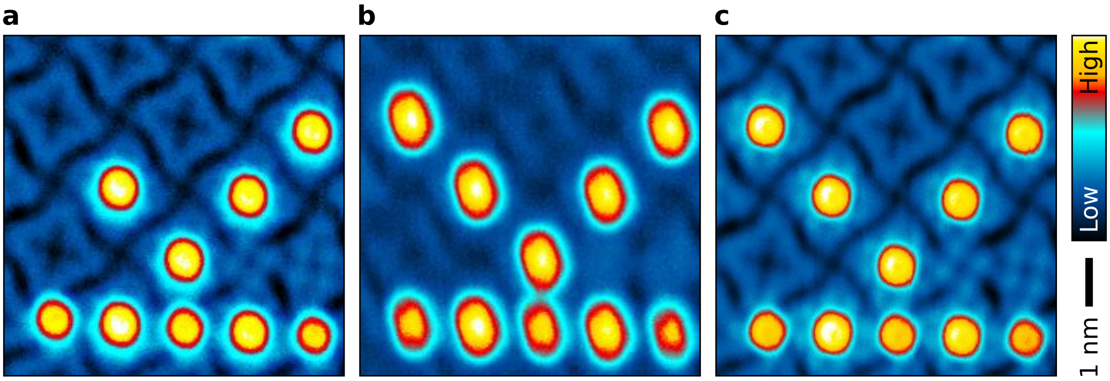

Figure 5.29: (a–b) Three consecutive topographs of the same sample area measured at $I = 70\,\mathrm{pA}$ and $V = 100\,\mathrm{mV}$. In between (a) and (b), a molecule in the top left corner was metallized. During that process the foremost Pb atom was removed from the STM tip, resulting in a presumably three-atomic tip (b). In between (b) and (c), a PbPc molecule outside of the scan area was demetallized. The additional Pb atom leads back to a one-atomic tip, as demonstrated by the high resolution in (c).

This manipulation technique does not only allow the manipulation of single molecules, it can also be used to add or remove single Pb atoms to/from the STM tip. In this way, STM tips with different apex configurations can be produced.

Such a tip manipulation is shown in Figure 5.29, where three consecutive topographs of the same spot on a domain B are displayed. The first topograph (Figure 5.29a) was taken with a one-atomic tip, as can be seen from the sharp resolution of the molecules. After metallizing a molecule in the top right corner, and thus removing the foremost Pb atom from the tip, the resolution deteriorates significantly (Figure 5.29b). The Pb atoms of the PbPc↑ molecules appear blurred and seem to have a triangular or trapezoidal shape, which presumably indicates a three-atomic tip. After adding another Pb atom by demetallizing a PbPc molecule outside of the scan area, a one-atomic tip was obtained again as demonstrated by the restored resolution in the final topograph (Figure 5.29c).

In conclusion, the system of PbPc on Pb(100) is perfectly suited to manipulate Pb tips atom by atom. Especially for contact experiments, e. g. shot-noise experiments[237], it might be interesting to use different tip geometries.

5.9 STS of Molecular Orbitals

Figure 5.30 shows dI/dV spectra taken on three types of molecules (PbPc↑, PbPc↓, and H_0Pc) within an ordered island of type A. Multiple resonances are observed, which we attribute to molecular orbitals. As already shown, the LUMO of PbPc↑ molecules inside ordered islands is very close to the Fermi level. Thus, it cannot be seen in the present measurement (a), as the interval between ±100 mV is skipped because of the measurement technique. On PbPc↓ and H_0Pc (b and c) however, LUMO resonances are observed at approximately 300 mV and 180 mV, respectively. Three additional peaks are observed on all three molecules, which I attribute to LUMO+1 to LUMO+3. At negative sample voltages, a peak was only observed on PbPc↑, which I attribute to its HOMO. The HOMO of (metal-)phthalocyanines has almost always the same four-fold symmetric shape with no intensity in the center of the molecule[213, 238, 239] where

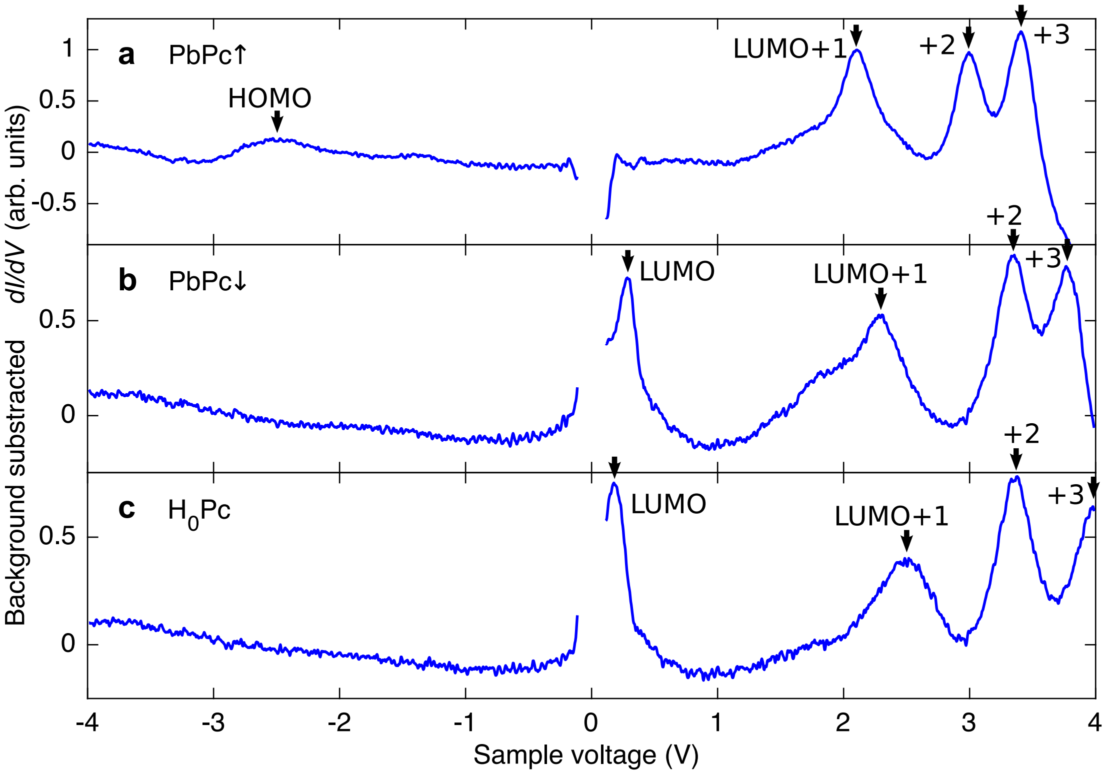

Figure 5.30: dI/dV spectra measured in constant-current mode with the tip positioned above (a) a PbPc↑, (b) a PbPc↓, and (c) an H_0Pc molecule inside an ordered island of domain A. Spectra at positive and negative sample voltage were taken separately, starting at $V = \pm 100\,\mathrm{mV}$ and with a setpoint of $I = 76\,\mathrm{pA}$. The sample voltage was modulated with an amplitude of $V_M = 14.1\,\mathrm{mV_{PP}}$ at a frequency of $f = 862.7\,\mathrm{Hz}$. A reference spectrum taken on the Pb(100) substrate has been subtracted. There are multiple resonances observable at positive sample voltage (marked by arrows), which I attribute to unoccupied molecular orbitals. In addition, there is a small peak observable at negative sample voltage on PbPc↑, which might correspond to the HOMO.

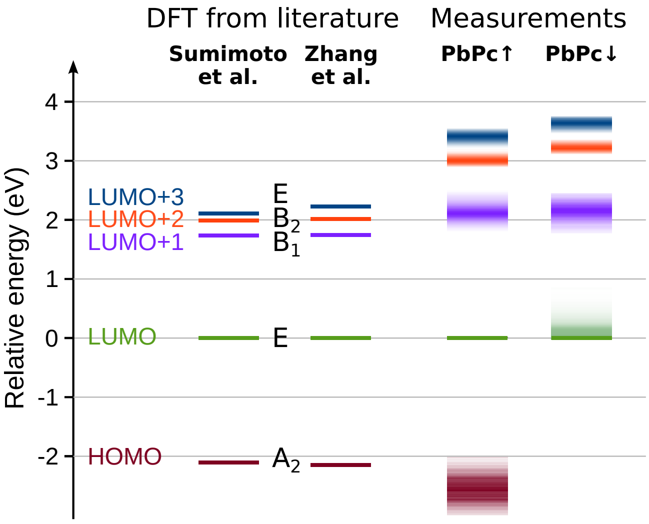

Figure 5.31: Comparison of the energies of the PbPc molecular orbitals from experiment to DFT results from literature. The relative energies with regard to the LUMO are shown. For the PbPc↑ I assume a LUMO energy of 0 meV. The calculated orbital energies are taken from References 242 (Sumimoto et al., 2012) and 243 (Zhang et al., 2006).

the spectra were recorded, which hampers its detection. Furthermore, spectral features of the sample are more pronounced at positive sample voltages in general[240, 241], which may also contribute to the fact that HOMO resonances were hardly observed.

Orbital	PbPc↑	PbPc↓	H_0Pc
LUMO+3	3.4	3.8	≥4.0
LUMO+2	3.0	3.3	3.4
LUMO+1	2.1	2.3	2.5
LUMO	0*	0.3	0.2
HOMO	-2.5		

Table 5.5: Energies of the molecular orbitals as derived from the STS measurements shown in Figure 5.30. The energies are given in eV relative to the Fermi energy.
*As shown before, the LUMO of PbPc↑ is very close to the Fermi energy.

The energies of all observed orbitals are listed in Table 5.5. The orbital energies of the three molecules are similar. On PbPc↑, however, all observed orbitals appear to be shifted to smaller energies by approximately 0.3 eV compared to PbPc↓. First, this observation fits to the fact that YSR states are only observed on PbPc↑ molecules, since the LUMO needs to be at the Fermi edge to be partially filled. Secondly, the rigid shift is compatible to electrostatic intermolecular interaction, which is claimed to be the underlying mechanism in the case of H_2Pc (see Section 4.2.2). The electrostatic quadrupole or dipole field of neighboring molecules would affect all molecular orbitals similarly. As already stated earlier, I assume that essentially the same interaction is responsible for the shift of the LUMO of PbPc.

DFT calculation results of the orbital energies of PbPc have been published in References 242 and 243. Figure 5.31 shows a comparison of these results to my measurements. Although the proportions of the energetic differences of the orbitals are similar, my measurements indicate significantly higher energies for the higher unoccupied orbitals. There are various possible explanations for this discrepancy. First, it is known that DFT calculations do not perform very well in determining energies of unoccupied states. Band gaps of semiconductors for example are gravely underestimated by many DFT calculations[244]. Secondly, the calculations were performed for molecules in gasphase. The orbital energies of adsorbed molecules might differ because of the contact to the substrate. Finally, the experimental values could be distorted by a voltage divider effect. Part of the voltage bias between tip and sample could already drop between substrate and molecule, which would lead to seemingly larger energetic differences among the orbitals.

Chapter 6
Conclusion and Outlook

H_2Pc and PbPc molecules on Pb(100) have been studied with STM. Both molecules are originally diamagnetic, but acquire a net magnetic moment upon cluster assembly or within self-assembled islands. This effect has been uncovered via the observation of YSR states. Furthermore, an energy shift of the LUMO of respective molecules down to the Fermi level was observed. Consequently, the magnetic moment is explained by a partial filling of this orbital. This claim is supported by the observed lateral distribution of the YSR states, which follows the distribution of the LUMO. As shown in Appendix A.2, AlPc molecules on Pb(100) behave very similar, which indicates that this phenomenon is rather general for (metal-)phthalocyanines on Pb(100). It was the first time that YSR states have been observed on originally diamagnetic molecules. Furthermore, it has been demonstrated that a magnetic moment of less than $0.1\,\mu_B$ is sufficient for this effect. Consequently, our findings open the route to a new class of YSR impurities.
The detailed analysis of the YSR and LUMO energies on different molecules allowed insight into the intermolecular interactions. Supported by DFT calculations and development of a phenomenological model, it has been shown that electrostatic interaction plays a significant role while hybridization between the molecules is negligible. Our findings furthermore stimulated the development of an Anderson impurity model based on the BdG approach[200] (see Section 4.1.3). Its application to other YSR impurities may lead to a better understanding of such systems.
The electrostatic quadrupole moment of single H_2Pc molecules was switched by targeted tautomerization, which allowed the fine tuning of the magnetic moments of neighboring molecules. Since this effect is well understood and highly controllable, it lends itself to the study of other molecules, e. g., by co-adsorption with H_2Pc. Appendix A.1 shows measurements on a yet unidentified molecule, i. e. molecule X (MX), which forms self-assembled supramolecules in combination with H_2Pc. Such single MX surrounded by eight H_2Pc molecules show multiple YSR states. It might be interesting to reproduce these supramolecules and study the effect of different H_2Pc tautomer configurations on the central molecule.
PbPc molecules posses a dipole moment depending on their vertical orientation. As demonstrated by our analysis, the resulting electrostatic field presumably has an effect on neighbor molecules similar to the quadrupole moment of H_2Pc. While the vertical orientation of PbPc molecules cannot be switched, SnPc molecules – which exhibit a similar non-planar structure – can[210–212]. Therefore, SnPc on Pb(100) seems to be an interesting system for future investigations.

The YSR resonances observed on PbPc have been utilized to measure vibrational excitations of the molecules. This new technique of YSR enhanced IETS offers a significantly higher sensitivity compared to earlier STM measurements of vibrational excitations. 46 different vibrational excitations have been observed on single molecules and compared to results from on-surface DFT calculations. While good agreement was found for the energies of the modes, their respective intensities could not be explained. Similar vibrational measurements on AlPc are shown in Appendix A.2 in comparison to PbPc, which demonstrate that small differences between the molecules may have a huge impact on the effective cross sections of vibrational modes. YSR enhanced IETS is a very suitable tool to further study these dependencies.

The high energy resolution of our measurements enabled us to observe small changes of the mode energies of less than 1 meV. Such energy shifts have been observed upon tip approach, in dependency of different neighbor molecules, and with increasing number of neighbor molecules. While the presented analysis is limited to a few simple correlations, detailed investigations on these dependencies may be a subject for future studies.

Furthermore, the high sensitivity allowed us to laterally map vibrational modes. Some similarities to the assigned calculated modes have been identified. However, the factors that influence the observed patterns of the modes remain puzzling and need to be investigated in further studies.

An important prerequisite for the success of YSR enhanced IETS are large relative heights of the YSR resonances. Although some reasons for different heights have been identified, this subject needs more investigation. Our latest analysis suggests that, in addition to the peak heights, the life time of the YSR excitation might play an important role with respect to the IETS sensitivity.

To take YSR enhanced IETS even further, it would be desirable to have YSR states on the tip of the STM. This configuration would allow for the investigation of non-magnetic, i. e. diamagnetic, molecules. In Appendix A.3, measurements on MnPc molecules are shown, which I tried to demetallize with the STM tip. However, instead of demetallizing the molecules, I picked them up, which nevertheless resulted in a YSR tip. To prevent interference of the IETS measurement by vibrational excitations of the molecule on the tip, a single atom YSR impurity would be preferable. Such a single-atom YSR tip has recently be achieved by others[44]. Its application to IETS will be an interesting subject.

Due to the properties of YSR resonances – like spectral intensity and sharpness, perfect spin polarization, etc. – YSR tips are a promising probe also for other phenomena. Recently it has been shown, that such tips can be used for spin-polarization measurements[44], detection of spin alignment[29], determination of lifetimes[38], or as probe for the superconducting phase[156]. Other applications may follow.

In the following appendices, first, measurements on further molecules, i. e. MX, AlPc, and MnPc, are presented (Appendix A). Afterward, the investigation of a Au-Pb surface layer is shown (Appendix B); followed by a self-derived method for deconvoluting measured dI/dV spectra and determining the intrinsic peak height asymmetry (Appendix C). Finally, the construction, test, and redesign of a NEG pump is presented (Appendix D).

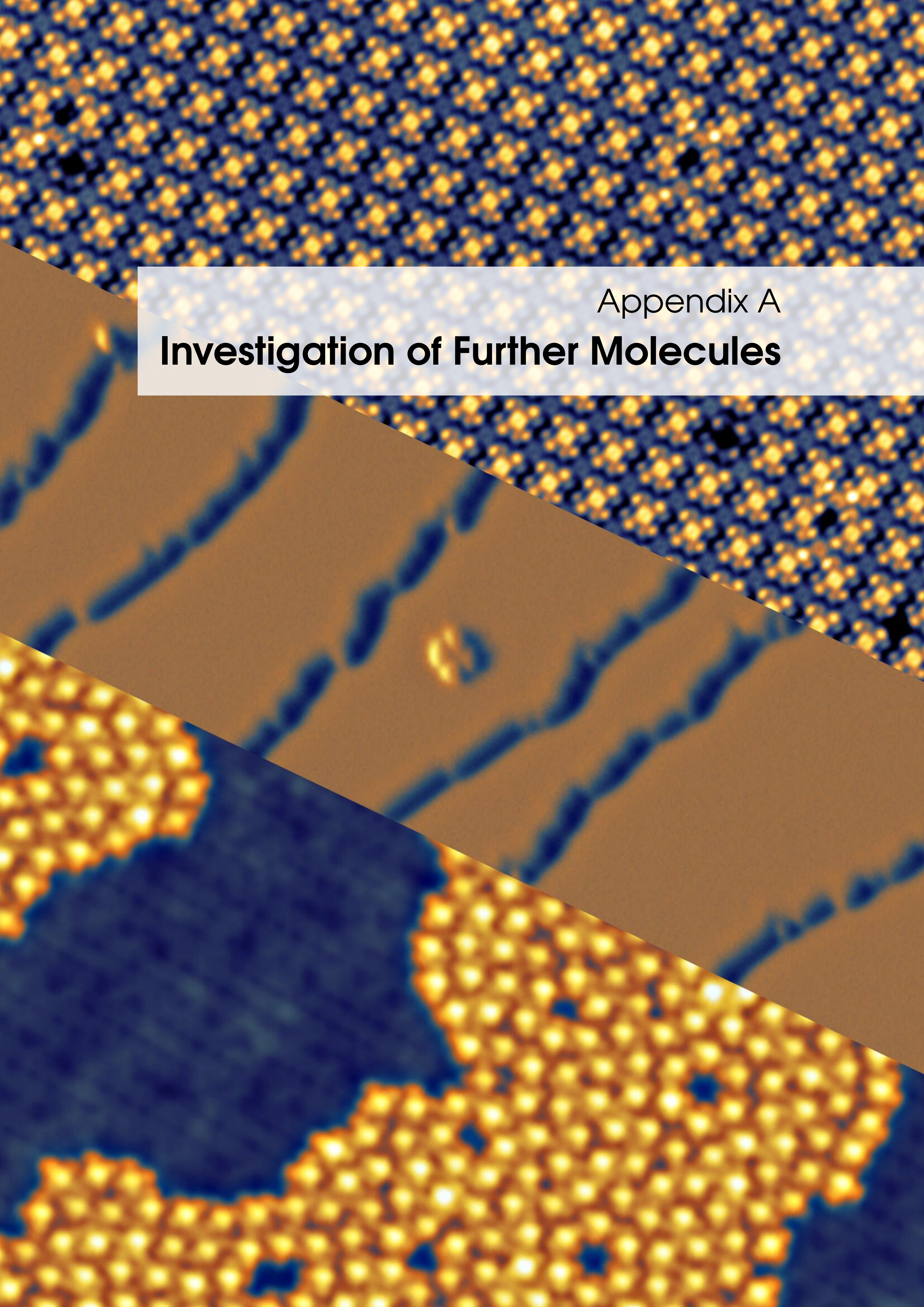

Appendix A

Investigation of Further Molecules

Previous page:
Topographs of three different samples. From top to bottom: I: Monolayer of AlPc molecules on Pb(100) ($I = 50\,\mathrm{pA}$, $V = 200\,\mathrm{mV}$). II: Single molecule X on Pb(100) with several step edges ($I = 55\,\mathrm{pA}$, $V = 273\,\mathrm{mV}$). The tunneling current is shown instead of the z position of the tip. III: MnPc molecules on a Au-Pb surface ($I = 100\,\mathrm{pA}$, $V = 100\,\mathrm{mV}$). All three topographs are shown at the same scale of about 37 nm in width.

A.1 Molecule X: Investigation of an Unknown Molecule

During studies of the free Pb(100) substrate in the *4K* setup I discovered an unknown molecule that was adsorbed on the surface. As it turned out, this molecule exhibits distinct YSR states and therefore attracted my particular interest. In contrast to H_2Pc and PbPc, even multiple YSR states have been observed on single molecules. Those individual states furthermore have a different lateral distribution as shown by dI/dV maps.

For convenience I will refer to the molecule as molecule X (MX). The measurements on MX are the oldest measurements presented in this thesis and inspired many of the later studies.

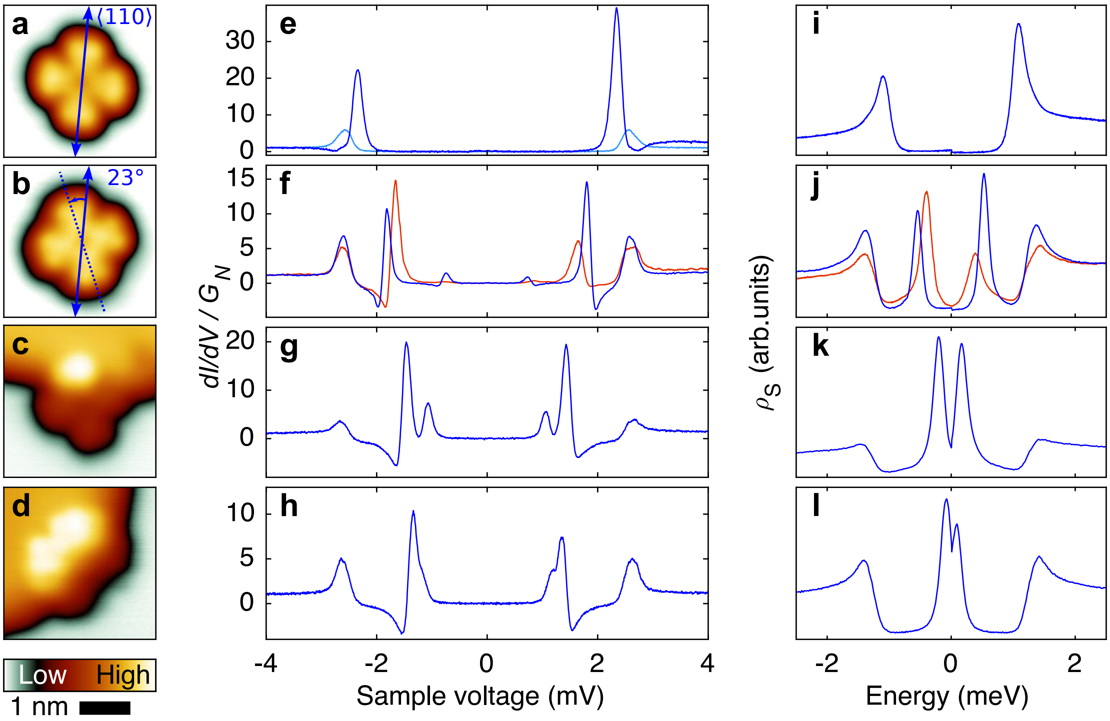

Figure A.1: (a–d) Topographs of four different MXs on Pb(100), measured at $V = 100\,\mathrm{mV}$ (a,b), $200\,\mathrm{mV}$ (c), and $600\,\mathrm{mV}$ (d) at a setpoint of $I \approx 80\,\mathrm{pA}$. While the molecule in (a) is oriented along the ⟨110⟩ surface direction, the molecule in (b) is rotated by 23° with respect to it. The molecules in (c,d) are lying across a Pb(100) step edge. (e–f) dI/dV spectra taken on the respective molecules. The spectra were taken at constant tip position [$I = 200\,\mathrm{pA}$, $V = 10\,\mathrm{mV}$ (e,f); $I = 100\,\mathrm{pA}$, $V = 6\,\mathrm{mV}$ (g,h)] with a modulation amplitude of $V_M = 113\,\mathrm{mV_{PP}}$ at a frequency of $f = 1164.2\,\mathrm{Hz}$ [$f = 1154.4\,\mathrm{Hz}$ for blue curve in (f)]. A spectrum measured on the Pb(100) substrate is shown as a light blue curve in (e) for comparison. The red curve in (f) was measured on the same molecule as the blue curve, but at a slightly different position. (i–l) Corresponding deconvolved DOSs $\rho_S(E)$ of the sample. The procedure to obtain $\rho_S(E)$ from the dI/dV spectra is detailed in Appendix C.

A.1.1 YSR States on Single Molecules

Figure A.1 shows topographs and dI/dV spectra taken on different MX on Pb(100). Single MX were found on the freshly prepared Pb(100) surface, often in the middle of atomically flat terraces of the substrate (a,b). Other molecules were found to lie across step edges (c,d). The placement of the molecules suggests that they are strongly bound to the substrate and do not diffuse during sample preparation. Otherwise, I would expect that they accumulate at step edges as was observed, e. g., for H_2Pc or PbPc on Pb(100).

YSR states were found on all of the X molecules. Most of them were oriented along the $\langle 110 \rangle$ surface direction (a) and showed YSR resonances close to the gap edges (e). However, I also found molecules that were rotated by approximately 23° with respect to that direction (b). Those molecules showed YSR resonances well within the gap (f). It seems that the different orientation alters the coupling to the substrate and thus leads to a lower YSR energy. Even lower YSR energies were observed on MX on step edges (g,h).

The peak height asymmetry varies significantly as illustrated by the corresponding sample DOSs shown in Figure A.1i–l. An inverted peak height asymmetry – as observed, e. g., in (l) compared to (i) – points toward a possible quantum phase transition. However, the situation is more intricate: While a single YSR state with essentially the same peak height asymmetry was observed across most of the molecules, the rotated molecule (b) exhibits YSR states with different energies and inverted asymmetries (f,j). This peculiarity is further illuminated by dI/dV maps presented below.

A.1.2 Mapping of YSR States

Figure A.2 shows topographs and dI/dV maps of two MX. The molecule shown in (a) is oriented along the $\langle 110 \rangle$ direction, while the molecule shown in (c) is rotated by 23°. A constant-current dI/dV map of the first molecule is presented in (b). It shows the lateral distribution of the YSR state since it was measured just outside the coherence peak ($V = 2.65\,\mathrm{mV}$), where the YSR resonances lead to a reduction of the differential conductance. Here, the YSR state is fourfold rotational and mirror symmetric and strongest on the lobes of the molecule, where even negative differential conductance is observed (purple area).

In (d,e) constant-height dI/dV maps are shown that were measured on the other molecule and within the superconducting gap, i. e. at $V = 2.20\,\mathrm{mV}$ and $2.05\,\mathrm{mV}$, respectively. The distribution of the negative differential conductance shown in (d) is quite similar to that of the reduced conductance in (b). In (d), however, the distribution of the YSR state is no longer mirror symmetric. This effect is caused by the rotation of the molecule with respect to the high symmetry direction of the substrate, which renders the system chiral.

On top of that, YSR states at different energies become visible. This phenomenon is demonstrated by the dI/dV map shown in (e). While a negative differential conductance is observed on most parts of the molecule (blue area), a positive differential conductance is eminent at one side of the lobes where the lowest negative differential conductance has been observed in (d). This observation is explained by the presence of an additional YSR resonance at slightly higher energy. The molecule does not only exhibit YSR states at different energies – as was already

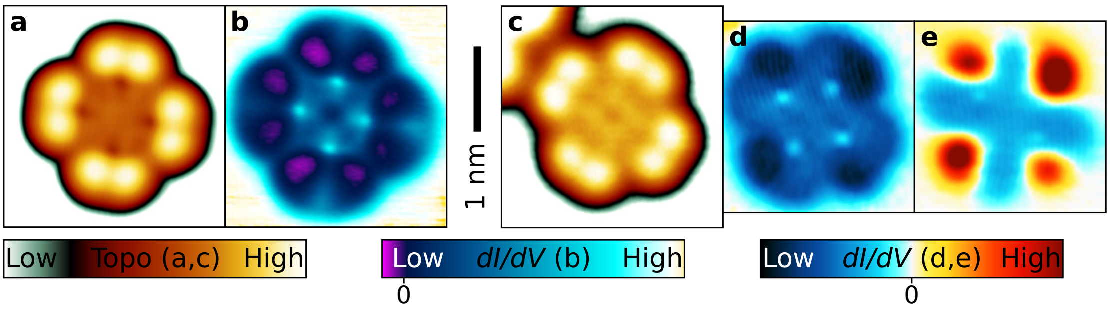

Figure A.2: (a) Topograph of a symmetrically aligned MX measured at $I = 102\,\text{pA}$ and $V = 2.65\,\text{mV}$. (b) Constant-current dI/dV map of the same molecule, measured simultaneously with (a). (c) Topograph of a rotated MX measured at $I = 93\,\text{pA}$ and $V = 10\,\text{mV}$. (d,e) Constant-height dI/dV maps of the same molecule, measured at $V = 2.20\,\text{mV}$ and $2.05\,\text{mV}$, respectively. All dI/dV maps were measured with a modulation amplitude of $V_M = 113\,\text{mV}_{\text{PP}}$ at a frequency of $f = 1164.2\,\text{Hz}$.

shown by dI/dV spectra (Figure A.1f) –, but those YSR states furthermore have different lateral distributions.

Multiple YSR states with varying lateral distributions were observed before and have been linked to different orbitals of the impurity[30,39,40]. Therefore, a possible explanation is that MX is presumably a MPc molecule whose LUMO is doubly degenerate in the gasphase and becomes partially filled and thus carries the YSR state. Here, however, it is somewhat hybridized with the substrate because of covalent bonding. In the case of the symmetrically aligned molecule, this hybrid orbital stays degenerate and a fourfold mirror symmetry is observed with a single YSR energy. In the chiral case of the rotated molecule, however, the degeneracy is presumably lifted with the result of two separate orbitals that both carry a YSR state but at slightly different energies. The lift of degeneracy could be explained by a bridge-site adsorption of the rotated MX.

A.1.3 Self-Assembled Molecular Clusters

As a next step, I evaporated H_2Pc molecules onto the Pb(100) crystal. The idea was to have a known phthalocyanine molecule side by side with the MX for direct comparison. Most of the H_2Pc molecules formed ordered islands at the step edges of the substrate (not shown). In addition I made a surprising observation: The self-assembly of 3×3 clusters, where eight H_2Pc molecules attach to a single MX.

Figure A.3 shows measured data of such clusters. An overview topograph of a single Pb(100) terrace with several clusters is shown in (a), while the topograph of a single cluster is shown in (b). The geometry of the molecule arrangement is similar to that of the H_2Pc enneamers of type C (see Figure 4.11). Both handednesses of chiral clusters are present in the overview (a), which explains the apparent different orientations of the clusters.

Figure A.3c shows a dI/dV map of the single cluster, where the signature of YSR states is clearly visible on the central MX (blue area). Its distribution is very similar to that of the isolated MX

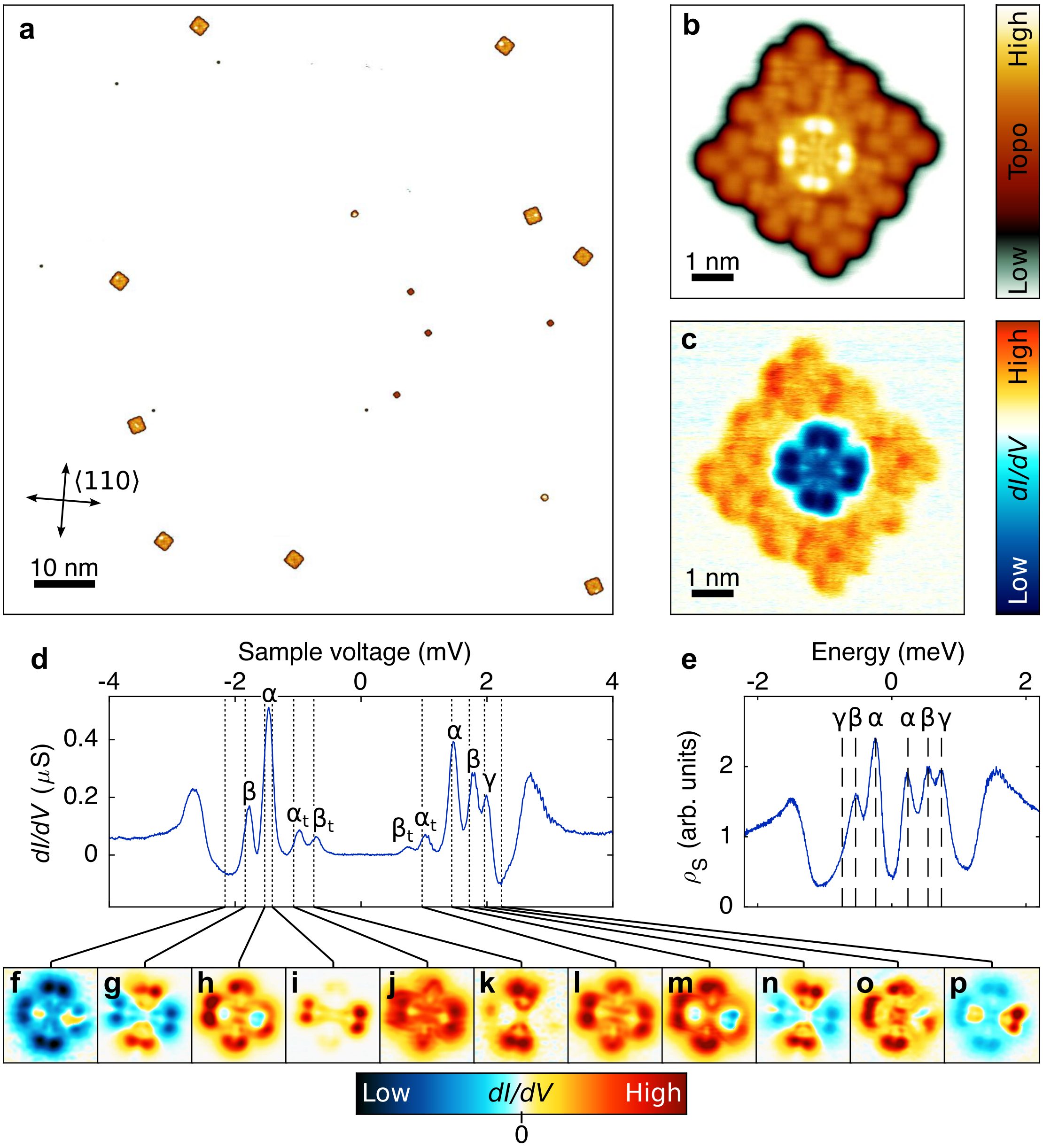

Figure A.3: (a) Overview topograph of an atomically flat Pb(100) terrace with several self-assembled $(H_2Pc)_8MX$ clusters on it. It was measured at a setpoint of $I = 140\,\mathrm{pA}$ and a sample voltage of $V = 289\,\mathrm{mV}$. (b) Topograph of a single cluster measured at $I = 205\,\mathrm{pA}$ and $V = 2.7\,\mathrm{mV}$. (c) Simultaneously measured dI/dV map of the cluster. A reduction of the differential conductance (blue area) indicates the YSR states on the MX in the center. (d) dI/dV spectrum taken on the top lobe of the MX showing several in gap peaks. The spectrum was measured at constant tip position with $I = 400\,\mathrm{pA}$ at $V = 5\,\mathrm{mV}$. (e) Deconvolved sample DOS, which exhibits YSR resonances at at least three different energies (marked by dashed vertical lines and labeled *alpha* to *gamma*). (f–p) Constant-height dI/dV maps of the MX measured at different voltages as indicated by dotted vertical lines in (d). All dI/dV measurements were taken with a modulation amplitude of $V_M = 113\,\mu\mathrm{V_{PP}}$ at a frequency of $f = 1164.2\,\mathrm{Hz}$.

observed before (Figure A.2b). On the MX in the cluster, however, multiple YSR states are present as revealed by dI/dV measurements. (d) shows a single corresponding dI/dV spectrum that features a multitude of in gap resonances. The deconvolved DOS (e) shows that there are separate YSR states at at least three different energies, which I label by α, β, and γ. The in gap peaks in (d) have been labeled accordingly with thermal YSR peaks marked by a subscript t.
Figure A.3f–p shows constant-height dI/dV maps of the central MX measured at different voltages inside the superconducting gap. These measurements reveal the different lateral distributions of the YSR states. The maps measured on the peaks assigned to state α (h,i,j,l,m) show dominant intensities on the left and right lobe, while the maps assigned to state β (g,k,n) show dominant intensities on the top and bottom lobe. State γ on the other hand seems to be rather evenly distributed (o), which is also reflected by the maps (f,p) measured at voltages outside of the peaks where the negative differential conductance is assumingly dominated by the YSR state with the highest energy, i. e. state γ.

A.1.4 Origin and Identification

The appearance of MX in the STM measurements strongly suggests that it is some kind of phthalocyanine molecule, most probably a metal phthalocyanine (MPc). Many different molecules have been studied in the *4K* laboratory prior to these measurements, including different MPc species. Especially CoPc has been evaporated extensively inside the UHV chamber. However, I have not been able to reproduce the observed molecule by preparation of CoPc on Pb(100). I have tried some other MPc species including FePc, ZnPc, CuPc, and NiPc in addition, but they did not resemble MX either.

The by far best agreement was finally found in chlorinated aluminum phthalocyanine (ClAlPc) molecules. ClAlPc on Pb(100) was studied by Chao Li in the *mK* setup just recently and I was able to compare his measurements with mine of MX. Single ClAlPc molecules can orient itself with the Cl atom to the substrate. Such ClAlPc↓ molecules do not only match MX in its appearance in topography, they also show YSR states of similar YSR energy and asymmetry.
This match furthermore explains the apparent strong coupling of MX to the substrate. It has been reported that chlorinated MPc molecules bind covalently to Cu(111) when the Cl atom is placed toward the substrate[245, 246]. I assume, the same happens for ClAlPc↓ on Pb(100).
Although ClAlPc↓ matches MX very well, I cannot tell for sure that MX is ClAlPc↓. Further measurements on ClAlPc are necessary to verify the assumption. Comparative measurements on other chlorinated MPc molecules might help to rule out alternative explanations.
But even if this assignment is settled, the source of these molecules remains puzzling. To my knowledge, ClAlPc molecules – or any other chlorinated MPc – have never been studied in the *4K* laboratory.

A.2 AlPc on Pb(100)

Chao Li studied ClAlPc molecules on Pb(100). Some of the molecules lose the Cl atom and become AlPc during sample preparation. Together with Chao Li, I observed YSR states and vibrational excitations on AlPc. This section briefly reports about the corresponding findings. AlPc on Pb(100) is another example that demonstrates that the emergence of YSR states might be a rather general phenomenon for phthalocyanine molecules on Pb(100).

A.2.1 YSR States on AlPc

We observed a LUMO resonance at approximately 200 meV on isolated AlPc molecules on Pb(100), very similar to H_2Pc or PbPc. No YSR states have been found in this case. However, when assembling multiple AlPc molecules into a cluster, the LUMO shifts to smaller energies and a YSR state emerges. Figure A.5 shows respective measurements. The LUMO shifts by $\approx$35 meV per additional neighboring molecule, i. e., the same value I have observed for H_2Pc molecules. This finding suggests that the mechanism of the underlying intermolecular interaction is the same as for H_2Pc, independent of the molecular core. The central molecule of the pentamer shown in (e) furthermore exhibits elevated protrusions very similar to what has been observed on H_2Pc molecules carrying YSR states. In the case of AlPc, four neighboring molecules are sufficient to obtain YSR states.

In addition to single molecules and manually assembled clusters, we observed a self-assembled monolayer of AlPc molecules. Figure A.4 shows respective measurements. The AlPc monolayer is similar to the H_2Pc monolayer: A checkerboard pattern is observed, where molecules with

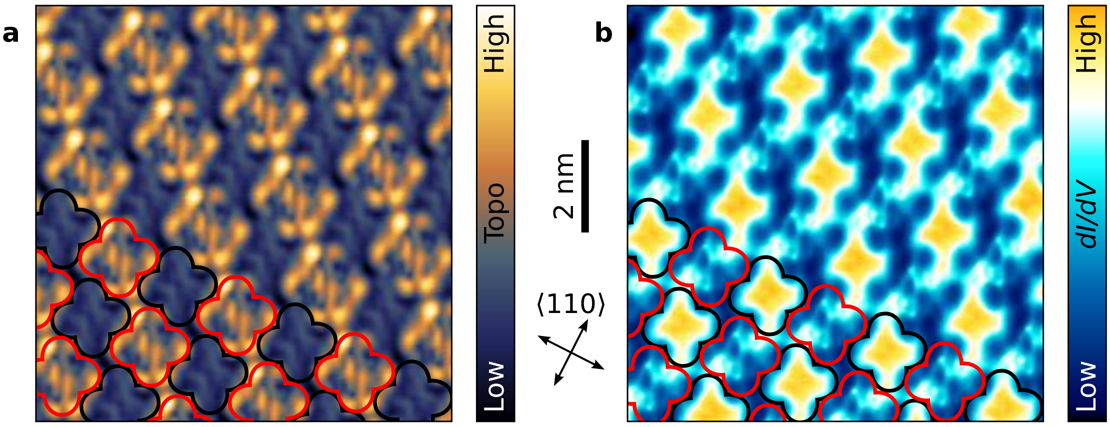

Figure A.4: (a) Topograph of an AlPc monolayer on Pb(100). It was measured at a setpoint of $I = 500\,\text{pA}$ and a sample voltage of $V = 5\,\text{mV}$. The molecules arrange in a checkerboard pattern. (b) Constant-current dI/dV map of the same area, measured at $I = 200\,\text{pA}$, $V = 2.6\,\text{mV}$, $V_M = 50\,\mu\text{V}_{\text{PP}}$, and $f = 831\,\text{Hz}$. YSR states are indicated by a reduced differential conductance (blue area). The outlines of some molecules are shown in the bottom left corner, whereby the two molecular groups are marked by red and black outlines, respectively. Only the molecules of the first group exhibit YSR states.

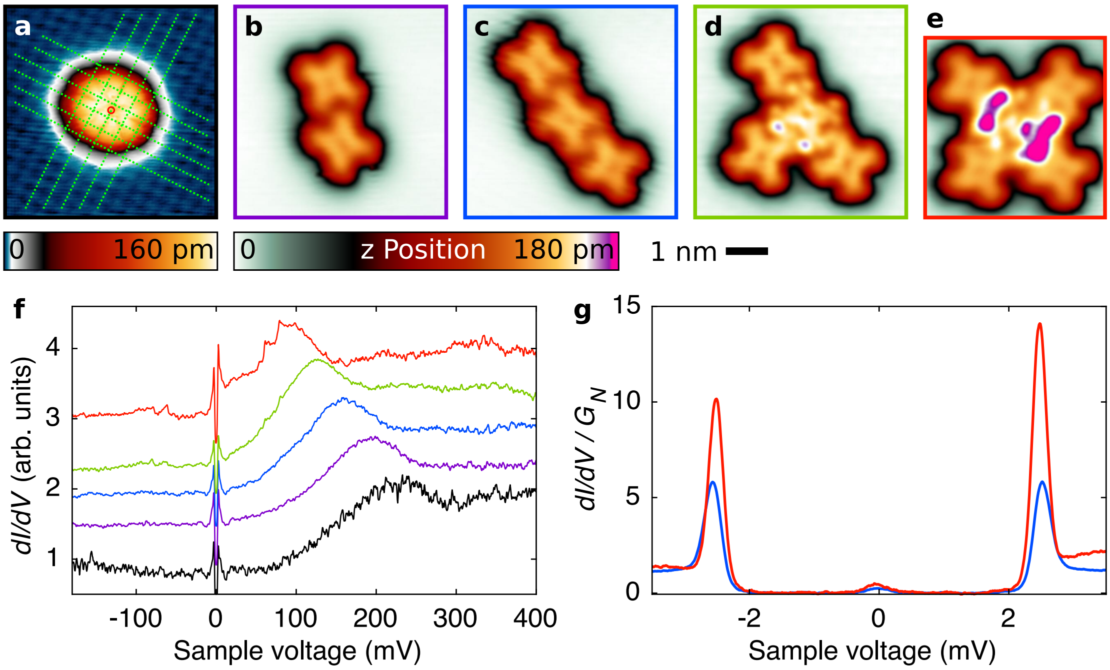

Figure A.5: Assembly of a cluster of five AlPc molecules. (a–e) Corresponding consecutive topographs measured at $I = 100\,\mathrm{pA}$ [$I = 1\,\mathrm{nA}$ in (a)] and $V = 10\,\mathrm{mV}$. In (a), dotted green lines interpolate the Pb lattice that is resolved around the molecule, which indicates that the AlPc molecule is adsorbed with its center on a bridge-site of the Pb(100) lattice (red circle). Elevated protrusions are visible on the central molecule of the pentamer [pink area in (e)], very similar to those observed on H_2Pc molecules carrying YSR states. (f) dI/dV spectra taken on the central molecule. From bottom to top, the spectra were taken on the isolated molecule, the dimer, the trimer, the tetramer, and the pentamer [(a–e), respectively]. The STM tip was kept at fixed position ($I = 3\,\mathrm{nA}$ [$1\,\mathrm{nA}$ on the isolated molecule], $V = 500\,\mathrm{mV}$) above the center of the molecule in the center of the respective cluster. A modulation voltage of $V_M = 1\,\mathrm{mV_{PP}}$ at a frequency of $f = 831\,\mathrm{Hz}$ was used. (g) Spectra of the superconducting gap measured on the central molecule of the trimer (blue curve) and of the pentamer (red curve). Signatures of YSR states are visible on the pentamer. The spectra were taken at a constant tip position ($I = 300\,\mathrm{pA}$, $V = 10\,\mathrm{mV}$) with a modulation voltage of $V_M = 100\,\mathrm{\mu V_{PP}}$ at a frequency of $f = 831\,\mathrm{Hz}$. All measurements shown in this figure were carried out by Chao Li. The data are shown with his permission.

and without YSR states alternate. Furthermore, the distribution of the YSR states follows a twofold symmetric pattern, which looks very similar to that of the LUMO of H_2Pc. In the case of AlPc, however, the two-fold symmetric YSR orbitals are aligned parallel to each other across the whole monolayer. In this way, the whole structure becomes two-fold symmetric in itself. While the monolayers of H_2Pc and PbPc represent $\left(\begin{smallmatrix}5 & 3\\ -3 & 5\end{smallmatrix}\right)$ superstructures, the AlPc monolayer seems to be arranged in a slightly more dense $\left(\begin{smallmatrix}4 & 4\\ -4 & 4\end{smallmatrix}\right)$ lattice. The symmetry axes of the AlPc molecules enclose an angle of ≈18° (with YSR, red outline) and ≈27° (without YSR, black outline) to the ⟨110⟩ surface direction. The two-fold symmetry of the structure can be explained by assuming that the AlPc molecules adsorb with their centers on bridge-sites instead on-top of substrate Pb atoms. Figure A.5a shows that this is the case for the isolated AlPc.

A.2.2 Vibrational Excitations of AlPc

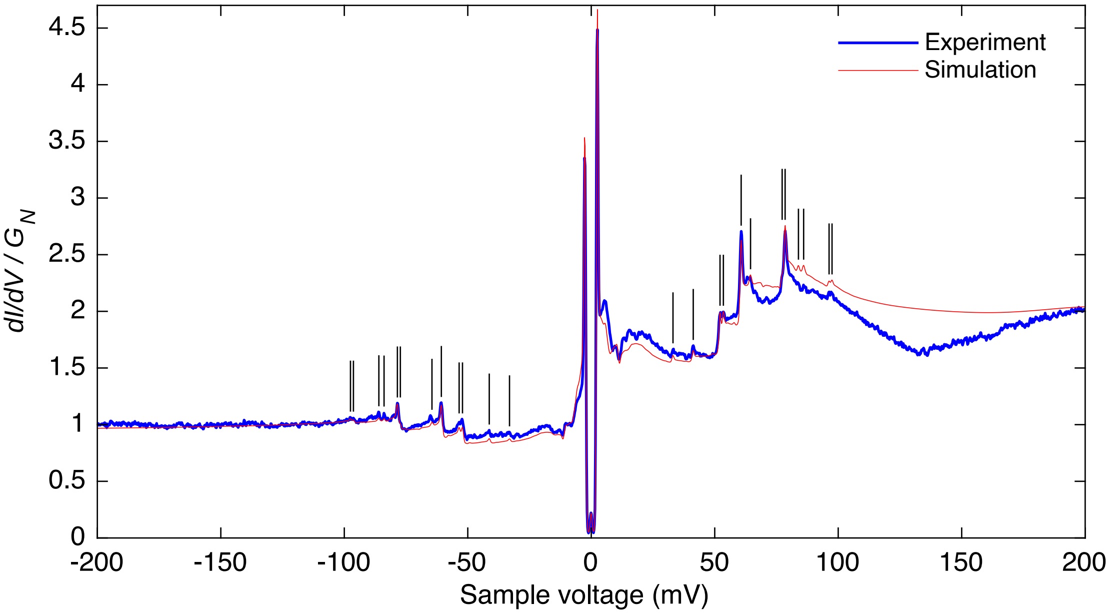

Figure A.6: Spectrum of vibrational excitations on AlPc. A measured dI/dV spectrum is shown (blue) together with a simulation (red). The measurement was taken at constant tip position ($I = 2\,\mathrm{nA}$, $V = 200\,\mathrm{mV}$) with $V_M = 1\,\mathrm{mV_{PP}}$ and $f = 831\,\mathrm{Hz}$. The peaks of the vibrational excitations are marked by vertical black lines.

In addition to YSR states, we also observed vibrational excitations on AlPc molecules via YSR enhanced IETS. Below, I will briefly present the findings and compare them to the case of PbPc.

Figure A.6 shows a dI/dV spectrum measured centrally above an AlPc molecule with YSR states inside an ordered island. 12 separate inelastic excitations are visible at both positive and negative sample voltage (marked by vertical black lines). In addition, a simulated spectrum is shown, which reproduces the measurement fairly well. The simulated spectrum was calculated as detailed in Section 5.4.3. The effective cross-sections η, as obtained from this simulation, are shown in Table A.1 together with the energies of the excitations.
We did only observe vibrational excitations with cross-sections of $\eta \geq 1\%$. On PbPc I observed values down to $\eta \approx 0.1\%$. It seems that the sensitivity for vibrational modes is reduced by one order of magnitude on AlPc. There are several reasons for this discrepancy: First, a significantly longer acquisition time was used for the measurements taken on PbPc leading to a better signal to noise ratio. Furthermore, the energy resolution was lower during our measurements on AlPc (partly due to a higher modulation amplitude). Most importantly, however, the relative YSR peak height was much smaller on AlPc than on PbPc leading to an additional reduction of the sensitivity in IETS.
Figure A.7 shows a comparison of IETS spectra taken on PbPc and AlPc. The difference in energy resolution and sensitivity is apparent. Consequently, fewer vibrational excitations are observed on AlPc.

Table A.1: Observed vibrational excitations on AlPc. Energies and estimates of the effective cross-sections were obtained by simulating the measured spectrum.

Energy (meV)	η (%)	Energy (meV)	η (%)
30.6	1.0	74.8	2.0
38.8	1.5	76.0	8.0
49.6	5.5	81.4	1.2
51.0	3.0	83.5	1.2
58.2	11.0	93.8	1.0
62.0	1.5	95.0	1.0

For nearly all observed excitations, there are excitations on PbPc at similar energies. In the case of PbPc, we have assigned the observed vibrational excitations to calculated vibrational modes (see Section 5.4). Troels Markussen has carried out a similar calculation for AlPc. Its results, however, have to be taken with caution, since an incorrect adsorption geometry was assumed. A rough comparison of the calculated modes showed, that modes with similar displacement patterns have similar energies on both systems. Especially for the modes observed at approximately 50, 84, and 95 meV a direct agreement of the assigned modes of PbPc and AlPc was found.

The effective cross-sections of the excitations, however, are very different on AlPc compared to PbPc. This effect is presumably caused by differences of the molecules themselves. An influence of the STM tip is excluded, because essentially the same effective cross-sections have always been observed on PbPc (or AlPc for that matter), regardless of the tip. The dI/dV spectra were taken centrally above the metal centers, which means that differences in their chemical bonds and hybridization with the rest of the molecule may significantly influence how certain vibrational modes are stimulated by the tunneling current. After all, AlPc is in a planar configuration and PbPc is not, as confirmed by DFT calculations.

Furthermore, the symmetry of the YSR states may play a role. On AlPc it is two-fold symmetric, while a four-fold symmetry was observed on PbPc. Since the vibrational excitations are measured by resonantly tunneling into the YSR states, the symmetry of the latter may influence which modes are stimulated and which are not.

In conclusion, YSR enhanced IETS has been demonstrated on a second molecule other than PbPc. Our findings underline the fact that large heights of the YSR peaks are crucial to obtain a high sensitivity.

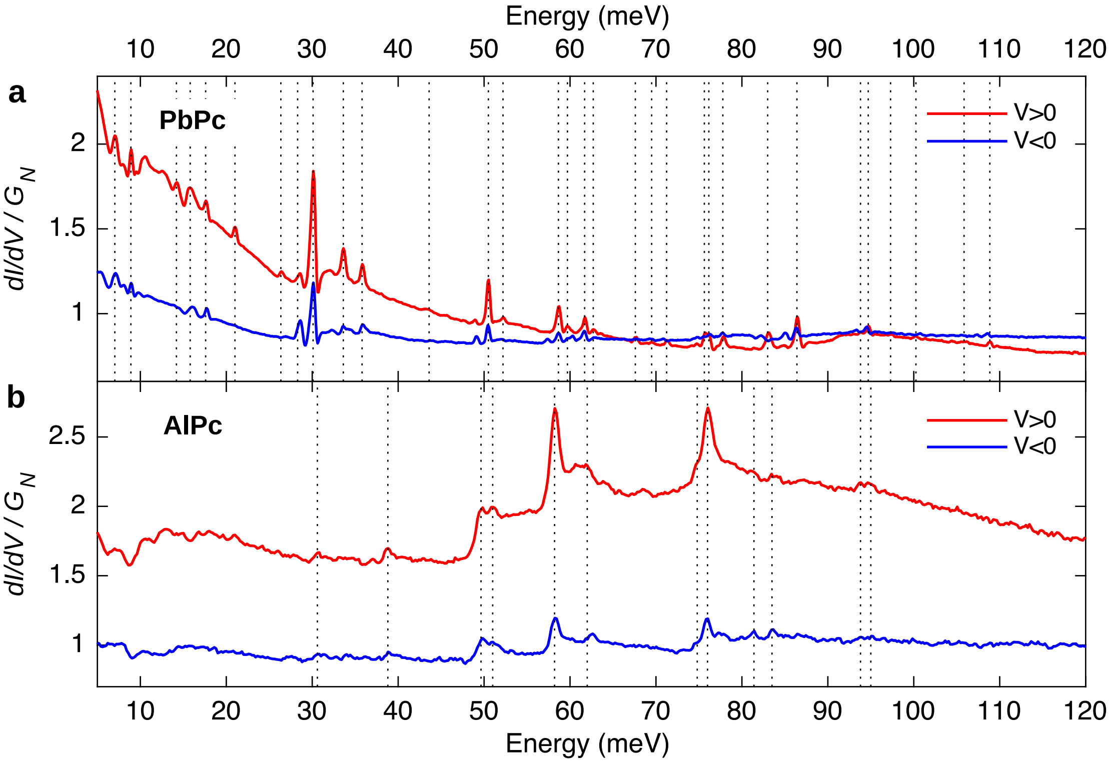

Figure A.7: Comparison of spectra taken on (a) PbPc↑ and (b) AlPc. The parts of the spectra taken at positive (red) and negative (blue) sample voltage polarity are shown, shifted by the YSR peak position such that the vibrational energies can be directly read from the abscissa. Peaks of vibrational excitations are marked by vertical dotted lines. The spectrum shown in (a) is the same as the one shown in Section 5.3, Figures 5.11 and 5.12 ($I = 4\,\mathrm{nA}$, $V = 200\,\mathrm{mV}$, $V_M = 0.5\,\mathrm{mV_{PP}}$, $f = 831\,\mathrm{Hz}$). The spectrum shown in (b) is the same as the one shown in Figure A.6 ($I = 2\,\mathrm{nA}$, $V = 200\,\mathrm{mV}$, $V_M = 1\,\mathrm{mV_{PP}}$, $f = 831\,\mathrm{Hz}$).

A.3 MnPc and YSR States on the Tip

YSR enhanced IETS, as demonstrated so far, relies on YSR states in the molecule to be investigated. One possible pathway of transferring this technique to non-magnetic molecules without YSR states would be to use a tip that carries the YSR state itself. This approach would enable the investigation of vibrational excitations on virtually any molecule adsorbed on a superconducting surface.

The fabrication of YSR tips, however, is challenging. The easiest way could be to pick up a magnetic molecule from the surface. In this case, however, vibrational excitations of both the molecule on the tip and the one on the sample would be visible and hardly distinguishable. It is therefore preferable to use a mono-atomic magnetic impurity on the tip.

I tried to use the demetallation technique on MnPc molecules to obtain an STM tip with a YSR state carried by a single Mn atom. It has been demonstrated that single Mn atoms on Pb show high YSR resonances[23, 39]. The results of my approach are discussed in the following. Unfortunately, I had no success in demetallizing MnPc, but instead picked up individual molecules with the tip, which nevertheless resulted in an STM tip with YSR states.

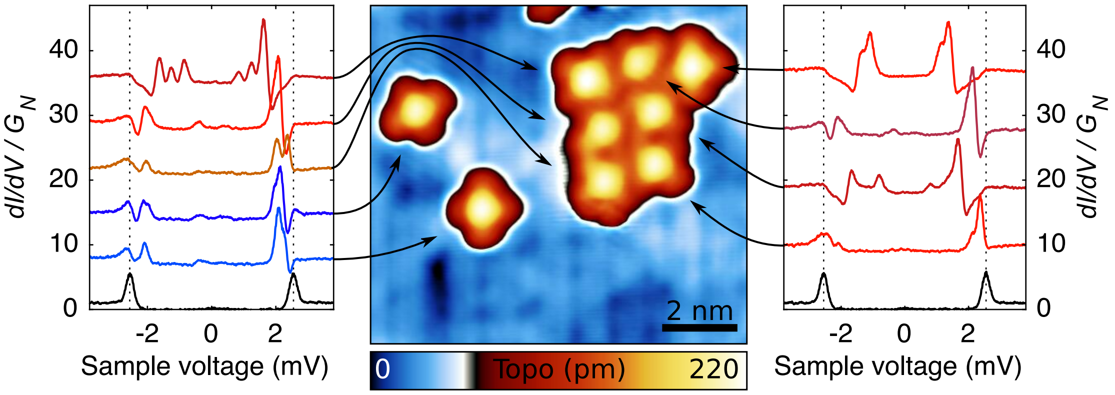

Figure A.8: Topograph of MnPc molecules on a Au-Pb substrate together with dI/dV spectra taken on them. The topograph was measured at a setpoint of $I = 100\,\text{pA}$ and a sample voltage of $V = 500\,\text{mV}$. The dI/dV spectra have been recorded above the centers of the MnPc molecules as indicated by arrows and exhibit YSR resonances at various energies. In addition, spectra taken on the pristine substrate are shown at the bottom (black curves). The positions of the coherence peaks are marked by vertical dotted lines for reference. The dI/dV spectra have been recorded at constant tip position ($I = 100\,\text{pA}$, $V = 500\,\text{mV}$) with a modulation of $V_M = 30\,\mu\text{V}_{\text{PP}}$ at a frequency of $f = 831\,\text{Hz}$. They are vertically offset for clarity. All measurements presented in this figure were conducted by Marten Treichel and are shown with his permission.

A.3.1 YSR States on MnPc

Together with Marten Treichel I evaporated MnPc onto the Pb(100) crystal that happened to be covered by the Au-Pb layer that will be presented in detail in Appendix B. On this substrate, the molecules do not form ordered islands, but rather accumulate disorderly.

Figure A.8 shows a topograph of multiple MnPc molecules on the Au-Pb substrate together with dI/dV spectra measured on them. All of the MnPc molecules exhibit YSR states. While the spectra taken on the isolated molecules (blue curves) look similar, the ones taken on the clustered molecules vary substantially (red curves). Multiple YSR resonances are present even on the isolated molecules.
Similar spectra have been measured on MnPc molecules on Pb(111)[35,37,140]. Up to three separate YSR states have been observed, which has been explained by a spin $S = 1$ configuration split by magnetic anisotropy[37,157].
The variation of YSR energies inside the cluster may come from different reasons. First, it could be due to a similar mechanism as discussed for H_2Pc and PbPc, where intermolecular interaction leads to an energy shift of molecular orbitals and finally to a change of the magnetic configuration and/or coupling to the substrate of the individual molecules. Secondly, the different adsorption sites and alignments of the molecules could effect their YSR energies. Lastly, however, it could also be due to intermolecular coupling of the YSR states by magnetic interaction[25,34,247].
Further investigations on MnPc are required to settle that issue. However, I recommend to use a Pb(100) substrate without the additional Au-Pb layer, since Pb(100) is better understood and offers fewer different adsorption sites for the molecules.

A.3.2 YSR States on the Tip

I tried to demetallize single MnPc molecules with the same technique used for the demetallation of PbPc (Section 5.8). Figure A.9I,II shows topographs taken before and after a respective manipulation step on three different molecules (a–c). In each case, the whole molecule was removed and presumably attached to the STM tip. Figure A.9III shows corresponding dI/dV spectra taken on the pristine substrate before (blue) and after (red) the manipulation. In each case, the unperturbed superconducting gap of Pb tip and Au-Pb substrate is observed beforehand, while clear YSR resonances become visible afterwards. The YSR energies vary strongly from case to case. Furthermore, the YSR peak heights barely exceed the heights of the coherence peaks. Both parameters strongly depend on the exact adsorption site and geometry of the molecule at the tip, which is, unfortunately, beyond my control and observation.

Although YSR states on the STM tip were achieved, the approach of fabricating YSR tips suitable for YSR enhanced IETS by demetallizing MnPc failed. As an alternative approach, I recommend picking up single magnetic adatoms with the tip, which has been demonstrated to succeed in the fabrication of YSR tips[44].

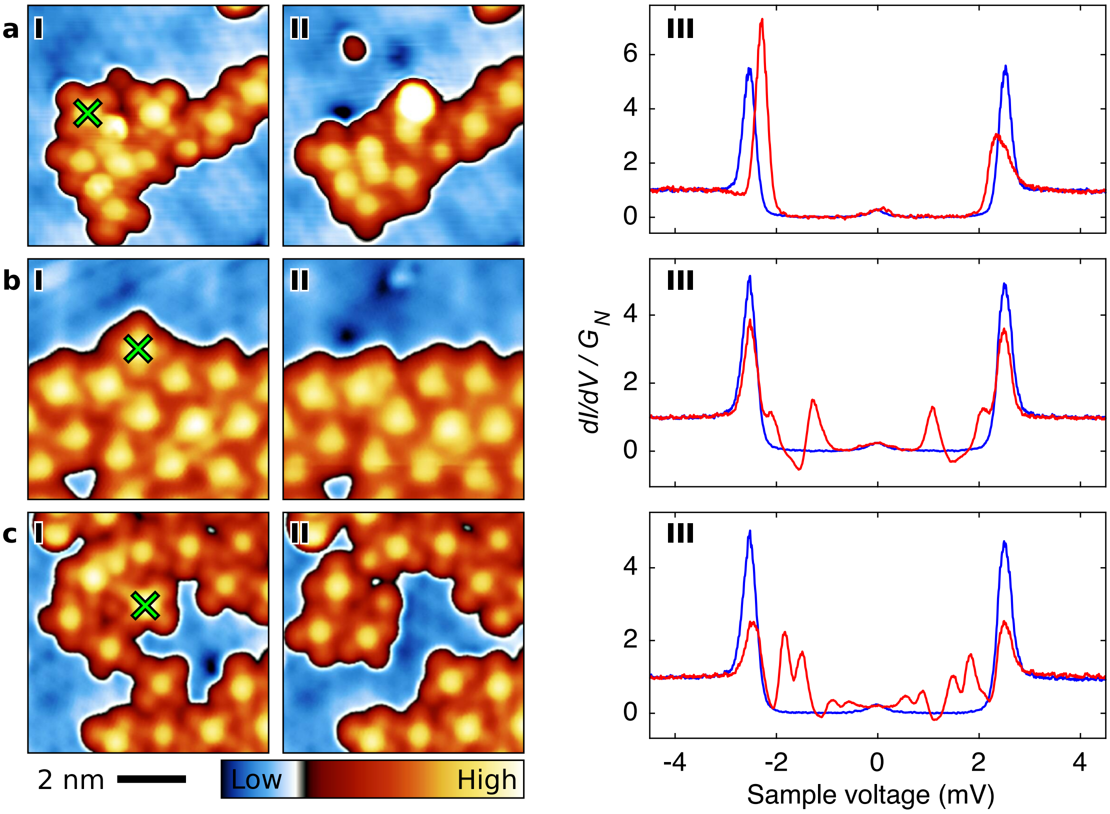

Figure A.9: Topographs taken (I) before and (II) after a MnPc molecule was transferred to the tip. The respective molecule is marked by a cross in (I). The topographs were measured at $I = 100\,\mathrm{pA}$ and $V = 100\,\mathrm{mV}$ [$V = 30\,\mathrm{mV}$ in (Ia)]. (III) dI/dV spectra taken on the pristine Au-Pb substrate before (blue curve) and after (red curve) the manipulation. No (pronounced) YSR resonances are visible before (after) the manipulation. The spectra were recorded at constant tip position [$I = 500\,\mathrm{pA}$, $V = 5\,\mathrm{mV}$; $I = 200\,\mathrm{pA}$ in (IIa)] with a modulation of $V_M = 30\,\mathrm{\mu V_{PP}}$ at a frequency of $f = 831\,\mathrm{Hz}$.

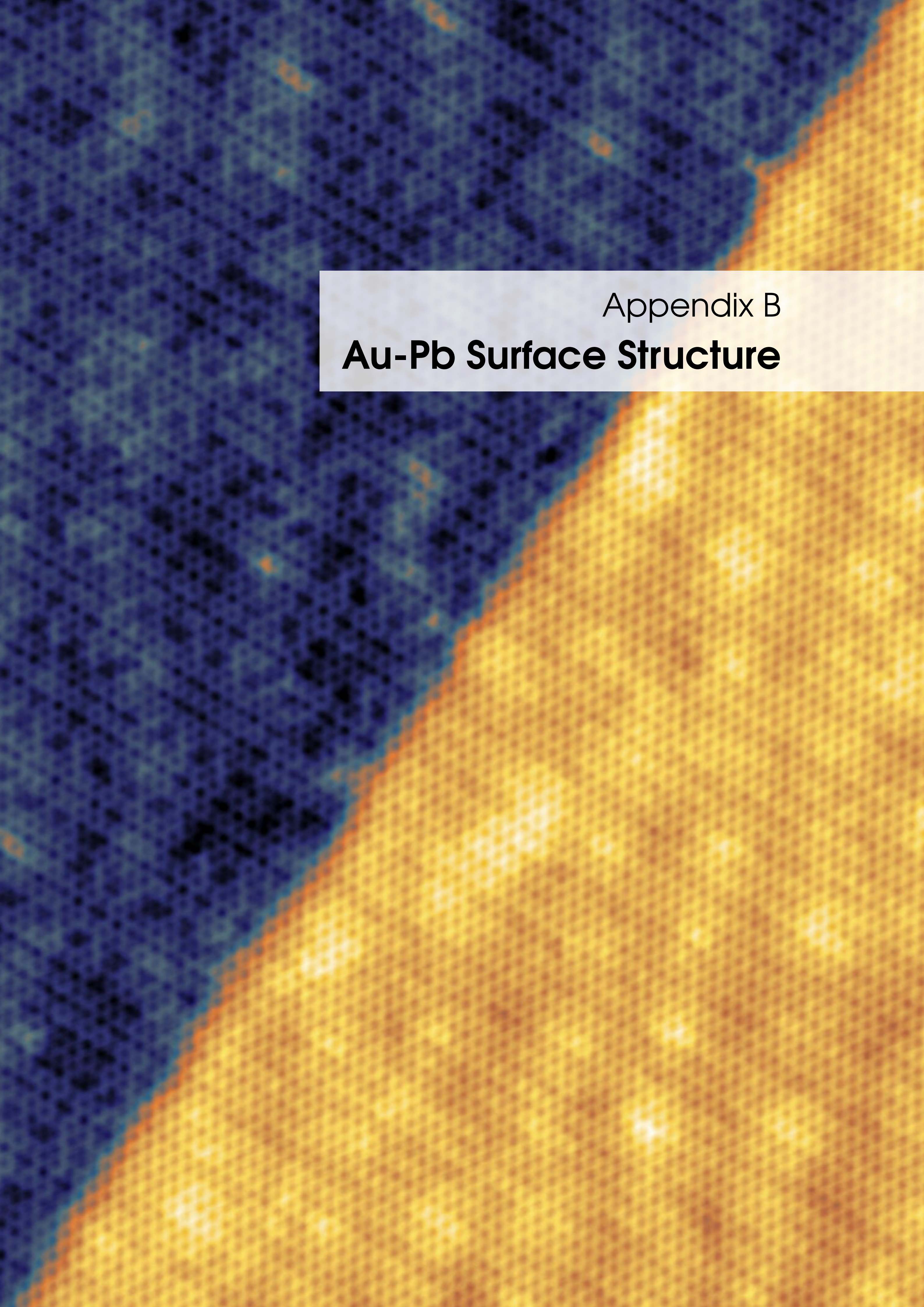

Appendix B

Au-Pb Surface Structure

Previous page:
Topograph of a Au-Pb surface structure on a Pb(100) single crystal. The sample voltage was set to $V = 100\,\mathrm{mV}$ and the setpoint to $I = 100\,\mathrm{pA}$. The section shown measures approximately $35\,\mathrm{nm} \times 50\,\mathrm{nm}$. Parts of the same topograph are revisited in Figure B.2a and Figure B.5b.

This chapter reports on a Au-Pb surface structure I observed on a Pb(100) crystal. Although the preparation of this alloy was unintended, the findings might be interesting for one or the other. In particular, Au_2Pb has attracted special interest in recent years, since it is discussed as a candidate for topological superconductivity[248,249]. In my case, the material is most probably $AuPb_3$, as indicated by Auger electron spectroscopy (AES) (see Section B.3).

B.1 Preparation of the Au-Pb Surface Structure

During my efforts to minimize the electronic spectral broadening of the setup, I experimented with different electric contacts to the sample. The single crystal is clamped onto a sample holder, which is built out of titanium and molybdenum. Originally, the electronic contact to the sample is made via several components and screws in series. To improve the contacting, I installed a gold wire, which directly connected the contacting fin of the sample holder with the single crystal itself (Figure B.1). In addition, I replaced the original contacting fin made out of titanium with a gold coated one out of copper. Unfortunately, this modification did not reduce the electronic broadening. Instead, the gold wire partly merged with the Pb single crystal into a Au-Pb alloy, which ultimately lead to the formation of an ordered Au-Pb crystal structure covering the whole sample surface.

It is in fact known that Au can diffuse into Pb with remarkably high diffusion rates[250,251]. It was reported that when brought into direct contact, a $AuPb_2$ phase can form between Au and Pb even at room temperature[252]. Furthermore, the melting point of such a Au-Pb alloy can be even lower than for pure Pb. At a mixing ratio of 84.1 % Pb to 15.9 % Au, the melting temperature drops down to 212.5 °C [253]. It is therefore plausible that a Au-Pb alloy (presumably $AuPb_2$ or $AuPb_3$) formed at the contact area of Au wire and Pb crystal, which then melted during the annealing of the sample and covered the crystal surface.

Because the amount of Au from the wire is small in comparison to the whole Pb single crystal, I assume that there is unmodified bulk Pb beneath the Au-Pb surface. This assumption is supported by the fact that I observed the same superconducting gap on the Au-Pb surface as on the Pb crystal. $AuPb_2$ and $AuPb_3$ have a smaller critical temperature than pure Pb[253,254] and therefore a smaller superconducting gap would be expected. Unfortunately, I cannot further specify the thickness of the Au-Pb layer.

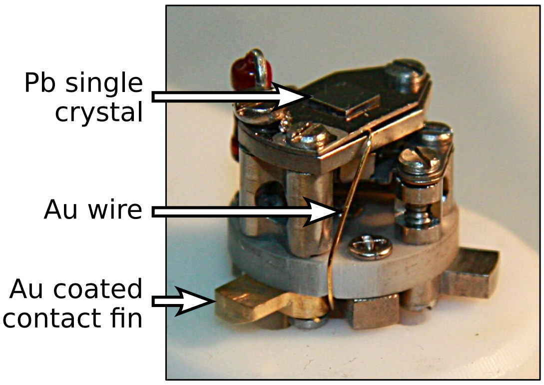

Figure B.1: Modified sample holder. A gold wire was installed to improve the electric contacting of the crystal. It had no effect on the electronic broadening, but instead lead to the formation of a Au-Pb alloy on the crystal surface.

B.2 STM Measurements

In the STM, I observed very large atomically flat terraces, sometimes extending over the whole scan area of 0.25 µm^2 without a single step edge. At small sample voltages, the surface features a honeycomb pattern, as shown in Figure B.2a. The length of the corresponding primitive translation vector is $a \approx 560\,\mathrm{pm}$. The observed structure can not be explained by, e. g., a 2×1 superstructure on Pb(100), which might also give the impression of a hexagonal structure, since the observed hexagonal lattice is not commensurable to the Pb(100) surface.

Furthermore, the hexagonal pattern is superimposed by larger irregular structures of few nm in size (see also chapter title image on page 145). The locations and dimensions of these structures do not depend on the sample voltage. It is therefore unlikely that standing waves are involved. I assume instead that those larger structures are due to a misalignment with the underlying Pb crystal and/or caused by disorder of the Au-Pb structure itself.

As shown in Figure B.2b, a rectangular lattice structure becomes visible at higher sample voltages. The lengths of the corresponding translation vectors are $b \approx 1.16\,\mathrm{nm}$ and $c \approx 1.57\,\mathrm{nm}$. The rectangular lattice is neither commensurable with the hexagonal one, nor to the Pb(100) surface. This claim is also supported by the Fourier analysis of the topographs, which will be shown in the following.

As shown in Figure B.2c, distinct patterns are observed at even higher voltages. For example groups of four adjacent elevations are observed repeatedly. However, those medium sized patterns seem to be randomly distributed within the rectangular lattice. Thus, they are probably due to different kinds of lattice defects.

Figure B.3 shows the 2D Fourier transform of the topograph that is shown partly in Figure B.2a. Two sublattices have been identified, which correspond to the lattices already observed in real space (Figure B.2 a and b). Furthermore, it becomes obvious that the two lattices are indeed incommensurable and are even slightly rotated against each other.

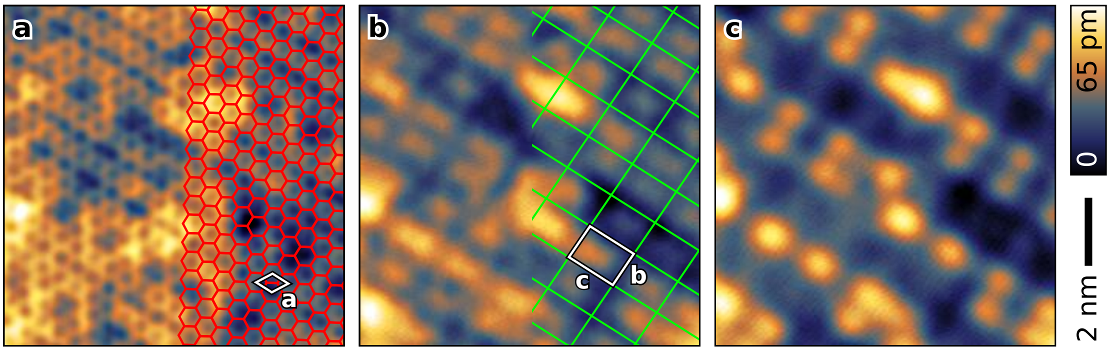

Figure B.2: Topographs of the Au-Pb surface structure. All topographs have been taken on the identical position of the sample, measured at sample voltages of (a) $V = 0.1\,\mathrm{V}$, (b) $V = 1.7\,\mathrm{V}$ and (c) $V = 2.5\,\mathrm{V}$, with a setpoint of $I = 100\,\mathrm{pA}$. (a) A honeycomb pattern is visible at small voltages as emphasized by a corresponding overlayed lattice (red). The honeycomb structure is superimposed by larger irregular patterns. (b) At higher voltages, a rectangular structure becomes visible (green lattice).

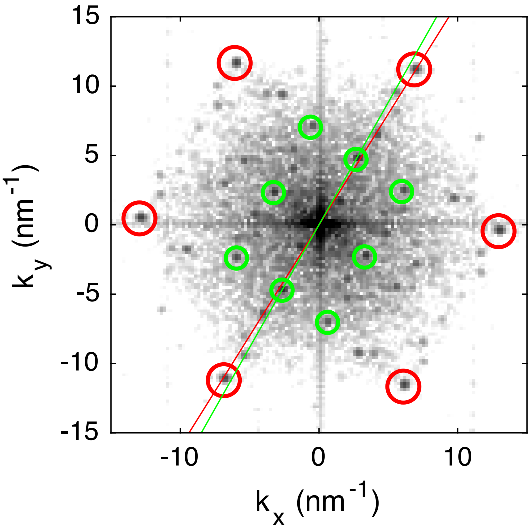

Figure B.3: 2D Fourier transform of a topograph of the Au-Pb surface structure. A magnified part of the topograph is shown in Figure B.2a. Two sublattices are identified. The respective spots belonging to a hexagonal (rectangular) lattice are marked by red (green) circles. The two sublattices are slightly rotated against each other, as demonstrated by straight lines, each of which was placed through two opposite spots of the respective sublattice. A Hanning window function was used to calculate the Fourier transform.

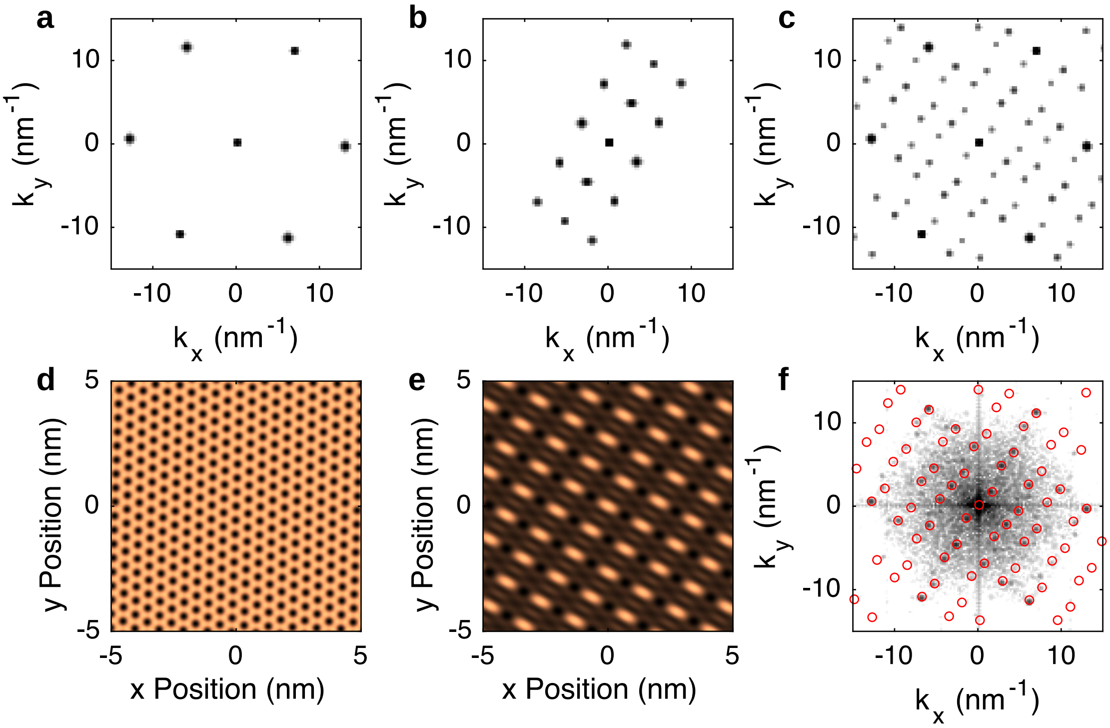

Figure B.4: Simulation of the Fourier transform of the structure. A hexagonal and a rectangular lattice are simulated. (d,e) Real space lattices, and (a,b) Fourier transforms, respectively. (c) Fourier transform of the product of the two lattices. It exhibits many additional spots, which reproduce the pattern observed in the experiment. (f) Fourier transform of a measured topograph (same as in Figure B.3). The positions of the spots of the Fourier transform of the simulated lattice are marked by red circles and match the experimental spots very well.

However, many more spots are observed in addition to the spots I have directly assigned to the two sublattices. As shown in Figure B.4, those additional spots can be explained by the combination of both sublattices. First, hexagonal and rectangular lattices were simulated in real space and Fourier space (Figure B.4a/d and b/c, respectively). Figure B.4c shows the Fourier transform of the product of both lattices. It resembles the pattern observed in experiment very well as demonstrated by the overlay in Figure B.4f.
I have also analyzed the Fourier transforms of topographs measured at higher sample voltages (up to $V = 5.9\,\mathrm{V}$ in increments of $\Delta V = 0.2\,\mathrm{V}$). However, no additional spots have been observed, nor did I find any evidence for standing wave patterns from quasiparticle interference.

In addition to the topographs of the structure itself, also a domain boundary was observed. Figure B.5 shows a topograph of a boundary between two domains of the Au-Pb surface layer. The honeycomb patterns of both domains are offset from each other by half a translation vector. Furthermore a step edge has been observed as shown in Figure B.5b. Its apparent height of only $\approx$72 pm is small compared with the height of a Pb(100) substrate step (250 pm). The honeycomb surface structure, however, continues seamlessly across the edge.

I also deposited PbPc and MnPc molecules onto the Au-Pb surface (Figure B.5 c and d, respectively). Although the same parameters were used for the evaporation as in the other experiments before, the molecules did not form ordered islands like on Pb(100), but remained rather unordered.

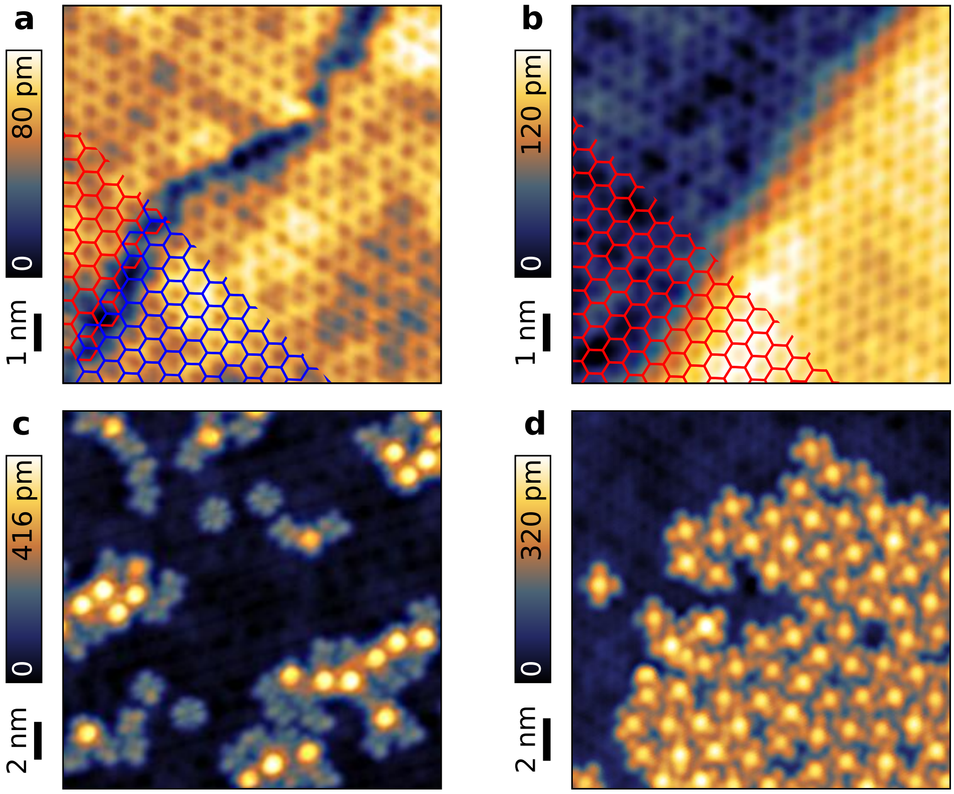

Figure B.5: (a) Topograph of a domain boundary of the surface reconstruction. The honeycomb structures of the two domains are offset from each other. (b) Topograph of a step edge with a height of only about 72 pm. The surface structure continues smoothly. (c) Topograph of PbPc molecules on the Au-Pb surface. (d) Topograph of MnPc molecules on the Au-Pb surface. In both cases (c,d), the molecules do not form ordered structures like on a Pb(100) surface. Scan parameters: $I = 100\,\mathrm{pA}$ (a–d), $V = 50\,\mathrm{mV}$ (a), $V = 100\,\mathrm{mV}$ (b–d).

B.3 AES Measurement

Finally, AES was used to estimate the composition of the surface layer. Figure B.6 shows a corresponding measured spectrum. Six peak dip features are visible, which I assigned to characteristic features of either Au or Pb. During the AES measurement, the sample was probably not placed exactly at the focus of the cylindrical mirror analyzer of the spectrometer, which explains the constant offset of approximately 5 eV between my measurement and the values from literature. Reference spectra for all elements are available, e. g., in the *Handbook of Auger Electron Spectroscopy*[255]. The reference spectra for Au and Pb were the only ones that were able to explain the observations.

I assigned the observed peak dip features to the reference features of Au at 43, 56, 66, and 69 V and Pb at 90 and 94 V. Furthermore, I measured the peak-peak amplitudes I and compared them with the respective amplitudes I_{ref} in the reference spectra to estimate the Au-Pb ratio. For this analysis, the relative sensitivity S of the elements has to be taken into account. At a primary energy of $E_p = 3\,\mathrm{keV}$, the values $S_{\mathrm{Au}} = 0.018$ and $S_{\mathrm{Pb}} = 0.01$ were obtained from the respective diagram [255, p. 13]. The relative weight χ is then calculated by

$$\chi = \frac{I}{I_{\mathrm{ref}} \cdot S} \,. \tag{B.57}$$

All corresponding values are shown in Table B.1. In total, I obtained relative weights of $\chi_{\mathrm{Au}} = 11 \pm 2$ and $\chi_{\mathrm{Pb}} = 33 \pm 4$ for Au and Pb, respectively. The Au-Pb ratio is therefore $1 : 3^{+1.1}_{-0.8}$, which suggests $\mathrm{AuPb_3}$ as surface material.

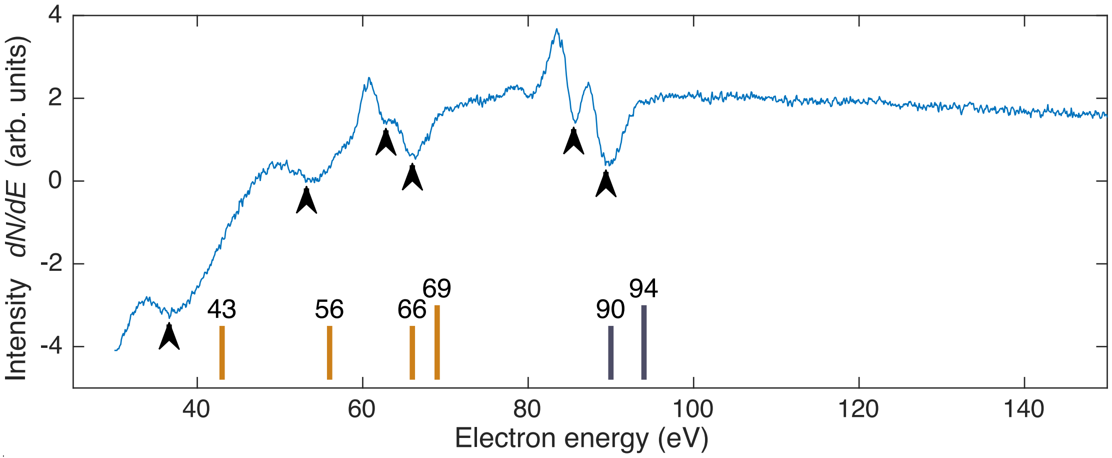

Figure B.6: Auger electron spectrum measured on the Au-Pb sample (primary electron energy $E_p = 3\,\mathrm{keV}$). Six peak dip features are visible in total (marked by black arrows). Reference spectra in the literature[255] report very similar features for Au or Pb (corresponding energies marked by vertical lines at the bottom, orange and gray respectively).

Feature #	Peak-Peak amplitude I	Reference (Energy / eV)	Reference amplitude I_{ref}	Relative weight χ
1	0,5	Au (43)	2,2	13
2	0,5	Au (56)	0,8	(34)
3	1,1	Au (66)	6,0	10
4	1,0	Au (69)	5,8	9
5	2,3	Pb (90)	6,2	37
6	2,0	Pb (94)	7,0	29

Table B.1: Analysis of the observed AES peaks by assignment to peaks from Reference 255. The relative weight of the second feature is excluded from the evaluation, as it deviates strongly.

It is possible in principle that the proportion of gold in the surface layer is higher. If the Au-Pb layer was very thin, the AES signal for Pb could be enhanced by the underlying Pb crystal. However, the AES features evaluated are in the energy range of 40 eV to 100 eV, where the escape depth of the Auger electrons is very small, namely in the range of about one to four monolayers[256]. In view of the STM results, I assume that the Au-Pb layer is at least several monolayers thick. The AES measurement therefore most likely reflects the real composition of the surface alloy.

B.4 Crystallographic Structure of AuPb$_3$

The crystallographic structure of bulk AuPb$_3$ is tetragonal scalenohedral with 16 atoms per unit cell[257,258]. The primitive unit cell is shown in Figure B.7a. There exist crystal planes with square or rectangular, but none with strict hexagonal symmetry. However, I identified a crystallographic plane where the gold atoms are arranged in a hexagonal like face centered rectangular lattice (Figure B.7b, red lattice). The in-plane distances of neighboring gold atoms are 608 pm and 682 pm, which is close to the length of the translation vector of 560 pm of the hexagonal structure I observed in experiment. The lattice vectors of the rectangular lattice itself (green lattice in Figure B.7b) have a length of 608 pm and 1222 pm. Therefore, the unit cell of this structure is much smaller than that of the observed rectangular lattice.

Although the AES measurement points toward AuPb$_3$ as surface material and there are indeed some similarities of AuPb$_3$ to the observed structures, there are also some distinct differences and observations that cannot be explained by the bulk structure of AuPb$_3$. Especially the slight rotation and incommensurability of the two observed lattices with each other cannot be explained by a single homogeneous crystallographic structure. The observations suggest instead that the hexagonal lattice belongs to a top layer or surface reconstruction. Furthermore, the underlying Au-Pb layers might differ from the shown bulk structure as they are grown on a Pb(100) substrate. In addition, STM topographs at higher sample voltages indicate that the structure is probably interspersed with lattice defects. Further measurements, e. g., by LEED and more precise AES, are probably necessary to clarify the observed structure.

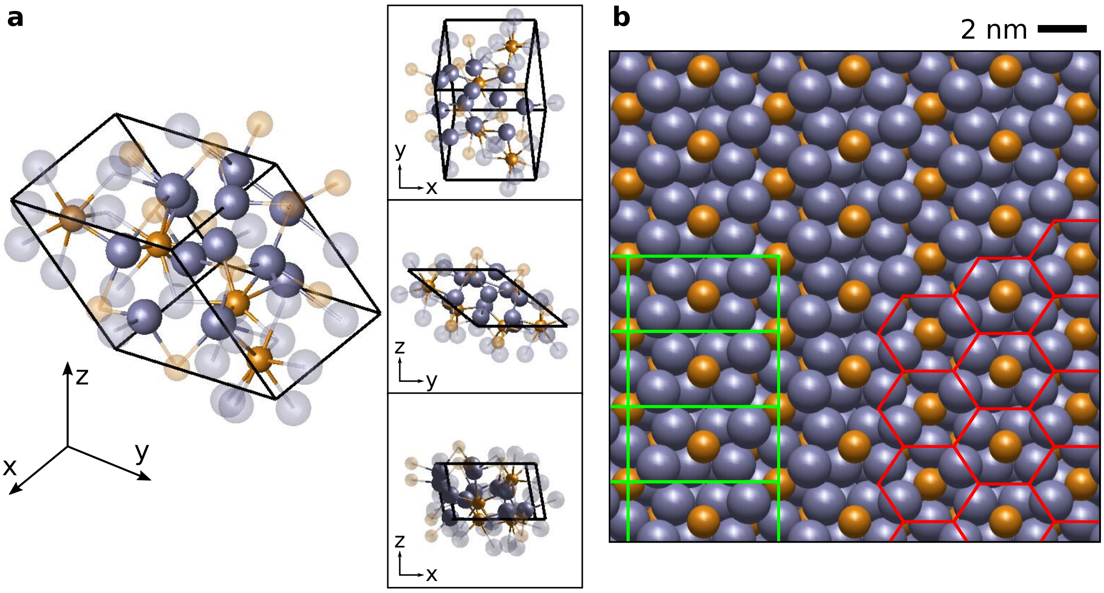

Figure B.7: (a) Primitive unit cell of the $AuPb_3$ bulk structure[257]. All three lattice vectors of the unit cell have a length of 916 pm. Atoms inside the unit cell are shown opaque, while neighboring atoms outside of it are shown transparent. Connections are drawn between atoms that are less than 350 pm apart. (b) A specific crystallographic plane shows a hexagonal like structure (indicated by a red lattice) of gold atoms with in-plane distances between neighboring gold atoms of 608 pm and 682 pm. Over all, the structure is rectangular as indicated by the green lattice. The lengths of the corresponding lattice vectors are 608 pm and 1222 pm.

Appendix C
Deconvolution of *dI/dV* Spectra

In the following, a way to deconvolve dI/dV spectra that were measured with a superconducting tip is derived. The goal is to obtain the pristine DOS of the sample.

I start with the voltage derivative of Equation 2.4:

$$\begin{aligned}\frac{dI}{dV}(V) \propto \int_{-\infty}^{+\infty} dE \cdot \rho_S(E) \cdot \Bigg[& \frac{d\rho_T(E-eV)}{dV} \cdot \left(f(E-eV) - f(E)\right) \\ & + \rho_T(E-eV) \cdot \frac{df(E-eV)}{dV} \Bigg].\end{aligned} \tag{C.58}$$

Then, g_T is defined by taking the term in square brackets in Equation C.58, substituting with $\omega = eV - E$ and dividing by e:

$$g_T(\omega, V) = \frac{d\rho_T(-\omega)}{d\omega} \cdot \left[f(-\omega) - f(eV-\omega)\right] + \rho_T(-\omega) \cdot \frac{df(-\omega)}{d\omega}. \tag{C.59}$$

For $E = eV - \omega \gg 0$ ($E = eV - \omega \ll 0$) $f(eV - \omega) \to 0$ ($f(eV-\omega) \to 1$) and $g_T(\omega)$ becomes independent from V. Accordingly, $g_T^+(\omega)$ is defined for $E \gg 0$ ($g_{\mathrm{tip}}^-(\omega)$ for $E \ll 0$):

$$\begin{aligned} g_T^+(\omega) &= \frac{d\rho_T(-\omega)}{d\omega} \cdot \left[f(-\omega)\right] + \rho_T(-\omega) \cdot \frac{df(-\omega)}{d\omega} \\ g_T^-(\omega) &= \frac{d\rho_T(-\omega)}{d\omega} \cdot \left[f(-\omega) - 1\right] + \rho_T(-\omega) \cdot \frac{df(-\omega)}{d\omega} \end{aligned} \tag{C.60}$$

E is the energy relative to the Fermi level of the sample and will be used as parameter for the DOS to be calculated by this procedure.
In the following, $g_T^+(\omega)$ and $g_T^-(\omega)$ are used as approximation in the case of $E > 0$ and $E < 0$, respectively. In other words, $f(eV - \omega)$ is approximated as a step function. This approach is justified for small temperatures, when the transition region of $f(eV - \omega)$ is inside the superconducting gap of the sample. Equation C.58 can then be rewritten as a convolution:

$$\begin{aligned}\frac{dI}{dV}(V) &\propto \int_{-\infty}^{+\infty} dE \cdot \rho_s(E) g_T(eV - E, V) \\ &\approx \int_{-\infty}^{0} dE \cdot \rho_S(E) g_T^-(eV - E) + \int_{0}^{\infty} dE \cdot \rho_S(E) g_T^+(eV - E)\ ,\end{aligned} \tag{C.61}$$

which provides ρ_S by using the convolution theorem:

$$\rho_S(E) = \begin{cases} \mathcal{F}^{-1}\left\{\frac{\mathcal{F}\{\frac{dI}{dV}\}}{\mathcal{F}\{g_T^+\}}\right\} & E > 0 \\ \mathcal{F}^{-1}\left\{\frac{\mathcal{F}\{\frac{dI}{dV}\}}{\mathcal{F}\{g_T^-\}}\right\} & E < 0. \end{cases} \tag{C.62}$$

$\mathcal{F}$ and $\mathcal{F}^{-1}$ are the Fourier transform and inverse Fourier transform operators, respectively. The DOS of the sample $\rho_S(E)$ can be directly calculated via Equation C.62 by using the measured dI/dV curve. All that is needed, is the DOS of the tip $\rho_T(E)$, which can be calculated via Equation 2.11. The parameters needed can be estimated by fitting dI/dV spectra taken on the pristine substrate.
However, because of the limited energy resolution, the dI/dV spectra are smoothed, which in turn effectively reduces the sampling frequency. I therefore apply a cut-off ($1/300\,\mu\text{eV}$) to the Fourier transform of the dI/dV spectra.

An example of a deconvolved sample DOS $\rho_S(E)$ is shown in Figure C.1a (black curve), along with the tip DOS $\rho_T(E)$ used for deconvolution (inset). Figure C.1b shows the original dI/dV spectrum (black curve). To check the accuracy of the method, the dI/dV spectrum is reproduced using Equation 2.4 taking the deconvolved sample DOS $\rho_S(E)$. This spectrum is shown in Figure C.1b along with the raw spectrum. Small deviations are present in the superconducting gap, but overall the original spectrum is reproduced. This result justifies the approximation done in Equation C.61.

C.1 Intrinsic Peak Height Asymmetry

The deconvolved sample DOS $\rho_S(E)$ (black curve in Figure C.1a) can be used to obtain the intrinsic peak height asymmetry $\chi*$, which is a key parameter to characterize YSR states. Unfortunately, the peak height asymmetry χ observable in $\rho_S(E)$ is not only influenced by the YSR states themselves, but also might be due to a non-constant normal-conducting sample DOS at the Fermi edge. To compensate this effect, the slope of the normal-conducting sample DOS is estimated by a linear fit to $\rho_S(E)$ outside of the superconducting gap, $|E| > 3\,\text{meV}$ (red dotted line in Figure C.1a). By dividing $\rho_S(E)$ by the linear fit, the slope-corrected sample DOS (blue curve) is obtained. The intrinsic peak height asymmetry $\chi*$ is now calculated from the

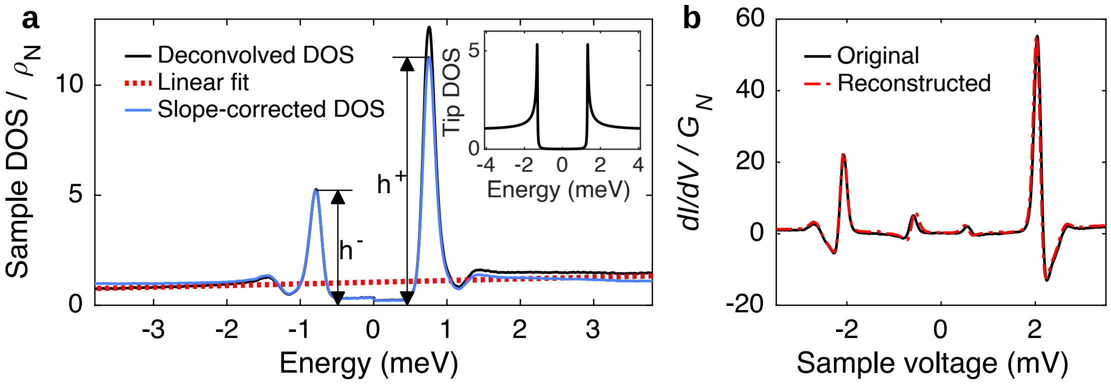

Figure C.1: (a) Deconvolved sample DOS obtained from the dI/dV spectrum shown in (b) (black curve). A straight line was fitted to the sample DOS for $|E| > 3\,\mathrm{meV}$ (red dotted line). The sample DOS was then divided by the straight line, which gives the slope-corrected DOS (blue curve). By this procedure, the intrinsic peak-height asymmetry $\chi*$ is retrieved. The inset shows the tip DOS used for the deconvolution of the dI/dV spectrum. (b) Original dI/dV spectrum (black curve) along with the reconstructed spectrum (red dashed curve) calculated from the deconvolved sample DOS using Equation 2.4.

respective peak heights h^+ and h^- at positive and negative sample voltage, respectively:

$$\chi* = \frac{h^+ - h^-}{h^+ + h^-} \tag{C.63}$$

The influence of non-constant normal-conducting DOS on the asymmetry of the coherence peaks was theoretically investigated by Hirsch[259]. He assumed a slope in the normal-conducting DOS of the superconductor itself and deduced a relation to the peak height asymmetry which is different to what is supposed above. However, the situation is different in my experiments, since the observed slope of the spectral background originates in the LUMO of the molecule. The coherence peaks, on the other hand, are a feature of the substrate, which exhibits an approximately constant normal-conducting DOS close to the Fermi level. Therefore, a simple multiplicative relation of the coherence peaks to the slope of the spectral background is assumed.

Appendix D

Construction of a NEG-Pump

Previous page:
NEG pump that has been built by ourselves. Its construction and characterization are subject of this chapter.

D.1 Introduction

Non evaporable getters (NEGs) are porous alloys that bind gas molecules via metallic surface sorption and are therefore utilized as vacuum pumps. After an initial activation at higher temperatures, NEG pumps do not require any external supply during operation. Furthermore, they do not include any moving parts, are free of magnetic fields, compact and lightweight. Nonetheless, NEG pumps provide high pumping rates (especially for hydrogen) and are used to achieve extremely high vacua[260, 261]. They are therefore highly suitable to pump the UHV chamber of a STM, especially during measurement operation when other pumps have to be switched off.

The most efficient way of installing NEGs in a UHV system is to coat the inner walls of the chamber with the getter material[262]. This technique was developed at the CERN and is used in the Large Hadron Collider[263]. For that purpose there are getter materials available that can be activated during bakeout of the chamber at temperatures below 200 °C [264], which suits the typical temperature limitations during a bakeout of an STM setup. Instead of that approach, however, in STM setups usually compact NEG pumps are used, like the CapaciTorr® NEG pumps commercially available from *SAES Getters*[265]. The compact design has the advantage that the NEG pump can be installed in a small section of the UHV chamber that can be separated from the STM chamber. In doing so, the NEG material can be kept under vacuum while venting the STM chamber for maintenance. In this way, the getter material is spared and the lifetime of the pump is increased.

Since the operating principle of NEG pumps is rather simple, my work group decided to build one on our own. Lars Mühlenberend made a design (Figure D.1) and also ordered all needed parts, including the NEG material.
My task was to assemble, test and install the pump. Furthermore I made a new improved design, which will be shown at the end of this chapter.

D.2 Getter Material

We use St 707® from SAES[266, 267] as getter material, consisting of a zirconium-vanadium-iron alloy (70 % Zr, 24.6 % V, 5.4 % Fe). This alloy is characterized by a medium activation temperature of approximately 400 °C. In the chosen design variant St 707/CTAM/30D[268], this getter material is pressed as a powder onto both sides of a constantan strip (55 % Cu, 45 % Ni). With a powder thickness of roughly 70 µm, the strip is covered by approximately $20\,\mathrm{g\,m^{-1}}$ of St 707. The advantage of this implementation is that it is easy to handle and that the getter material can be activated by resistive heating of the strip. The specific resistivity of constantan at room temperature is $5 \times 10^{-7}\,\Omega\,\mathrm{m}$ and it is very stable to higher temperatures (less than 0.1 % change per 100 °C)[269]. The strip has a width of 3 cm, a thickness of 0.2 mm and ≈1.7 m of it are used for the pump. The resistance of the installed strip is therefore ≈140 mΩ.

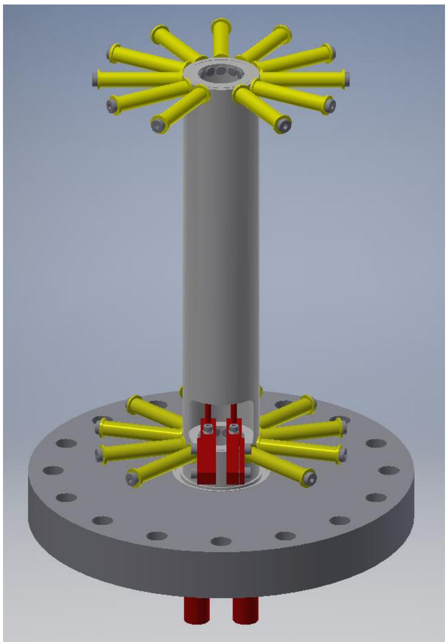

Figure D.1: NEG pump design by Lars Mühlenberend. A CF100 flange is used as basis. A strip with the getter material (not shown) will be placed around the ceramic sleeves (yellow), which are radially aligned at the top and the bottom of a stainless steel cylinder. The ends of the strip will be contacted via two copper clamps (red), which are connected to a feedthrough embedded in the CF flange.

D.3 Assembly

The parts for the pump were thoroughly cleaned and assembled according to the design from Lars Mühlenberend. In addition, a thermocouple type K was installed at one of the upper ceramic sleeves to enable a direct temperature measurement during the activation process. Finally the St 707 strip was carefully installed. Unfortunately, it was not possible to use as many of the strip as originally planned without introducing a short circuit between neighboring sleeves, where the strip is diverted. Therefore some of the ceramic sleeves had to be omitted as can be seen at the final assembly shown in Figure D.2a. In total (170 ± 10) cm of the strip were installed, which corresponds to (34 ± 2) g of the St 707 getter material.

After the assembly, the pump was installed inside a steel cylinder connected to a gate valve. Laterally to the cylinder, an additional feedthrough for the thermocouple as well as a pressure gauge (Pfeiffer CompactFull Range BA Gauge, Type PBR 260) were mounted as shown in Figure D.2b. At the end, this whole assembly was mounted on a vacuum chamber, whereby the gate valve allows the NEG pump to be separated from the chamber when needed.

D.3.0.1 Cost Summary

In the following, a rough cost breakdown is given in order to classify the financial expenditure. I will only give the pure material costs for the pump itself (Figure D.2a) without all the peripheral installation. The St 707/CTAM/30D getter strip with a total length of 10 m cost 1570 €. However, I only used ≈1.7 m of it, for which I account for 300 €. This results in total expenditure of less than 900 € as listed in Table D.1.

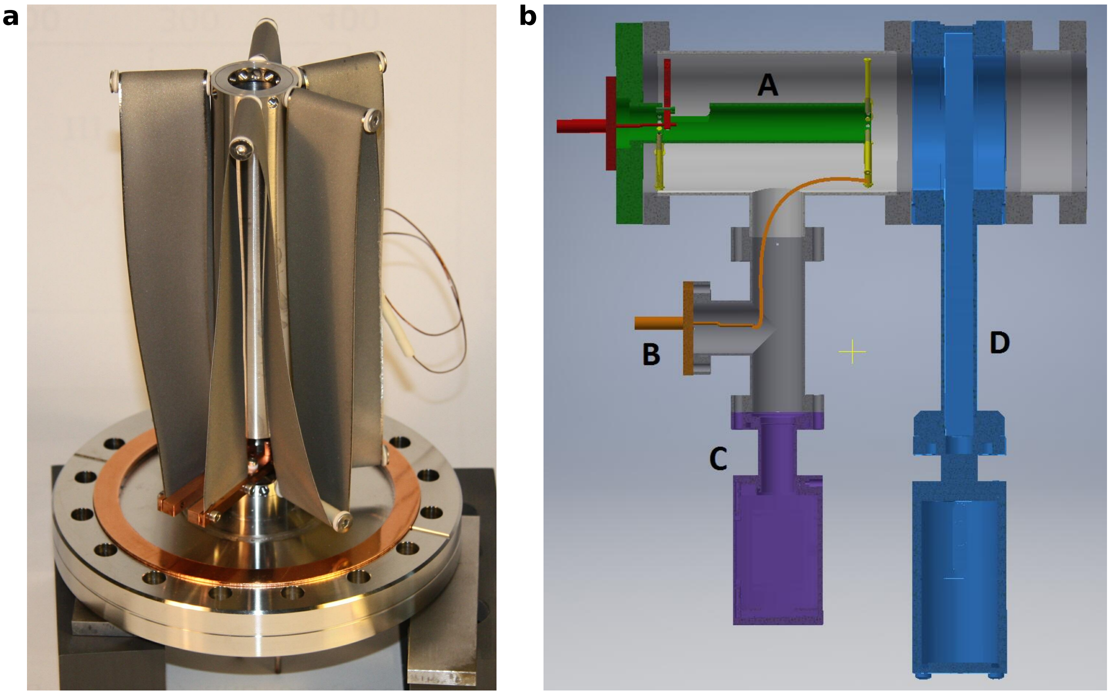

Figure D.2: (a) The assembled NEG pump. Not all of the provided ceramic sleeves could be used. The installed NEG strip is therefore shorter than initially planned. (b) A schematic cross-section of the pump and its peripheral devices. The pump (A) sits in a steel cylinder connected to a gate valve (blue, D). Laterally to the pump, a pressure gauge (purple, C) and an additional feedthrough (B) for the thermocouple (orange) are installed.

Table D.1: Expenditure on materials for the self-built NEG pump. The values are roughly rounded.

Part	Cost
St 707 getter	300 €
Flange	150 €
Feedthrough	250 €
Ceramic and Al_2O_3 parts	70 €
Steel and Copper parts	50 €
Screws	15 €
Total	835 €

D.4 Test and Characterization

D.4.1 Test Setup

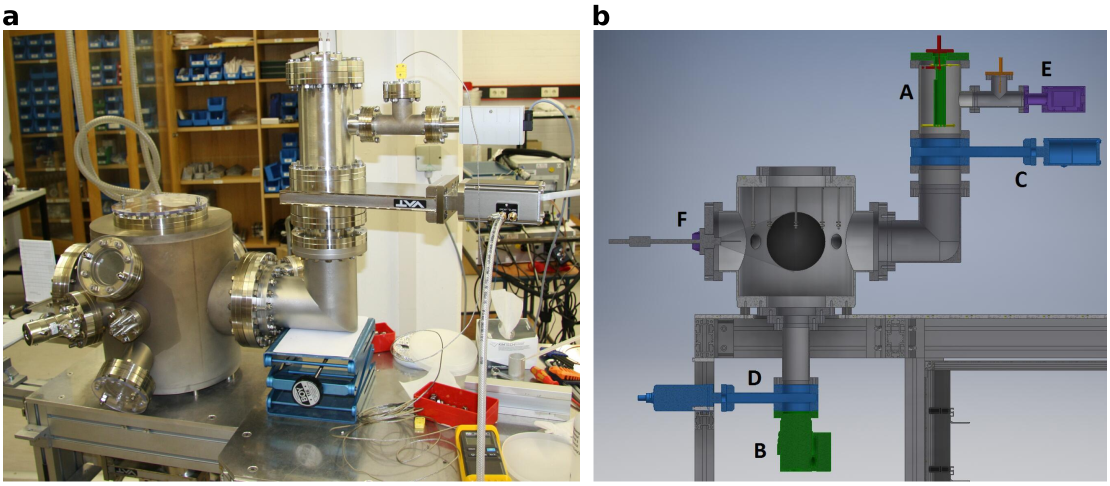

Figure D.3: (a) The test chamber with the NEG pump mounted. (b) A schematic cross-section of the test chamber with the NEG pump. The test chamber can be pumped by both the NEG pump (A) and a TMP (B). Both pumps can be separated from the test chamber via gate valves (C & D). In addition to the pressure gauge at the NEG pump (E), a second pressure gauge is installed directly at the test chamber (F).

To test the NEG pump and estimate its pumping capability, it was mounted on a test chamber as shown in Figure D.3. The test chamber has been designed and built by Lars Mühlenberend[270]. A turbomolecular pump (TMP) from Pfeiffer (Type: TMU 071 P) was used as primary vacuum pump. Both the TMP as well as the NEG pump could be separated via gate valves from the test chamber. An additional pressure gauge (Pfeiffer Compact Full Range Gauge, Type PKR 251) was installed to the chamber. Furthermore, a fine dosing valve and a mass spectrometer were mounted.

After assembly, the whole setup was baked and the NEG pump was activated. For the latter, a current of 40 A was applied to the NEG strip. To fully activate the getter material, a temperature above 400 °C was kept for 28 min with a maximum of 417 °C as measured with the thermocouple. After bakeout and with both pumps running, a base pressure of 7×10^{-11} torr was measured via the mass spectrometer. Unfortunately, both pressure gauges were out of range with a minimal pressure of 5×10^{-9} mbar and 5×10^{-10} mbar for the pressure gauge at the test chamber and the NEG pump respectively.

D.4.2 Measurement of the Pumping Speed

The pumping speed of TMP and NEG pump is independent of the pressure when dealing with high vacuum[271]. Therefore it is a good measure of the efficiency of such pumps. However, the pumping speed strongly depends on the type of gas being pumped. Typically, NEG pumps achieve the highest pumping speeds for hydrogen, while inert gases are not pumped at all. In the following, pure nitrogen is used as test gas, which enables the comparison with other pumps, since pumping speeds for nitrogen are given by most manufacturers.

Basically, the pumping speed S of a pump can be estimated by measuring the base pressure p_B achieved with a given leakage rate Q (Reference 271, Equation 5.2):

$$p_B = \frac{Q}{S} \tag{D.64}$$

Here, a fine dosing valve is used to insert nitrogen into the test chamber. The leakage rate Q of the fine dosing valve at a specific setting can be determined by measuring the rise of the pressure $p(t)$ in the chamber with all pumps disconnected (Reference 271, Equation 5.3):

$$p(t) = p(t=0) + \frac{Q \cdot t}{V}, \tag{D.65}$$

with V being the Volume of the chamber. Here, $V = 29.3\,\mathrm{l}$ as determined via the CAD model of the chamber in Autodesk Inventor.

When a pump is connected to the chamber, a base pressure sets in. The pumping speed of the pump can then be determined with Equation D.64. In the following, the pump was connected at first while setting the fine dose valve to a fixed leak rate. Then, the base pressure was recorded and after that, the pump was disconnected to measure the leak rate as described above.

However, the pumping speed determined in this way is the effective pumping speed. Its value might be significantly lower than the gross pumping speed, since it is reduced, e. g., by pipe sections through which the pump is connected to the chamber.

D.4.2.1 Pumping speed of the TMP

In a first step, the pumping speed of the TMP is determined.

The pumping speed for nitrogen is given as $S_{N_2} = 60\,\mathrm{l\,s^{-1}}$ by the manufacturer[272]. However, this pumping speed is reduced by a splinter shield and the gate valve and CF63 tube, which connect the TMP to the actual test chamber. The splinter shield reduces the pumping speed by approximately 15%[272]. The conductance of the connection piece of gate valve and CF63 tube has been determined nomographically (Reference 271, p. 158). With a diameter of 63 mm and a length of 245 mm measured from the flange of the TMP to the interior wall of the main chamber a conductance of $L = (89 \pm 9)\,\mathrm{l\,s^{-1}}$ is obtained. The effective pumping speed of the TMP is therefore calculated as follows (Reference 271, p. 15, Equation 1.24):

$$S_{\mathrm{eff,N_2}} = \frac{1}{\frac{1}{0.85 \cdot S_{N_2}} + \frac{1}{L}} = (32 \pm 2)\,\mathrm{l\,s^{-1}} \tag{D.66}$$

Measurement	p_B (mbar)	q (mbar/s)	S (l/s)
#1	6.2E-9	4.8E-9	22.5
#2	6.8E-9	5.0E-9	21.5
#3	1.17E-8	8.8E-9	21.9
#4	2.56E-8	22.5E-9	25.7

Table D.2: Measured values for the base pressure p_B achieved with the TMP at a reduced leak rate of $q = \frac{Q}{V}$. S is the resulting effective nitrogen pumping speed of the TMP.

For comparison, the pumping speed of the TMP was measured as described above. In Table D.2 the results of four measurements are shown. The mean value of the effective pumping speed is therefore $(23 \pm 2)\,\mathrm{l\,s^{-1}}$, which is much smaller than the calculated one from above.

D.4.2.2 Pumping speed of the NEG pump

The pumping speed of the NEG pump was determined in the same way. Here, the volume of the test chamber is $V = 29.5\,\mathrm{l}$. It deviates from the value noted before due to volume changes caused by (dis-)connecting the gate valves. The measured data are shown in Table D.3 and leads to an average effective pumping speed of $(32 \pm 6)\,\mathrm{l\,s^{-1}}$. It should be noted that the effective nitrogen pumping speed of the self built NEG pump is higher than that of the commercial TMP.

Measurement	p_B (mbar)	q (mbar/s)	S (l/s)
#1a	2.05E-8	3.43E-8	49.3
#1b	2.00E-8	2.01E-8	29.6
#1c	1.46E-8	1.42E-8	28.6
#2	9.1E-9	8.17E-9	26.5
#3	8.6E-9	7.78E-9	26.7
#4	1.55E-8	1.53 E-8	29.2
#5	7.8E-8	8.91E-8	31.4
#6	3.24E-8	3.25E-8	29.6
#7	2.64E-8	2.61E-8	29.1
#8	6.25E-8	6.49E-8	30.6
#9	1.02E-7	1.25E-7	36.0

Table D.3: Measured values for the base pressure p_B achieved with the NEG pump at a reduced leak rate of $q = \frac{Q}{V}$. S is the resulting effective nitrogen pumping speed of the NEG pump.

However, the gross pumping speed is of higher interest for comparing with other pumps. The NEG pump was connected via an angled tube piece to the chamber, which reduces the effective pumping speed. The conductance of this connection piece has been determined nomographically to $L = (174 \pm 10)\,\mathrm{l\,s^{-1}}$. Here, the angle $\Theta = 90°$ of the tube is taken into account by calculating an effective length l_{eff} of the tube (Reference 271, p. 17, Equation 1.32):

$$l_{\text{eff}} = l_{\text{axial}} + 1.33 \cdot \frac{\Theta}{180°} \cdot d = 512\,\text{mm}, \tag{D.67}$$

where $l_{\text{axial}} = 446\,\text{mm}$ is the axial length of the connection piece. Its diameter is $d = 100\,\text{mm}$. In analogy to Equation D.66, the gross pumping speed of the NEG pump is calculated as:

$$S_{N_2} = \frac{1}{\frac{1}{S_{\text{eff}}} - \frac{1}{L}} \approx (39 \pm 10)\,\text{l}\,\text{s}^{-1} \tag{D.68}$$

D.4.2.3 Comparison to other NEG pumps

In order to classify the determined pumping speed of our NEG pump it is compared to similar pumps in the following.
Kikuchi et al. report about a self built NEG pump where they also used St 707/CTAM/30D-strips as getter material[273]. For this pump, they determined a nitrogen pumping speed of $S_{N_2} = 25\,\text{l}\,\text{s}^{-1}$ [274], which is slightly less than in our case, even though they used significantly more getter material, namely 2.85 m of the strip. The difference in pumping speed might come from the different pump design. Kikuchi et al. arranged the strip more densely. Furthermore, they use indirect heating via a tantalum wire installed in the center of the pump for the activation of the NEG. This arrangement might lead to an inhomogeneous heating of the getter material and thus less pumping capability.
Kodama et al. also report more recently about self built NEG pumps, where they used NEG pills comprising a Zr-V-Fe alloy identical to St 707[275,276]. With their best performing NEG pump, they achieved a nitrogen pumping speed of 17 to $35\,\text{l}\,\text{s}^{-1}$ using 72 g of the getter material[275]. Still, our NEG pump shows a better efficiency considering that we used less than half as much getter material.
The latest commercially available NEG pumps from SAES use different getter materials like St 172, which is based on St 707[277]. The CapaciTorr® D 200 for example uses 28 g of St 172[278]. It is much more compact than the self built NEG pumps, sitting on a CF35 flange and with a length of only 88 mm. Still, a nitrogen pumping speed of $60\,\text{l}\,\text{s}^{-1}$ is achieved[278].

In conclusion, our NEG pump performs very well, especially in comparison to similar self built pumps. However, the performance of a commercial NEG pump is not reached. The self built pump can still be a reasonable low cost alternative, in particular when the extra weight and the space needed do not matter much.

D.4.2.4 Hydrogen pumping speed

I did not determine the pumping speed of our NEG pump for hydrogen directly. However, the hydrogen pumping speed of similar NEG pumps like the one from Kikuchi et al. and also of the CapaciTorr® D 200 is 3.3 times higher than the corresponding nitrogen pumping speed[274,278]. The pumps from Kodama et al. reach an even higher ratio[275]. Taking the factor of 3.3, our NEG pump achieves an extrapolated hydrogen pumping speed of $S_{H_2} = (105 \pm 20)\,\text{l}\,\text{s}^{-1}$.

D.5 Installation at the STM Chamber

After the pump had been successfully tested, it was mounted in January 2016 to the STM chamber of the STM apparatus built by Lars Mühlenberend[270]. A test in may 2016 showed that the NEG pump was able to further reduce the minimal pressure, dominated by hydrogen, by approximately 30% – although an ion getter pump, a titanium sublimation pump, and two TMPs were already running. Thus, the self built NEG pump is considered a success.

D.6 Saturation and Life Time

NEG materials bind various residual gases via surface sorption. At room temperature, those compounds deposit on the surface until it is completely covered. The pumping capability decreases and pumping comes to a halt. To restore the pumping capability, the surface of the NEG pump needs to be reactivated, which is done by heating the getter material. At higher temperatures, the pumped compounds become mobile and diffuse into the getter material. For St 707 20 min at 400 °C are sufficient for full activation[266]. However, a NEG pump cannot be reactivated an unlimited number of times, since the getter material becomes saturated at some point.

D.6.1 Pumping Capacity

The pumping capacity of the NEG pump depends of course on the gases pumped. In the brochure for SORB-AC wafer modules[279], which are also equipped with St 707 strips, SAES gives the following rule of thumb for the amount of gases pumped before a replacement of the getter is required:

$$n_{\mathrm{CO}} + n_{\mathrm{CO_2}} + \frac{1}{5}n_{\mathrm{O_2}} + \frac{1}{3}n_{\mathrm{H_2O}} + \frac{1}{4}n_{\mathrm{N_2}} = 2.2\,\mathrm{torr}\cdot\mathrm{l/g} \tag{D.69}$$

With 34 g of getter material, our pump has therefore a capacity of approximately 100 mbar l. To better assess this value, two rough estimates are done in the following:

1. I assume that the NEG pump has a pumping speed of $40\,\mathrm{l\,s^{-1}}$. In the chamber to be pumped be a residual gas of pure carbon monoxide at a pressure of 1×10^{-9} mbar. Then, the time needed to pump an amount of 100 mbar l is 81.3 years.

2. When venting the NEG pump, its surface will be completely covered by a monolayer of adsorbates. The St 707 strip has an effective getter surface of $1500\,\mathrm{cm^2\,m^{-1}}$[280], which gives an effective surface area of approximately $2500\,\mathrm{cm^2}$. With an assumed particle density of $1\times10^{16}\,\mathrm{cm^{-1}}$ this area is covered by approximately $2.5\times10^{19} = 4.2\times10^{-5}$ mol, which corresponds to an amount of approximately 1 mbar l. Thus, our NEG pump could be vented and reactivated one hundred times before reaching its maximal capacity.

D.6.2 Saturation

Even before reaching full surface coverage, the pumping capability of the NEG pump decreases significantly with the amount of pumped gases. In the St 707 brochure[266], the sorption characteristics of St 707 for hydrogen, carbon monoxide and nitrogen are given. At room temperature, the nitrogen pumping speed of an St 707 pellet with a surface area of $50\,\mathrm{mm}^2$ decreases by more than $50\,\%$ after an amount of $0.1\,\mathrm{cm}^3\mathrm{torr} \approx 7.5 \times 10^{-5}\,\mathrm{mbar\,l}$ had been pumped. By extrapolation from this value, an amount of $0.375\,\mathrm{mbar\,l}$ is obtained for our NEG pump. At a mean pumping speed of $20\,\mathrm{l\,s^{-1}}$, it would take approximately 217 days at a pressure of $1 \times 10^{-9}\,\mathrm{mbar}$ of pure nitrogen gas to reach that amount.
However, in a typical STM UHV chamber a pressure below $1 \times 10^{-9}\,\mathrm{mbar}$ is reached, which is dominated by hydrogen. In such an environment, it takes much longer to decrease the pumping speed of the NEG pump by $50\,\%$.
Normally, a reactivation of the NEG pump after each bake out of the chamber or at least every few years should be sufficient to obtain a good pumping capability.

D.6.3 Hydrogen Pumping

In contrast to other gases, hydrogen is not bound permanently to the getter material. Instead, it can be released into the vacuum. Furthermore, it dissolves into the getter material even at room temperature. In theory, a state of equilibrium will be reached after a long time at a given temperature T, with a homogeneous concentration Q of hydrogen in the getter material and a hydrogen partial pressure p in the vacuum. This state of equilibrium follows Sieverts' Law[266]:

$$\log_{10}\left(\frac{p}{\mathrm{torr}}\right) = 4.8 + 2 \cdot \log_{10}\left(Q \cdot \frac{\mathrm{g}}{\mathrm{torr} \cdot \mathrm{l}}\right) - \frac{6116\,\mathrm{K}}{T} \tag{D.70}$$

At room temperature and at a partial pressure of only $1 \times 10^{-11}\,\mathrm{mbar}$, this relation would lead to a hydrogen concentration of approximately $400\,\mathrm{mbar\,l\,g^{-1}}$. However, the St 707 already becomes brittle at a concentration of approximately $Q_{\mathrm{max}} = 27\,\mathrm{mbar\,l\,g^{-1}}$ [266]. It is recommended to not exceed this concentration, if embrittlement is a concern. Fortunately, it takes some time for the state of equilibrium to be reached in a typical UHV environment, as demonstrated in the following:
Under the assumption of a vacuum with a partial pressure of hydrogen of $p_{\mathrm{H_2}} = 1 \times 10^{-9}\,\mathrm{mbar}$, and with a hydrogen pumping speed of the NEG pump (34 g of St 707) to be $100\,\mathrm{l\,s^{-1}}$, the hydrogen concentration Q_{max} is reached after ≈300 years of continuous pumping.

But even when exposed to air (hydrogen partial pressure of approximately $6 \times 10^{-4}\,\mathrm{mbar}$ [281]), a critical hydrogen concentration is not reached immediately, since the NEG becomes passivated and the hydrogen pumping speed is decreased drastically. For long term storage, the St 707 should be kept under vacuum or in a protective gas atmosphere anyway.
During activation, the pumping capability for hydrogen will be fully restored. At a temperature of 400 °C and a typical pressure of $1 \times 10^{-6}\,\mathrm{mbar}$, the hydrogen concentration in the getter material is reduced to approximately $0.16\,\mathrm{mbar\,l\,g^{-1}}$.

D.7 Redesign

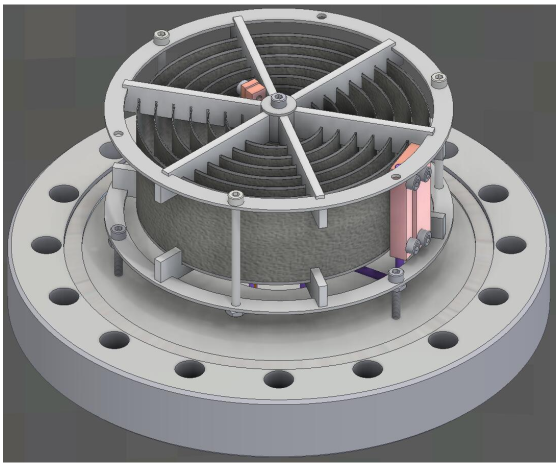

Figure D.4: Redesign of the NEG pump. The strip is arranged in a spiral, which results in a more compact pump.

Since the first attempt to build a NEG pump by ourselves was successful and there is still most of the St 707/CTAM/30D strip left (ca. 8.3 m), it suggests itself to build further NEG pumps. However, the experience gained during the construction of the first pump has stimulated a new design.

The redesign was made in Autodesk Inventor (just like the first design by Lars Mühlenberend) and is shown in Figure D.4. Again, a CF100 flange is used as a basis. In contrast to the first design, the NEG strip is arranged in a spiral. This layout brings multiple advantages: First, it should be easier to assemble the pump, since nearly no bending of the strip is needed, which is already delivered rolled up in a spiral. Secondly, the pump becomes much more compact and finally the area of the strip that is covered by other building parts is minimal. However, in this design only ca. 1 m of the getter strip is used. To increase the amount of getter material, it is possible to stack multiple of those spirals on top of each other. Alternatively, a larger basis flange could be used to allow for more turns of the strip. The final decision on which way to go, however, depends on the location of use.

Lastly, in the new design a single four-pin feedthrough is used for the heating current and the thermocouple together.

Acknowledgments

At this point I would like to thank all the people who have supported me in my scientific work by giving me advice and practical help. Without them this thesis would not have been possible. My special thanks goes to:

- Prof. Dr. Richard Berndt, who gave me the opportunity to work in his group and thereby not only provided me with an income, but also supplied me with excellent working equipment. He showed great confidence in me and gave me a lot of freedom to follow my own ideas. Nevertheless, he was always there when I needed him and helped with valuable suggestions – not least in the writing of this thesis.
- Prof. Dr. Kai Rossnagel, who kindly agreed to be the second reviewer of my work.
- Prof. Dr. Katharina Franke, who managed to write a third review of my work within a few days, which allowed us to keep the date for the defense.
- Dr. Alexander Weismann, who has stood by me in all scientific matters, be it measurements or repairs in the laboratory, analysis and interpretation of data, or physical understanding. Without his optimism I might have failed. My thanks in addition for proofreading this thesis.
- Jun.-Prof. Dr. Manuel Gruber, for his commitment on the subject of H_2Pc, contributing DFT calculations, and pushing the publication. His support in analyzing the data and improving the interaction model was crucial. Furthermore, he gave valuable suggestions for the measurements on H_2Pc and PbPc.
- Dr. Troels Markussen, for the fruitful cooperation on the subject of PbPc vibrations, especially for sacrificing his spare time to contribute excellent calculation results.
- Dr. Nicolás Lorente and Dr. Marie-Laure Bocquet, for stimulating discussion on molecular orbitals.
- Dr. Christian Ast, for helpful feedback to my conference posters.
- Dr. Thomas Jürgens, for his supervision in the early days of my doctorate and his technical aid with respect to the IT infrastructure. His kind support and perseverance, when not everything went as it should, were encouraging.
- René Woltmann, for his excellent technical support. More than once he saved the continuation of the measurements by manufacturing essential spare parts. On top of that, he built customized sample-holders and crucibles.

- Jörg Neubauer, for maintaining crucial laboratory equipment.
- Claudia Läufer and her predecessor Monika Seeger, for their kindness and help in all bureaucratic matters.
- the IT department of the physics institute under the direction of Ulf Stender, for installation and maintenance of the IT systems, and for providing me access to my data when the network failed.
- Dr. Chao Li, for the cooperation on the subject of AlPc. His cheerfulness has brightened my day.
- Marten Treichel, for the cooperation on the subject of MnPc, his help in laboratory tasks, and the joint Labview programming.
- Dr. Johannes Schöneberg, Michael Mohr, and Dr. Torben Jasper-Tönnies, for introducing me to the *4K* laboratory and for their support during the experiments.
- all other current and former work group members, for a very friendly working atmosphere. My thanks especially to those with whom I collaborated in the laboratories or went on conferences, in particular: Dr. Garima Saraswat, Sven Johannsen, Nafise Kalantari, Dr. Neda Noei, Ricarda Reuter, Niklas Ide, Dr. Alexandre Artaud, Dr. Tomoki Sueyoshi, Dr. Ling Fu, Dr. Jie Hou, Alexander Köbke, and Tyko Hansteen.
- my wife Louise-Marie, for her unconditional support, and for proofreading parts of this thesis.

Finally, I am grateful for funding from the European Union's Horizon 2020 program (COSMICS, grant No. 766726) and the Deutsche Forschungsgemeinschaft (SFB 677).

Bibliography

[1] Luh Yu. *Bound State in Superconductors with Paramagnetic Impurities.* Acta Physica Sinica, **21**(1):75–91 (1965). https://doi.org/10.7498/aps.21.75. [pp. 1, 23, and 38]

[2] Hiroyuki Shiba. *Classical Spins in Superconductors.* Progress of Theoretical Physics, **40**(3):435–451 (Jan 1968). https://doi.org/10.1143/PTP.40.435. [pp. 1, 23, and 38]

[3] A.I. Rusinov. *On the Theory of Gapless Superconductivity in Alloys Containing Paramagnetic Impurities.* JETP, **29**(6):1101 (Dec 1969). http://www.jetp.ac.ru/cgi-bin/e/index/e/29/6/p1101?a=list. [pp. 1, 23, and 38]

[4] Andreas Heimes, Panagiotis Kotetes, and Gerd Schön. *Majorana Fermions from Shiba States in an Antiferromagnetic Chain on Top of a Superconductor.* Physical Review B, **90**(6):060507 (Aug 2014). https://doi.org/10.1103/PhysRevB.90.060507. [p. 1]

[5] Falko Pientka, Yang Peng, Leonid Glazman, and Felix von Oppen. *Topological Superconducting Phase and Majorana Bound States in Shiba Chains.* Physica Scripta, **2015**(T164):014008 (Aug 2015). https://doi.org/10.1088/0031-8949/2015/T164/014008. [p. 1]

[6] Rémy Pawlak, Silas Hoffman, Jelena Klinovaja, Daniel Loss, and Ernst Meyer. *Majorana Fermions in Magnetic Chains.* Progress in Particle and Nuclear Physics, **107**:1–19 (Jul 2019). https://doi.org/10.1016/j.ppnp.2019.04.004. [p. 1]

[7] C.w.j. Beenakker. *Search for Majorana Fermions in Superconductors.* Annual Review of Condensed Matter Physics, **4**(1):113–136 (Apr 2013). https://doi.org/10.1146/annurev-conmatphys-030212-184337. [p. 1]

[8] Alexei Yu. Kitaev. *Fault-Tolerant Quantum Computation by Anyons.* Annals of Physics, **303**(1):2–30 (Jan 2003). https://doi.org/10.1016/S0003-4916(02)00018-0, first published on arXiv (1997): https://arxiv.org/abs/quant-ph/9707021. [p. 1]

[9] Jason Alicea. *New Directions in the Pursuit of Majorana Fermions in Solid State Systems.* Reports on Progress in Physics, **75**(7):076501 (Jun 2012). https://doi.org/10.1088/0034-4885/75/7/076501. [p. 1]

[10] Stevan Nadj-Perge, Ilya K. Drozdov, B. Andrei Bernevig, and Ali Yazdani. *Proposal for Realizing Majorana Fermions in Chains of Magnetic Atoms on a Superconductor.* Physical Review B, **88**(2):020407 (Jul 2013). https://doi.org/10.1103/PhysRevB.88.020407. [p. 1]

[11] Stevan Nadj-Perge, Ilya K. Drozdov, Jian Li, et al. *Observation of Majorana Fermions in Ferromagnetic Atomic Chains on a Superconductor.* Science, **346**(6209):602–607 (Oct 2014). https://doi.org/10.1126/science.1259327. [pp. 1, 23, and 24]

[12] Michael Ruby, Falko Pientka, Yang Peng, et al. *End States and Subgap Structure in Proximity-Coupled Chains of Magnetic Adatoms*. Physical Review Letters, **115**(19):197204 (Nov 2015). `https://doi.org/10.1103/PhysRevLett.115.197204`. [pp. 1 and 24]

[13] Rémy Pawlak, Marcin Kisiel, Jelena Klinovaja, et al. *Probing Atomic Structure and Majorana Wavefunctions in Mono-Atomic Fe Chains on Superconducting Pb Surface*. npj Quantum Information, **2**(1):1–5 (Nov 2016). `https://doi.org/10.1038/npjqi.2016.35`. [pp. 1 and 24]

[14] Benjamin E. Feldman, Mallika T. Randeria, Jian Li, et al. *High-Resolution Studies of the Majorana Atomic Chain Platform*. Nature Physics, **13**(3):286–291 (Mar 2017). `https://doi.org/10.1038/nphys3947`. [pp. 1 and 24]

[15] Michael Ruby, Benjamin W. Heinrich, Yang Peng, Felix von Oppen, and Katharina J. Franke. *Exploring a Proximity-Coupled Co Chain on Pb(110) as a Possible Majorana Platform*. Nano Letters, **17**(7):4473–4477 (Jul 2017). `https://doi.org/10.1021/acs.nanolett.7b01728`. [pp. 1 and 24]

[16] Sangjun Jeon, Yonglong Xie, Jian Li, et al. *Distinguishing a Majorana Zero Mode Using Spin-Resolved Measurements*. Science, **358**(6364):772–776 (Nov 2017). `https://doi.org/10.1126/science.aan3670`. [p. 1]

[17] Jian Li, Sangjun Jeon, Yonglong Xie, Ali Yazdani, and B. Andrei Bernevig. *Majorana Spin in Magnetic Atomic Chain Systems*. Physical Review B, **97**(12):125119 (Mar 2018). `https://doi.org/10.1103/PhysRevB.97.125119`. [p. 1]

[18] Howon Kim, Alexandra Palacio-Morales, Thore Posske, et al. *Toward Tailoring Majorana Bound States in Artificially Constructed Magnetic Atom Chains on Elemental Superconductors*. Science Advances, **4**(5):eaar5251 (May 2018). `https://doi.org/10.1126/sciadv.aar5251`. [pp. 1 and 24]

[19] A. Kamlapure, L. Cornils, J. Wiebe, and R. Wiesendanger. *Engineering the Spin Couplings in Atomically Crafted Spin Chains on an Elemental Superconductor*. Nature Communications, **9**(1):3253 (Aug 2018). `https://doi.org/10.1038/s41467-018-05701-8`. [pp. 1 and 24]

[20] Deung-Jang Choi, Nicolas Lorente, Jens Wiebe, et al. *Colloquium: Atomic Spin Chains on Surfaces*. Reviews of Modern Physics, **91**(4):041001 (Oct 2019). `https://doi.org/10.1103/RevModPhys.91.041001`. [p. 1]

[21] Eva Liebhaber, Lisa M. Rütten, Gaël Reecht, et al. *Quantum Spins and Hybridization in Artificially-Constructed Chains of Magnetic Adatoms on a Superconductor*. Nature Communications, **13**(1):2160 (Apr 2022). `https://doi.org/10.1038/s41467-022-29879-0`. [pp. 1 and 24]

[22] Gerbold C. Ménard, Sébastien Guissart, Christophe Brun, et al. *Coherent Long-Range Magnetic Bound States in a Superconductor*. Nature Physics, **11**(12):1013–1016 (Dec 2015). `https://doi.org/10.1038/nphys3508`. [pp. 1 and 24]

[23] Michael Ruby, Falko Pientka, Yang Peng, et al. *Tunneling Processes into Localized Subgap States in Superconductors*. Physical Review Letters, **115**(8):087001 (2015). `https://doi.org/10.1103/PhysRevLett.115.087001`. [pp. 1, 24, 87, and 141]

[24] Nino Hatter, Benjamin W. Heinrich, Daniela Rolf, and Katharina J. Franke. *Scaling of Yu-Shiba-Rusinov Energies in the Weak-Coupling Kondo Regime*. Nature Communications, **8**(1):2016 (2017). `https://doi.org/10.1038/s41467-017-02277-7`. [pp. 1, 24, and 38]

[25] Shawulienu Kezilebieke, Marc Dvorak, Teemu Ojanen, and Peter Liljeroth. *Coupled Yu-Shiba-Rusinov States in Molecular Dimers on NbSe*$_2$. Nano Letters, **18**(4):2311–2315 (Apr 2018). `https://doi.org/10.1021/acs.nanolett.7b05050`. [pp. 1, 10, 24, 38, 90, and 142]

[26] Michael Ruby, Benjamin W. Heinrich, Yang Peng, Felix von Oppen, and Katharina J. Franke. *Wave-Function Hybridization in Yu-Shiba-Rusinov Dimers*. Physical Review Letters, **120**(15):156803 (Apr 2018). `https://doi.org/10.1103/PhysRevLett.120.156803`. [pp. 1 and 24]

[27] Deung-Jang Choi, Carlos García Fernández, Edwin Herrera, et al. *Influence of Magnetic Ordering between Cr Adatoms on the Yu-Shiba-Rusinov States of the* $\beta-\mathrm{Bi_2Pd}$ *Superconductor*. Physical Review Letters, **120**(16):167001 (Apr 2018). `https://doi.org/10.1103/PhysRevLett.120.167001`. [pp. 1 and 24]

[28] Eva Liebhaber, Sergio Acero González, Rojhat Baba, et al. *Yu–Shiba–Rusinov States in the Charge-Density Modulated Superconductor NbSe*$_2$. Nano Letters, **20**(1):339–344 (Jan 2020). `https://doi.org/10.1021/acs.nanolett.9b03988`. [pp. 1 and 24]

[29] Haonan Huang, Jacob Senkpiel, Ciprian Padurariu, et al. *Spin-Dependent Tunneling between Individual Superconducting Bound States*. Physical Review Research, **3**(3):L032008 (Jul 2021). `https://doi.org/10.1103/PhysRevResearch.3.L032008`. [pp. 1, 24, and 128]

[30] Philip Beck, Lucas Schneider, Levente Rózsa, et al. *Spin-Orbit Coupling Induced Splitting of Yu-Shiba-Rusinov States in Antiferromagnetic Dimers*. Nature Communications, **12**(1):2040 (Apr 2021). `https://doi.org/10.1038/s41467-021-22261-6`. [pp. 1, 24, and 133]

[31] Archana Mishra, Pascal Simon, Timo Hyart, and Mircea Trif. *Yu-Shiba-Rusinov Qubit*. PRX Quantum, **2**(4):040347 (Dec 2021). `https://doi.org/10.1103/PRXQuantum.2.040347`. [p. 1]

[32] Luka Pavešić and Rok Žitko. *Qubit Based on Spin-Singlet Yu-Shiba-Rusinov States*. Physical Review B, **105**(7):075129 (Feb 2022). `https://doi.org/10.1103/PhysRevB.105.075129`. [p. 1]

[33] Ali Yazdani, B. A. Jones, C. P. Lutz, M. F. Crommie, and D. M. Eigler. *Probing the Local Effects of Magnetic Impurities on Superconductivity*. Science, **275**(5307):1767–1770 (1997). `https://doi.org/10.1126/science.275.5307.1767`. [pp. 1, 23, 24, 38, and 87]

[34] Shuai-Hua Ji, Tong Zhang, Ying-Shuang Fu, et al. *High-Resolution Scanning Tunneling Spectroscopy of Magnetic Impurity Induced Bound States in the Superconducting Gap of Pb Thin Films*. Physical Review Letters, **100**(22):226801 (Jun 2008). `https://doi.org/10.1103/PhysRevLett.100.226801`. [pp. 1, 23, 24, 26, and 142]

[35] K. J. Franke, G. Schulze, and J. I. Pascual. *Competition of Superconducting Phenomena and Kondo Screening at the Nanoscale*. Science, **332**(6032):940–944 (2011). `https://doi.org/10.1126/science.1202204`. [pp. 1, 23, 24, 26, 38, 81, and 142]

[36] Johannes Bauer, Jose I. Pascual, and Katharina J. Franke. *Microscopic Resolution of the Interplay of Kondo Screening and Superconducting Pairing: Mn-Phthalocyanine Molecules Adsorbed on Superconducting Pb(111).* Physical Review B, **87**(7):075125 (2013). https://doi.org/10.1103/PhysRevB.87.075125. [pp. 1 and 26]

[37] Nino Hatter, Benjamin W. Heinrich, Michael Ruby, Jose I. Pascual, and Katharina J. Franke. *Magnetic Anisotropy in Shiba Bound States Across a Quantum Phase Transition.* Nature Communications, **6**:8988 (Nov 2015). https://doi.org/10.1038/ncomms9988. [pp. 1, 24, 26, and 142]

[38] Haonan Huang, Ciprian Padurariu, Jacob Senkpiel, et al. *Tunnelling Dynamics between Superconducting Bound States at the Atomic Limit.* Nature Physics, pp. 1–5 (Jul 2020). https://doi.org/10.1038/s41567-020-0971-0. [pp. 1, 24, and 128]

[39] Michael Ruby, Yang Peng, Felix von Oppen, Benjamin W. Heinrich, and Katharina J. Franke. *Orbital Picture of Yu-Shiba-Rusinov Multiplets.* Physical Review Letters, **117**(18):186801 (Oct 2016). https://doi.org/10.1103/PhysRevLett.117.186801. [pp. 1, 24, 26, 133, and 141]

[40] Deung-Jang Choi, Carmen Rubio-Verdú, Joeri de Bruijckere, et al. *Mapping the Orbital Structure of Impurity Bound States in a Superconductor.* Nature Communications, **8**:15175 (May 2017). https://doi.org/10.1038/ncomms15175. [pp. 1, 24, 26, and 133]

[41] Haonan Huang, Robert Drost, Jacob Senkpiel, et al. *Quantum Phase Transitions and the Role of Impurity-Substrate Hybridization in Yu-Shiba-Rusinov States.* Communications Physics, **3**(1):1–9 (Nov 2020). https://doi.org/10.1038/s42005-020-00469-0. [pp. 1 and 24]

[42] L. Cornils, A. Kamlapure, L. Zhou, et al. *Spin-Resolved Spectroscopy of the Yu-Shiba-Rusinov States of Individual Atoms.* Physical Review Letters, **119**(19):197002 (Nov 2017). https://doi.org/10.1103/PhysRevLett.119.197002. [pp. 1 and 24]

[43] Dongfei Wang, Jens Wiebe, Ruidan Zhong, Genda Gu, and Roland Wiesendanger. *Spin-Polarized Yu-Shiba-Rusinov States in an Iron-Based Superconductor.* Physical Review Letters, **126**(7):076802 (Feb 2021). https://doi.org/10.1103/PhysRevLett.126.076802. [pp. 1 and 24]

[44] Lucas Schneider, Philip Beck, Jens Wiebe, and Roland Wiesendanger. *Atomic-Scale Spin-Polarization Maps Using Functionalized Superconducting Probes.* Science Advances, **7**(4):eabd7302 (Jan 2021). https://doi.org/10.1126/sciadv.abd7302. [pp. 1, 128, and 142]

[45] Jan Homberg, Alexander Weismann, Richard Berndt, and Manuel Gruber. *Inducing and Controlling Molecular Magnetism through Supramolecular Manipulation.* ACS Nano, **14**(12):17387–17395 (Nov 2020). https://doi.org/10.1021/acsnano.0c07574. [pp. 2, 37, 88, and 90]

[46] Blender Online Community. *Blender – A Free and Open-Source 3D Creation Suite.* Blender Foundation, Stichting Blender Foundation, Amsterdam (2022). http://www.blender.org. [p. 6]

[47] G. Binnig, H. Rohrer, Ch. Gerber, and E. Weibel. *Tunneling through a Controllable Vacuum Gap.* Applied Physics Letters, **40**(2):178–180 (Jan 1982). https://doi.org/10.

1063/1.92999. [p. 7]

[48] G. Binnig, H. Rohrer, Ch. Gerber, and E. Weibel. *Surface Studies by Scanning Tunneling Microscopy*. Physical Review Letters, **49**(1):57–61 (Jul 1982). https://doi.org/10.1103/PhysRevLett.49.57. [p. 7]

[49] Julian Chen. *Introduction to Scanning Tunneling Microscopy Third Edition*. Oxford University Press (Jan 2021). ISBN 978-0-19-885655-9. [p. 7]

[50] Ke Bian, Christoph Gerber, Andreas J. Heinrich, et al. *Scanning Probe Microscopy*. Nature Reviews Methods Primers, **1**(1):1–29 (May 2021). https://doi.org/10.1038/s43586-021-00033-2. [p. 7]

[51] Bert Voigtländer. *Scanning Probe Microscopy*. NanoScience and Technology. Springer, Berlin, Heidelberg (2015). ISBN 978-3-662-45240-0. https://doi.org/10.1007/978-3-662-45240-0_1. [pp. 7 and 8]

[52] G. Binnig, H. Rohrer, Ch. Gerber, and E. Weibel. *7 × 7 Reconstruction on Si(111) Resolved in Real Space*. Physical Review Letters, **50**(2):120–123 (Jan 1983). https://doi.org/10.1103/PhysRevLett.50.120. [p. 7]

[53] B. C. Stipe, M. A. Rezaei, and W. Ho. *Single-Molecule Vibrational Spectroscopy and Microscopy*. Science, **280**(5370):1732–1735 (Jun 1998). https://doi.org/10.1126/science.280.5370.1732. [pp. 7, 11, 85, and 87]

[54] Saw-Wai Hla, Kai-Felix Braun, Bernhard Wassermann, and Karl-Heinz Rieder. *Controlled Low-Temperature Molecular Manipulation of Sexiphenyl Molecules on Ag(111) Using Scanning Tunneling Microscopy*. Physical Review Letters, **93**(20):208302 (Nov 2004). https://doi.org/10.1103/PhysRevLett.93.208302. [p. 7]

[55] Peter Liljeroth, Jascha Repp, and Gerhard Meyer. *Current-Induced Hydrogen Tautomerization and Conductance Switching of Naphthalocyanine Molecules*. Science, **317**(5842):1203–1206 (Aug 2007). https://doi.org/10.1126/science.1144366. [p. 7]

[56] Alexander Sperl, Jörg Kröger, and Richard Berndt. *Controlled Metalation of a Single Adsorbed Phthalocyanine*. Angewandte Chemie, **123**:5406 – 5409 (2011). https://doi.org/10.1002/ange.201100950. [pp. 7, 45, and 121]

[57] Alexander Sperl, Jörg Kröger, and Richard Berndt. *Demetalation of a Single Organometallic Complex*. Journal of the American Chemical Society, **133**(29):11007–11009 (Jul 2011). https://doi.org/10.1021/ja203199q. [pp. 7 and 121]

[58] John G. Simmons. *Generalized Formula for the Electric Tunnel Effect between Similar Electrodes Separated by a Thin Insulating Film*. Journal of Applied Physics, **34**(6):1793–1803 (Jun 1963). https://doi.org/10.1063/1.1702682. [p. 7]

[59] J. Bardeen. *Tunnelling from a Many-Particle Point of View*. Physical Review Letters, **6**(2):57–59 (Jan 1961). https://doi.org/10.1103/PhysRevLett.6.57. [p. 8]

[60] J. Tersoff and D. R. Hamann. *Theory and Application for the Scanning Tunneling Microscope*. Physical Review Letters, **50**(25):1998–2001 (Jun 1983). https://doi.org/10.1103/PhysRevLett.50.1998. [p. 8]

[61] Jerry Tersoff and Donald R. Hamann. *Theory of the Scanning Tunneling Microscope.* Physical Review B, **31**(2):805–813 (Jan 1985). `https://doi.org/10.1103/PhysRevB.31.805`. [pp. 8 and 9]

[62] MathWorks. *MATLAB – The Language of Technical Computing.* The MathWorks Inc., Natick, Massachusetts (2021). Multiple versions used including: 8.5.0 (R2015), 9.6.0 (R2019a), 9.9.0 (R2020b), 9.10.0 (R2021a), `https://www.mathworks.com/products/matlab.html`. [pp. 8 and 32]

[63] M. Ziegler, N. Néel, A. Sperl, J. Kröger, and R. Berndt. *Local Density of States from Constant-Current Tunneling Spectra.* Physical Review B, **80**(12):125402 (Sep 2009). `https://doi.org/10.1103/PhysRevB.80.125402`. [pp. 9 and 113]

[64] L. Esaki and P. J. Stiles. *Study of Electronic Band Structures by Tunneling Spectroscopy: Bismuth.* Physical Review Letters, **14**(22):902–904 (May 1965). `https://doi.org/10.1103/PhysRevLett.14.902`. [p. 9]

[65] Mike Meade. *Lock-in Amplifiers: Principles and Applications.* IEE Electrical Measurement Series. Peter Peregrinus Ltd, London (1983). ISBN 0-906048-94-X. e-edition (2013) available: `http://archive.org/details/Lock-inAmplifiersPrinciplesAndApplications`. [p. 9]

[66] Laurent Limot. *Broadening in Scanning Tunneling Spectroscopy.* Internal Document (2005). [pp. 9 and 10]

[67] Manuel Gruber, Alexander Weismann, and Richard Berndt. *The Kondo Resonance Line Shape in Scanning Tunnelling Spectroscopy: Instrumental Aspects.* Journal of Physics: Condensed Matter, **30**(42):424001 (2018). `https://doi.org/10.1088/1361-648X/aadfa3`. [pp. 9 and 56]

[68] Michael Ruby, Benjamin W. Heinrich, Jose I. Pascual, and Katharina J. Franke. *Experimental Demonstration of a Two-Band Superconducting State for Lead Using Scanning Tunneling Spectroscopy.* Physical Review Letters, **114**(15):157001 (2015). `https://doi.org/10.1103/PhysRevLett.114.157001`. [pp. 10, 22, 38, and 78]

[69] R. C. Jaklevic and J. Lambe. *Molecular Vibration Spectra by Inelastic Electron Tunneling.* Physical Review, **165**(3):821–832 (Jan 1968). `https://doi.org/10.1103/PhysRev.165.821`. [p. 10]

[70] Markus Ternes. *Scanning Tunneling Spectroscopy at the Single Atom Scale.* Ph.D. thesis, École Polytechnique Fédérale de Lausanne, Lausanne (2006). `https://infoscience.epfl.ch/record/64356`. [p. 10]

[71] Martin Ziegler. *Exploring Structural, Electronic, Magnetic, and Vibrational Properties of Nanostructures with a Scanning Tunneling Microscope.* Ph.D. thesis, Christian Albrechts Universität zu Kiel, Kiel (2009). `https://macau.uni-kiel.de/receive/diss_mods_00004416`. [p. 10]

[72] J. Klein, A. Léger, M. Belin, D. Défourneau, and M. J. L. Sangster. *Inelastic-Electron-Tunneling Spectroscopy of Metal-Insulator-Metal Junctions.* Physical Review B, **7**(6):2336–2348 (Mar 1973). `https://doi.org/10.1103/PhysRevB.7.2336`. [p. 10]

[73] J. M. Rowell, P. W. Anderson, and D. E. Thomas. *Image of the Phonon Spectrum in the Tunneling Characteristic Between Superconductors*. Physical Review Letters, **10**(8):334–336 (Apr 1963). https://doi.org/10.1103/PhysRevLett.10.334. [p. 11]

[74] H. Gawronski, M. Mehlhorn, and K. Morgenstern. *Imaging Phonon Excitation with Atomic Resolution*. Science, **319**(5865):930–933 (Feb 2008). https://doi.org/10.1126/science.1152473. [p. 11]

[75] L. Vitali, M. A. Schneider, K. Kern, L. Wirtz, and A. Rubio. *Phonon and Plasmon Excitation in Inelastic Electron Tunneling Spectroscopy of Graphite*. Physical Review B, **69**(12):121414 (Mar 2004). https://doi.org/10.1103/PhysRevB.69.121414. [p. 11]

[76] J. K. Gimzewski, J. K. Sass, R. R. Schlitter, and J. Schott. *Enhanced Photon Emission in Scanning Tunnelling Microscopy*. Europhysics Letters (EPL), **8**(5):435–440 (Mar 1989). https://doi.org/10.1209/0295-5075/8/5/007. [p. 11]

[77] Edward McCann and Vladimir I. Fal'ko. *A Tunnel Junction between a Ferromagnet and a Normal Metal: Magnon-Assisted Contribution to Thermopower and Conductance*. Journal of Magnetism and Magnetic Materials, **268**(1):123–131 (Jan 2004). https://doi.org/10.1016/S0304-8853(03)00485-2. [p. 11]

[78] C. L. Gao, A. Ernst, G. Fischer, et al. *Spin Wave Dispersion on the Nanometer Scale*. Physical Review Letters, **101**(16):167201 (Oct 2008). https://doi.org/10.1103/PhysRevLett.101.167201. [p. 11]

[79] T. Balashov, A. F. Takács, M. Däne, et al. *Inelastic Electron-Magnon Interaction and Spin Transfer Torque*. Physical Review B, **78**(17):174404 (Nov 2008). https://doi.org/10.1103/PhysRevB.78.174404. [p. 11]

[80] A. J. Heinrich, J. A. Gupta, C. P. Lutz, and D. M. Eigler. *Single-Atom Spin-Flip Spectroscopy*. Science, **306**(5695):466–469 (Oct 2004). https://doi.org/10.1126/science.1101077. [p. 11]

[81] R. C. Jaklevic and J. Lambe. *Molecular Vibration Spectra by Electron Tunneling*. Physical Review Letters, **17**(22):1139–1140 (Nov 1966). https://doi.org/10.1103/PhysRevLett.17.1139. [pp. 11 and 85]

[82] N. Lorente and M. Persson. *Theory of Single Molecule Vibrational Spectroscopy and Microscopy*. Physical Review Letters, **85**(14):2997–3000 (Oct 2000). https://doi.org/10.1103/PhysRevLett.85.2997. [pp. 11 and 86]

[83] B. N. J. Persson and A. Baratoff. *Inelastic Electron Tunneling from a Metal Tip: The Contribution from Resonant Processes*. Physical Review Letters, **59**(3):339–342 (Jul 1987). https://doi.org/10.1103/PhysRevLett.59.339. [p. 11]

[84] Jing Guo, Jing-Tao Lü, Yexin Feng, et al. *Nuclear Quantum Effects of Hydrogen Bonds Probed by Tip-Enhanced Inelastic Electron Tunneling*. Science, **352**(6283):321–325 (Apr 2016). https://doi.org/10.1126/science.aaf2042. [p. 12]

[85] B. W. Heinrich, L. Braun, J. I. Pascual, and K. J. Franke. *Protection of Excited Spin States by a Superconducting Energy Gap*. Nature Physics, **9**(12):765–768 (Dec 2013). https://doi.org/10.1038/nphys2794. [p. 12]

[86] K. Grove-Rasmussen, H. I. Jørgensen, B. M. Andersen, et al. *Superconductivity-Enhanced Bias Spectroscopy in Carbon Nanotube Quantum Dots.* Physical Review B, **79**(13):134518 (Apr 2009). `https://doi.org/10.1103/PhysRevB.79.134518`. [p. 12]

[87] Sifan You, Jing-Tao Lü, Jing Guo, and Ying Jiang. *Recent Advances in Inelastic Electron Tunneling Spectroscopy.* Advances in Physics: X, **2**(3):907–936 (May 2017). `https://doi.org/10.1080/23746149.2017.1372215`. [p. 13]

[88] H. Kamerlingh Onnes. *The Resistance of Pure Mercury at Helium Temperatures.* Communications from the Laboratory of Physics at the University of Leiden, **12**(120):1 (1911). [p. 14]

[89] H. Kamerlingh Onnes. *Further Experiments with Liquid Helium. C. On the Change of Electric Resistance of Pure Metals at Very Low Temperatures Etc. IV. The Resistance of Pure Mercury at Helium Temperatures.* KNAW, Proceedings, **13 II**:1274–1276 (1911). `https://www.dwc.knaw.nl/toegangen/digital-library-knaw/?pagetype=publDetail&pId=PU00013358`. [p. 14]

[90] H. Kamerlingh Onnes. *The Liquefaction of Helium.* KNAW, Proceedings, **11**:168–185 (1909). `https://www.dwc.knaw.nl/toegangen/digital-library-knaw/?pagetype=publDetail&pId=PU00013525`. [p. 14]

[91] G. W. Webb, F. Marsiglio, and J. E. Hirsch. *Superconductivity in the Elements, Alloys and Simple Compounds.* Physica C: Superconductivity and its Applications, **514**:17–27 (Jul 2015). `https://doi.org/10.1016/j.physc.2015.02.037`. [p. 14]

[92] P. J. Ford and G. A. Saunders. *The Rise of the Superconductors.* CRC Press, Boca Raton (Oct 2004). ISBN 978-0-203-64631-1. `https://doi.org/10.1201/9780203646311`. [p. 14]

[93] Elliot Snider, Nathan Dasenbrock-Gammon, Raymond McBride, et al. *Room-Temperature Superconductivity in a Carbonaceous Sulfur Hydride.* Nature, **586**(7829):373–377 (Oct 2020). `https://doi.org/10.1038/s41586-020-2801-z`. [p. 14]

[94] Neeraj Khare (ed.). *Handbook of High-Temperature Superconductor.* CRC Press, New York (May 2003). ISBN 978-0-429-21384-7. `https://doi.org/10.1201/9780203911846`. [p. 14]

[95] Fred M. Ašner. *High Field Superconducting Magnets.* Oxford Science Publications. Clarendon Press, Oxford (1999). ISBN 978-0-19-851764-1. [p. 14]

[96] John Clarke and Alex I. Braginski (eds.). *The SQUID Handbook, Volume 1.* Wiley-VCH Verlag GmbH & Co. KGaA, Weinheim (May 2004). ISBN 3-527-40229-2. `https://doi.org/10.1002/3527603646.fmatter`. [p. 14]

[97] Mathias Noe, Frank Merschel, Lutz Hofmann, et al. *New Medium Instead of High Voltage Power Systems by Using High-Temperature Superconductivity; Neue Mittel, statt konventioneller Hochspannungsnetze durch Hochtemperatur-Supraleitung.* In *ETG-Fachbericht*, vol. 130. VDE Verlag GmbH Berlin, Offenbach, Würzburg (Jul 2011). ISBN 978-3-8007-3376-7. `https://www.osti.gov/etdeweb/biblio/21533325`. [p. 14]

[98] Mark Stemmle, Frank Merschel, Mathias Noe, and Achim Hobl. *AmpaCity — Advanced Superconducting Medium Voltage System for Urban Area Power Supply.* In *2014 IEEE PES T D Conference and Exposition*, pp. 1–5 (Apr 2014). `https://doi.org/10.1109/`

TDC.2014.6863566. [p. 14]

[99] Morten Kjaergaard, Mollie E. Schwartz, Jochen Braumüller, et al. *Superconducting Qubits: Current State of Play*. Annual Review of Condensed Matter Physics, **11**(1):369–395 (2020). https://doi.org/10.1146/annurev-conmatphys-031119-050605. [p. 14]

[100] He-Liang Huang, Dachao Wu, Daojin Fan, and Xiaobo Zhu. *Superconducting Quantum Computing: A Review*. Science China Information Sciences, **63**(8):180501 (Jul 2020). https://doi.org/10.1007/s11432-020-2881-9. [p. 14]

[101] Frank Arute, Kunal Arya, Ryan Babbush, et al. *Quantum Supremacy Using a Programmable Superconducting Processor*. Nature, **574**(7779):505–510 (Oct 2019). https://doi.org/10.1038/s41586-019-1666-5. [p. 14]

[102] *IBM Unveils Breakthrough 127-Qubit Quantum Processor*. IBM Newsroom (Nov 2021). https://newsroom.ibm.com/2021-11-16-IBM-Unveils-Breakthrough-127-Qubit-Quantum-Processor. [p. 14]

[103] Matthew Sparkes. *IBM Creates Largest Ever Superconducting Quantum Computer* (Nov 2021). https://www.newscientist.com/article/2297583-ibm-creates-largest-ever-superconducting-quantum-computer/. [p. 14]

[104] Michael Tinkham. *Introduction to Superconductivity*. McGraw-Hill, New York, second edition edn. (1996). ISBN 0-07-064878-6. [pp. 14, 15, and 17]

[105] Rudolf Gross and Achim Marx. *Applied Superconductivity : Josephson Effect and Superconducting Electronics* (2009). https://www.semanticscholar.org/paper/Applied-Superconductivity-%3A-Josephson-Effect-and-Gross-Marx/d3fb5141e0203f234e879872febf9f0e522d427e. [pp. 14 and 15]

[106] Harald Ibach and Hans Lüth. *Supraleitung*. In *Festkörperphysik: Einführung in die Grundlagen*, Springer-Lehrbuch, pp. 287–360. Springer, Berlin, Heidelberg (2009). ISBN 978-3-540-85795-2. https://doi.org/10.1007/978-3-540-85795-2_10. [p. 14]

[107] J. Bardeen, L. N. Cooper, and J. R. Schrieffer. *Theory of Superconductivity*. Physical Review, **108**(5):1175–1204 (Dec 1957). https://doi.org/10.1103/PhysRev.108.1175. [pp. 15, 16, and 17]

[108] J. Bardeen, L. N. Cooper, and J. R. Schrieffer. *Microscopic Theory of Superconductivity*. Physical Review, **106**(1):162–164 (Apr 1957). https://doi.org/10.1103/PhysRev.106.162. [p. 15]

[109] Leon N. Cooper. *Bound Electron Pairs in a Degenerate Fermi Gas*. Physical Review, **104**(4):1189–1190 (Nov 1956). https://doi.org/10.1103/PhysRev.104.1189. [p. 15]

[110] Herbert Fröhlich. *Interaction of Electrons with Lattice Vibrations*. Proceedings of the Royal Society of London. Series A. Mathematical and Physical Sciences, **215**(1122):291–298 (Dec 1952). https://doi.org/10.1098/rspa.1952.0212. [p. 15]

[111] D. J. Scalapino, Y. Wada, and J. C. Swihart. *Strong-Coupling Superconductor at Nonzero Temperature*. Physical Review Letters, **14**(4):102–105 (Jan 1965). https://doi.org/10.1103/PhysRevLett.14.102. [p. 15]

[112] D. J. Scalapino, J. R. Schrieffer, and J. W. Wilkins. *Strong-Coupling Superconductivity. I.* Physical Review, **148**(1):263–279 (Aug 1966). https://doi.org/10.1103/PhysRev.148.263. [p. 15]

[113] G.M. Eliashberg. *Interactions between Electrons and Lattice Vibrations in a Superconductor.* JETP, **11**(3):696–702 (Sep 1960). http://jetp.ras.ru/cgi-bin/e/index/e/11/3/p696?a=list. [p. 15]

[114] Bascom S. Deaver and William M. Fairbank. *Experimental Evidence for Quantized Flux in Superconducting Cylinders.* Physical Review Letters, **7**(2):43–46 (Jul 1961). https://doi.org/10.1103/PhysRevLett.7.43. [p. 15]

[115] R. Doll and M. Näbauer. *Experimental Proof of Magnetic Flux Quantization in a Superconducting Ring.* Physical Review Letters, **7**(2):51–52 (Jul 1961). https://doi.org/10.1103/PhysRevLett.7.51. [p. 15]

[116] R. D. Parks. *Quantized Magnetic Flux in Superconductors: Experiments Confirm Fritz London's Early Concept That Superconductivity Is a Macroscopic Quantum Phenomenon.* Science, **146**(3650):1429–1435 (Dec 1964). https://doi.org/10.1126/science.146.3650.1429. [p. 15]

[117] B. D. Josephson. *Possible New Effects in Superconductive Tunnelling.* Physics Letters, **1**(7):251–253 (Jul 1962). https://doi.org/10.1016/0031-9163(62)91369-0. [pp. 15 and 20]

[118] N. N. Bogoliubov. *A New Method in the Theory of Superconductivity. I.* JETP, **7**(1):41 (Jul 1958). http://www.jetp.ac.ru/cgi-bin/e/index/e/7/1/p41?a=list. [p. 16]

[119] Ivar Giaever. *Energy Gap in Superconductors Measured by Electron Tunneling.* Physical Review Letters, **5**(4):147–148 (Aug 1960). https://doi.org/10.1103/PhysRevLett.5.147. [p. 16]

[120] Robert C. Dynes, Venkatesh Narayanamurti, and J. P. Garno. *Direct Measurement of Quasiparticle-Lifetime Broadening in a Strong-Coupled Superconductor.* Physical Review Letters, **41**(21):1509–1512 (1978). https://doi.org/10.1103/PhysRevLett.41.1509. [p. 16]

[121] Bernhard Mühlschlegel. *Die thermodynamischen Funktionen des Supraleiters.* Zeitschrift für Physik, **155**(3):313–327 (Jun 1959). https://doi.org/10.1007/BF01332932. [p. 17]

[122] Ivar Giaever and Karl Megerle. *Study of Superconductors by Electron Tunneling.* Physical Review, **122**(4):1101–1111 (May 1961). https://doi.org/10.1103/PhysRev.122.1101. [p. 17]

[123] Pierre-Gilles de Gennes. *Superconductivity of Metals and Alloys.* W.A. Benjamin, New York (1966). [p. 18]

[124] Supriyo Datta, Philip F Bagwell, and M P Anantram. *Scattering Theory of Transport for Mesoscopic Superconductors.* ECE Technical Reports. Purdue University, West Lafayette, Indiana (Jan 1996). https://docs.lib.purdue.edu/ecetr/107. [pp. 18 and 19]

[125] Jian-Xin Zhu. *Bogoliubov-de Gennes Method and Its Applications*, vol. 924 of *Lecture Notes in Physics.* Springer International Publishing, Cham, first edn. (2016). ISBN 978-3-319-31312-2. https://doi.org/10.1007/978-3-319-31314-6. [pp. 18, 19, and 27]

[126] A. F. Andreev. *The Thermal Conductivity of the Intermediate State in Superconductors.* Soviet Physics JETP, **19**(5):1228–1231 (Nov 1964). `http://www.jetp.ac.ru/cgi-bin/e/index/e/19/5/p1228?a=list`. [p. 18]

[127] M. Octavio, M. Tinkham, G. E. Blonder, and T. M. Klapwijk. *Subharmonic Energy-Gap Structure in Superconducting Constrictions.* Physical Review B, **27**(11):6739–6746 (Jun 1983). `https://doi.org/10.1103/PhysRevB.27.6739`. [p. 20]

[128] Elke Scheer, Nicolás Agraït, Juan Carlos Cuevas, et al. *The Signature of Chemical Valence in the Electrical Conduction through a Single-Atom Contact.* Nature, **394**(6689):154–157 (Jul 1998). `https://doi.org/10.1038/28112`. [p. 20]

[129] O. Naaman, W. Teizer, and R. C. Dynes. *Fluctuation Dominated Josephson Tunneling with a Scanning Tunneling Microscope.* Physical Review Letters, **87**(9):097004 (Aug 2001). `https://doi.org/10.1103/PhysRevLett.87.097004`. [p. 20]

[130] P. Townsend and J. Sutton. *Investigation by Electron Tunneling of the Superconducting Energy Gaps in Nb, Ta, Sn, and Pb.* Physical Review, **128**(2):591–595 (Oct 1962). `https://doi.org/10.1103/PhysRev.128.591`. [p. 22]

[131] G. I. Rochlin. *Determination of the Anisotropy of the Energy Gap in Superconducting Pb by Superconductive Tunneling.* Physical Review, **153**(2):513–532 (Jan 1967). `https://doi.org/10.1103/PhysRev.153.513`. [p. 22]

[132] B. L. Blackford and R. H. March. *Tunneling Investigation of Energy-Gap Anisotropy in Superconducting Bulk Pb.* Physical Review, **186**(2):397–399 (Oct 1969). `https://doi.org/10.1103/PhysRev.186.397`. [p. 22]

[133] G. I. Lykken, A. L. Geiger, K. S. Dy, and E. N. Mitchell. *Measurement of the Superconducting Energy Gap and Fermi Velocity in Single-Crystal Lead Films by Electron Tunneling.* Physical Review B, **4**(5):1523–1530 (Sep 1971). `https://doi.org/10.1103/PhysRevB.4.1523`. [p. 22]

[134] Alan J. Bennett. *Theory of the Anisotropic Energy Gap in Superconducting Lead.* Physical Review, **140**(6A):A1902–A1920 (Dec 1965). `https://doi.org/10.1103/PhysRev.140.A1902`. [p. 22]

[135] Hyoung Joon Choi, David Roundy, Hong Sun, Marvin L. Cohen, and Steven G. Louie. *The Origin of the Anomalous Superconducting Properties of MgB 2.* Nature, **418**(6899):758–760 (Aug 2002). `https://doi.org/10.1038/nature00898`. [p. 22]

[136] A. Floris, A. Sanna, S. Massidda, and E. K. U. Gross. *Two-Band Superconductivity in Pb from* Ab Initio *Calculations.* Physical Review B, **75**(5) (Feb 2007). `https://doi.org/10.1103/PhysRevB.75.054508`. [p. 22]

[137] Benjamin W. Heinrich, Jose I. Pascual, and Katharina J. Franke. *Single Magnetic Adsorbates on S-Wave Superconductors.* Progress in Surface Science, **93**(1):1–19 (2018). `https://doi.org/10.1016/j.progsurf.2018.01.001`. [pp. 23, 25, 38, and 81]

[138] Michael A. Woolf and F. Reif. *Effect of Magnetic Impurities on the Density of States of Superconductors.* Physical Review, **137**(2A):A557–A564 (Jan 1965). `https://doi.org/10.1103/PhysRev.137.A557`. [p. 23]

[139] Michael E. Flatté and Jeff M. Byers. *Local Electronic Structure of a Single Magnetic Impurity in a Superconductor*. Physical Review Letters, **78**(19):3761–3764 (1997). `https://doi.org/10.1103/PhysRevLett.78.3761`. [pp. 23, 26, and 27]

[140] J. Brand, S. Gozdzik, N. Néel, et al. *Electron and Cooper-Pair Transport Across a Single Magnetic Molecule Explored With a Scanning Tunneling Microscope*. Physical Review B, **97**(19):195429 (2018). `https://doi.org/10.1103/PhysRevB.97.195429`. [pp. 24, 38, and 142]

[141] Laëtitia Farinacci, Gelavizh Ahmadi, Gaël Reecht, et al. *Tuning the Coupling of an Individual Magnetic Impurity to a Superconductor: Quantum Phase Transition and Transport*. Physical Review Letters, **121**(19):196803 (2018). `https://doi.org/10.1103/PhysRevLett.121.196803`. [pp. 24, 47, and 90]

[142] Luigi Malavolti, Matteo Briganti, Max Hänze, et al. *Tunable Spin–Superconductor Coupling of Spin 1/2 Vanadyl Phthalocyanine Molecules*. Nano Letters, **18**(12):7955–7961 (2018). `https://doi.org/10.1021/acs.nanolett.8b03921`. [pp. 24, 26, 38, and 47]

[143] Laëtitia Farinacci, Gelavizh Ahmadi, Michael Ruby, et al. *Interfering Tunneling Paths through Magnetic Molecules on Superconductors: Asymmetries of Kondo and Yu-Shiba-Rusinov Resonances*. Physical Review Letters, **125**(25):256805 (Dec 2020). `https://doi.org/10.1103/PhysRevLett.125.256805`. [p. 24]

[144] Carmen Rubio-Verdú, Javier Zaldívar, Rok Žitko, and Jose Ignacio Pascual. *Coupled Yu-Shiba-Rusinov States Induced by a Many-Body Molecular Spin on a Superconductor*. Physical Review Letters, **126**(1) (Jan 2021). `https://doi.org/10.1103/PhysRevLett.126.017001`. [pp. 24 and 87]

[145] Felix Küster, Ana M. Montero, Filipe S. M. Guimarães, et al. *Correlating Josephson Supercurrents and Shiba States in Quantum Spins Unconventionally Coupled to Superconductors*. Nature Communications, **12**(1):1108 (Feb 2021). `https://doi.org/10.1038/s41467-021-21347-5`. [p. 24]

[146] Felix Küster, Sascha Brinker, Samir Lounis, Stuart S. P. Parkin, and Paolo Sessi. *Long Range and Highly Tunable Interaction between Local Spins Coupled to a Superconducting Condensate*. Nature Communications, **12**(1):6722 (Nov 2021). `https://doi.org/10.1038/s41467-021-26802-x`. [p. 24]

[147] Shawulienu Kezilebieke, Rok Žitko, Marc Dvorak, Teemu Ojanen, and Peter Liljeroth. *Observation of Coexistence of Yu-Shiba-Rusinov States and Spin-Flip Excitations*. Nano Letters, **19**(7):4614–4619 (2019). `https://doi.org/10.1021/acs.nanolett.9b01583`. [pp. 24 and 38]

[148] Xing Yang, Yuan Yuan, Yang Peng, et al. *Observation of Short-Range Yu-Shiba-Rusinov States with Threefold Symmetry in Layered Superconductor 2H-NbSe 2*. Nanoscale (2020). `https://doi.org/10.1039/D0NR01383H`. [p. 24]

[149] Anand Kamlapure, Lasse Cornils, Rok Žitko, et al. *Correlation of Yu–Shiba–Rusinov States and Kondo Resonances in Artificial Spin Arrays on an s-Wave Superconductor*. Nano Letters, **21**(16):6748–6755 (Aug 2021). `https://doi.org/10.1021/acs.nanolett.1c00387`. [p. 24]

[150] Lucas Schneider, Manuel Steinbrecher, Levente Rózsa, et al. *Magnetism and In-Gap States of 3d Transition Metal Atoms on Superconducting Re.* npj Quantum Materials, **4**(1) (Dec 2019). https://doi.org/10.1038/s41535-019-0179-7. [p. 24]

[151] Damianos Chatzopoulos, Doohee Cho, Koen M. Bastiaans, et al. *Spatially Dispersing Yu-Shiba-Rusinov States in the Unconventional Superconductor FeTe0.55Se0.45.* Nature Communications, **12**(1):298 (Jan 2021). https://doi.org/10.1038/s41467-020-20529-x. [p. 24]

[152] Gerbold C. Ménard, Sébastien Guissart, Christophe Brun, et al. *Two-Dimensional Topological Superconductivity in Pb/Co/Si(111).* Nature Communications, **8**(1):2040 (Dec 2017). https://doi.org/10.1038/s41467-017-02192-x. [p. 24]

[153] Jacob Senkpiel, Carmen Rubio-Verdú, Markus Etzkorn, et al. *Robustness of Yu-Shiba-Rusinov Resonances in the Presence of a Complex Superconducting Order Parameter.* Physical Review B, **100**(1):014502 (Jul 2019). https://doi.org/10.1103/PhysRevB.100.014502. [p. 24]

[154] Hao Ding, Yuwen Hu, Mallika T. Randeria, et al. *Tuning Interactions between Spins in a Superconductor.* Proceedings of the National Academy of Sciences, **118**(14):e2024837118 (Apr 2021). https://doi.org/10.1073/pnas.2024837118. [p. 24]

[155] Haonan Huang, Robert Drost, Jacob Senkpiel, et al. *Magnetic Impurities on Superconducting Surfaces: Phase Transitions and the Role of Impurity-Substrate Hybridization.* arXiv, p. 1912.05607 (2019). https://doi.org/10.1038/s42005-020-00469-0. [pp. 24 and 47]

[156] S. Karan, H. Huang, C. Padurariu, et al. *Superconducting Quantum Interference at the Atomic Scale.* arXiv:2102.12521 [cond-mat.supr-con] (Feb 2021). http://arxiv.org/abs/2102.12521. [pp. 24 and 128]

[157] D. Jacob, M. Soriano, and J. J. Palacios. *Kondo Effect and Spin Quenching in High-Spin Molecules on Metal Substrates.* Physical Review B, **88**(13):134417 (Oct 2013). https://doi.org/10.1103/PhysRevB.88.134417. [pp. 24 and 142]

[158] Markus Etzkorn, Matthias Eltschka, Berthold Jäck, Christian R. Ast, and Klaus Kern. *Mapping of Yu-Shiba-Rusinov States from an Extended Scatterer.* arXiv:1807.00646 [cond-mat.supr-con] (Jul 2018). http://arxiv.org/abs/1807.00646. [p. 24]

[159] R. S. Deacon, Y. Tanaka, A. Oiwa, et al. *Tunneling Spectroscopy of Andreev Energy Levels in a Quantum Dot Coupled to a Superconductor.* Physical Review Letters, **104**(7):076805 (Feb 2010). https://doi.org/10.1103/PhysRevLett.104.076805. [p. 24]

[160] B. M. Andersen, K. Flensberg, V. Koerting, and J. Paaske. *Nonequilibrium Transport through a Spinful Quantum Dot with Superconducting Leads.* Physical Review Letters, **107**(25):256802 (Dec 2011). https://doi.org/10.1103/PhysRevLett.107.256802. [p. 24]

[161] Anders Jellinggaard, Kasper Grove-Rasmussen, Morten Hannibal Madsen, and Jesper Nygård. *Tuning Yu-Shiba-Rusinov States in a Quantum Dot.* Physical Review B, **94**(6):064520 (Aug 2016). https://doi.org/10.1103/PhysRevB.94.064520. [p. 24]

[162] K. Grove-Rasmussen, G. Steffensen, A. Jellinggaard, et al. *Yu–Shiba–Rusinov Screening of Spins in Double Quantum Dots*. Nature Communications, **9**(1):2376 (Jun 2018). https://doi.org/10.1038/s41467-018-04683-x. [p. 24]

[163] A. García Corral, D. M. T. van Zanten, K. J. Franke, et al. *Magnetic-Field-Induced Transition in a Quantum Dot Coupled to a Superconductor*. Physical Review Research, **2**(1):012065 (Mar 2020). https://doi.org/10.1103/PhysRevResearch.2.012065. [p. 24]

[164] Zoltán Scherübl, Gergő Fülöp, Cătălin Paşcu Moca, et al. *Large Spatial Extension of the Zero-Energy Yu–Shiba–Rusinov State in a Magnetic Field*. Nature Communications, **11**(1):1834 (Apr 2020). https://doi.org/10.1038/s41467-020-15322-9. [p. 24]

[165] G. O. Steffensen, J. C. Estrada Saldaña, A. Vekris, et al. *Direct Transport between Superconducting Subgap States in a Double Quantum Dot*. Physical Review B, **105**(16):L161302 (Apr 2022). https://doi.org/10.1103/PhysRevB.105.L161302. [p. 24]

[166] Joshua O. Island, Rocco Gaudenzi, Joeri de Bruijckere, et al. *Proximity-Induced Shiba States in a Molecular Junction*. Physical Review Letters, **118**(11):117001 (Mar 2017). https://doi.org/10.1103/PhysRevLett.118.117001. [p. 24]

[167] A. V. Balatsky, I. Vekhter, and Jian-Xin Zhu. *Impurity-Induced States in Conventional and Unconventional Superconductors*. Reviews of Modern Physics, **78**(2):373–433 (May 2006). https://doi.org/10.1103/RevModPhys.78.373. [pp. 25 and 26]

[168] Jun Kondo. *Resistance Minimum in Dilute Magnetic Alloys*. Progress of Theoretical Physics, **32**(1):37–49 (Jul 1964). https://doi.org/10.1143/PTP.32.37. [p. 26]

[169] Koji Satori, Hiroyuki Shiba, Osamu Sakai, and Yukihiro Shimizu. *Numerical Renormalization Group Study of Magnetic Impurities in Superconductors*. Journal of the Physical Society of Japan, **61**(9):3239–3254 (Sep 1992). https://doi.org/10.1143/JPSJ.61.3239. [pp. 26 and 81]

[170] Osamu Sakai, Yukihiro Shimizu, Hiroyuki Shiba, and Koji Satori. *Numerical Renormalization Group Study of Magnetic Impurities in Superconductors. II. Dynamical Excitation Spectra and Spatial Variation of the Order Parameter*. Journal of the Physical Society of Japan, **62**(9):3181–3197 (Sep 1993). https://doi.org/10.1143/JPSJ.62.3181. [p. 26]

[171] Cătălin Paşcu Moca, Eugene Demler, Boldizsár Jankó, and Gergely Zaránd. *Spin-Resolved Spectra of Shiba Multiplets from Mn Impurities in ${\text{MgB}}_{2}$*. Physical Review B, **77**(17):174516 (May 2008). https://doi.org/10.1103/PhysRevB.77.174516. [p. 26]

[172] Michael E. Flatté and Jeff M. Byers. *Local Electronic Structure of Defects in Superconductors*. Physical Review B, **56**:11213–11231 (Nov 1997). https://doi.org/10.1103/PhysRevB.56.11213. [pp. 27 and 102]

[173] Thomas Hofe. *Electron Dynamics of Cs Covered Cu(111) : A Scanning Tunneling Spectroscopy Investigation at Low Temperatures*. Ph.D. thesis, Christian Albrechts Universität zu Kiel, Kiel (Jul 2006). https://macau.uni-kiel.de/receive/diss_mods_00001614. [p. 31]

[174] R. Gaisch, J. K. Gimzewski, B. Reihl, et al. *Low-Temperature Ultra-High-Vacuum Scanning Tunneling Microscope*. Ultramicroscopy, **42–44**:1621–1626 (Jul 1992). https://doi.org/10.1016/0304-3991(92)90495-6. [p. 31]

[175] *USM1300 | UNISOKU Co., Ltd.* http://www.unisoku.com/products/usm1300.html. [p. 31]

[176] David Nečas and Petr Klapetek. *Gwyddion: An Open-Source Software for SPM Data Analysis.* Open Physics, **10**(1):181–188 (Feb 2012). https://doi.org/10.2478/s11534-011-0096-2. [p. 32]

[177] F. H. Moser and A. L. Thomas. *The Phthalocyanines. Vol. 2 Manufacture and Applications.* CRC Press, Boca Raton, FL, United States (Jan 1983). https://www.osti.gov/biblio/5524912. [p. 33]

[178] Peter Gregory. *Industrial Applications of Phthalocyanines.* Journal of Porphyrins and Phthalocyanines, **4**(4):432–437 (Jun 2000). https://doi.org/10.1002/(SICI)1099-1409(200006/07)4:4<432::AID-JPP254>3.0.CO;2-N. [p. 33]

[179] Miles A. Dahlen. *The Phthalocyanines A New Class of Synthetic Pigments and Dyes.* Industrial & Engineering Chemistry, **31**(7):839–847 (Jul 1939). https://doi.org/10.1021/ie50355a012. [p. 33]

[180] Makoto Iwase, Atsushi Suzuki, Tsuyoshi Akiyama, and Takeo Oku. *Fabrication and Characterization of Phthalocyanine-Based Organic Solar Cells.* Materials Sciences and Applications, **5**(5):278–284 (Mar 2014). https://doi.org/10.4236/msa.2014.55033. [p. 33]

[181] Karen Loraine Macena Santos, Rafaella Moreno Barros, Diego Paulo da Silva Lima, et al. *Prospective Application of Phthalocyanines in the Photodynamic Therapy against Microorganisms and Tumor Cells: A Mini-Review.* Photodiagnosis and Photodynamic Therapy, **32**:102032 (Dec 2020). https://doi.org/10.1016/j.pdpdt.2020.102032. [p. 33]

[182] J. Michael Gottfried. *Surface Chemistry of Porphyrins and Phthalocyanines.* Surface Science Reports, **70**(3):259–379 (Nov 2015). https://doi.org/10.1016/j.surfrep.2015.04.001. [p. 33]

[183] Clément Barraud, Karim Bouzehouane, Cyrile Deranlot, et al. *Unidirectional Spin-Dependent Molecule-Ferromagnet Hybridized States Anisotropy in Cobalt Phthalocyanine Based Magnetic Tunnel Junctions.* Physical Review Letters, **114**(20):206603 (2015). https://doi.org/10.1103/PhysRevLett.114.206603. [p. 38]

[184] Mirko Cinchetti, V. Alek Dediu, and Luis E. Hueso. *Activating the Molecular Spinterface.* Nature Materials, **16**(5):507–515 (2017). https://doi.org/10.1038/nmat4902. [p. 38]

[185] Sophie Delprat, Marta Galbiati, Sergio Tatay, et al. *Molecular Spintronics: The Role of Spin-Dependent Hybridization.* Journal of Physics D: Applied Physics, **51**(47):473001 (2018). https://doi.org/10.1088/1361-6463/aad9dc. [p. 38]

[186] Xi Chen, Ying-Shuang Fu, Shuai-Hua Ji, et al. *Probing Superexchange Interaction in Molecular Magnets by Spin-Flip Spectroscopy and Microscopy.* Physical Review Letters, **101**(19):197208 (2008). https://doi.org/10.1103/PhysRevLett.101.197208. [p. 38]

[187] Aitor Mugarza, Cornelius Krull, Roberto Robles, et al. *Spin Coupling and Relaxation Inside Molecule–Metal Contacts.* Nature Communications, **2**:490 (2011). https://doi.org/10.1038/ncomms1497. [pp. 38, 41, and 43]

[188] Tadahiro Komeda, Hironari Isshiki, Jie Liu, et al. *Observation and Electric Current Control of a Local Spin in a Single-Molecule Magnet.* Nature Communications, **2**:217 (2011).

https://doi.org/10.1038/ncomms1210. [p. 38]

[189] Timothy Moorsom, May Wheeler, Taukeer Mohd Khan, et al. *Spin-Polarized Electron Transfer in Ferromagnet / C_{60} Interfaces*. Physical Review B, **90**(12):125311 (2014). https://doi.org/10.1103/PhysRevB.90.125311. [p. 38]

[190] Manuel Gruber, Fatima Ibrahim, Samy Boukari, et al. *Exchange Bias and Room-Temperature Magnetic Order in Molecular Layers*. Nature Materials, **14**(10):981–984 (2015). https://doi.org/10.1038/nmat4361. [p. 38]

[191] Fatma Al Ma'Mari, Timothy Moorsom, Gilberto Teobaldi, et al. *Beating the Stoner Criterion Using Molecular Interfaces*. Nature, **524**(7563):69–73 (2015). https://doi.org/10.1038/nature14621. [p. 38]

[192] Maider Ormaza, Roberto Robles, Nicolas Bachellier, et al. *On-Surface Engineering of a Magnetic Organometallic Nanowire*. Nano Letters, **16**(1):588–593 (2016). https://doi.org/10.1021/acs.nanolett.5b04280. [p. 38]

[193] Jesús Martínez-Blanco, Christophe Nacci, Steven C. Erwin, et al. *Gating a Single-Molecule Transistor With Individual Atoms*. Nature Physics, **11**(8):640–644 (2015). https://doi.org/10.1038/nphys3385. [p. 38]

[194] Niko Pavliček, Ingmar Swart, Judith Niedenführ, Gerhard Meyer, and Jascha Repp. *Symmetry Dependence of Vibration-Assisted Tunneling*. Physical Review Letters, **110**(13):136101 (2013). https://doi.org/10.1103/PhysRevLett.110.136101. [pp. 40 and 55]

[195] Chao Li, Zhongping Wang, Yan Lu, Xiaoqing Liu, and Li Wang. *Conformation-Based Signal Transfer and Processing at the Single-Molecule Level*. Nature Nanotechnology, **12**(11):1071–1076 (2017). https://doi.org/10.1038/nnano.2017.179. [p. 41]

[196] J. Kröger, H. Jensen, R. Berndt, R. Rurali, and N. Lorente. *Molecular Orbital Shift of Perylenetetracarboxylic-Dianhydride on Gold*. Chemical Physics Letters, **438**:249–253 (2007). https://doi.org/10.1016/j.cplett.2007.03.001. [p. 43]

[197] Fabian Mohn, Leo Gross, Nikolaj Moll, and Gerhard Meyer. *Imaging the Charge Distribution Within a Single Molecule*. Nature Nanotechnology, **7**(4):227–231 (2012). https://doi.org/10.1038/nnano.2012.20. [p. 45]

[198] Peter Liljeroth, Jascha Repp, and Gerhard Meyer. *Current-Induced Hydrogen Tautomerization and Conductance Switching of Naphthalocyanine Molecules*. Science, **317**(5842):1203–1206 (2007). https://doi.org/10.1126/science.1144366. [pp. 45 and 46]

[199] Jens Kügel, Aimee Sixta, Markus Böhme, Andreas Krönlein, and Matthias Bode. *Breaking Degeneracy of Tautomerization—Metastability From Days to Seconds*. ACS Nano, **10**(12):11058–11065 (2016). https://doi.org/10.1021/acsnano.6b05924. [pp. 45 and 46]

[200] Alexander Weismann, Jan Homberg, Manuel Gruber, and Richard Berndt. *Anderson Impurity Model Parameters from Spectroscopy of Impurities on Superconductors*. Unpublished. [pp. 47, 57, and 127]

[201] J.-D. Pillet, P. Joyez, Rok Žitko, and M. F. Goffman. *Tunneling Spectroscopy of a Single Quantum Dot Coupled to a Superconductor: From Kondo Ridge to Andreev Bound States.* Physical Review B, **88**:045101 (2013). `https://doi.org/10.1103/PhysRevB.88.045101`. [p. 48]

[202] P. Wahl, L. Diekhöner, M. A. Schneider, and K. Kern. *Background Removal in Scanning Tunneling Spectroscopy of Single Atoms and Molecules on Metal Surfaces.* Review of Scientific Instruments, **79**(4):043104 (Apr 2008). `https://doi.org/10.1063/1.2907533`. [p. 50]

[203] Chao Li, Zhongping Wang, Yan Lu, Xiaoqing Liu, and Li Wang. *Conformation-Based Signal Transfer and Processing at the Single-Molecule Level.* Nature Nanotechnology, **12**(11):1071–1076 (Nov 2017). `https://doi.org/10.1038/nnano.2017.179`. [p. 51]

[204] John P. Perdew, Kieron Burke, and Matthias Ernzerhof. *Generalized Gradient Approximation Made Simple.* Physical Review Letters, **77**(18):3865–3868 (1996). `https://doi.org/10.1103/PhysRevLett.77.3865`. [pp. 58 and 93]

[205] Florian Weigend and Reinhart Ahlrichs. *Balanced Basis Sets of Split Valence, Triple Zeta Valence and Quadruple Zeta Valence Quality for H to Rn: Design and Assessment of Accuracy.* Physical Chemistry Chemical Physics, **7**(18):3297–3305 (2005). `https://doi.org/10.1039/B508541A`. [p. 58]

[206] Stefan Grimme, Jens Antony, Stephan Ehrlich, and Helge Krieg. *A Consistent and Accurate Ab Initio Parametrization of Density Functional Dispersion Correction (DFT-D) for the 94 Elements H-Pu.* The Journal of Chemical Physics, **132**(15):154104 (2010). `https://doi.org/10.1063/1.3382344`. [p. 58]

[207] C. Julian Chen. *Introduction to Scanning Tunneling Microscopy.* Oxford University Press, New York (1993). [p. 58]

[208] Katharina Scheil, Nicolás Lorente, Marie-Laure Bocquet, et al. *Adatom Coadsorption with Three-Dimensional Cyclophanes on Ag(111).* The Journal of Physical Chemistry C, **121**(45):25303–25308 (Nov 2017). `https://doi.org/10.1021/acs.jpcc.7b08953`. [p. 68]

[209] Yongfeng Wang, Jörg Kröger, Richard Berndt, and Werner Hofer. *Structural and Electronic Properties of Ultrathin Tin–Phthalocyanine Films on Ag(111) at the Single-Molecule Level.* Angewandte Chemie International Edition, **48**(7):1261–1265 (Feb 2009). `https://doi.org/10.1002/anie.200803305`. [p. 72]

[210] Marius Toader and Michael Hietschold. *Tuning the Energy Level Alignment at the SnPc/Ag(111) Interface Using an STM Tip.* The Journal of Physical Chemistry C, **115**(7):3099–3105 (Feb 2011). `https://doi.org/10.1021/jp111478v`. [pp. 72 and 127]

[211] Roman Forker, Marco Gruenewald, Falko Sojka, et al. *Fraternal Twins: Distinction between PbPc and SnPc by Their Switching Behaviour in a Scanning Tunnelling Microscope.* Journal of Physics: Condensed Matter, **31**(13):134004 (Feb 2019). `https://doi.org/10.1088/1361-648X/aafeae`. [pp. 72 and 127]

[212] Ruoning Li, Tianhao Wu, Yifan Wang, et al. *SnPc Molecules on Surfaces Studied by Scanning Tunneling Microscopy.* Journal of Cluster Science, **30**(5):1259–1266 (Sep 2019). `https://doi.org/10.1007/s10876-019-01610-y`. [pp. 72 and 127]

[213] J. D. Baran, J. A. Larsson, R. A. J. Woolley, et al. *Theoretical and Experimental Comparison of SnPc, PbPc, and CoPc Adsorption on Ag(111).* Physical Review B, **81**(7):075413 (Feb 2010). `https://doi.org/10.1103/PhysRevB.81.075413`. [pp. 74 and 123]

[214] Nobutsugu Hamamoto, Hiromitsu Sonoda, Michinori Sumimoto, Kenji Hori, and Hitoshi Fujimoto. *Theoretical Study on Crystal Polymorphism and Electronic Structure of Lead(II) Phthalocyanine Using Model Dimers.* RSC Advances, **7**(14):8646–8653 (2017). `https://doi.org/10.1039/C6RA27269J`. [p. 80]

[215] H. Yamane, H. Honda, H. Fukagawa, et al. *HOMO-band Fine Structure of OTi- and Pb-phthalocyanine Ultrathin Films: Effects of the Electric Dipole Layer.* Journal of Electron Spectroscopy and Related Phenomena, **137–140**:223–227 (Jul 2004). `https://doi.org/10.1016/j.elspec.2004.02.054`. [p. 80]

[216] A. Sperl, J. Kröger, and R. Berndt. *Electronic Superstructure of Lead Phthalocyanine on Lead Islands.* The Journal of Physical Chemistry A, **115**(25):6973–6978 (Jun 2011). `https://doi.org/10.1021/jp112169s`. [p. 81]

[217] Jan Homberg, Alexander Weismann, Troels Markussen, and Richard Berndt. *Resonance-Enhanced Vibrational Spectroscopy of Molecules on a Superconductor.* to be published in Physical Review Letters (Jul 2022). `https://journals.aps.org/prl/accepted/ef077Y92C1117d78d2d055b01f87192a27539570c`.
A preprint of the manuscript has been published on arXiv (Feb 2022): `http://arxiv.org/abs/2202.08820`. [pp. 85, 86, 87, 88, 89, 90, 91, and 92]

[218] Katharina J Franke and Jose Ignacio Pascual. *Effects of Electron–Vibration Coupling in Transport Through Single Molecules.* Journal of Physics: Condensed Matter, **24**(39):394002 (Oct 2012). `https://doi.org/10.1088/0953-8984/24/39/394002`. [pp. 86 and 87]

[219] Benjamin Doppagne, Michael C. Chong, Etienne Lorchat, et al. *Vibronic Spectroscopy with Submolecular Resolution from STM-Induced Electroluminescence.* Physical Review Letters, **118**:127401 (Mar 2017). `https://doi.org/10.1103/PhysRevLett.118.127401`. [p. 86]

[220] Francesca Matino, Guillaume Schull, Felix Köhler, et al. *Electronic Decoupling of a Cyclophane from a Metal Surface.* PNAS, **108**(3):961–964 (2011). `https://doi.org/10.1073/pnas.1006661107`. [p. 86]

[221] F. Schwarz, Yongfeng Wang, Werner A. Hofer, et al. *Electronic and Vibrational States of Single Tin–Phthalocyanine Molecules in Double Layers on Ag(111).* The Journal of Physical Chemistry C, **119**(27):15716–15722 (2015). `https://doi.org/10.1021/acs.jpcc.5b03392`. [p. 86]

[222] X. H. Qiu, G. V. Nazin, and W. Ho. *Vibrationally Resolved Fluorescence Excited with Submolecular Precision.* Science, **299**:542–546 (2003). [p. 86]

[223] Z.-C. Dong, X.-L. Guo, A. S. Trifonov, et al. *Vibrationally Resolved Fluorescence from Organic Molecules near Metal Surfaces in a Scanning Tunneling Microscope.* Physical Review Letters, **92**:086801 (Feb 2004). `https://doi.org/10.1103/PhysRevLett.92.086801`. [p. 86]

[224] QuantumATK version T-2022.03, Synopsys QuantumATK (www.synopsys.com/silicon/quantumatk.html). [p. 88]

[225] Søren Smidstrup, Troels Markussen, Pieter Vancraeyveld, et al. *QuantumATK: an Integrated Platform of Electronic and Atomic-Scale Modelling Tools*. Journal of Physics: Condensed Matter, **32**(1):015901 (oct 2019). `https://doi.org/10.1088/1361-648x/ab4007`. [pp. 88 and 95]

[226] Matthias Scheffler. *The Influence of Lateral Interactions on the Vibrational Spectrum of Adsorbed CO*. Surface Science, **81**(2):562–570 (Mar 1979). `https://doi.org/10.1016/0039-6028(79)90120-1`. [p. 88]

[227] Michael Endlich, Anja Michl, Jan Hildisch, Stefan Müller, and Jörg Kröger. *Energy and Spectroscopic Line Shape of the C–O Stretch Mode on Ir(111) in the Presence of Organic Molecules*. The Journal of Physical Chemistry C, **120**(21):11490–11497 (Jun 2016). `https://doi.org/10.1021/acs.jpcc.6b01399`. [p. 88]

[228] Magnus Paulsson, Thomas Frederiksen, Hiromu Ueba, Nicolás Lorente, and Mads Brandbyge. *Unified Description of Inelastic Propensity Rules for Electron Transport through Nanoscale Junctions*. Physical Review Letters, **100**(22):226604 (Jun 2008). `https://doi.org/10.1103/PhysRevLett.100.226604`. [p. 89]

[229] J.-T. Lü, R. B. Christensen, G. Foti, et al. *Efficient Calculation of Inelastic Vibration Signals in Electron Transport: Beyond the Wide-Band Approximation*. Physical Review B, **89**:081405 (Feb 2014). `https://doi.org/10.1103/PhysRevB.89.081405`. [pp. 94 and 96]

[230] Tue Gunst, Troels Markussen, Kurt Stokbro, and Mads Brandbyge. *Inelastic Vibrational Signals in Electron Transport across Graphene Nanoconstrictions*. Physical Review B, **93**:245415 (Jun 2016). `https://doi.org/10.1103/PhysRevB.93.245415`. [pp. 94 and 96]

[231] T. Frederiksen, M. Paulsson, M. Brandbyge, and A.-P. Jauho. *Inelastic Transport Theory from First Principles: Methodology and Application to Nanoscale Devices*. Physical Review B, **75**:205413 (May 2007). `https://doi.org/10.1103/PhysRevB.75.205413`. [p. 94]

[232] Jochen Heyd, Gustavo E. Scuseria, and Matthias Ernzerhof. *Hybrid Functionals Based on a Screened Coulomb Potential*. The Journal of Chemical Physics, **118**(18):8207–8215 (2003). `https://doi.org/10.1063/1.1564060`. [p. 95]

[233] Jochen Heyd, Gustavo E. Scuseria, and Matthias Ernzerhof. *Erratum: "Hybrid Functionals Based on a Screened Coulomb Potential" [J. Chem. Phys. 118, 8207 (2003)]*. The Journal of Chemical Physics, **124**(21):219906 (2006). `https://doi.org/10.1063/1.2204597`, `https://doi.org/10.1063/1.2204597`. [p. 95]

[234] S. L. Dudarev, G. A. Botton, S. Y. Savrasov, C. J. Humphreys, and A. P. Sutton. *Electron-Energy-Loss Spectra and the Structural Stability of Nickel Oxide: An LSDA+U Study*. Physical Review B, **57**:1505–1509 (Jan 1998). `https://doi.org/10.1103/PhysRevB.57.1505`. [p. 95]

[235] Richard M. Badger. *A Relation Between Internuclear Distances and Bond Force Constants*. The Journal of Chemical Physics, **2**(3):128–131 (Mar 1934). `https://doi.org/10.1063/1.1749433`. [p. 118]

[236] J. G. Rodrigo, H. Suderow, and S. Vieira. *On the Use of STM Superconducting Tips at Very Low Temperatures*. The European Physical Journal B - Condensed Matter and Complex Systems, **40**(4):483–488 (Aug 2004). https://doi.org/10.1140/epjb/e2004-00273-y. [p. 120]

[237] Andreas Burtzlaff, Alexander Weismann, Mads Brandbyge, and Richard Berndt. *Shot Noise as a Probe of Spin-Polarized Transport through Single Atoms*. Physical Review Letters, **114**(1):016602 (Jan 2015). https://doi.org/10.1103/PhysRevLett.114.016602. [p. 122]

[238] A. Lee, D. Kim, S.-H. Choi, et al. *Theoretical Study on Phthalocyanine, Pyrazinoporphyrazine and Their Complexation with Mg2+ and Zn2+*. Molecular Simulation, **36**(3):192–198 (Mar 2010). https://doi.org/10.1080/08927020903177641. [p. 123]

[239] Päivi Järvinen, Sampsa K. Hämäläinen, Mari Ijäs, Ari Harju, and Peter Liljeroth. *Self-Assembly and Orbital Imaging of Metal Phthalocyanines on a Graphene Model Surface*. The Journal of Physical Chemistry C, **118**(24):13320–13325 (Jun 2014). https://doi.org/10.1021/jp504813v. [p. 123]

[240] T. Klitsner, R. S. Becker, and J. S. Vickers. *Observation of the Effect of Tip Electronic States on Tunnel Spectra Acquired with the Scanning Tunneling Microscope*. Physical Review B, **41**(6):3837–3840 (Feb 1990). https://doi.org/10.1103/PhysRevB.41.3837. [p. 124]

[241] J E Griffith and G P Kochanski. *Scanning Tunneling Microscopy*. Annual Review of Materials Science, **20**(1):219–244 (1990). https://doi.org/10.1146/annurev.ms.20.080190.001251. [p. 124]

[242] Michinori Sumimoto, Teruyuki Honda, Yukio Kawashima, Kenji Hori, and Hitoshi Fujimoto. *Theoretical and Experimental Investigation on the Electronic Properties of the Shuttlecock Shaped and the Double-Decker Structured Metal Phthalocyanines, MPc and M(Pc)$_2$ (M = Sn and Pb)*. Dalton Transactions, **41**(23):7141–7150 (2012). https://doi.org/10.1039/C2DT30187C. [pp. 124 and 125]

[243] Yuexing Zhang, Xianxi Zhang, Zhongqiang Liu, Hui Xu, and Jianzhuang Jiang. *Comparative Density Functional Theory Study of the Structures and Properties of Metallophthalocyanines of Group IV B*. Vibrational Spectroscopy, **40**(2):289–298 (Mar 2006). https://doi.org/10.1016/j.vibspec.2005.11.004. [pp. 124 and 125]

[244] Diola Bagayoko. *Understanding Density Functional Theory (DFT) and Completing It in Practice*. AIP Advances, **4**(12):127104 (Dec 2014). https://doi.org/10.1063/1.4903408. [p. 125]

[245] A. Gerlach, T. Hosokai, S. Duhm, et al. *Orientational Ordering of Nonplanar Phthalocyanines on Cu(111): Strength and Orientation of the Electric Dipole Moment*. Physical Review Letters, **106**(15):156102 (Apr 2011). https://doi.org/10.1103/PhysRevLett.106.156102. [p. 135]

[246] Tianchao Niu, Miao Zhou, Jialin Zhang, Yuanping Feng, and Wei Chen. *Dipole Orientation Dependent Symmetry Reduction of Chloroaluminum Phthalocyanine on Cu(111)*. The Journal of Physical Chemistry C, **117**(2):1013–1019 (Jan 2013). https://doi.org/10.1021/jp310196k. [p. 135]

[247] Xue Zhang, Christoph Wolf, Yu Wang, et al. *Electron Spin Resonance of Single Iron Phthalocyanine Molecules and Role of Their Non-Localized Spins in Magnetic Interactions.* Nature Chemistry, **14**(1):59–65 (Jan 2022). `https://doi.org/10.1038/s41557-021-00827-7`. [p. 142]

[248] Leslie M. Schoop, Lilia S. Xie, Ru Chen, et al. *Dirac metal to topological metal transition at a structural phase change in* Au_2Pb *and prediction of* $\mathbb{Z}_2$ *topology for the superconductor.* Physical Review B, **91**(21):214517 (Jun 2015). `https://doi.org/10.1103/PhysRevB.91.214517`. [p. 147]

[249] Yun Wu, Gil Drachuck, Lin-Lin Wang, et al. *Electronic structure of the topological superconductor candidate* Au_2Pb*.* Physical Review B, **98**(16):161107 (Oct 2018). `https://doi.org/10.1103/PhysRevB.98.161107`. [p. 147]

[250] William Chandler Roberts-Austen. *On the Diffusion of Metals.* Philosophical Transactions of the Royal Society of London. Series A, **187**:383–415 (Jan 1896). `https://doi.org/10.1098/rsta.1896.0010`. [p. 147]

[251] W. Seith and A. Keil. *Diffusion in Au-Pb- Und Ag-Pb-Legierungen.* Zeitschrift für Physikalische Chemie, **22B**(1):350–358 (Mar 1933). `https://doi.org/10.1515/zpch-1933-2231`. [p. 147]

[252] C. Weaver and L. C. Brown. *Diffusion in Evaporated Films of Gold-Lead.* Philosophical Magazine, **8**(92):1379–1393 (Aug 1963). `https://doi.org/10.1080/14786436308207301`. [p. 147]

[253] H. Okamoto and T. B. Massalski. *The Au-Pb (Gold-Lead) System.* Bulletin of Alloy Phase Diagrams, **5**(3):276–284 (Jun 1984). `https://doi.org/10.1007/BF02868553`. [p. 147]

[254] H. L. Caswell. *Superconducting properties of* $AuPb_3$ *and* $AuPb_2$*.* Solid State Communications, **2**(10):323–324 (Oct 1964). `https://doi.org/10.1016/0038-1098(64)90536-8`. [p. 147]

[255] Lawrence E. Davis, Noel C. MacDonald, Paul W. Palmberg, Gerald E. Riach, and Roland E. Weber. *Handbook of Auger Electron Spectroscopy.* Physical Electronics Industries, Eden Prairie, Minnesota, second edn. (1976). [pp. 152 and 153]

[256] John Lannon and Charter Stinespring. *Auger Electron Spectroscopy in Analysis of Surfaces.* In R.A. Meyers (ed.), *Encyclopedia of Analytical Chemistry*, pp. 9033–9047. John Wiley and Sons Ltd, Chichester (2000). ISBN 978-0-470-02731-8. `https://doi.org/10.1002/9780470027318.a2503`. [p. 153]

[257] The Materials Project. *Materials Data on* Pb_3Au (2020). `https://doi.org/10.17188/1204821`. [pp. 153 and 154]

[258] R. Wang and B. C. Giessen. *A B-Element-Rich Representative of the* α*-*V_3S *Type:* $AuPb_3$*.* Metallurgical and Materials Transactions B, **2**(8):2195 (Aug 1971). `https://doi.org/10.1007/BF02917550`. [p. 153]

[259] J. E. Hirsch. *Slope of the Superconducting Gap Function in* $\mathrm{Bi_2Sr_2CaCu_2O_{8+\delta}}$ *Measured by Vacuum Tunneling Spectroscopy.* Physical Review B, **59**(18):11962–11973 (May 1999). `https://doi.org/10.1103/PhysRevB.59.11962`. [p. 157]

[260] Cristoforo Benvenuti and Paolo Chiggiato. *Obtention of Pressures in the* 10^{-14} *Torr Range by Means of a Zr-V-Fe Non Evaporable Getter.* Vacuum, **44**(5):511–513 (May 1993). https://doi.org/10.1016/0042-207X(93)90084-N. [p. 161]

[261] P. Chiggiato. *Production of Extreme High Vacuum with Non Evaporable Getters.* Physica Scripta, **T71**:9–13 (Jan 1997). https://doi.org/10.1088/0031-8949/1997/T71/002. [p. 161]

[262] C. Benvenuti, J. M. Cazeneuve, P. Chiggiato, et al. *A Novel Route to Extreme Vacua: The Non-Evaporable Getter Thin Film Coatings.* Vacuum, **53**(1):219–225 (May 1999). https://doi.org/10.1016/S0042-207X(98)00377-7. [p. 161]

[263] J. M. Jimenez. *LHC: The World's Largest Vacuum Systems Being Operated at CERN.* Vacuum, **84**(1):2–7 (Aug 2009). https://doi.org/10.1016/j.vacuum.2009.05.015. [p. 161]

[264] Cristoforo Benvenuti, Paolo Chiggiato, Pedro Costa Pinto, et al. *Vacuum Properties of TiZrV Non-Evaporable Getter Films.* Vacuum, **60**(1):57–65 (Jan 2001). https://doi.org/10.1016/S0042-207X(00)00246-3. [p. 161]

[265] SAES Getters. *Capacitorr NEG Pumps.* https://www.saesgetters.com/products-functions/products/vacuum-pumps/capacitorr-neg-pumps. [p. 161]

[266] SAES Getters. *St 707 – Non Evaporable Getters Activatable at Low Temperatures.* https://psec.uchicago.edu/getters/St%20707%20Brochure.pdf. [pp. 161, 168, and 169]

[267] C. Boffito, B. Ferrario, P. della Porta, and L. Rosai. *A Nonevaporable Low Temperature Activatable Getter Material.* Journal of Vacuum Science and Technology, **18**(3):1117–1120 (Apr 1981). https://doi.org/10.1116/1.570852. [p. 161]

[268] SAES Getters. *St 707 Strips* (2012). https://www.saesgetters.com/sites/default/files/St%20707%20Strips_0.pdf. [p. 161]

[269] J. R. Davis. *ASM Specialty Handbook: Copper and Copper Alloys.* ASM International (2001). ISBN 0-87170-726-8. [p. 161]

[270] Lars Mühlenberend. *Aufbau eines Ultrahochvakuum-Tieftemperatur-Rastertunnelmikroskops.* PhD thesis, Christian Albrechts Universität zu Kiel, Kiel (Feb 2015). https://macau.uni-kiel.de/receive/diss_mods_00016531. [pp. 164 and 168]

[271] Walter Umrath. *Grundlagen der Vakuumtechnik* (1997).
Leybold (2016) available online: https://www.leyboldproducts.de/media/pdf/10/0f/8b/FVT_Grundlagen_der_Vakuumtechnik_DE591eea2256c34.pdf. [pp. 165 and 167]

[272] Pfeiffer Vacuum Technology AG. *Betriebsanleitung – Turbomolekular-Drag-Pumpe mit Antriebselektronik TC 600.* Pfeiffer Vacuum Technology AG (2003). [p. 165]

[273] Takashi Kikuchi, Hirokazu Tanaka, Akio Toyoshima, and Kazuhiko Mase. *Construction of Simple Non-Evaporable Getter Assemblies Using St707 Strips.* Journal of the Vacuum Society of Japan, **53**(9) (2010). https://doi.org/10.3131/jvsj2.53.533. [p. 167]

[274] Takashi Kikuchi, Kazuhiko Mase, and Fumio Watanabe. *Construction of Simple Non-Evaporable Getter Assemblies Using St 707 Strips or St 172 Modules.* Journal of the Vacuum Society of Japan, **55**(1) (2012). https://doi.org/10.3131/jvsj2.55.21. [p. 167]

[275] Hiraku Kodama, Shinya Ohno, Masatoshi Tanaka, et al. *Low-Cost, High-Performance Nonevaporable Getter Pumps Using Nonevaporable Getter Pills*. Journal of Vacuum Science & Technology A, **34**(5):051601 (Aug 2016). `https://doi.org/10.1116/1.4961050`. [p. 167]

[276] Kazuhiko Mase, Masato Tanaka, Naoya Ida, Hiraku Kodama, and Takashi Kikuchi. *Development of Low-Cost, High-Performance Non-Evaporable Getter (NEG) Pumps*. AIP Conference Proceedings, **1741**(1):030015 (Jul 2016). `https://doi.org/10.1063/1.4952838`. [p. 167]

[277] SAES Getters. *St 171® and St 172 – Sintered Porous Getters* (2007). `https://www.saesgetters.com/sites/default/files/St%20171%20-%20172_Sintered%20Porous%20Getters_1.pdf`. [p. 167]

[278] SAES Group. *CapaciTorr® Pumps*. `https://www.saesgetters.com/sites/default/files/CapaciTorr%20UHV%20general%20%2B%20D%20%20pumps.pdf`. [p. 167]

[279] SAES Getters. *SORB-AC® Getter Wafer Modules and Panels (B.VS.09.02)*. `https://www.jlab.org/accel/inj_group/vacuum/WP_modules.pdf`. [p. 168]

[280] SAES Getters. *St707 - Non Evaporable Getters Activatable at Low Temperatures*. (as cited earlier). The effective surface area of the St 707 strips is given as $1500\,\mathrm{cm}^2\,\mathrm{g}^{-1}$ in this Reference. However, there is probably a typing error in the unit, and instead a value of $1500\,\mathrm{cm}^2\,\mathrm{m}^{-1}$ is assumed. [p. 168]

[281] Eugen Glueckauf and G. P. Kitt. *The Hydrogen Content of Atmospheric Air at Ground Level*. Quarterly Journal of the Royal Meteorological Society, **83**(358):522–528 (1957). `https://doi.org/10.1002/qj.49708335808`. [p. 169]